LEABHARLANN CHOLÁISTE NA TRÍONÓIDE, BAILE ÁTHA CLIATH | TRINITY COLLEGE LIBRARY DUBLIN
Ollscoil Átha Cliath | The University of Dublin

Terms and Conditions of Use of Digitised Theses from Trinity College Library Dublin

Copyright statement

All material supplied by Trinity College Library is protected by copyright (under the Copyright and Related Rights Act, 2000 as amended) and other relevant Intellectual Property Rights. By accessing and using a Digitised Thesis from Trinity College Library you acknowledge that all Intellectual Property Rights in any Works supplied are the sole and exclusive property of the copyright and/or other IPR holder. Specific copyright holders may not be explicitly identified. Use of materials from other sources within a thesis should not be construed as a claim over them.

A non-exclusive, non-transferable licence is hereby granted to those using or reproducing, in whole or in part, the material for valid purposes, providing the copyright owners are acknowledged using the normal conventions. Where specific permission to use material is required, this is identified and such permission must be sought from the copyright holder or agency cited.

Liability statement

By using a Digitised Thesis, I accept that Trinity College Dublin bears no legal responsibility for the accuracy, legality or comprehensiveness of materials contained within the thesis, and that Trinity College Dublin accepts no liability for indirect, consequential, or incidental, damages or losses arising from use of the thesis for whatever reason. Information located in a thesis may be subject to specific use constraints, details of which may not be explicitly described. It is the responsibility of potential and actual users to be aware of such constraints and to abide by them. By making use of material from a digitised thesis, you accept these copyright and disclaimer provisions. Where it is brought to the attention of Trinity College Library that there may be a breach of copyright or other restraint, it is the policy to withdraw or take down access to a thesis while the issue is being resolved.

Access Agreement

By using a Digitised Thesis from Trinity College Library you are bound by the following Terms & Conditions. Please read them carefully.

I have read and I understand the following statement: All material supplied via a Digitised Thesis from Trinity College Library is protected by copyright and other intellectual property rights, and duplication or sale of all or part of any of a thesis is not permitted, except that material may be duplicated by you for your research use or for educational purposes in electronic or print form providing the copyright owners are acknowledged using the normal conventions. You must obtain permission for any other use. Electronic or print copies may not be offered, whether for sale or otherwise to anyone. This copy has been supplied on the understanding that it is copyright material and that no quotation from the thesis may be published without proper acknowledgement.

DEVELOPMENT AND OPTIMISATION OF OPTICAL INTERFEROMETRIC TECHNIQUES FOR SURFACE METROLOGY

A thesis submitted for the degree of Doctor of Philosophy to the Department of Pure and Applied Physics University of Dublin

June 1999

By
Brian Bowe B. Sc (Appl. Sc.)

School of Physics
Dublin Institute of Technology

TRINITY COLLEGE
- 7 FEB 2000
LIBRARY DUBLIN

Thesis
5321

Acknowledgements

During the years it took to complete this thesis I received advice, support and encouragement from many people. I would particularly like to thank my supervisor at the Dublin Institute of Technology, Dr Vincent Toal for his constant support, encouragement and practical help.

I would also like to thank my research colleagues in the Laboratory of Holographic applications and the Centre for Industrial and Engineering Optics. I would especially like to thank Dr. Suzanne Martin for all her help and always being there when help was needed.

Thanks also to the staff of the School of Physics in Kevin Street for the valuable assistance. I am particularly indebted to Mr. Joe Keogh and Mr. James Callis for all their help and advice with the computer and electronic aspects of my research. I would like to acknowledge the help and friendship of the postgraduate students, especially Tara Kneafsey for her work on shearing interferometry.

In the European Commission Joint Research Centre (JRC), Ispra, Italy, I would like to thank Dr Daniel Albrecht and Mr. Andreas Langhoff for their input into my research while at the JRC. I am grateful to Ing. A. C. Lucia, for allowing me the opportunity to work in the JRC. Thanks also to Dr. Robert Kenny for his assistance and advice. Particular thanks to Dr. Colin Forno for his input into my research and giving me a greater understanding of interferometry. I would particularly like to thank Dr. Maurice Whelan, for our discussions on optical metrology and his help and friendship.

Special thanks to my family for their support and encouragement over the last four years and especially to my wife Carol without whom this would not have been possible

DECLARATION

This thesis has not been submitted as an exercise for a degree at any other university. Apart from the assistance mentioned in the acknowledgements, the work is entirely my own. I agree that Trinity College Library may lend or copy this thesis upon request.

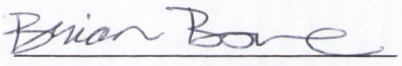

Development and Optimisation of Optical Interferometric Techniques for Surface Metrology.

Brian Bowe

Abstract

Optical surface metrology techniques offer many advantages over conventional methods. These include a greater sensitivity, improved lateral and vertical resolution, non-contact and full-field measurements and the fact that they are not subject to electromagnetic influence. However there has been reluctance in industry to adopt these techniques. Reasons include complicated operation and analysis procedures, the use of high-power and dangerous lasers, expensive systems and the requirement for a mechanically stable environment. The objective of the research described in this thesis was to utilise recent developments in relevant technologies (physics, computer technology, and data acquisition) to develop industrial prototype systems.

The new systems described have been developed as optical interferometers for high precision surface metrology. They have been optimised so that they can be used easily in an industrial environment. In order to facilitate their use in industry, the systems have been designed to be stable, portable, and robust. User-friendly software has been developed to control the interferometric systems and to facilitate efficient and accurate data analysis.

The first system is a new white light interferometric surface profiler. This system has proven to be a very efficient surface profiler capable of profiling optically smooth surfaces with a resolution of 0.06 μm. It has a theoretically unlimited range, allowing the system to measure step heights of the order of a few centimetres with an error of only 0.03 μm.

The second system is a dual in-plane electronic speckle pattern interferometer used for measuring complete in-plane surface displacements. This innovative system has no moving parts and still allows the quantitative measurement of displacement in both the horizontal and vertical directions. It uses liquid crystal devices for both switching between illumination planes and for phase shifting. Advanced control software has also been developed, which controls and synchronises the beam illumination with the image acquisition. It also performs the image analysis to produce surface displacement maps.

A third system that uses both white light and speckle techniques has also been developed as a versatile surface profiler. This system has a large range and high sensitivity and unlike most commercial systems is not limited to any particular surface finish.

All three systems have been extensively tested with excellent results. Tests were also carried out on the liquid crystal devices to characterise their behaviour and to determine their suitability for use in interferometry.

Summary

This thesis is the result of an extensive and detailed investigation into optical interferometric systems for surface metrology. It describes the development and application of three interferometric systems as well as extensive testing carried out to characterise liquid crystal devices.

Chapter 1 begins by introducing the basic ideas of surface metrology and non-destructive testing (NDT), along with its uses and applications. An overview is presented of both conventional and optical techniques used for surface metrology.

Chapter 2 describes the theory of the physics of coherence and interferometry. Detailed descriptions of white light interferometry, its uses, data analysis and currently available systems are given. The theoretical background of the speckle effect is outlined along with a brief history of the development of the electronic speckle pattern interferometry (ESPI) technique. The different optical configurations and applications are described as well as the current state of the technology. This chapter concludes by describing fringe and phase analysis procedures.

Chapter 3 details the development and optimisation of the white light interferometric surface profiler. The data acquisition and analysis algorithms are described and results from tests carried out using this profiler are presented.

Chapter 4 details the development and optimisation of the dual in-plane electronic speckle pattern interferometer. The different systems developed during the course of the research are described along with extensive tests carried out to assess the system's performance.

Chapter 5 describes work carried out in the European Commission Joint Research Centre on the development of a dual white light and ESPI contouring system.

Chapter 6 is a study of the characteristics of liquid crystals devices and in particular the use of liquid crystal devices as phase shifters and polarisation rotators. These tests were carried out to ensure that the devices could be used in the ESPI systems described in the previous chapters. Although, this is presented as the last experimental chapter, the results from these tests are used in Chapter 4.

All chapters are liberally referenced allowing the reader to refer to relevant ideas or alternative techniques.

The thesis concludes by outlining the progress made and the conclusions reached. Three surface metrology techniques have been developed and optimised. Each system is found to be efficient and constitutes a significant improvement on previously described systems.

Relevant Publications and Presentations

Journals

1. B. Bowe and V. Toal, "White light interferometric surface profiler", Optical Engineering, 37, 1796-1799, 1998.
2. B, Bowe, S. Martin, V. Toal, A. Langhoff, and M. Whelan, "Dual in-plane electronic speckle pattern interferometry system with electro-optical switching and phase shifting" Appl. Opt., 38, 666-673, 1999.
3. V. Toal, S. Martin, A. Burden, B. Bowe, "Non-destructive testing using electronic speckle pattern interferometry", Insight, British Journal of Non-Destructive Testing, 41, 135-140, 1999.

Conference Proceedings

1. B. Bowe and V. Toal, "A white light interferometric surface profiler", OESI Optical Engineering Conf. Proc., Dublin, Ireland, May 1996. (Award for best presentation)
2. B. Bowe and V. Toal, "A white light interferometer for surface profiling", IOP Applied Optics and Opto-Electronics Conf. Proc., Reading, England, September 1996.
3. V. Toal, B. Bowe, S. Martin, "Innovative ESPI system", Conf. Proc., Conf. Proc., OESI Optics and Opto-electronics, Galway, Ireland, May 1997.
4. B. Bowe and V. Toal, "A white light surface profiler" Conf. Proc., IOP Optical Sensing, Dublin, Ireland November 1997.
5. E. Cadoni, B. Bowe and D. Albrecht, "Application of ESPI technique to evaluate the crack propagation zone of pre-notched clay elements", International Conference on Applied Optical Metrology, Balatonfured, Hungary, June 1998.
6. B. Bowe, F. O'Neill, S. Sheridan, "The fabrication and testing of holographic plates using LabVIEW", Conf. Proc., Instrumentation and Control, Dublin, Ireland, June 1998.
7. B. Bowe, V. Toal and M. Whelan, "White Light and Speckle Interferometric Surface Profiler" International Workshop on Optical Measurement, April 13-15, Liverpool, England, April 1999.
8. V. Toal, S. Martin, B. Bowe, A. Burden, "ESPI in Non-destructive Testing", " International Workshop on Optical Measurement, April 13-15, Liverpool, England, April 1999.

European Reports

1. B. Bowe "Optimisation of Optical Metrology Techniques" European Commission Technical Note No.I.97.145, 1997.
2. B. Bowe and D. Albrecht, "In-plane ESPI tests on building materials", European Commission Technical Note No. I.98.1.57, 1998.

3. B. Bowe and M. Whelan, "Dual speckle and white light interferometric surface profiler", European Commission Technical Note No. I.99.08, 1999.
4. B. Bowe and M. Whelan, "Use of liquid crystal devices in active interferometry", European Commission Technical Note, To Be Published, 1999.

Conference Poster Presentations

1. B. Bowe, S. Martin, V. Toal, and M. Whelan, "Advanced electronic speckle pattern interferometry", IOP Spring Meeting, Waterford, Ireland, 1998.
2. F. O'Neill, B. Bowe, S. Martin, S. Sheridan, "Testing of Holographic Optical Elements", International Postgraduate Conference, Dublin, Ireland, November, 1998.
3. B. Bowe, A. Burden and V. Toal, "Electronic speckle pattern interferometry for non-destructive testing applications" IOP Spring Meeting, Cavan, Ireland, 1999.

Articles

1. B. Bowe and V. Toal, "Surface roughness by non-contact surface profilometry", The Irish Scientist Year Book 1996.
2. B. Bowe, "Holographic system automation using LabVIEW", National Instruments User Solutions, Spring, 1999.

CONTENTS

Chapter 1 Introduction **1**
1.1 Surface Metrology 1
1.2 Non-Destructive Testing of Materials 3
1.3 Surface Profiling 11
1.4 Research Objective 16

Chapter 2 Theory **19**
2.1 White Light Interferometers 19
2.2 Speckle Interferometers 49
2.3 Fringe Analysis 80

Chapter 3 White Light Interferometer **92**
3.1 Introduction 92
3.2 Development of White Light Profiler 93
3.3 Practical Considerations 103
3.4 Results 115
3.5 Conclusion 131

Chapter 4 Dual In-Plane ESPI system **134**
4.1 Introduction 134
4.2 Development of Prototype 136
4.3 System Operation 156
4.4 Measurement of Crack Propagation in Clay Components 162
4.5 Displacement and Strain Measurement 182
4.6 Quantitative Results from Phase Shifting 187
4.7 Discussion 195

Chapter 5 Dual Electronic Speckle Pattern Contouring / White Light Interferometer **198**
5.1 Introduction 198
5.2 Development of Optical System 201
5.3 Results 210
5.4 Conclusion 221

Chapter 6 Characterisation of Liquid Crystal modulators for use in active interferometers **224**
6.1 Introduction 224
6.2 Liquid Crystal devices 227
6.3 Experimental characterisation of Liquid Crystal modulators 240
6.4 Results 246
6.5 Conclusion 256

Chapter 7 Conclusions **260**
7.1 White Light Interferometer 260
7.2 Dual In-Plane ESPI System 261
7.3 Dual White Light and ESPI Contouring System 263
7.4 Summary 264

Appendix A 266
Appendix B 271
Appendix C 278
Appendix D 296
Appendix E 297

References 300

Chapter 1 Introduction

1.1 Surface Metrology

As manufacturing tolerances become tighter, there is a corresponding increase in the demands on metrology techniques for monitoring these tolerances [1]. The need for quality control and performance testing has become an integral part of the production procedure. Safety and quality standards are rising constantly due to legislation and the need to curtail costs associated with the repair of equipment and structures. High precision surface metrology techniques allow the exact surface parameters and the mechanical properties of materials to be ascertained [2]. The mechanical properties can be obtained by measuring the behaviour of the surface under known loading conditions. Surface metrology techniques can also be used for the detection of defects such as cracks and inhomogenities [3]. Surface metrology [4] can be divided into two categories; the measurement of the surface shape and roughness and the measurement of the surface behaviour under excitation.

There are many different techniques used to measure both surface shape and displacement and although optical techniques offer many advantages there has been reluctance in industry to adopt these techniques. The reasons for this include complicated operation and analysis procedures, the use of high-power and therefore dangerous lasers, expensive systems as well as the requirement for a mechanically stable environment. However, over the last few years there has been a significant increase in research into the development and applications of optical methods for surface metrology [5]. This has been due to a number of factors such as greater familiarity with laser techniques, the availability of new commercial equipment and developments in solid-state detector arrays and image processing. The advantages of the optical techniques over the more conventional techniques include a greater sensitivity, improved lateral and vertical resolution, non-contact, they allow a full field measurement and are not subject to electromagnetic

influence. Among the methods used are classical interferometry, holographic interferometry [6], moiré methods [7], speckle techniques [8], and white light interferometry [9].

Some of the techniques involve applying an excitation force to the material, which, when removed, is restored to its initial state. During the time when the material is subjected to the force, its behaviour is studied to obtain information about its mechanical properties. The techniques can also be used to locate cracks and flaws and to study the effects that these defects have on the overall performance of the material. There are many different non-destructive testing (NDT) techniques in use today, including acoustic emission [10], ultrasound [11], x-ray scanning [12], electrical strain gauging [13] and optical techniques [5].

The ability to measure accurately the surface profile of an object is also very important in many applications. The most common method used for the measurement of surface shape is stylus profilometry [14]. In this technique a mechanical transducer, called a stylus, is dragged across a surface and its movement in the vertical direction is recorded to obtain a surface profile. As this is a point measurement, the stylus is dragged across the surface many times until the whole surface or the area of interest has been mapped. Optical techniques are also used to measure surface shape but the commercial optical systems tend to be complex and relatively expensive [15].

The purpose of the research described in this thesis was to develop and optimise new advanced systems that could easily be used in an industrial environment. These new systems, which would make use of physical phenomena such as polarisation and variable retardance, would be stable, portable, robust and easy to use. The other objective of this research was to develop an efficient optical surface profiler, which uses a simple and inexpensive setup. In the next sections an overview of the non-optical and optical techniques for surface displacement measurement and surface profiling is given.

1.2 Non-Destructive Testing of Materials

1.2.1 Conventional Techniques

Non destructive testing is the technology by which standards of material quality, component reliability and systems safety are monitored and maintained. In the structural and mechanical engineering fields the measurement of object deformation under loading conditions can provide useful information about the mechanical properties of the material [16]. An understanding of the behaviour of the material under normal loading conditions is vital, as this provides information that can be used to prevent failure. The material behaviour can be used to identify samples with defects or inhomogeneities. In some instances it is not necessary to load the material, as certain techniques can still monitor the structure for defects and fatigue. Another test commonly performed is the measurement of crack propagation, which again provides information on the mechanical properties of the material. Various techniques are used to measure surface displacements, crack propagation or simply detect the presence of defects. These techniques include acoustic emission, ultrasound, x-ray scanning, electrical strain gauging and optical techniques.

1.2.1.1 Ultrasound

Ultrasound is one the most commonly used techniques for NDT [11]. A transducer that is coupled to a test object emits ultrasonic pulses in the frequency range 1 MHz to 20 MHz. The pulses travel though the object and are either reflected, diffracted or refracted by defects or discontinuities in the material. A receiver is used to detect the pulses on the other side of the material or, more typically, the returning echo signal. The loss in signal amplitude is then used to determine the existence of a defect and its size. The advantages of this technique include its ability to detect deep sub-surface defects, which cannot be detected by other NDT techniques. There is also no need to apply a force to the material. However, its disadvantages include complex image analysis [17,18] and the fact the ultrasound

transducer generally needs to be in direct contact with the test object or must have a suitable coupling medium between it and the object's surface, e.g. water. For this reason the technique tends not to be versatile and is usually designed with a specific application in mind. Although this is a non-optical technique, it is becoming very popular to use a pulsed laser to generate the ultrasonic wave [19,20].

1.2.1.2 Acoustic Emission

Many materials will, when subjected to stress, emit acoustic waves arising from energy released as the material undergoes plastic deformation and fracture [10]. These acoustic waves propagate through the material to the surface where they are detected using high sensitivity piezoelectric materials. The technique is commonly applied in the study of fatigue and crack propagation [21,22].

1.2.1.3 X-Ray Scanning

X-Rays are more widely known for biological applications than as an NDT technique for materials testing. However, because they have a high penetrating power they are useful for examining almost any structure [12]. The rays pass through the specimen and are detected at the other side usually by photographic film. As in the biological applications, the developed film shows up areas where attenuation is lowest as darker regions. The differences in intensity will be caused by differences in thickness and density of the object. In this way sub-surface defects are easily recognizable. The obvious disadvantage of this technique is the dangerous effects the radiation can have on biological tissue. The interpretation of the developed film also demands both experience and skill [23].

1.2.1.4 Electrical Transducers

The measurement of the deformations under loading conditions is usually obtained in mechanical tests by means of strain gauges applied directly to the object, or by displacement transducers connected at points of interest [13]. Variations in length

cause changes in resistance of the strain gauge material, which can be measured using a suitable circuitry, for example a Wheatstone bridge, to give accurate measurements of strain. However both these methods provide values averaged over the evaluated area only and it is often not possible to assume with certainty that the presence of a gauge does not affect the measurements. This influence is especially dramatic when small specimens are studied and for this reason non-contact techniques are increasingly used for material characterisation and structural evaluation [24].

1.2.2 Optical Methods

Optical NDT methods have high sensitivity and they allow a full-field analysis of the inspected area without any need for physical contact with the surface. They can sometimes provide more or different information where the other techniques fail or can not be applied. For example, in the analysis of building materials it is possible to obtain information about the displacement distribution over the whole surface. Therefore the strain distribution and crack formation and propagation in structures can be easily observed. The main optical interferometric techniques for measuring deformations are photoelasticity [25], moiré methods, holographic interferometry and speckle techniques [26].

1.2.2.1 Photoelasticity

Photoelastic stress analysis is an extremely powerful technique, which enables a complete stress analysis to be carried out on even complicated structures [27]. It is capable of supplying solutions to both two and three dimensional stress problems. Generally, the technique involves making a scale model in a suitable transparent plastic and placing the model in a beam of polarised light, in an instrument called a polariscope. In general, birefringence occurs in regions of stress in the plastic so that the plane of polarisation of the light is rotated and an analyser crossed with the polariser renders these regions visible as a fringe pattern. The fringes in these patterns can be interpreted to give information about the magnitude of the principle

stresses that are present in the model. Then, by using a simple formula, the stresses in the actual component can be determined even though the component material may be steel, aluminium, ceramic or even plastic.

1.2.2.2 Moiré Method

In general the term moiré denotes a regular pattern in the form of a series of parallel or crossed lines. In optics the effect arises when two gratings or grids are placed in proximity with one another with a small angle between the grating lines. The resulting pattern has a lower spatial frequency than those of the individual gratings, the exact value depending on the angle between the lines of the two gratings. To measure in-plane displacement, that is, perpendicular to the viewing direction, on the surface of an object a grating is attached to the surface [28]. The second grating can be obtained by using straight line interference fringes of known spacing. This interference fringe pattern is superimposed on the other grating. When the surface is displaced, the attached grating also moves producing a typical moiré fringe pattern. The fringe patterns can be recorded using a CCD camera and analysed to produce quantitative displacement data. The obvious disadvantage of this technique is the requirement that a grating must be in contact with the surface, which may not be applicable in some applications. To measure out-of-plane displacements, that is, parallel to the viewing direction, a fringe pattern may be projected at an angle to the viewing direction without the need for a physical grating. This pattern is recorded either photographically or with a video camera and framestore. Then the object is displaced and the new fringe pattern is recorded. This fringe pattern is then superimposed on the first to produce a moiré fringe pattern that represents the displacement that has taken place.

1.2.2.3 Holographic Interferometry

The principle of holographic interferometry is that it records the complete pattern of waves emanating from the object, both in amplitude and phase by combining it with an off-axis carrier wave [29]. The interference of the two coherent wavefronts is recorded on a photographic plate. To measure surface displacements,

two such wave patterns are recorded when the object is in its original and deformed states, and these are combined to give an interference fringe pattern, called an interferogram, related to the movement that has taken place. The fringes actually represent contours of equal displacement, with each successive fringe representing a change in displacement of the object approximately one-half the wavelength of the light source used in the recording process. The fringes can be observed in real time by removing the photographic plate after the first exposure, developing it and replacing it in the same position. The hologram produced is then reconstructed using the reference beam and any movement of the object will then produce interference fringes. A major disadvantage of this technique is the inability to independently measure displacements in different planes. The fact that the exposed plate must be developed and then returned to its original position had curtailed its use as a NDT technique until the development of digital holography.

1.2.2.4 Speckle Techniques

The coherence of laser light leads to the appearance of the phenomenon of speckle, that is, the grainy appearance of a scattering surface when illuminated by coherent light [8]. The speckle arises due to the interference that occurs between the light rays as they are scattered by different points on the surface. The resultant amplitude at any point in space is due to a set of vectors with random phase differences. The amplitude has a value which varies between zero and a maximum value determined by the magnitudes and phases of the individual amplitudes. As the point in space is varied the resultant amplitude and hence the intensity will have a different value. It is this random intensity variation which is the speckle effect. The speckle effect occurs only when the surface is optically rough, i.e. its height variation is of the order of, or greater than, the wavelength of the illuminating beam. The size of the speckles is governed by the wavelength of light used and the aperture of the viewing system.

There are two main speckle techniques applied to surface displacement measurement; speckle photography and speckle interferometry [8]. In speckle photography, light scattered from an object is recorded on a photographic plate

before and after deformation. Two speckle patterns are produced which are identical except that one is displaced relative to the other by an amount, which depends on the extent of the displacement of the object and the magnification of the imaging system. The speckle displacement can be determined by illuminating the developed plate and viewing the diffracted light in the Fourier plane. The Fourier fringes produced can be used to calculate the objects displacement. The fact that the plates must be developed and then analysed slows down the process and speckle photography is therefore not a very commonly used technique. However, recent developments in digital speckle photography speed up the process by eliminating the need for photographic plates [30]. In this situation a surface is imaged onto a CCD array and the image is sent to a computer. After the surface has been displaced another image is sent to the computer where it is digitally added to the image taken before the displacement. The resultant image can then be analysed using digital Fourier techniques. The extremely simple optical set-up of the technique makes it an ideal tool for non-destructive testing.

A digital version of single exposure speckle photography has been used for the full-field monitoring of velocity and flow-fields [31]. This technique is based on the fact that the spatial contrast of a time-integrated speckle pattern depends on the velocity of the surface or scatterer producing the pattern.

In electronic speckle pattern interferometry (ESPI) a speckle pattern is formed by illuminating the surface of the object to be tested, with laser light [32,33]. This speckle pattern is imaged onto a CCD array where it is allowed to interfere with a reference wave, which may, or may not, be speckled. The resultant speckle pattern is then transferred to a frame grabber on board a computer where it is saved in memory and displayed. When the object has been deformed, or displaced, the resultant speckle pattern changes due to the change in path difference between the wavefront from the surface and the reference wave. This second resultant speckle pattern is transferred to the computer and subtracted from, or added to, the previously stored pattern and the result is rectified. The resulting interferogram is then displayed on the monitor as a pattern of dark and bright fringes, called correlation fringes, as the fringes are produced by correlating the intensities of the

resultant speckle patterns taken before and after displacement. It is possible to continuously grab frames while a deformation is occurring and subtract them in succession from the first speckle pattern, in real-time. In this way it is possible to observe the real time formation and the progressive changes of the fringe pattern related to the deformation of the surface.

The method was first investigated in Loughborough University [34,35] as a way of measuring surface displacements caused by deforming an object. Since then many different configurations have been designed and used in a variety of applications. The similarities between ESPI and holography interferometry led to the term TV Holography being used to describe this technique [36]. The result of both techniques is a fringe pattern where the fringes represent contours of equal displacement. In both techniques the fringes result from a change in phase between an object and a reference wave. The main advantage of ESPI over holographic interferometry is that it enables real-time correlation fringes to be displayed directly upon a computer monitor without any form of photographic processing or plate relocation. This comparative ease of operation allows the technique to be extended to considerably more complex problems in deformation analysis. ESPI also allows the displacement in different planes to be measured separately. Furthermore ESPI does not require high-resolution recording media and imposes less stringent conditions on vibration isolation and ambient light. These advantages have led to an increase in the use of ESPI in a wide variety of applications.

Depending on the optical configuration of the ESPI system it can be made sensitive to out-of-plane displacements, i.e. parallel to the observation direction, or in-plane displacements, i.e. perpendicular to the line of sight, or both. For an out-of-plane system [37] the object is viewed normal to the surface and illuminated by one beam, the object beam, at an angle near normal. The resulting speckle pattern is imaged onto the CCD array where it interferes with a reference beam. The reference beam is aligned with the light coming from each particular part of the surface under study. The ESPI subtraction fringe patterns that are produced, represent contours of equal displacement along the viewing direction.

In an in-plane system [38] two beams illuminate the object at equal angles to the viewing direction, each generating its own speckle patterns. This technique measures only the displacement along a particular direction that lies normal to the line of sight of the system and in the plane of the two illumination beams. To measure strain, the displacement on the plane of the surface can be measured and its variation as a function of distance in any direction can be calculated. Speckle interferometry can do this independently of any displacement taking place in the direction normal to the surface, whereas holographic interferometry cannot without careful fringe analysis [6]. For complete in-plane displacement measurement two such systems are needed, which measure the displacement in the same plane but in orthogonal directions. The calculated displacements can then be vectorially added together to produce the resultant in-plane displacement. By combining a dual in-plane system, i.e. sensitive to displacements in both the horizontal and vertical directions, with an out-of-plane system, it is possible to determine three-dimensional deformation of an object by recording three interferograms, each with different sensitivity vectors.

The fringe patterns obtained by the ESPI technique represent contours of equal displacement. The spacing of the fringes is inversely proportional to the displacement and, in in-plane systems, the fringes are aligned perpendicularly to the direction of the displacement. Two consecutive dark or bright represent a displacement whose exact value depends on the wavelength of the light used and the geometrical setup of the ESPI system. The value of this displacement is called the fringe sensitivity term. The displacement between two points can be easily calculated by simply counting the number of fringes between those points and multiplying by the fringe sensitivity term. This can be a slow and tedious process when analysing complex fringe patterns and there is a relatively large error associated with this technique. However, with high-speed digital computers the fringes can be quickly processed using automatic fringe analysis and precision phase measuring techniques to provide accurate quantitative results. The most common techniques for this interferogram interpretation are the Fourier Transform [39] and phase-shifting methods [40]. Phase-shifting is used to obtain a fringe pattern which depicts the phase change, in the range 0 and 2π, that occurred

between the two speckle patterns. It is based on the introduction of a known amount of lateral shift, called the phase-step, into the interferometric pattern and the effect is a movement of intensity peaks across the pattern. The phase change is introduced either in the form of calibrated phase steps or as continuous periodic phase modulation. By analysing the intensity patterns taken at each step the phase (modulo 2π) can be calculated. These fringe patterns can be unwrapped to produce absolute phase maps that can be subsequently analysed to obtain accurate displacement maps.

The ESPI technique was developed over twenty five years ago [34] and there have been many different systems developed. However the first ESPI systems used electronic signal processing to produce the fringes which were then analysed using fringe detection techniques [30]. As the fringe quality tended to be poor and the errors quite large, the technique had very little practical application and never became widely used in industry. However, over the last ten years with the developments in phase shifting and unwrapping algorithms, CCD technology and image processing, the ESPI technique is becoming the most common optical method for deformation testing [41]. It has been used for inspection of crevice corrosion [42], evaluation of composite materials [43], deformation measurements in automotive components [44], crack measurement [45], masonry testing [46], strain analysis of spot welds [47], vibration measurement [48] and has even been applied to the study and conservation of paintings [49]. It has also been used to monitor and measure the surface behaviour, vibrations and deformations of objects heated up to temperatures of +3000°C [50, 51].

1.3 Surface Profiling

The performance of certain products greatly depends on the shape and finish of the surface, for example ball bearings, optical components, some biomedical materials and computer chips. Creating precise finishes and on such objects requires precise ways of measuring the shape of the surface. The surface finish is closely related to the machining or manufacturing process and so measuring the surface provides

information on the accuracy of the machining tool or manufacturing process. Profilometry is the measurement of the surface height variations of an object. It can be divided into two areas; the measurement of surface shape, or the departure of the shape from an ideal shape, sometimes called form [52], and the measurement of the roughness. Generally, the height variations when measuring roughness have a much smaller period than the variations when measuring shape or form. Therefore the measurement of roughness requires instruments with both high lateral and vertical resolution. The smoothness, or roughness, of a surface is a very important parameter in many electronic, optical and mechanical components. Many techniques, for example optical interferometry, and many stylus profilers, used to measure the shape of a surface offer excellent depth resolution but are limited in lateral or spatial resolution. Part of this thesis describes the development of instruments to measure surface height variations in the range 60 nm to approximately 2.5 cm with a sensitivity of 60 nm. It must be noted however that the boundary between the measurement of surface shape and surface roughness is arbitrary and in some cases it is possible to measure both these parameters.

1.3.1 Stylus Profilometry

The classical tool and the industrial standard for measuring surface profiles is the mechanical stylus [14]. The stylus probe is passed across the surface and its movement, as it follows the surface profile, is measured. This is still the standard surface profiling technique and can offer high precision allowing the measurement of surface roughness [53]. However, the stylus technique has its disadvantages. There are limits in lateral resolution, set by the size of the probe tip; peaks that are narrower than the probe tip will be recorded as being broader than they really are, while the probe will be physically incapable of reaching the bottom of narrow troughs. This reduced lateral resolution results in a loss of surface height information and results depend on the shape of the stylus. In addition, the stylus probe technique measures the profile along a line of the surface, and, if the entire surface is to be mapped, many such lines must be scanned. It can also have difficulties measuring highly curved or convoluted surfaces with steep slopes.

However, the major drawback of the technique is that it involves contact with the surface. The stylus probe tip can damage or alter the surface, which for many applications makes it unsuitable as a profiler.

Another commonly used technique is the atomic force microscope (AFM) [54] and its variation the scanning force microscope (SFM) [54], which although based on non-optical techniques, generally use optical methods to amplify and measure the signal.

1.3.2 Optical Techniques

Optical profilers can offer better lateral resolution, whole field analysis, high-speed measurements and non-destructive examination of the shape of the surface. These techniques exploit the wave nature of light to produce extremely accurate measurements of surface shapes. The techniques involve no physical contact with the surface to be studied. Many different optical surface profiling techniques have been developed to improve on the mechanical technique. The optical techniques can be divided into two categories based on the coherence of the light used. Low coherence techniques include white light interferometry [56], coherence radar [57], coherence scanning [58], correlation microscopy [59] and interference microscopy [60]. The principle of these techniques is essentially the same. They only differ in their optical set-up and data acquisition and analysis. The use of monochromatic or coherent sources forms the basis of the other category. This includes laser profilometry [61], phase-shifting interferometry, speckle and holographic techniques [8], fringe projection [7] and depth of focus methods [62].

The techniques described in this thesis are white light interferometry and a speckle technique, called electronic speckle pattern interferometric (ESPI) contouring. They are both used to measure the shape of surfaces, and although they use different light sources and data acquisition and analysis algorithms, they have similar optical configurations. The white light technique is better suited to discontinuous optically smooth surfaces, while the speckle technique is used on

continuous optically rough surfaces. Therefore the techniques can be combined together into one system which can be used as an extremely versatile profiler.

1.3.2.1 Speckle Technique

As described previously the speckle phenomenon has been greatly utilised in optical surface metrology to measure surface displacements. The speckle effect has also been used to measure surface roughness [63,64]. The ESPI techniques described previously are usually used for displacement and strain analysis. However they can be used for contouring purposes as well. Contouring is the measurement of variations in height and thus the surface profile of an object. Using the ESPI system sensitive to out-of-plane displacements, the surface is illuminated sequentially by a master wavefront (a plane wave for profiling) at two wavelengths λ_1 and λ_2. The difference between the wavelengths is usually of the order of 10 nm. The first image is recorded and the second is subtracted from it and the result rectified to produce the interferogram. This fringe pattern represents the difference in phase along the viewing direction between the surface and the master wavefront. If the master wavefront is a plane wave, the fringe pattern represents the surface profile and the interferogram can be analysed as before. These profilers offer excellent vertical resolution but the range has been a limitation. They are only suitable for continuous surfaces since discontinuous surfaces that introduce a phase shift of 2π, for example, between adjacent measurement points would produce phase ambiguity errors. This means that height differences greater than the wavelength of the light source between two adjacent points cannot be accurately measured.

The fringe sensitivity is inversely proportional to the change in wavelength. Therefore to obtain high resolution a large change in wavelength is needed. The need for two coherent wavelengths has curtailed the use of this technique, as a system that uses two laser sources is limited to one fringe sensitivity. The ideal source for this technique is a tunable laser with at least 50 nm tunable wavelength range. With the recent advances in laser diodes [65] and in particular the

availability of tunable laser diodes, ESPI contouring can become the ideal contouring system, as it has no moving parts and provides immediate results.

1.3.2.2 White Light Techniques

The inability of the ESPI contouring technique to measure surface height variations greater than the wavelength of the light source is also true for classical phase-shifting interferometry [PSI] techniques [66] used to measure heights of optically smooth surfaces. These PSI techniques are used to obtain three-dimensional images of surfaces that are smooth, relative to the wavelength of the monochromatic source. They offer excellent vertical resolution but the range is a limitation. They are only suitable for continuous surfaces since as in ESPI, discontinuous surface which introduce a phase shift of 2π, for example, between adjacent measurement points would result in phase ambiguity errors. A number of techniques had been developed to extend this range including heterodyne interferometry and multiple wavelength interferometry [67-69]. However, these methods are still limited to ranges of the order of 10 μm.

A number of techniques that use white light interferometry (WLI) methods [70-72] were developed to overcome the limitations of phase-shifting interferometric techniques. The white light interferometers allow surface profiling with high accuracy over a virtually unlimited range with no phase ambiguity errors, making them more suitable for profiling stepped or discontinuous surfaces. One of the first techniques to utilize the short coherence of the white light source was the scanning interference microscope [73-74]. This shares many features with confocal microscopy [75] and has been used to inspect semiconductor wafers and integrated circuits [76]. An alternative method is the coherence radar [57]. This detects the occurrence of interference while scanning the object in depth. In a Michelson interferometer setup the object takes the place of one of the mirrors. At the beginning of the procedure the other mirror, the reference mirror, is positioned further from the beamsplitter than the object. By moving the mirror step-by-step closer to the beamsplitter, the reference plane scans the object surface. A pixel modulates only when the optical path difference between the reference mirror and

the corresponding point on the object's surface is less than the coherence length of the light source used. By mapping the point in the scan at which interference occurs for each pixel, a three dimensional image of the surface profile can be mapped.

This white light technique differs from conventional microscopic interferometers in which depth accuracy is limited by the aperture [57]. The entire image field is viewed at one time without the need for scanning the surface in both x and y directions. However, a common problem is the vast amount of data, which generally increases the acquisition and analysis time. Many different techniques have been used with these profilers to speed up the analysis, including Fourier and phase-shifting methods [77-79]. This thesis describes a white light interferometric profiler based on the coherence radar. It uses two algorithms that do not involve Fourier or phase-shifting techniques. Instead, they deal with the data in a simple manner requiring very little analysis and involve simple computer programs, thus reducing the acquisition and analysis time. One of the algorithms is used when profiling optically smooth surfaces and the other when profiling optically rough surfaces. The resolution can be as low as 60 nm for smooth surfaces and of the order of a few μm for rough surfaces

1.4 Research Objective

As mentioned previously, the purpose of the research described in this thesis was to develop and optimise new advanced systems that could easily be used in an industrial environment. The ultimate objective was the development of ideal optical interferometric systems for use in high precision surface metrology. As will be shown in the next chapters, optical techniques offer many advantages over conventional techniques used in industry today. The reluctance to use these techniques in industry must be overcome if optical interferometric systems are to become standard industrial techniques. In order to do this, the optical systems must be developed for practical applications and not just for use in the laboratory. The first step in this process would be an extensive literature research into the optical

techniques used both in research and industry to identify areas of possible improvement. Areas where advances in computer technology, physics and data analysis could be exploited were also identified. The advances in computer technology include faster computers, dedicated hardware, faster data acquisition boards, and user friendly software. The advances in laser technology and liquid crystal device technology and in particular the ability to control the retardance could be utilised. Recent developments in phase analysis and data processing algorithms could also be used to allow further optimization and extend the potential applicability of the interferometric techniques.

For practical applications the systems would be stable, portable, robust and easy to use. To achieve this, the systems must utilise compact optical devices that do not require high voltages or power consumption. Another objective was to develop user-friendly software to control the optical systems and peripheral equipment and to facilitate rapid data analysis. It is hoped that these developments will help the surface metrology industry move towards non-contact portable computer-controlled systems for measuring and analysing surface displacements and shape. The successful realization of these objectives would greatly assist the transfer of optical surface metrology techniques into industry. A further motivation of the research was that many of these techniques could be implemented at much lower cost than hitherto.

Two separate techniques were used and optimised during the course of this research, white light interferometry and electronic speckle pattern interferometry. Chapter 2 provides a detailed description of these techniques along with the theory on which they are based. Chapter 3 describes the new white light interferometric surface profiler and Chapter 4 describes the advanced dual in-plane electronic speckle pattern interferometer (ESPI) used for surface displacement measurement. These chapters also provide results from tests and experiments carried out using these systems. The ESPI system uses liquid crystal devices for beam steering and manipulation as well as for phase shifting. Chapter 6 provides a brief theory of liquid crystal technology and the configuration of liquid crystal devices. It also describes extensive tests that were carried out to characterise these devices and the

results are presented. In Chapter 5 a new dual white light and ESPI contouring system is described along with results obtained.

Much of the work described in this thesis was carried out in the European Commission Joint Research Centre, Ispra, Italy.

Chapter 2 Theory

2.1 White Light Interferometry

2.1.1 Interference and Coherence

In order to describe a coherence scanning interferometer it is necessary to first describe the principles on which it is based, namely, interference and coherence. In this section, interference between two beams of the same frequency is described. It is then shown that an interference pattern cannot be produced between waves of different frequencies, unless the difference is very small relative to the frequencies. This result will be used to show how interference occurs in a Michelson interferometer when a white light source is used. The effect that the coherent properties of real sources have on the interference pattern is explained. It will become clear that coherence can be defined in a number of different ways.

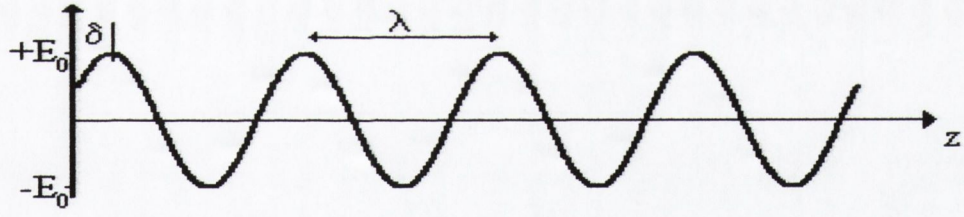

Fig. 2.1 An electromagnetic wave travelling in the z-direction.

Interference occurs when two or more waves overlap in space. Figure 2.1 shows an electromagnetic wave, travelling in the z-direction that can be described mathematically [80] by the following equation

$$E(z,t) = E_0 \cos\left[2\pi\left(\frac{z}{\lambda} - \upsilon t\right) + \delta\right] \qquad \text{Equation 2.1}$$

and letting $k = 2\pi/\lambda$ and $\omega = 2\pi\upsilon$ this becomes

$$E(z,t) = E_0 \cos[kz - \omega t + \delta] \qquad \text{Equation 2.2}$$

The argument of the cos-function is termed the phase and δ is the phase constant. Other parameters involved are E_0 the amplitude, λ the wavelength, υ the frequency and k the wavenumber. The phase difference between two points along the propagation direction of a plane wave is equal to the geometrical path length difference multiplied by the wave number. The refractive index of the medium through which the light is passing must also be taken into account. In general when a plane wave propagates in the direction of a unit vector n, the expression describing the field at an arbitrary point with radius vector r = (x,y,z) is given by

$$E(x,y,z,t) = E_0 \cos[k\mathbf{n}\bullet\mathbf{r} - 2\pi\upsilon t + \delta] \qquad \text{Equation 2.3}$$

This equation can also be written in complex form [80] as

$$E(x,y,z,t) = \mathrm{Re}\{E_0 e^{i(\phi - 2\pi\upsilon t))}\} \qquad \text{Equation 2.4}$$

where

$$\phi = k\mathbf{n}\bullet\mathbf{r} + \delta \qquad \text{Equation 2.5}$$

is the spatially dependent phase. For interference between waves of the same frequency, only the spatial complex amplitude is important and not the time-dependent part. Therefore,

$$E = E_0 e^{i\phi} \qquad \text{Equation 2.6}$$

describes not only a plane wave, but a general three-dimensional wave where both the amplitude E_0 and the phase ϕ may be functions of x, y, and z. Two waves of equal amplitude can be described as

$$E_1 = E_0 e^{i\phi_1}$$ Equation 2.7a

$$E_2 = E_0 e^{i\phi_2}$$ Equation 2.7b

According to electromagnetic theory [81] and the principle of superposition the resultant electric field is simply the sum of the component waves. However, since the only measurable quantity is the intensity [81], the time average of the square of the sum of the two waves is used as follows

$$\langle E^2 \rangle = \langle (E_1 + E_2) \rangle^2 = \langle E_1^2 \rangle + \langle E_2^2 \rangle + 2\langle E_1 E_2 \rangle$$ Equation 2.8

From electromagnetic theory, the intensity of a wave is proportional to the square of the electric field of the light wave. As only the relative intensities are of interest here, the proportionality constants can be ignored and $<E_1^2>$ can simply be replaced by I_1. The resultant intensity is then given by

$$I = I_1 + I_2 + 2\langle E_1 E_2 \rangle$$ Equation 2.9

I_1 and I_2, the intensities of the two component waves, are independent of each other so all information about the interference is contained in the third term. This is called the interference term and if it is equal to zero at all points in space, the waves do not interfere and are said to be incoherent. Maxwell's equations [81] can be used to show that, because of the transverse nature of light, light waves polarised at right angles to one another do not interfere and so the interference term is always equal to zero. Assuming that the waves are travelling in the same direction and propagating in the same plane, the resultant interference term now becomes

$$I = I_1 + I_2 + 2\sqrt{I_1 I_2}\cos\Delta\phi$$ Equation 2.10

where

$\Delta\phi = \phi_1 - \phi_2$ Equation 2.11

is the phase difference between the waves. If the components have equal amplitudes, $I_1 = I_2 = I_0$ and

$$I = 2I_0[1 + \cos\Delta\phi]$$

or

$$I = 4I_0 \cos^2(\Delta\phi/2)$$ Equation 2.12

where the intensity varies between 0 and $4I_o$, as shown in Figure 2.2.

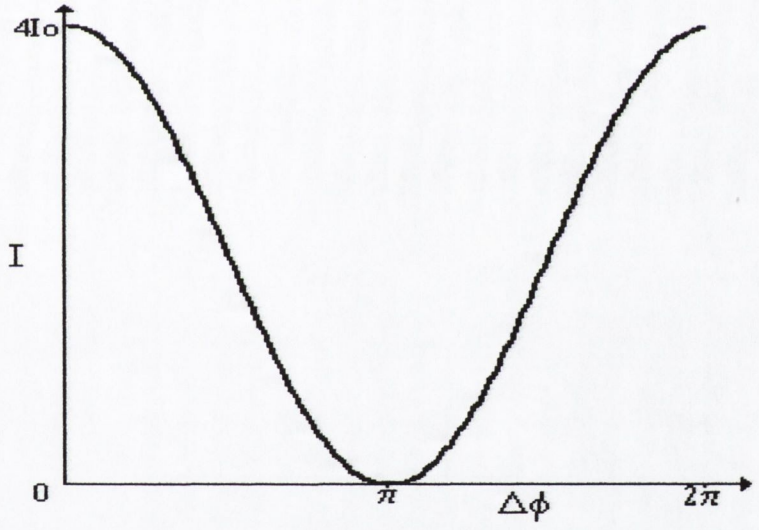

Fig. 2.2 A graph of the intensity of the interference as a function of phase change.

Equation 2.9 shows the resultant intensity is not just the sum of two intensities, I_1 and I_2. From Equation 2.12, it is clear that at various points in space, the resultant intensity can be greater, less than, or equal to the sum of the two component intensities. The resultant value depends on $\Delta\phi$, the phase difference between the two waves at any particular point. When

$\Delta\phi = (2n + 1)\pi$, for $n = 0, 1, 2,\ldots$

cos $\Delta\phi$ = -1 and the resultant intensity reaches its minimum value. This condition is shown in Figure 2.3A, where the two waves are in anti-phase. This type of interference is referred to as total destructive interference as the resultant intensity is zero if the two component intensities, I_1 and I_2, are equal.

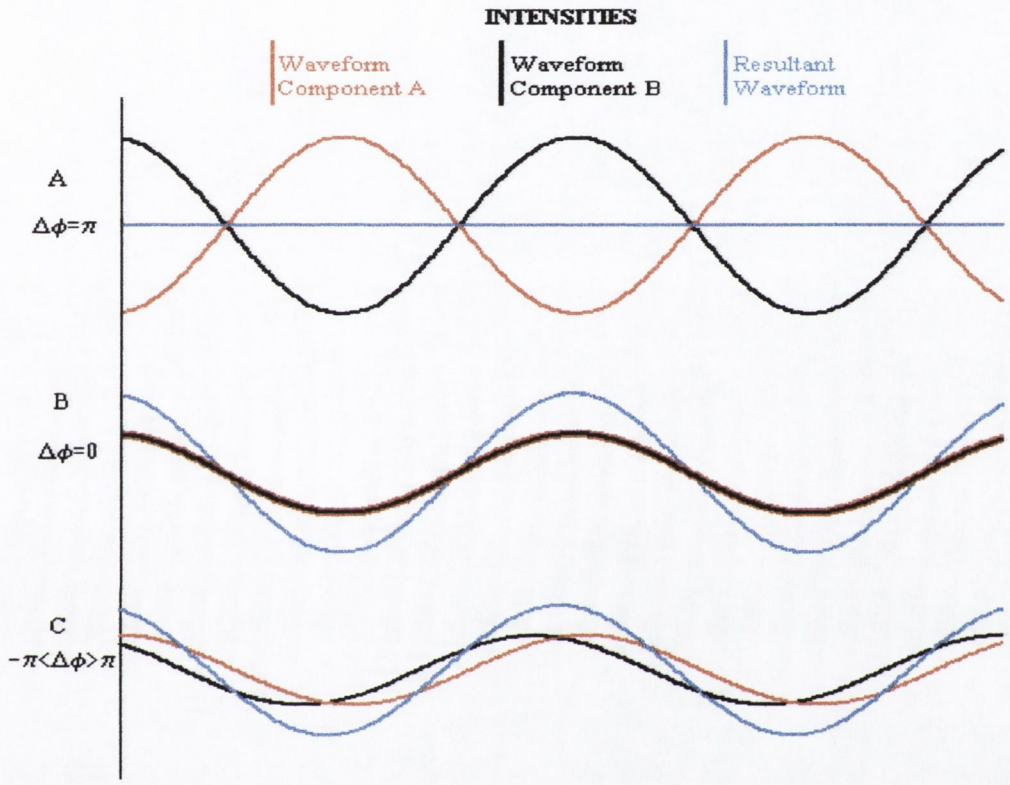

Fig. 2.3 Interference between two waves when; A, the phase difference is π; B, the phase difference is zero and; C, the phase difference is somewhere between $-\pi$ and $+\pi$.

When

$\Delta\phi = 2n\pi$, for n = 0, 1, 2,...

cos $\Delta\phi$ = 1 and a maximum in the resultant intensity is obtained. Figure 2.3B shows two waves traveling in phase with one another with a phase difference equal to zero. This is called total constructive interference. If the phase-difference

in somewhere between $-\pi$ and $+\pi$, the resultant waveform looks similar to the wave in Figure 2.3C. When the two interfering waves have the same frequency the phase difference between them is only dependent on the path difference, d, and is given by

$$\Delta\phi = \frac{2\pi}{\lambda} d \qquad \text{Equation 2.13}$$

When there is no path difference, $d = 0$ so $\Delta\phi = 0$ and when $d = n\lambda$, $\Delta\phi = 2n\pi$ and constructive interference occurs. When $d = (2n + 1)\lambda/2$, $\Delta\phi = (2n + 1)\lambda$ and destructive interference occurs. In Figure 2.4a, the two equal intensity plane wave fields, interfering on the screen, have an angle equal to zero between them and therefore the path difference between the two fields is constant everywhere on the screen. The intensity level will be constant throughout the resultant interference field and will be somewhere between 0 and $4I_o$, with the exact value depending on the phase difference between the two plane waves. If, however, the wave fields have angle greater than zero between them, as in Figure 2.4b, the path difference will vary across the screen. Therefore, the resultant intensity level will vary across the screen producing dark and light regions known as interference fringes. The spacing and shape of the fringes depends on the angle between the waves and on the shape of the fields themselves. For example if two plane waves interfere on the screen [6] the fringe spacing, d, is given by

$$d = \frac{\lambda}{2\sin\theta/2} \qquad \text{Equation 2.14}$$

Equation 2.10 describes the interference between two waves that have the same frequency. It assumes that the phase difference is not changing with time. The time averaging performed when measuring intensity becomes very important when trying to obtain interference between waves of different frequencies.

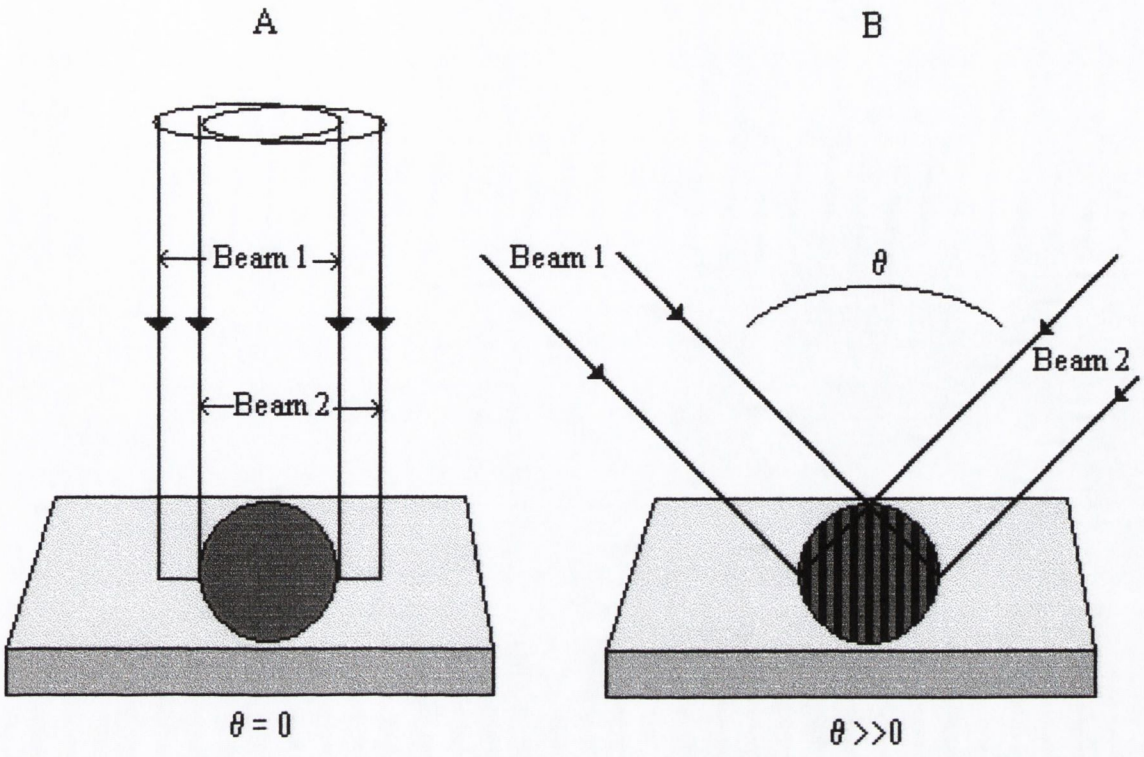

Fig. 2.4 Interference between two beams; A, The angle between the beams is zero; B, Interference fringes are formed when the angle is greater than zero.

To measure interference, the temporal variations of the phase, caused by the difference in the frequencies, must be small during T, the measurement period. In real terms, this means the detector, e.g. the eye or a CCD camera, must have a faster response time than the variations in the intensity caused by the phase difference fluctuating. It will now be shown that the length of time in which the variations in the phase can be ignored, and interference obtained, is dependent on the difference in the frequency between the two waves.

Two waves of different frequencies, but equal amplitudes, travelling in the z-direction can be described mathematically [82] as

$$E_1(z,t) = E_0 \cos[k_1 z - \omega_1 t + \delta_1] \qquad \text{Equation 2.15a}$$

$$E_2(z,t) = E_0 \cos[k_2 z - \omega_2 t + \delta_2] \qquad \text{Equation 2.15b}$$

When added together they produce a resultant carrier wave with a frequency equal to the average of the two component frequencies. The amplitude of this carrier is modulated by a harmonic wave whose frequency is equal to one-half of the difference between the component frequencies. This is referred to as the beat frequency. The resultant amplitude is given by

$$E(z,t) = 2E_0\cos(kz-\omega t)\cos(\Delta kz-\Delta\omega t) \qquad \text{Equation 2.16}$$

where $k = (k_1 + k_2) / 2$, $\omega = (\omega_1 + \omega_2) / 2$ and

$$\Delta\omega = \frac{\omega_2 - \omega_1}{2} \qquad \text{Equation 2.17}$$

is the beat frequency. Again, as the intensity is the measured quantity it is necessary to calculate the time average of the amplitude squared. This results in the following equation for the resultant intensity

$$I(z) = 4E_0{}^2\left\langle\cos^2(\omega t - kz)\right\rangle\left\langle\cos^2(\Delta\omega t - \Delta kz)\right\rangle \qquad \text{Equation 2.18}$$

The measurement of this quantity is its average taken over a time, T. Using the time average, the measured intensity becomes

$$I(z) = 2I_0 + \frac{2I_0}{\Delta\omega T}\left[\cos\left[\Delta\omega(2t_0 + T) - 2\Delta kz\right]\sin\Delta\omega T\right] \qquad \text{Equation 2.19}$$

From Equation 2.19, it can be seen that if $\Delta\omega T >> 1$, then the resultant intensity at a position z is equal to the sum of the intensities of the component waves and there is no interference term. When the second term is so small it can neglected, the waves are said to be incoherent. If $\Delta\omega << 1$, so that $\sin\Delta\omega T \approx \Delta\omega T$, Equation 2.19 can be written as

$$I(z) = 2I_0 + 2I_0\cos\left[\Delta\omega(2t_0 + T) - 2\Delta kz\right] \qquad \text{Equation 2.20}$$

In this case the detector's response time will allow the observation of the interference pattern so that the waves are now considered coherent. From the condition that $\Delta\omega T<<1$, we see that T must be less than a time τ_c, given by the inverse of the difference in frequency. This time τ_c is referred to as the coherence time. The greater the difference in the frequencies of the components the smaller the coherence time. Therefore observable interference between waves of different frequencies is only possible if the difference in frequency is sufficiently small for the detector to measure the interference term. This result can be extended to the interference of a number of waves of different frequencies. In the case of most real sources, which have a continuous distribution of frequencies, $\Delta\omega$ becomes the frequency bandwidth [82]. This result is used later, when interference using a white light source in a Michelson interferometer is discussed

Equation 2.19 shows the restrictions placed on obtaining interference between waves of different frequencies. For this reason interference is usually obtained from waves which originated from the same source and so have the same frequency. If the source is a monochromatic source, such as a laser, it would be reasonable to presume that interference would be observed no matter what the path difference between the beams. However, pure monochromatic sources do not exist and all light sources emit light of more than one frequency. The property of the source that restricts the interference between two light waves from that source is called coherence. Coherence has already been described in terms of interference, but the same property can also be visualized in terms of the light from the source itself. Later, coherence is again discussed in terms of interference, as the effect of using a broadband source in a Michelson interferometer is investigated.

An ideal monochromatic light source emits an electromagnetic wave as shown in Fig. 2.1 and described by Equation 2.1. Knowing the phase at any one point along the wave, it is possible to calculate the phase at any other point. In other words, the shape of the wave at a point P1 will be correlated with that at every other point along the wave. This wave is said to have perfect coherence. In reality, there is no

perfectly monochromatic source and all sources emit waves of more than one frequency. Figure 2.5A shows the spectrum of an ideal monochromatic source with perfect coherence. Figures 2.5B and 2.5C show the typical frequency spectra emitted from a laser source and a white light source respectively. For a source to be perfectly coherent it must only emit one frequency or, in other words, have a bandwidth of zero. The laser is referred to as a monochromatic source, but even the laser has a finite bandwidth. Therefore, since perfectly monochromatic sources do not exist, neither do perfectly coherent sources. Similarly, for a source to be totally incoherent it must have an infinite bandwidth and no such sources exist. All light sources have some degree of coherence and are said to be partially coherent.

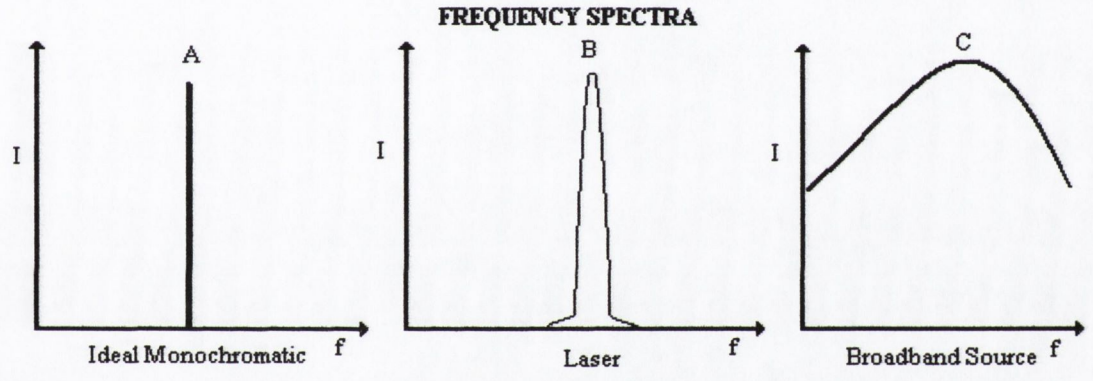

Fig. 2.5 Frequency spectra of; A, an ideal monochromatic source; B, a laser source and; C, a broadband source.

Partially coherent light can be illustrated as a series of randomly phased sinusoidal wave trains of finite length, as shown in Figure 2.6. After each wave train, there is a random phase jump and so the disturbance at any point will only be correlated with that at all the other points along the same wave train. The wave trains can be viewed as having the same length and exist for a time τ_c, which is the coherence time given by the inverse of the frequency bandwidth. Light from sources, such as lasers, which have a small bandwidth essentially behave like monochromatic sources for intervals shorter than the coherence time τ_c. The length of the wave train in space is termed the coherence length, $l_c = \tau_c c$. In effect the coherence length is the distance over which it is possible to predict the phase of the light wave at a given point. This property is called the temporal or longitudinal

coherence of a light source. Obviously a broadband source has a small temporal coherence length, while a laser has a much greater coherence length.

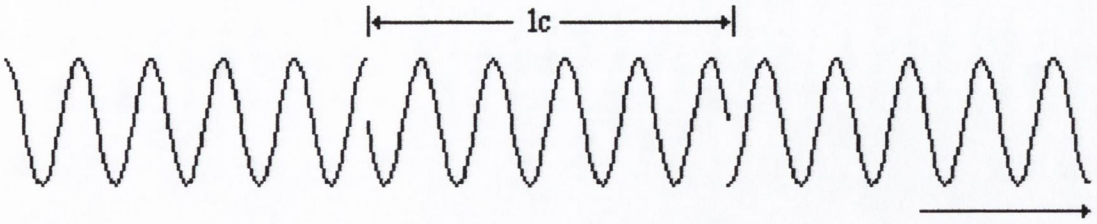

Fig. 2.6 Partially coherent light can be visualized as a series of sinusoidal wavetrains of a finite length equal to the coherence length of the source.

The effect the coherence length has on the interference between two beams of light from the same source can now be investigated. Figure 2.7 shows two light waves of equal amplitude produced from the same source and recombined to interfere, at the screen at P, after having traveled different paths. The waves will obviously have the same coherence length, lc. After the source emits one wave train there is a random change in phase as it emits the next. To show this clearly the wavetrains are coloured in Figure 2.7. In Figure 2.7A, the two waves have traveled equal path lengths and the phase difference between them remains constant in time, as identical wave trains are always recombining. The interference between these two beams is described by Equation 2.10. Figure 2.7B shows the situation when one of the waves has traveled a distance l_c greater than the other wave. The result is that there are now two independent wavetrains overlapping and the phase difference between the two beams varies as each new wavetrain is emitted. At any instant in time the interference is still described by Equation 2.10, but now the phase difference fluctuates as each new train passes. As a result, cos $\Delta\phi$ varies randomly between -1 and $+1$ and when averaged over many wave trains it becomes zero. Therefore the resultant intensity is just $I = 2I_o$.

Figure 2.7C shows the situation where the path difference is somewhere between zero and l_c. Over many wave trains, the phase difference varies in a time period, τ, proportional to the path difference. It will remain constant for a time period

proportional to τ_c - τ, where τ_c is the coherence time. The result will be a stable interference pattern described by Equation 2.10, but with a reduced contrast.

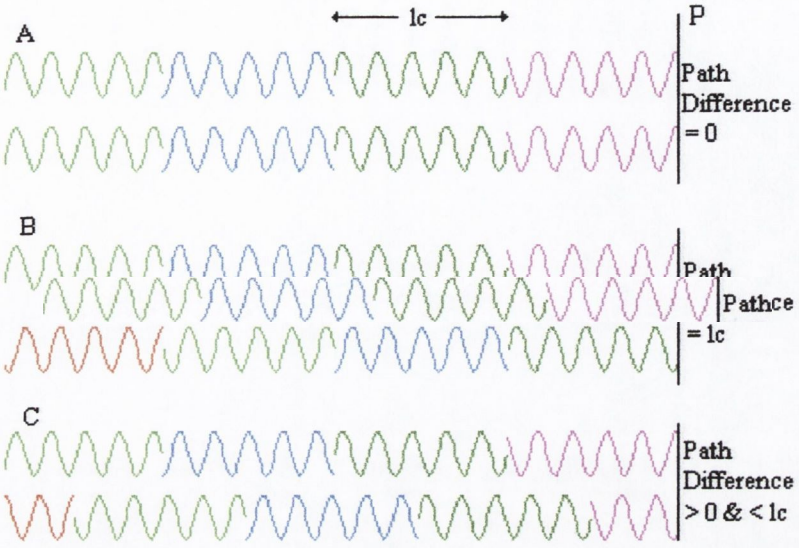

Fig. 2.7 Interference between two beams that have travelled different paths; A, The path difference is equal to zero; B, The path differnce is equal to the coherence length; C, The path difference is greater than zero, but less than the coherence length.

The part coherence plays in interference is now clear. To allow for the coherence property Equation 2.10 can be written as

$$I = I_1 + I_2 + 2\sqrt{I_1 I_2}\,|\gamma(\tau)|\cos\Delta\phi \qquad \text{Equation 2.21}$$

where $\gamma(\tau)$ is the coherence term.

The quality of an interference pattern can be described quantitatively using the visibility V, as first expressed concisely by Michelson [82],

$$V = \frac{I_{max} - I_{min}}{I_{max} + I_{min}} \qquad \text{Equation 2.22}$$

where I_{max} and I_{min} are two adjacent maxima and minima of the fringe pattern, respectively. As cos $\Delta\delta$ varies between –1 and +1, I_{max} and I_{min} can be expressed as

$$I_{max} = I_1 + I_2 + 2\sqrt{I_1 I_2}|\gamma(\tau)| \qquad \text{Equation 2.23a}$$

$$I_{min} = I_1 + I_2 - 2\sqrt{I_1 I_2}|\gamma(\tau)| \qquad \text{Equation 2.23b}$$

Using these equations, the visibility can be expressed as

$$V = \frac{2\sqrt{I_1 I_2}|\gamma(\tau)|}{I_1 + I_2} \qquad \text{Equation 2.24}$$

Clearly, $\gamma(\tau)$ is exactly equal to the visibility of the interference pattern, if $I_1 = I_2$. It is called the complex degree of coherence and is a measure of the ability of two wave fields to interfere.

The temporal degree of coherence is dependent on the temporal coherence of the source itself. In effect, the maximum path difference between the two waves for which $\gamma(\tau)$ is greater than zero, is the coherence length of the source. Spatial coherence is used to describe the coherence of a wave field at two points in space. Figure 2.8 shows two points on the same wave field, or wavefront, emitted from the source S. The spherical lines in this figure only describe the shape of the wavefront and not the wavelength. The wavelength will obviously remain constant everywhere. In a spatially incoherent source there is no correlation between the phases of the two points. This phenomenon can be measured using Young's double aperture experiment, as shown in Figure 2.8. The wave field is alaysed at the two points P1 and P2, by observing the resultant interference pattern on the screen.

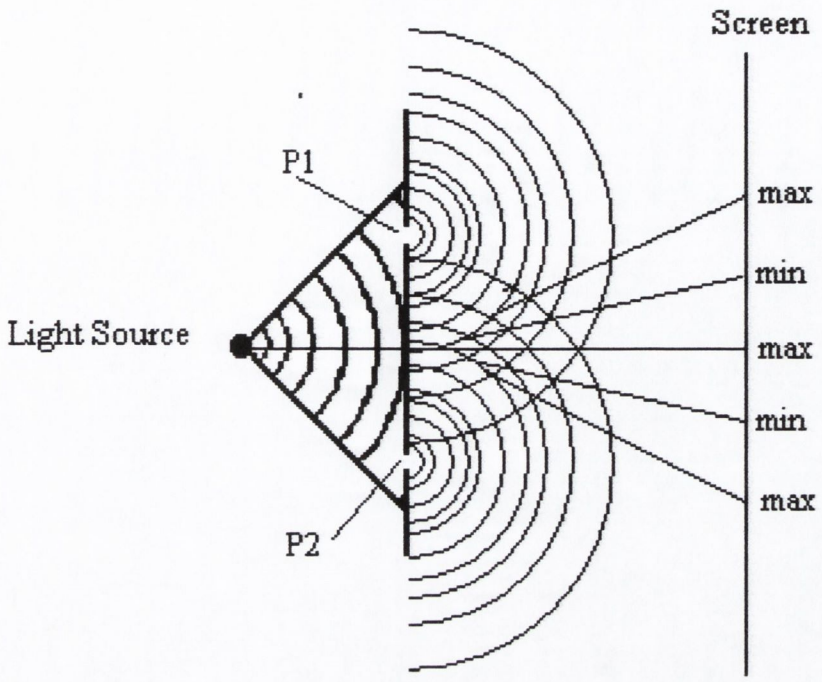

Fig. 2.8 Young's double-slit experiment.

In the same way as the temporal degree of coherence is a measure of the interference visibility as a function of the path difference, the spatial degree of coherence is a measure of the visibility as a function of the spatial distance between P1 and P2. The contrast of the fringes produced on the screen is a measure of the degree of spatial coherence between the light waves emanating from points P1 and P2. As the distance between P1 and P2, increases the spatial coherence between the two decreases and so too does the contrast of the fringes. The distance at which the spatial coherence is equal to zero is called the spatial coherence length. It is obvious that the closer the source is to an ideal point source the greater the spatial coherence length.

In summary, for two beams to produce a stable interference pattern they must be coherent, i.e. they must have a phase relationship that does not vary with time. An observable interference pattern will not occur between light beams from two separate sources. Using one source the emitted beam is split in two which are then recombined to form an interference pattern. For interference to occur, the maximum path difference between the two beams is the temporal coherence

length of the source and the temporal coherence is inversely proportional to the frequency bandwidth of the source.

2.1.2 The Michelson Interferometer

The Michelson interferometer, shown in Figure 2.9, was designed over a hundred years ago but is still used in many applications today [81].

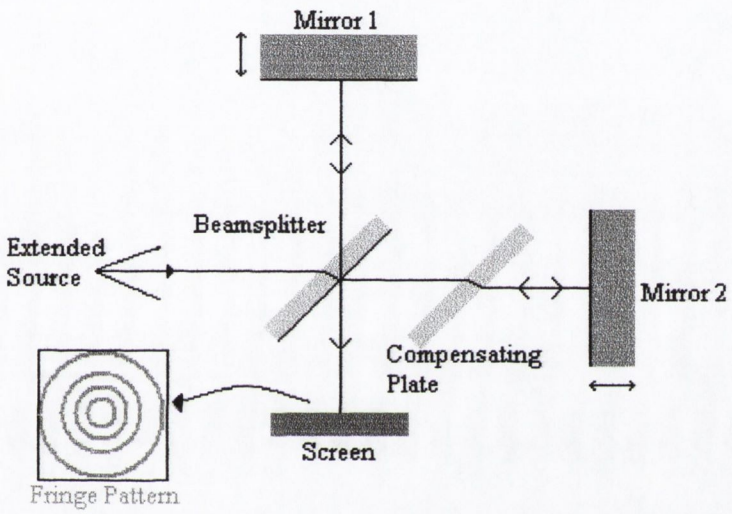

Fig 2.9 Schematic of a Michelson Interferometer.

This type of interferometer is described as an amplitude-splitting interferometer as the beamsplitter is used to divide the light into two beams of equal amplitude. The two beams travel along orthogonal paths called the arms of the interferometer. A mirror is placed at the end of each arm to reflect the beams back to the beamsplitter where they are recombined. One of the beams passes through the beamsplitter three times whereas the other wave only travels through it once. A compensator plate is placed in the shorter path so that both beams travel through the same thickness of glass. If the two recombined beams are coherent they will interfere and the interference pattern can be seen on the screen. A point source will generate spherical waves that produce an interference pattern of circularly

symmetric fringes if d, the difference in path lengths between the arms, is a constant across the whole field. The total phase difference for a bright fringe is

$$\Delta\phi = \frac{4\pi d\cos\theta}{\lambda} \qquad \text{Equation 2.25}$$

where θ is the angle between the normal and the beam at the center of the bright fringe. When a fringe appears at the center of the pattern the phase difference is simply

$$\Delta\phi = \frac{4\pi d}{\lambda} \qquad \text{Equation 2.26}$$

The fringe order m of the fringe is given by

$$m = \frac{2d\cos\theta}{\lambda} \qquad \text{Equation 2.27}$$

and the highest fringe order occurs at the center where

$$m_{max} = \frac{2d}{\lambda} \qquad \text{Equation 2.28}$$

As the path difference increases a bright fringe will move out from the center of the pattern and a new bright fringe of a higher order will take its place. By counting the number of fringes as one of mirrors is moved, it is possible to calculate the actual path length change by using Equation 2.28. From Equation 2.10, the resultant intensity at the center of the fringe pattern is given by

$$I = I_1 + I_2 + 2\sqrt{I_1 I_2}\cos\left(\frac{4\pi d}{\lambda}\right) \qquad \text{Equation 2.29}$$

It is clear from the previous definition of coherence that when a monochromatic source is used the maximum optical path difference between the two arms of the

interferometer that will still produce an observable fringe pattern is the coherence length of the source. When the optical path difference between the two beams is near to zero the visibility or contrast of the fringes is at its maximum. As the optical path difference is increased, the contrast decreases and eventually equals zero when the path difference is greater than the coherence length. In the last section it was shown how Young's experiment could be used to measure the spatial coherence of a source. In the same way, the Michelson interferometer can be used to measure the temporal coherence length.

It was shown in the last section that two waves of different frequency could only produce an observable fringe pattern under certain conditions. When a source that contains more than one frequency is used in a Michelson, a wave in one arm can only interfere with the wave in the other arm that has the same frequency. The output intensity is therefore the sum of the intensities associated with the interference between each frequency component. To show the effects this has on the resultant interference, it will be assumed that two monochromatic sources are used in a Michelson at the same time. It is also assumed that the interference between the two different frequencies, ω_1 and ω_2, cannot be detected and so the output intensity is just the sum of the intensities produced by the two interference patterns. If Equation 2.29 is written in terms of the frequency instead of the wavelength, the result is

$$I = I_1 + I_2 + 2\sqrt{I_1 I_2}\cos\left(\frac{2\omega d}{c}\right) \qquad \text{Equation 2.30}$$

In a Michelson the two waves that are added together can originate at different times. The difference in time depends on the path difference between the two arms and is given by

$$t = \frac{2d}{c} \qquad \text{Equation 2.31}$$

Equation 2.30 can now be written as

$$I = I_1 + I_2 + 2\sqrt{I_1 I_2}\cos(\omega t)$$ Equation 2.32

The resultant output intensity, I_T, from the Michelson interferometer is then the addition of the interference pattern intensities associated with the two frequencies. If the background intensities of the two patterns are I_{o1} and I_{o2}, then

$$\begin{aligned} I_T &= I_{t1} + I_{t2} \\ &= I_{o1} + I_{o2} + I_{o1}\cos\omega_1 t + I_{o2}\cos\omega_2 t \\ &= I_O(1+\zeta) \end{aligned}$$ Equation 2.33

where $I_0 = I_{o1} + I_{o2}$, and

$$\zeta(t) = \frac{I_{o1}}{I_O}\cos\omega_1 t + \frac{I_{o2}}{I_O}\cos\omega_2 t$$ Equation 2.34

is the interference term of the resultant output. When the optical path difference between the two arms of the interferometer is zero, $\zeta(t)$ has its maximum value

$$\zeta(t) = \frac{I_{o1} + I_{o2}}{I_O} = 1$$ Equation 2.35

When $\zeta(t) = 0$ there is no resultant interference pattern and the resultant intensity is just I_0, and if $I_{o1} = I_{o2} = \frac{1}{2}I_O$, this can be written as

$$\zeta(t) = \cos\left(\frac{\omega_1 + \omega_2}{2}\right)t + \cos\left(\frac{\omega_1 - \omega_2}{2}\right)t$$ Equation 2.36

which will be zero whenever

$$\frac{\omega_1 + \omega_2}{2}t = \pi(f_2 - f_1)t = \frac{\pi}{2}$$

$$\Delta f = \frac{1}{2t}$$ Equation 2.37

An interference pattern will not be observed in the resultant intensity pattern, if the time delay between the waves in the arms of the interferometer is greater than, or equal to, t, where t is given by

$$t = \frac{1}{2\Delta f}$$ Equation 2.38

or in other words when the path difference, d_m, between the mirrors is

$$d_m = \frac{c}{2\Delta f}$$ Equation 2.39

The optical path difference, d, between the arms of the interferometer is twice the value of d_m. From this equation it is clear that smaller the difference in frequency the greater the allowable time difference between the two beams for interference to occur. Also, the greater the allowable time, the longer the maximum path difference allowed in order to observe interference, which is the coherence length of the source, where the source is now a mixture of two frequencies. This can be extended to more than two frequencies, in which case Δf in the above equations becomes the frequency bandwidth. This is the true definition of coherence and the reason why no source has an infinite coherence length. Every real source has a finite bandwidth and as such the total interference pattern is, in effect, always a sum of interference patterns between waves of different frequencies. The smaller the bandwidth the longer the coherence length so, as expected, lasers have a relatively long coherence length while broadband sources, such as white light, have very short coherence lengths. This completes the overview of interference and coherence and the next section shows how these properties are used for optical surface profiling in white light interferometers.

2.1.3 White-light Interferometric Surface Profiling

A white light source is a broadband source with a frequency bandwidth spanning the range of visible spectrum, i.e. approximately 4.3 to 7.5 x 10^{14} Hz. This range has a spectral width roughly equal to $\Delta f = 3 \times 10^{14}$ Hz, which corresponds to a coherence length of approximately one micrometer. Therefore, when white light is used in a Michelson interferometer, interference will only occur when the optical path difference between the beams in each arm is less than a micrometer. It is this property that had led to the use of white light interferometers for such things as optical ranging, optical thickness measurement and surface profiling.

As mentioned in Chapter 1, laser based phase-shifting optical profilers are widely used for surface height measurements [15]. However these techniques are usually limited to surfaces which are smooth relative to the wavelength of the monochromatic source. They have a range limited by the wavelength of the light. A number of techniques were developed to extend this range including heterodyne interferometry and multiple wavelength interferometry [67]. However even these techniques are limited to ranges of the order of 10 micrometers. The phase ambiguity present in these techniques is not present in white light techniques. It is for this reason that much interest has been shown in white light techniques such as white light interferometry (WLI), coherence radar, coherence scanning interferometry, correlation interferometry, interference microscopy and low coherence interferometry[70]. Despite the different names, these techniques share many characteristics and really only differ in the data acquisition and analysis.

There are many different types of white light interferometric surface profilers, but the objective is always the same; to find the location of the interference region for each point on the surface. The object is placed in an interferometric set-up, typically a Michelson interferometer, in the place of one of the mirrors. The other mirror is then moved, to change the optical path difference between the beams incident on the surface and on the mirror. Interference will occur when the optical path difference is less that the coherence length of the source. As the height of the

surface varies across the field, at any one time interference will occur only in the regions on the surface for which the optical path difference is less than l_c. In this way the profiler can obtain information height information on the object's surface by locating the interference, or coherence region, for every point. To improve the sensitivity, some of the systems go further than this and locate the peak modulation within the coherence region. However, a major problem arises because of the large three-dimensional data arrays and the associated analysis.

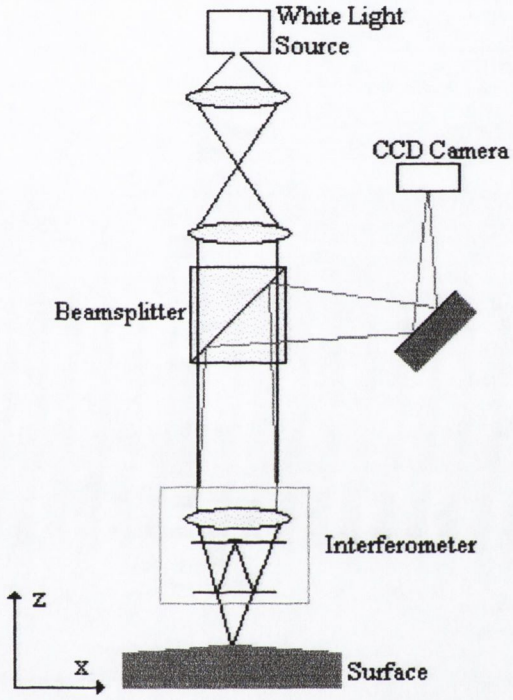

Fig. 2.10 A Mirau coherence scanning interferometer.

One of the first techniques to utilize the short coherence of the white light source was the coherence scanning microscope [71]. These systems use either a Mirau [83], Linnik [84], or a Michelson [85] interferometric configuration. The most commonly used Mirau arrangement is shown in Figure 2.10. The optical configuration of this technique has similarities with confocal microscopy. The object is scanned along the z-axis by either moving it or the interferometer. Figure 2.11 shows the intensity of the white light fringes that result from monitoring one point (x,y) in the image as the object is scanned in the z direction. The envelope of the fringes gives the coherence function.

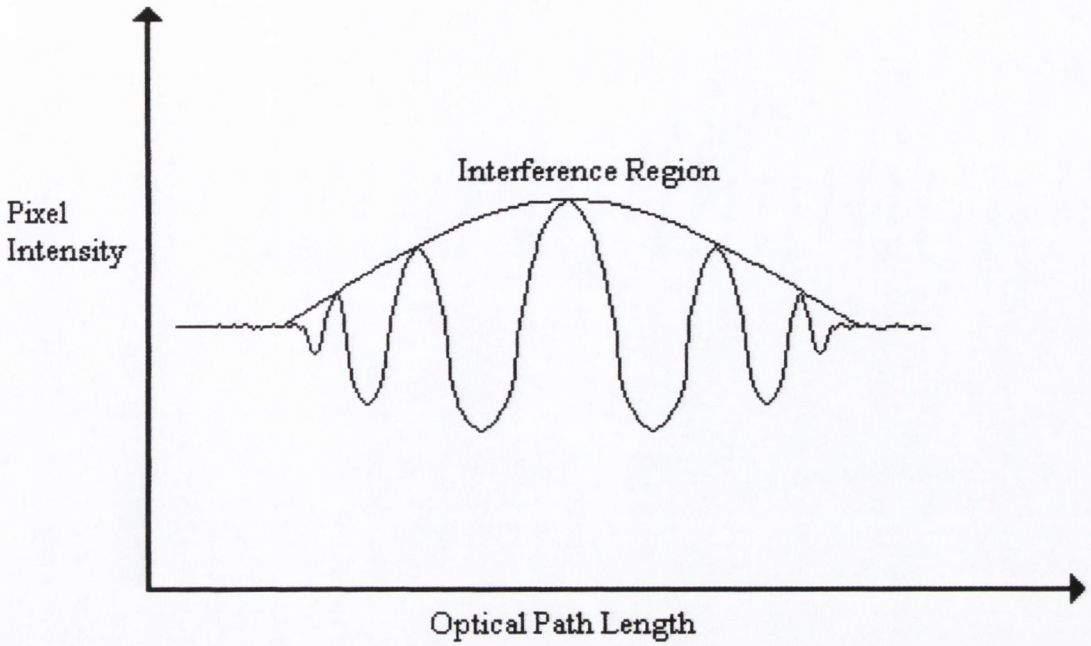

Fig 2.11 The interference signal obtained in one pixel as the optical path length of the reference arm is increased. The peak of the envelope of the fringes corresponds to the point of equal optical path lengths.

The fringes can be demodulated to find the peak amplitude of the envelope and the z-location of the peak. After this point has been located for that position on the surface, the surface is translated in the x-direction and the peak amplitude is located for the next point. After each row in the x-direction has been scanned the surface is translated in the y-direction and the next row along the x-direction is scanned. This continues until the whole surface has been mapped. The locations of the coherence region in the z-plane, for each point on the surface, are then used to build a three dimensional image of the surface. This technique is slow as the surface must be translated not only along the z-axis but also along both the x and y axes. It does have the advantage over the mechanical stylus technique in that it is non-contact and has a better lateral resolution. The vertical resolution really depends on the data analysis technique but it can have a sub-nanometer resolution. The system can also be used as a full-field technique over very small areas, and this is the set-up commonly used in commercial systems [86]. These systems are limited to looking at small areas and tend to have a very limited range. A comparison between the commercial systems and the system described in this thesis is given in Chapter 3.

Another important disadvantage is the complexity of the mounting stage. To achieve accurate translations along three axes requires very expensive equipment. To achieve its highest vertical resolution requires complex algorithms for data analysis. For these reasons the commercial coherence scanning interferometric surface profilers tend to be very expensive. These profilers are also very limited to certain types of surfaces, e.g. rough or smooth, continuous or discontinuous. The lateral dimensions of the surface are also limited to the scanning range in the x and y directions, which is typically of the order of a couple of centimeters. One of the objectives of the research detailed in this thesis was to develop a much faster and cheaper profiler that would have performance capabilities comparable to the coherence scanning surface profilers. However it would not be as limited and should be able to profile different types of surfaces of various dimensions. The ultimate aim was to develop an optical profiler that has a large range, is fast, accurate and offers a high resolution.

To eliminate the need for scanning in the x-y plane, a full-field technique has to be used. A full-field white light interferometry technique allows surface profiling with high accuracy over a large range, but unlike confocal microscopy or coherence scanning microscopy, these techniques allow the entire image field to be captured using a CCD camera in one instant without the need for scanning apertures. The interference regions are located along the z-axis for each pixel in the image as the object or reference mirror is moved. Collimated incoherent light ensures that these regions can be considered independently of (x,y) location.

The optical set-up of the white light profiler, described in this thesis, is essentially a Michelson interferometer with one of the mirrors replaced by the surface to be profiled, as shown in Figure 2.12. The surface is imaged onto a CCD camera using a telescopic lens system. An aperture at the Fourier plane of the first lens ensures that only collimated light returning from the surface is imaged onto the 512 x 512 CCD array. The profiler utilises the short coherence length of the white light source. As described in the previous section, the visibility of the interference, at any point in the image, between the light reflected from the mirror

and surface, decreases rapidly from its maximum, at zero optical path difference, to zero at optical path differences greater than the coherence length of the source.

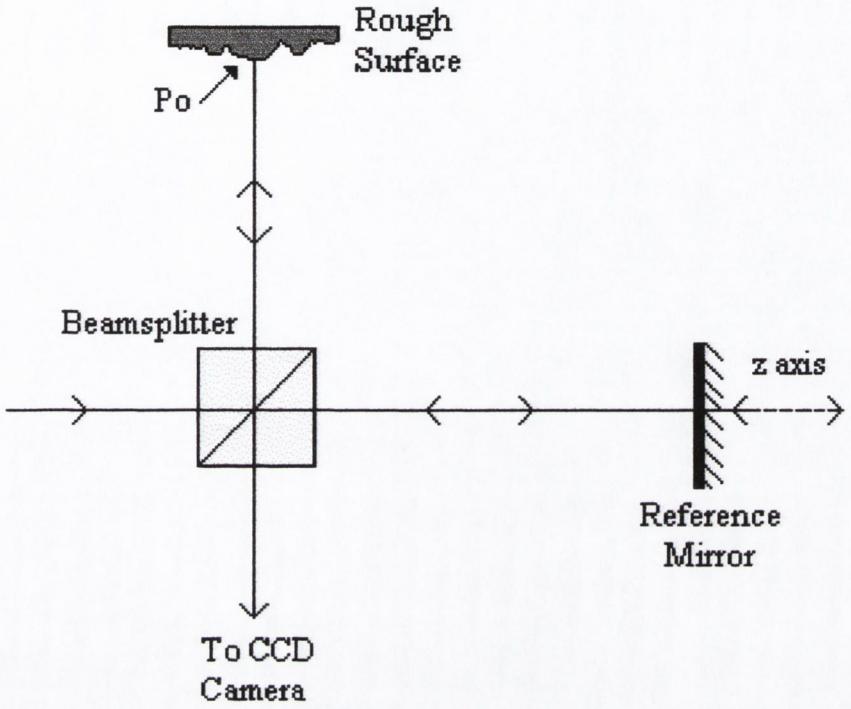

Fig 2.12 A schematic of the white light profiler. It is essentially a Michelson interferometer with one of the mirrors replaced by the object whose surface is to be measured.

In Figure 2.12, if the light paths from point P_0 and from the reference mirror are equal, interference will be seen in the pixels corresponding to that point and every other point on the surface for which the optical path difference is less than the coherence length. As the reference mirror is moved along the z-axis, the points of interference change to new points corresponding again to approximately equal optical path lengths. Figure 2.13 shows a single pixel intensity graph obtained from a detector placed in the image plane of the profiler as the optical path difference is varied through zero. The interference region occurs at zero optical path difference and is only a couple of microns wide. For each pixel in the frame this region must be identified and the corresponding frame number within the scan located.

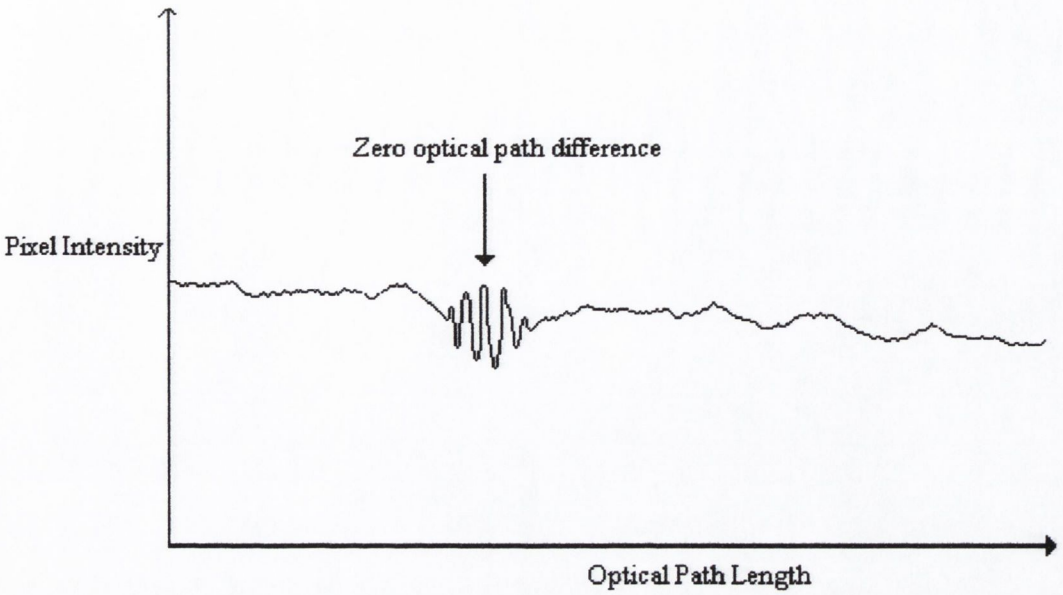

Fig 2.13 The pixel intensity as the reference mirror is translated along the z axis. The interference region is centered around zero optical path difference.

During profiling, the reference mirror is moved along the z-axis and frames are grabbed continuously. These frames are analysed so that at the end of the scan the interference region has been located for each pixel in terms of the frame number in which the interference, or coherence, region occurred. The initial result from a scan is a two dimensional map in which the gray level of each pixel is the frame number in which interference occurred in that pixel. The distance traveled by the reference mirror between consecutive frames is precisely controlled, so the relative positions of these frames within the scan are known. A simple three-dimensional curve fitting technique is used on these positions of maximum intensity to build an image of the surface. The lateral resolution depends on the number of pixels on the CCD array and the size of the surface area. The vertical resolution depends on the accuracy with which the interference region, or even the peak modulation within this region, can be detected. The speed of the profiler also depends on the algorithms used in the data analysis. In other words, the overall performance of the profiler depends mainly on the data acquisition and analysis technique.

2.1.4 Data Acquisition and Analysis

A major problem with any white light interferometric profiler is the vast amount of data, which slows the data acquisition and analysis, due to the associated computational burden. A typical scanning coherence interferometer will take 100 intensity value readings for each of the 250,000 positions in the x-y plane. The first problem arises from the amount of memory needed to store all this data, approximately 25 Mbytes when an 8-bit intensity resolution is used. The second is the length of time required to analyse the acquired data. In the scanning interferometers, the profiling time is further increased by the time required to scan in the x, y and z directions. In the full-field technique, the surface is only scanned in the z direction and the frames recorded by the CCD camera can be acquired at 25 frames per second. Typically, 100 frames are taken, with each frame containing approximately 250,000 pixels. This amount of data, 25 Mbytes, can be usually be acquired in under 5 seconds which is much faster than a scanning profiler. However both techniques are subject to lengthy data analysis times.

Various techniques can be used to analysis the data and usually involve complex [87] algorithms. In a practical system, intensity measurements are performed over a uniform array of x, y, and z values. The x and y array values are determined by the pixels of a CCD array. CCD arrays of 512 x 512 pixels are most common, with even larger formats becoming popular [88]. Three-dimensional data sets need significant memory storage capacity. The three main techniques used to analyse the data are digital signal processing, Fourier transforms and phase-shifting algorithms. These techniques are slow and/or involve complex computer programs to implement them and/or require large amounts of computer memory.

2.1.4.1 Digital Signal Processing

The digital signal processing (DSP) method suggested by Caber [70], is an efficient technique but requires high-speed DSP hardware. The speed of the data acquisition and analysis depends on the speed of the hardware. The technique can be used for full-field analysis using a 512 x 512 CCD camera, but even with the

high-speed hardware ten frames would still take approximately 20 seconds. Therefore a 100 μm scan with a step of 0.5 μm between each frame would take about 400 seconds. This time is, however, less than the time attainable using the other techniques mentioned above. But as well as requiring the high-speed DSP hardware it also uses a vast amount of data. The objective in all these techniques is to measure the degree of fringe modulation, or coherence, in the interference between the wave reflected from the surface and from the reference mirror. Figure 2.11 shows the signal detected in one pixel as the reference mirror is moved through optical path difference of zero. The purpose of the DSP technique is to demodulate the envelope of the fringe signal using digital filtering. If the modulation function is extracted from the signal and its peak is detected, the relative surface height can be measured for this position on the surface. If this is done for each point on the surface, a three-dimensional surface map can be made.

The fringe signal, shown in Figure 2.11, has a sinusoidal shape with a constant frequency. The amplitude of the fringes is modulated by another lower frequency, non-periodic envelope function. The intensity is described by

$$I(z) = m(z)\cos(2\pi fz + \theta) \qquad \text{Equation 2.40}$$

where m(z) is the modulation signal and f is the frequency of the fringes. This signal must be obtained for each of the 262,144 pixels. This is accomplished by moving the reference mirror in controlled steps and recording each frame. It is this data that requires such a large amount of memory. The signals are then high pass filtered to remove the DC and the low frequency components. The signals are then rectified and finally low pass filtered to output the modulation signal only. The positions of the peaks of these signals are then determined in terms of the frame number. A simple curve fitting is then used to map the surface. One important consideration in this technique is the sampling frequency when low pass filtering. The signal must not be under-sampled, thus violating the Nyquist theorem [89]. This technique is relatively fast but the complex computer programs required to control both the DSP board and the frame-grabber while also analyzing the data make this technique difficult to utilize. It is also limited to relatively smooth

surfaces, as the shape of the fringes must be accurately recorded. When the surface is rough this shape can be dramatically altered making this technique inappropriate.

2.1.4.2 Phase-shifting

The phase-shifting technique locates the point of maximum modulation for each pixel in the frame [57]. The reference mirror is translated along the z-axis using a DC stepper-motor and for each step, z_i, three intensity readings are taken corresponding to three different phases of the reference wave, $\phi 1 = 0°$, $\phi 2 = 120°$, and $\phi 3 = 240°$. This is achieved by mounting the reference mirror to a piezo-transducer (PZT), and this is attached to the DC stepper motor. The movement of the PZT for each phase step is calculated for the mean wavelength of the light source. The intensity at any pixel can be given by

$$I(z) = \bar{I} + A(z)\cos[2kz + \phi(z)] \qquad \text{Equation 2.41}$$

where A(z) and $\phi(z)$, the amplitude and phase, are functions of z. It can be shown [30] that the amplitude of the intensity modulation in each pixel is given by

$$A(z_i) = \left[\sum_i (I_i - \bar{I})^2\right]^{1/2} \qquad \text{Equation 2.42}$$

where

$$\bar{I} = \frac{1}{3}\sum_i I_i \qquad \text{Equation 2.43}$$

and I_i is the pixel intensity in the i^{th} frame. At each step of the DC motor, the reference mirror is moved by the PZT and a value for $A(z_i)$ is calculated for each pixel. At the end of the scan the position of the DC motor, where $A(z_i)$ had its maximum value is recorded for each pixel. In this way a three-dimensional profile of the surface can be made. This technique offers a high resolution with a

maximum depth accuracy that is of the order of the surface roughness. However, the acquisition of the intensity data and the calculation of the amplitude modulation for each pixel is a time-consuming process, making this technique slow. This is a major disadvantage in any full-field interferometric technique because of the errors caused by thermal and mechanical vibration and drift. Another advantage of this technique comes from the fact that the amplitude modulation is calculated at each point on the z-axis as the reference mirror is at that position, thus there is no need to store all the scan data, This means the technique does not need to use much memory. This phase-shifting technique was utilized as a comparison to the new technique described in this thesis and the results are discussed in Chapter 3.

The phase shifting technique is also used in commercial systems for calculating the relative phase at each point on the surface. It is possible to obtain height information from the phase data. This is however limited to optically smooth surfaces and has a very limited range. Step heights of greater than the mean wavelength of the light source cannot be accurately measured. The phase shifting technique is discussed in detail in Section 2.3.2 of this chapter.

2.1.4.3 Fast Fourier Transform

The fast Fourier transform (FFT) can also be used to obtain the position of the coherence region for each pixel in the frame [90]. If the scan takes 100 frames, the intensity data for each pixel is an array of 100 elements. To perform a FFT on just one of these arrays involves, of the order of, 100 $\log_2$ 100 floating-point multiplications followed by 100 multiplications for an optimized least square fit. These calculations have to be performed for all of the 262,144 pixels. Kino describes this technique in his papers [91], but briefly it involves a FFT of the data acquired as the reference mirror is translated. The negative and zero-frequency components are then removed. Finally the transform data is re-centered at the midpoint of the side-lobes and inverse transformed. In effect, this technique is the same as the Fourier transform method of fringe analysis that is described later in this chapter.

It can be assumed that mathematical operations such as multiplications, divisions, square roots and so on, are much more significant to calculation time than adding and subtraction operations. For the purpose of full-field interferometry the addition and subtraction can be performed faster than the CCD camera's framing rate. For this reason the three techniques described here are slow and complex. As mentioned in Chapter 1, the purpose of this research was to develop an optical interferometric profiler that is fast and efficient, with a high resolution and a relatively simple optical configuration. For this reason, none of the three techniques described are ideal for data analysis and acquisition.

The profiler described in this thesis uses either one of two algorithms, which do not involve any of the above mathematical techniques, instead they use only subtraction and addition operations. One algorithm can locate the interference region and the other the peak modulation within this region. The data is dealt with in a much more simple manner requiring very little analysis and less complex computer programs, thus greatly reducing acquisition time. Whereas the white light profilers that use the above techniques are limited to relatively smooth surfaces, as rough surfaces cause large errors in the algorithms, this system is versatile and can be used on many different surfaces. It is a full-field technique and can be set up easily with standard optical equipment. The algorithms are described in Chapter 3 along with the optical configuration, practical considerations and results.

2.2 Speckle Interferometry

2.2.1 Speckle

When a laser beam illuminates an optically rough surface the reflected light forms a speckle pattern, as shown in Figure 2.14. It is a direct consequence of the high coherence of the laser light described in the first section of this chapter. This speckle effect only occurs when the surface is optically rough, i.e. the height variation is of the order of, or greater than the wavelength of the illuminating light. A speckle pattern is the interference pattern produced by the coherent light reflected from different parts of the surface.

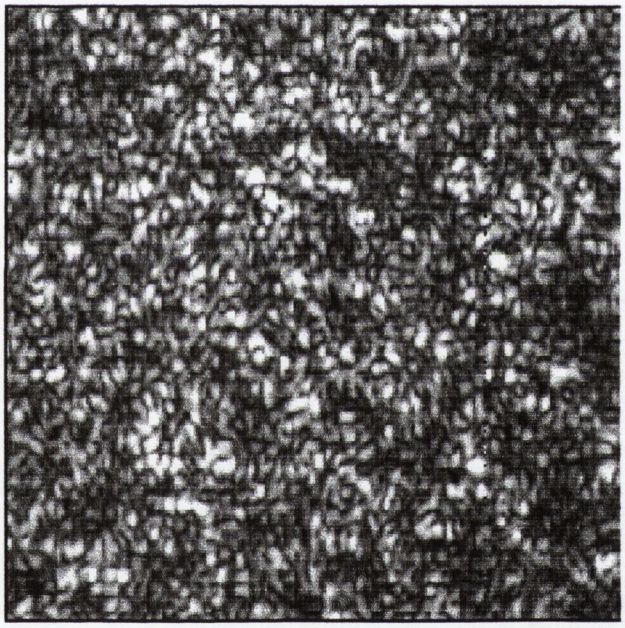

Fig. 2.14 A speckle pattern produced when a rough object is illuminated with coherent light

The amplitude of the light at any point in space is the sum of the amplitudes of the light contributed from each point on the surface. When an optically rough surface is illuminated by coherent light, every point on the surface acts as a source of spherical waves, reflecting the light back. From the previous section on interference, it is known that the complex amplitude of the scattered light at any point in space is the sum of the amplitudes of the contributions from each point. If the resultant amplitude is zero, a dark spot will be seen at that point in space,

whereas if all the rays arrive at the point in phase, an intensity maximum will be seen at the point. In Figure 2.15, a surface, in the x-y plane, whose surface height at any point (x,y) is given by $\xi(x,y)$, is illuminated by coherent light.

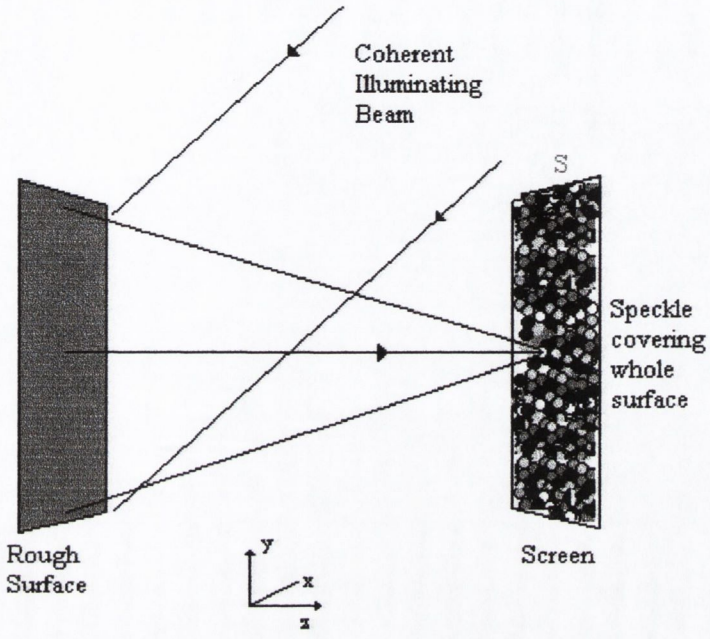

Fig. 2.15 The formation of objective speckle in the S plane.

The size of the speckles, at a given wavelength, observed in the light scattered, depends on the distance from the surface and the size of the illumination area [92]. Thus the spatial frequency of the speckle increases as the illuminated area increases. The complex amplitude U, at a point S(x,y) in space, may be written as [8]

$$U(x,y) = k\int_{-\infty}^{+\infty}\int a(x,y)\exp\left[\frac{2\pi i}{\lambda}G\xi(x,y)\right]dxdy \qquad \text{Equation 2.44}$$

Where k is a constant, a(x,y) is the complex amplitude of the light incident at (x,y) and G is a geometrical constant associated with the illumination and viewing directions. The integration is over the whole illuminated surface. Since the surface height varies randomly, the resultant amplitude also varies across S. The resultant amplitude has a value which varies between zero and a maximum value

determined by the magnitude and phase of the contributing amplitudes. As the point in space is varied, the resultant amplitude will have a different random value, and thus the intensity will vary randomly. This varying intensity pattern is known as the speckle effect.

Both Goodman [93] and Dainty [94] give detailed accounts of the speckle statistics, so only the results are given here. To understand how speckle interferometry works, it is important to know how a speckle pattern behaves. The speckle pattern at S, in Figure 2.15, will be similar in appearance to the speckle pattern shown in Figure 2.14. It can be shown that the standard deviation, σ of the intensity is given by

$$\sigma = \langle I \rangle \qquad \text{Equation 2.45}$$

where $\langle I \rangle$ is the mean intensity. The intensities at two points on the speckle pattern, will be closely related when the points are close to one another. As they move apart, the intensities become different and unrelated. R, the autocorrelation function, provides the relationship between the two points as a function of the distance between them. When the distance between them equals zero, $R = \langle I^2 \rangle$. The distance at which the intensities become unrelated provides an estimation for the size of the speckles. Goodman derived an expression for the autocorrelation function, where the surface, of dimensions of L x L, is illuminated by a beam of uniform intensity. From this, the average size of a speckle is Δx, given by

$$(\Delta x) = \frac{\lambda z}{L} \qquad \text{Equation 2.46}$$

where z is the distance between the viewing and object planes. Thus, the speckle size is inversely proportional to the size of the illuminated area. This type of speckle is termed objective speckle.

When an image is formed of the illuminated surface, the image is a similar speckle pattern. In this case, the size of the speckles in the image plane is dependent on the

aperture of the viewing system and the distance from the lens to the image plane. In Figure 2.16, a point P1 on the surface is imaged onto the image plane S, forming

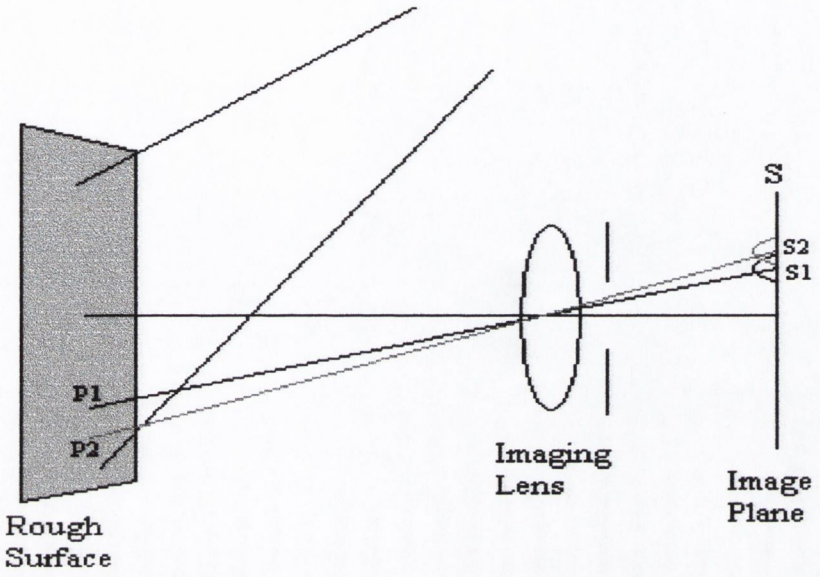

Fig. 2.16 The formation of subjective speckle in the S plane.

a diffraction pattern centered at S1. The amplitude distribution across the diffraction pattern is given by [8]

$$U(S) = A_o \exp\left(\frac{2\pi i \cos\theta}{\lambda}\right)\left|\frac{J_1(\pi b \sin\theta/\lambda)}{\pi b \sin\theta/\lambda}\right| \qquad \text{Equation 2.47}$$

where b is the width of the wavefront and J_1 is a first order Bessel function. Points around P1 will produce similar diffraction patterns which overlap onto S1. The amplitude, given by Equation 2.47, will be different for each diffraction pattern as the light from each point on the surface has a random phase produced by the random variations in the surface height. The point P2 makes no contribution to the complex amplitude at S1 as the diffraction pattern it produces has its first minimum overlapping with S1. The contributions from points further away from P1 than P2 are negligible as the secondary maxima are much smaller than the

primary maxima. Therefore, the intensity of the light at the point S1 is the sum of the intensity contributions from an area centered around P1 with a diameter d_o, given by twice the distance between P1 and P2. The distance, d_i, on the image plane between S1 and S2 can be derived from the Bessel function as

$$d_i = \frac{1.22\lambda v}{a} \qquad \text{Equation 2.48}$$

where a is the diameter of the viewing lens aperture and v is the distance from the lens to the image plane. Thus, the size of the speckle in the image plane is given by

$$d_{sp} = \frac{2.4\,\lambda v}{a} \qquad \text{Equation 2.49}$$

This corresponds to an object size [81] of

$$d_{obj} = \frac{2.4\,\lambda u}{a} \qquad \text{Equation 2.50}$$

Thus the size of the speckles in the image plane is dependent on the aperture of the imaging lens. This is called subjective speckle. In objective speckle, light from the entire illuminated surface contributes to every speckle, whereas in the subjective speckle, the light rays contributing to any one speckle can only come from a limited area on the object, the object speckle size. This is an important difference between the two types of speckle.

Goodman also calculated the probability density function of the speckle patterns intensity. It was found that the most probable intensity at any point is zero. It is this property that causes the high contrast observed in a speckle pattern.

When laser light was first used for optical surface metrology the speckle effect was regarded as a nuisance. It is still regarded as such in holography where speckle is regarded as noise. However, since 1970, when Leendertz [34] demonstrated the use of speckle to measure surface displacements, speckle has become an important

tool in optical surface metrology. It has some obvious advantages over the alternative mechanical techniques, in that it is a non-contact technique and allows for full-field analysis. Speckle techniques have been used to measure surface roughness [95], displacement [32], strain [96], slope change [97] and shape of many different surfaces [98]. The speckle techniques can be categorized under two headings; those that measure the positional changes of speckles; and those that measure the change in intensity in the speckles. Speckle photography [8] describes the first category and speckle interferometry includes the techniques that measure intensity changes caused by phase changes. The speckle technique described in this thesis is electronic speckle pattern interferometry.

2.2 Electronic Speckle Pattern Interferometry

Electronic speckle pattern interferometry (ESPI) is based on the coherent addition of a subjective speckle pattern scattered from an object and a reference field, which may or may not be speckled. It was first developed as a way of measuring surface displacements caused by deforming the object [35]. The introduction of the reference wave brings about a significant change in the behavior of the speckle pattern when the object is deformed. As the observed speckle pattern is formed by the interference of two coherent fields, the intensity of the resultant field depends on the relative phase distribution of the added fields. If the object is deformed the relative phase of the two fields will change causing a variation in the intensity of the resultant pattern. The deformed speckle pattern will match the initial pattern (correlated) if the variation of the path difference is an integral multiple of λ, the wavelength of the light source, and a total contrast change occurs (decorrelation) for a variation of an odd multiple of $\lambda/2$. Speckle pattern interferometry is based on the measurement of the changes in a speckle pattern, obtained by the coherent superposition of the two independent fields, as a function of the phase difference between the two fields. The fringes in speckle interferometry, arise from the correlation of the two speckle pattern intensity distributions obtained before and after a change in the relative phase. The regions of maximum correlation are

obtained as the locations of the points that have undergone a phase change of 2π, or its multiple, between the two resultant speckle patterns.

The first speckle pattern interferometers used photographic plates as the recording medium [8]. Leendertz developed the technique as a way of measuring surface displacements. In the early 1970s, Butters and Leendertz developed various speckle pattern interferometers for measuring displacements along various directions [8]. It was viewed as a more flexible technique than holographic interferometry despite the fringe quality being poorer. Speckle interferometers have the ability to be sensitive to displacements in only one direction and allow real-time displacement fringes to be observed. The fringe quality was usually poor when photographic recordings were made. When electronic recording and processing was used, the technique became known as electronic speckle pattern interferometry and later TV holography [99]. The fringe quality quickly improved with new processing techniques. The quality was still poor relative to holographic fringes and the fringe quality itself became a subject of debate [100]. In the 1970s most of the work done on ESPI concentrated on the development of the optical systems. In the early 1980s, research concentrated on the electronic processing and fringe quality [101-103]. The major area of research since then has been the development of fringe analysis software, including phase-shifting [104], Fourier transforms [105] and phase-unwrapping algorithms [106]. Over the last few years electronic processing has become unnecessary and the signals from the cameras are digitized. The correct term for this technique is "digital speckle pattern interferometry", but ESPI is still used to describe the technique. The advances in fringe analysis and image processing have surpassed the capabilities of many ESPI systems. For this reason in the last few years research into improving the optical systems themselves has been carried out by ESPI research groups and ESPI systems manufacturers [107-109].

In its simplest form, ESPI involves taking an image of the resultant speckle pattern produced when the reference field interferes with the object field. The object is then deformed or displaced and another image of the resultant speckle pattern is taken. The intensity of this pattern will have changed due to the change in phase,

between the two fields, caused by the displacement. A correlation is then performed on the two resultant intensity patterns, producing fringes describing the displacement. If both the reference and object field are speckle wavefronts, the complex amplitude of these wavefronts are given by

$$e_1 = E_{o1}e^{i\varphi 1} \qquad \text{Equation 2.51a}$$

and

$$e_2 = E_{o2}e^{i\varphi 2} \qquad \text{Equation 2.51b}$$

where E_{o1} and E_{o2} are the randomly varying amplitudes of the speckle patterns on the image plane. Similarly φ_1 and φ_2 are the randomly varying phase terms. From the first section of this chapter, the intensity recorded is given by

$$I = |E|^2 = E.E^* \qquad \text{Equation 2.52}$$

Therefore the resultant intensity is

$$\begin{aligned} I &= |E|^2 = E.E^* \\ &= |e_1 + e_2|^2 \\ &= \left(E_{o1}e^{i\varphi_1} + E_{o2}e^{i\varphi_{21}}\right)\left(E_{o1}e^{-i\varphi_1} + E_{o2}e^{-i\varphi_{21}}\right) \\ &= E_{o1}e^{i\varphi_1}E_{o1}e^{-i\varphi_1} + E_{o2}e^{i\varphi_{21}}E_{o2}e^{-i\varphi_{21}} + \\ &\quad + E_{o1}E_{o2}e^{i\varphi_1}e^{-i\varphi_{21}} + E_{o1}E_{o2}e^{-i\varphi_1}e^{i\varphi_{21}} \\ &= {E_{o1}}^2 + {E_{o2}}^2 + 2E_{o1}E_{o2}e^{i(\varphi_1-\varphi_2)}e^{-i(\varphi_1-\varphi_2)} \\ &= {E_{o1}}^2 + {E_{o2}}^2 + 2E_{o1}E_{o2}\cos(\phi) \end{aligned}$$

$$I = I_1 + I_2 + 2\sqrt{I_1 I_2}\cos(\phi) \qquad \text{Equation 2.53}$$

where $\phi = \varphi_2 - \varphi_1$. The fact that ϕ is a randomly varying term produces the resultant speckle pattern. It is clear from this equation that the resultant intensity oscillates between two values given by

$$I = I_1 + I_2 + 2\sqrt{I_1 I_2} \quad \text{Imax} \qquad \text{Equation 2.54a}$$

$$I = I_1 + I_2 - 2\sqrt{I_1 I_2} \quad \text{Imin} \qquad \text{Equation 2.54b}$$

After a change in the phase between the two beams the resultant intensity is given by

$$I = I_1 + I_2 + 2\sqrt{I_1 I_2}\cos(\phi + \Delta\phi) \qquad \text{Equation 2.55}$$

A correlation must be performed on the two intensity patterns described by equations 2.53 and 2.55 to find a relationship. The correlation coefficient $\rho(\Delta\phi)$ of two sets of random variables X and Y, is given by [110]

$$\rho_{XY} = \frac{\langle XY \rangle - \langle X \rangle \langle Y \rangle}{\sigma_X \sigma_Y} \qquad \text{Equation 2.56}$$

where

$$\sigma_X = \left(\langle X^2 \rangle - \langle X \rangle^2 \right)^{\frac{1}{2}} \qquad \text{Equation 2.57a}$$

and

$$\sigma_Y = \left(\langle Y^2 \rangle - \langle Y \rangle^2 \right)^{\frac{1}{2}} \qquad \text{Equation 2.57b}$$

If the two sets are independent, the correlation coefficient is equal to zero. Substituting equations 2.53 and 2.55 into this expression gives

$$\rho(\Delta\phi) = \frac{1}{2}(1 + \cos\Delta\phi) \qquad \text{Equation 2.58}$$

where it is assumed that $I_1 = I_2$. Thus the correlation is unity when

$$\Delta\phi = 2n\pi \qquad \text{Equation 2.59}$$

where n is an integer, and the correlation coefficient equals zero when

$$\Delta\phi = (2n + 1)\pi \qquad \text{Equation 2.60}$$

Thus correlation between the two images produces a fringe pattern defining contours of equal phase change. In electronic speckle pattern interferometry, the original interference which takes place is imaged by the CCD camera and the intensity data is digitized by a frame grabber, stored in the computer memory, and displayed on the monitor. This is called the reference image. After the object has been displaced, the frame grabber digitizes the new resultant speckle pattern and the reference image is subtracted from it. The intensities of the images are described by Equation 2.53 and 2.55, thus the intensity of the image produced by the subtraction is given by

$$\begin{aligned}
\Delta I = I_0 - I_t &= \left(I_1 + I_2 + 2\sqrt{I_1 I_2}\cos(\phi)\right) - \left(I_1 + I_2 + 2\sqrt{I_1 I_2}\cos(\phi + \Delta\phi)\right) \\
&= 2\sqrt{I_1 I_2}\left[\cos(\phi) - \cos(\phi + \Delta\phi)\right] \\
&= 2\sqrt{I_1 I_2}\left[-2\sin\left(\phi + \frac{\Delta\phi}{2}\right)\sin\left(-\frac{\Delta\phi}{2}\right)\right] \\
&= 4\sqrt{I_1 I_2}\left[\sin\left(\phi + \frac{\Delta\phi}{2}\right)\sin\left(\frac{\Delta\phi}{2}\right)\right] \qquad \text{Equation 2.61}
\end{aligned}$$

This equation describes an image that contains both negative and positive values. A monitor is only able to display positive values, so the result from the subtraction must be rectified. Mathematically, there are two easy ways to rectify; the absolute value of the sine terms; and the square function. The absolute value is easily carried out within the computer using an output look-up table that converts any negative value into a positive value. The result from the square of the image is given by

$$I = 4\left[I_o I_r \sin^2\left(\phi + \frac{1}{2}\Delta\phi\right)\sin^2\frac{1}{2}\Delta\phi \right]^{1/2} \qquad \text{Equation 2.62}$$

which can also be expressed as

$$I = 4I_o I_r (1 - \cos\Delta\phi) \qquad \text{Equation 2.63}$$

Again, when $\Delta\phi = 2n\pi$, I_{t1} and I_{t2} have maximum correlation and so the resultant intensity is zero. Minimum correlation occurs when $\Delta\phi = (2n + 1)\pi$ and the resultant intensity will be a maximum. Therefore Equation 2.63 represents a fringe pattern, which is identical in form to those obtained using the mathematical correlation in Equation 2.61. From a mathematical simulation, speckle patterns can be produces using Equations 2.53 and 2.55.

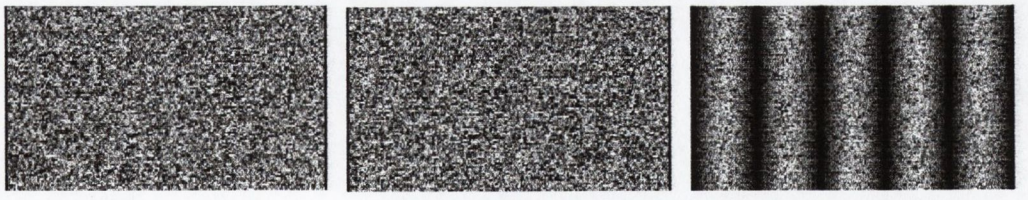

A. Initial Speckle Pattern

B. Speckle Pattern taken after change in phase

C. Fringe pattern resulting from the subtraction and rectification

Fig. 2.17 By correlating between the two speckle patterns A and B, the fringe pattern C is produced.

Figure 2.17 shows the results of this simulation and when mathematically subtracted and rectified produced the fringe pattern on the right. A similar fringe pattern is obtained when the two fields are added together. This technique is used in pulsed ESPI for measuring vibration and in ESPI contouring where the surface is illuminated simultaneously with two different wavelengths. Contouring ESPI is described in Section 2.2.4 of this chapter. Unlike the fringe pattern obtained by subtraction, areas of maximum correlation have the highest intensities in the addition fringe pattern. Using Equations 2.53 and 2.55, the resultant intensity is

$$I = 2I_o + 2I_r + 4\sqrt{I_o I_r}\cos\left(\phi + \frac{1}{2}\Delta\phi\right)\cos\frac{1}{2}\Delta\phi \qquad \text{Equation 2.64}$$

The obvious disadvantage of this technique is the reduced contrast, as the minimum intensity, which occurs in areas of minimum correlation is not equal to zero.

One of the major advantages of ESPI is its ability to display the formation and progressive changes of the fringe pattern in real-time. It is possible to take a reference frame and subtract it from all subsequent frames taken by the CCD camera. This can be done at the framing rate of the camera, typically 25 Hz. When the whole object is in the field of view and deformation starts the first dark fringe to appear is the zero-order fringe and corresponds of a phase change of zero, from equation 2.59; $\Delta\phi = 2n\pi$, where n is 0. At any point on the surface, the number of fringes between that point and the zero order fringe can be counted to give the total phase change at that point.

It is clear from Figure 2.17 that ESPI fringe patterns are inherently noisy. The fringe quality plays an important role in the performance of an ESPI system. The sensitivity and resolution of the technique depends on its ability to detect and analyse the fringes. The accuracy of the automatic fringe analysis techniques, like phase-shifting, also depends on the quality of the fringes. Poor visibility or very noisy fringes can cause large errors in the analysis. The contrast of the fringes is determined by the ratio of the mean intensity along the bright fringes to the mean

intensity along the dark fringes. The actual contrast that is obtained depends on whether subtraction or addition is used, the intensities of the beams and the degree of decorrelation that occurs. Deterioration in the ESPI fringe contrast is called decorrelation and the fringes can decorrelate even when there are only a couple of fringes on the screen. The various factors that cause this are; variation in phase across an individual speckle; speckle displacement; surface displacements in any direction other than the measured direction; rotation; and a change in wavelength. Research into improving and optimizing fringe contrast is continually being carried out [101]. The following paragraphs detail the steps to be taken to ensure optimum contrast.

The intensity of the speckle varies across the image and so to avoid losing any information the whole dynamic range of the camera should be used. This is accomplished by operating the camera at or just below saturation. As shown in the previous section, the size of the speckle in the image plane depends on the imaging lens aperture. Ideally the size of the speckles in the image should be identical to the size of the pixels. If the speckles were smaller than this more than one speckle would cover a pixel and the average of the two intensities is recorded. This averaging causes decorrelation in the fringe visibility which increases as the number of speckles filling each pixel increases. Therefore the aperture on the imaging lens should be set so that the spatial frequency of the speckle pattern should equal the maximum spatial frequency that the system can image. This aperture setting might not let sufficient light reach the array to saturate the camera. In this case there is a compromise between the speckle size and using the full dynamic range of the camera. This will ultimately depend on the laser power and the size of the illuminated area.

To obtain maximum contrast, the mean intensities of the two interfering wavefronts should be equal. This eliminates all background intensities and just leaves the interference terms after subtraction. Even after these steps have been taken and optimum fringe contrast is obtained, the contrast can quickly deteriorate due to speckle decorrelation. Using a smooth reference wave also helps improve the contrast as it increases the signal-to-noise ratio by reducing the noise due to the

speckle. The next paragraph describes some of the factors that cause this decorrelation and other causes that are particular to certain systems are explained in the following sections.

Speckle interferometry measures the change in intensity between two speckle patterns. It does this by imaging each speckle onto an element of an array and measuring the change in intensity of the light across that element. The light must come from the same speckle in both cases. If the surface is displaced such that the light incident on the pixel now comes from a different speckle, there will be no correlation between the two intensities. This will inevitably lead to decorrelation. Decorrelation begins as soon as the surface starts to be displaced. The effect is not noticed as ESPI measures such small displacements that the movement of the speckles is very small relative to the size of the speckles. If each speckle on the object is imaged onto just one pixel, and the object moves by the size of a speckle total decorrelation will occur.

One of the major causes of decorrelation in any ESPI system is vibration. If the speckles are moving as the frame is grabbed it has the effect of averaging the fringes and so reducing the contrast. Speckle movement can be caused by both air turbulence and mechanical instability. For this reason an ideal ESPI system will have no moving parts and be very compact and robust.

When the fringe spacing becomes comparable to the speckle size, the fringe visibility decreases and drops to zero when the fringe spacing equals the speckle size. Usually, the fringe visibility will drop off even before this happens because of the noisy nature of the ESPI fringes. It is usually not possible to get more than 20 fringes on an image of 512 x 512. It is then necessary to take a new reference frame and start the subtraction again.

Depending on the optical configuration of the interferometer, the ESPI systems can be made sensitive to displacements perpendicular to the viewing direction, called in-plane, or displacements parallel to the viewing direction, called out-of-plane. In

the next sections these optical configurations will be described and how the same set-ups can be used to measure the shape of surfaces.

2.2.3 Out-of-plane ESPI

The optical configuration of the Leendertz ESPI system is shown in Figure 2.18 [92]. It is similar to the Michelson interferometer but the mirrors have been replaced with non-specular surfaces. Leendertz used a photographic plate in the image plane and used a double exposure technique to obtain fringes by addition. The resultant speckle pattern in the image plane is formed by the interference of the two speckle fields scattered from the surfaces. The surfaces are illuminated by collimated light, normal to the surface. The distance from the image plane to the object along the optical axis is d_0. When one of the surfaces is deformed, the relative phase change between the waves at a point (x,y) in the image is given by [92]

$$\Delta\phi = \frac{4\pi d}{\lambda}\left(1 - \frac{x^2 + y^2}{4d_0^2}\right) = n\lambda \qquad \text{Equation 2.65}$$

where it is assumed there is virtually no movement of the surface in the x and y planes, and d is the displacement along the z-direction. From this equation, it is clear that the fringes obtained are only contours of equal out-of-plane displacement for the points lying close to the optical axis. A correction term for each point (x,y) is needed

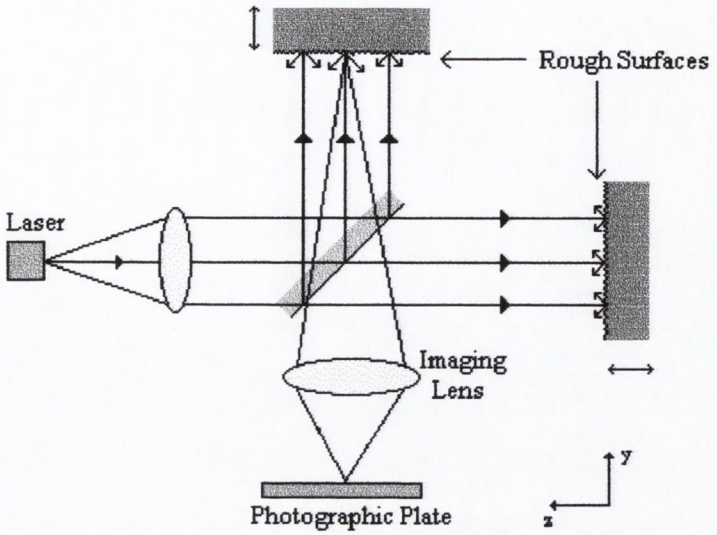

Fig. 2.18 The schematic of the Leendertz out-of-plane ESPI system.

when analyzing the fringes. If this term isn't used the error introduced is of the order of

$$\frac{\delta d}{d} = \frac{x^2 + y^2}{4d_0^2} = \frac{\tan^2\theta}{4} \qquad \text{Equation 2.66}$$

Obviously, this error will be greater the larger the surface and the closer it is to the imaging lens. However, in reality this error is usually very small and there are usually greater errors in the fringe analysis, making this error irrelevant. Thus, the phase change between the two fields at any point on the image can be given by

$$\Delta\phi = \frac{4\pi d}{\lambda} = n\lambda \qquad \text{Equation 2.67}$$

where n is the fringe order number. Maximum intensity correlation, between the images taken before and after deformation, occurs when $\Delta\phi = 2n\pi$ and minimum correlation occurs when $\Delta\phi = (2n + 1)\pi$. When the system is used with a CCD

camera, the frame taken before deformation is subtracted from the frame after, and the result rectified, producing a fringe pattern. Areas of maximum correlation are seen as dark fringes and correspond to a displacement of

$$d = \frac{n\lambda}{2} \qquad \text{Equation 2.68}$$

Areas of minimum correlation are seen as bright fringes and occur in areas where the out-of-plane displacement is

$$d = \frac{(n + 1/2)\lambda}{2} \qquad \text{Equation 2.69}$$

With image processing and advanced ESPI algorithms and software available today, the fact that there are two speckle beams in the system does not deteriorate the contrast of the fringes. However before these were available the use of two speckle fields in the system led to poor contrast fringes. An alternative out-of-plane system developed by Butters and Leendertz is shown in Figure 2.19 [92].

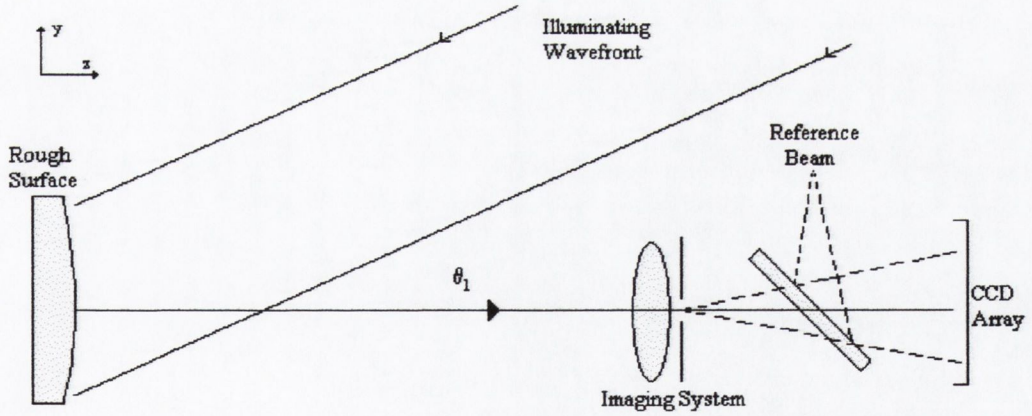

Fig. 2.19 The schematic of the Butters and Leendertz out-of-plane ESPI using a smooth reference beam.

In this system a smooth reference wave is added to the object speckle field along the optical axis. The resultant speckle pattern is the interference of the speckle field and the smooth reference field. The object is illuminated by a collimated wave in

the xz plane and making an angle of θ_1 to the surface normal. The phase change caused by an out-of-plane displacement has the form

$$\Delta\phi = \frac{2\pi}{\lambda}(n_i - n_v)\cdot d \qquad \text{Equation 2.70}$$

where n_i and n_v are the illumination and viewing directions respectively. This system is now sensitive to displacements along the x-direction, but this sensitivity is very small and so long as the illumination angle is kept to a minimum the phase change can be given by

$$\Delta\phi = \frac{2\pi(\cos\theta_1 + \cos\theta_2)d}{\lambda} \qquad \text{Equation 2.71}$$

where θ_2 is the viewing direction. In this system $\theta_2 = 0$, so the phase change is just

$$\Delta\phi = \frac{2\pi(1 + \cos\theta_1)d}{\lambda} \qquad \text{Equation 2.72}$$

A typical out-of-plane fringe pattern is shown in Figure 2.20A. Figure 2.20B shows the colour-coded displacement map after the fringes have been analysed. Fringe analysis is discussed in the next section. Two consecutive dark fringes represent a phase shift of 2π, so from Equation 2.72 they represent an out-of-plane displacement given by

$$d = \frac{\lambda}{1 + \mathrm{Cos}\theta} \qquad \text{Equation 2.73}$$

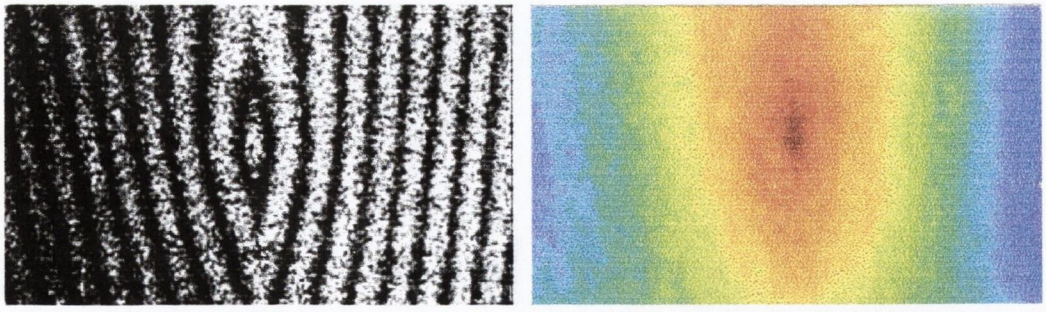

A Out-of-plane ESPI fringe pattern B Colour-coded surface displacement map

Fig. 2.20 A, An out-of –plane ESPI fringe pattern from a composite beam; B, The corresponding colour-coded displacement map.

2.2.3.1 Sources of Errors

A major source of errors in ESPI systems is rigid body motion. This motion does not usually decorrelate the fringes, instead it adds fringes to the pattern. For example, an object is compressed from above, along the y-direction and the out-of-plane expansion of the surface is measured. Fringes appear as the expansion starts, but if the surface now tilts out-of-plane or rotates the fringes caused by this movement are added to the pattern. Any out-of-plane ESPI system that uses an off-axis illumination beam is also sensitive to in-plane displacements, although this sensitivity is negligible if the illuminating angle is kept to a minimum. In deriving Equation 2.72, it was assumed the illuminating beams were collimated. If a diverging beam is used the sensitivity changes across the surface and Equation 2.72 can only be used along the optical axes. If this is overlooked when analyzing the fringes, there will be errors in the readings that increase as the position moves out from the center. Obviously when large surfaces are tested a diverging beam must be used. If a correction term isn't used when analysing the fringes the error can be reduced by illuminating and viewing the object from as far away as possible. Albrecht [150] calculated the maximum error to be 12% when an area of $1m^2$ is illuminated and viewed from 1 metre away.

There have been many different configurations of the out-of-plane ESPI system used in a wide variety of applications. Fiber-optic systems have been used to stabilize the fringes that move due to mechanical instability or thermal fluctuations

[111]. Fiber systems have been used for endoscopic ESPI to measure surface displacements on small areas that are in locations where direct light cannot reach [112]. Portable out-of-plane ESPI systems have been designed for use outside of laboratories [113]. These systems need to be robust and capable of taking measurements in a mechanically unstable environment. Out-of-plane ESPI has been used to measure deformations in artwork, old buildings and in fracture mechanics [114]. Even though the fringes can be analysed to retrieve quantitative data, the technique is commonly used as a detector of cracks and delaminations. If a homogeneous surface is compressed the fringe pattern is made up of parallel fringes. A defect or a point of delamination in the object causes the surface to move in an irregular way, which will be seen in the fringe pattern. A crack in an object becomes a source of fringes as the object surface moves more in that area. Figure 2.21 shows two such fringe patterns obtained from an out-of-plane system. The fringe pattern on the left was obtained when a force was applied to a plaster wall, in the z-direction. The discontinuity in the fringes is the location of a defect. The second fringe pattern was obtained from a plastic pipe subjected to a compression force, in the y-direction. Here, the sources of non-uniform fringes are locations of defects. It is important to note these techniques can be non-destructive and the objects return to their original state when the force is removed.

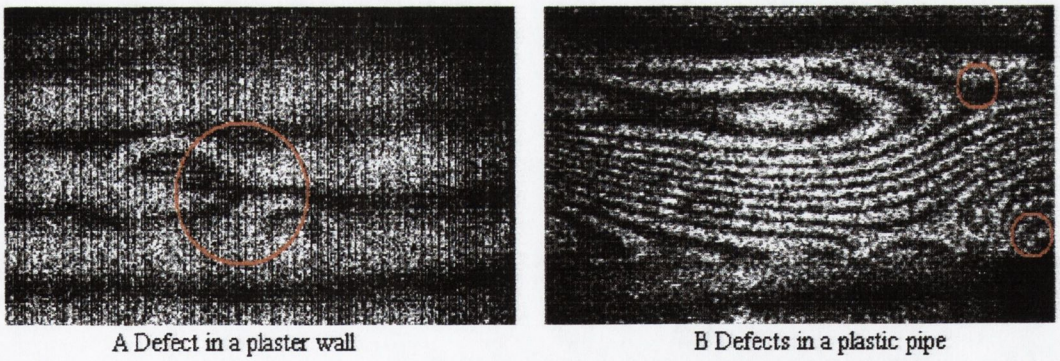

A Defect in a plaster wall B Defects in a plastic pipe

Fig. 2.21 Out-of-plane ESPI fringes can be used for detecting defects in materials; A, The anomaly in the fringe pattern is a defect in a plaster wall; B, Point sources of fringes in a compressed pipe indicate defects.

When quantitative results are required, out-of-plane ESPI can be used to calculate important mechanical properties of the material. It has also been used to measure such things as vibration of flutes [115], the deformation of materials at high

temperatures [51], vibration analysis of logs [116], mixing dynamics of transparent fluids [117] and vibrations of the basilar membrane [118].

2.2.3 In-plane ESPI

The optical configuration shown in Figure 2.22 produces fringes which are sensitive to in-plane displacements. The object lies in the xy plane and is illuminated by two collimated wavefronts, in the xz plane and making an angle θ with respect to the surface normal. The resulting speckle pattern in the image plane is the result of the interference of the two speckle fields corresponding to each of the two illuminating beams.

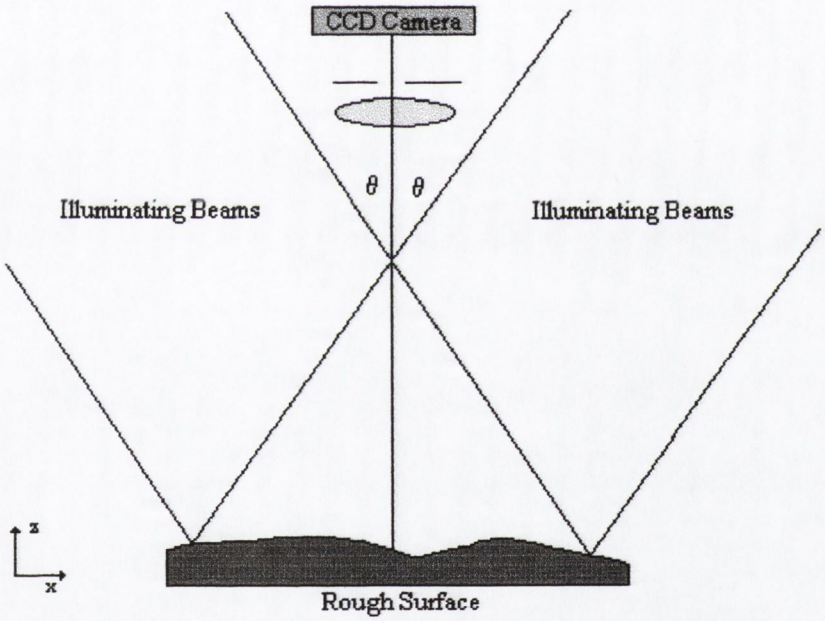

Fig. 2.22 A schematic of an in-plane ESPI system.

Any displacements in the z and y directions will not introduce a relative phase change between the two fields. Therefore this system allows in-plane displacements along the x-direction to be measured independently of any other displacement. The relative phase change between the two speckle patterns is given by

$$\Delta\phi = \frac{4\pi}{\lambda} d\sin\theta \qquad \text{Equation 2.74}$$

Errors can occur in these systems if the illuminating beams are not collimated and if they are not symmetrical around the viewing direction. From trigonometric analysis [92] the error can be shown to equal

$$\frac{\delta d}{d} = \frac{\delta\theta}{2}(\cot\theta) \qquad \text{Equation 2.75}$$

where $\delta\theta$ is the difference between the two illumination beam angles.

The system only measures displacement along a particular direction that lies normal to the viewing direction and is in the plane of the two illumination beams. In order to measure displacement along the y-direction in Figure 2.22, the illumination beams would have to be in the y-z plane. To make a system sensitive to displacement in both the x and y axes, four illumination beams are needed. This makes complete in-plane displacement measurement possible by vectorially adding the displacement in the x-direction to the displacement in the y-direction. If two pairs of beams illuminate the surface at the same time the resultant speckle pattern at any time will contain the cross interference terms of the beams. Therefore, no useful information can be obtained from these images. This restriction has lead to many different optical configurations, including the use of two lasers [107], shutters, two CCD cameras and different polarisation states [119]. As ESPI systems have such a high sensitivity, the use of moving parts is not ideal and this is a disadvantage of using two lasers and shutters.

The system that uses two cameras allows the surface to be illuminated by all four beams at the same time. It uses one laser whose output beam is split in two and the two beams are then aligned to have orthogonal states of polarisation. One beam is then split in two and used to measure the x-component. This beam is vertically polarised and the other beam, used to measure the y-component is horizontally polarised. Even though the surface is illuminated with all four beams at one time,

interference can only occur between beams in the same polarisation state. Figure 2.23 shows the schematic arrangement of the system. The two CCD cameras view the surface through the polarising beamsplitter, thus each camera will only see a pair of speckle patterns in the same polarisation state. Only the two vertically polarised speckle fields are incident on Camera 1 in Figure 2.23, thus the images from this camera can be used to

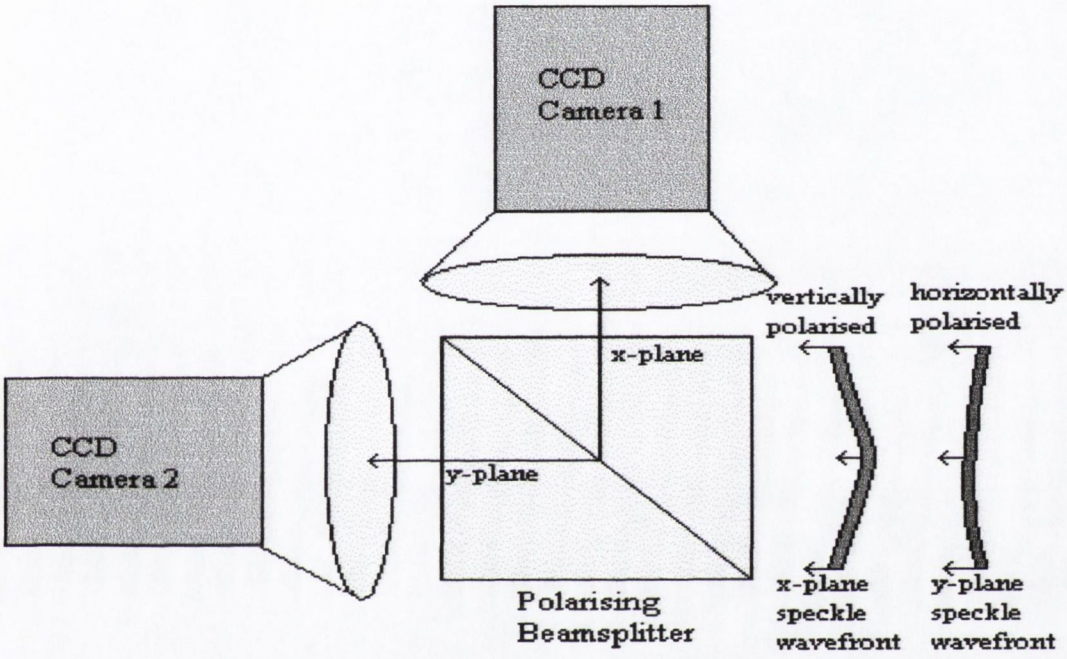

Fig. 2.23 The imaging arrangement in the two camera in-plane ESPI system.

measure displacement in the x-direction. Likewise, Camera 2 measures the displacement in the y-direction. This system has the advantage that the displacement in both the x-direction and y-direction can be measured at the same time. However the success of the measurements depends on the polarisation states of the two speckle fields incident on the cameras. These depend on the state of polarisation of the light incident on the surface, the dielectric properties of the surface and on the efficiency of the beamsplitter. The incident light can penetrate many surfaces where it is multiply scattered, thus depolarising the linear polarised beam. In ESPI white matt paint is frequently used as a surface preparation to produce a uniformly scattering surface, but this paint can change the polarisation of the incident light. Therefore the use of this system is limited to surfaces which do not change the polarisation of the light. The fact that the laser power is divided

between the two arms is also a disadvantage when large surface areas are measured. For these reasons this optical configuration is not commonly used and commercial system use shutters and more than one laser. The use of any mechanical device in any ESPI system should be avoided. Shutters and movable mirrors can cause mechanical instability. The use of more than one laser makes the commercial systems expensive and not very compact. In Chapter 4, a new dual in-plane ESPI system is described which has no moving parts and only uses one laser. Figure 2.24A shows a typical in-plane ESPI fringe pattern representing the surface displacements in the x-direction of a steel bar under a tensile force. The corresponding colour-coded surface displacement map is shown in Figure 2.24B. The meaning and analysis of the fringe pattern is discussed in the next section.

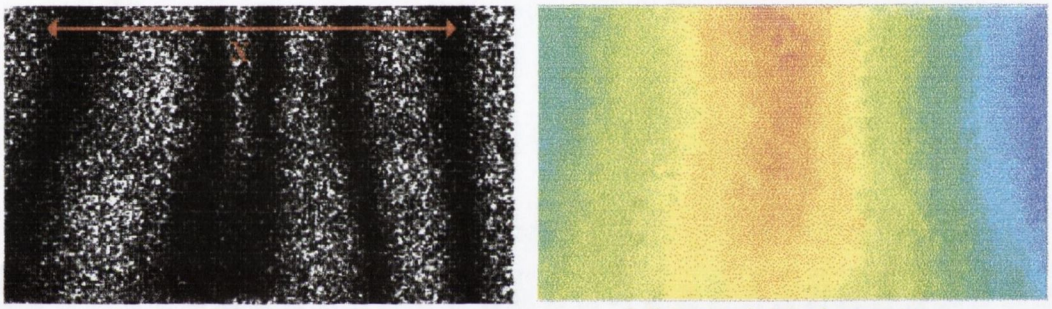

A In-plane ESPI fringe pattern B Colour-coded displacement map

Fig. 2.24 A, Fringe pattern representing the surface displacement, along the x-direction, in a steel beam under a tensile force; B, The corresponding colour-coded displacement map.

In-plane ESPI is frequently used in three-point bending tests to measure stress and strains. Like out-of-plane ESPI, in-plane ESPI can also be used to detect cracks and defects. Figure 2.25 shows in-plane displacement fringes acquired from a three-point bend test. The specimen is a clay tile with a notch in it. Under the three-point bend test a crack develops from the notch tip and travels up the specimen. The crack is seen in the fringe pattern as a source of the fringes. In this way in-plane ESPI can be used to measure the crack tip propagation which is used to calculate important mechanical properties. This process is described in Chapter 4 along with the results of tests carried out on clay samples.

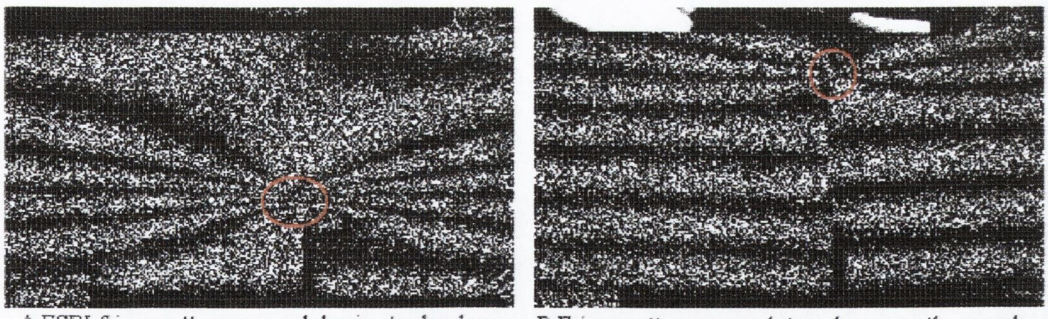

A ESPI fringe pattern as crack begins to develop B Fringe pattern as crack travels across the sample

Fig. 2.25 In-plane ESPI fringe patterns used to detect cracks in clay components.

2.2.4 Contouring ESPI

In 1978, Jones and Wykes developed an ESPI system for measuring the difference between the shape of two surfaces [8]. A change in the relative phase between the two waves, object and reference, is introduced by changing the wavelength of the light between successive frames. The optical setup of the system, as shown in Figure 2.26, is identical to the out-of-plane system developed by Leendertz. In this system the object is illuminated with the first wavelength λ_1 and an image is formed on the CCD array, where a smooth reference beam is added.

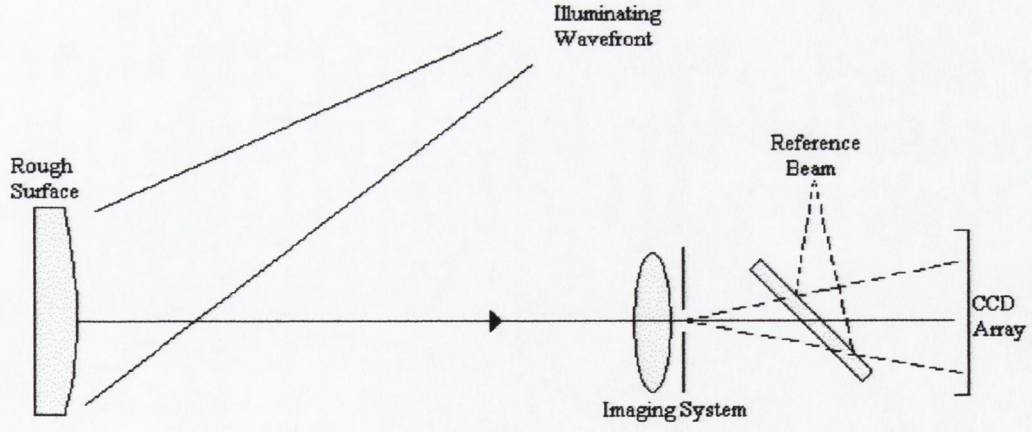

Fig. 2.26 The schematic of an ESPI contouring system using two wavelengths.

The resultant speckle pattern is grabbed and saved in memory. The wavelength of the light is then changed and a second image is grabbed and subtracted from the first to produce fringes. The fringe pattern obtained gives the difference in depth along the viewing direction between the surface and the master wavefront, i.e. the

wavefront used to illuminate the surface. If the master wavefront is flat, then the fringes represent the shape of the surface. The sensitivity of the fringes obtained is determined by the wavelength change between the frames.

As previously mentioned, addition can be used as the correlation technique to produce the fringes. Therefore the surface can be illuminated simultaneously by a master wavefront at wavelengths λ_1 and λ_2, and the resultant speckle patterns are automatically added together. This is possible because the speckle fields corresponding to the different wavelengths will not interfere with one another. However, as with all addition speckle techniques, the fringe contrast is reduced because the DC components are still present. Therefore subtraction techniques are preferred which means consecutively illuminating the surface with each wavelength. In order for this technique to work, there are restrictions imposed on the shape of the master wavefronts. The master wavefront must converge to a point with a single phase when reflected by a surface of specularly reflecting finish whose shape matches the shape of the surface to be measured. An example of a flat master wavefront is shown in Figure 2.27.

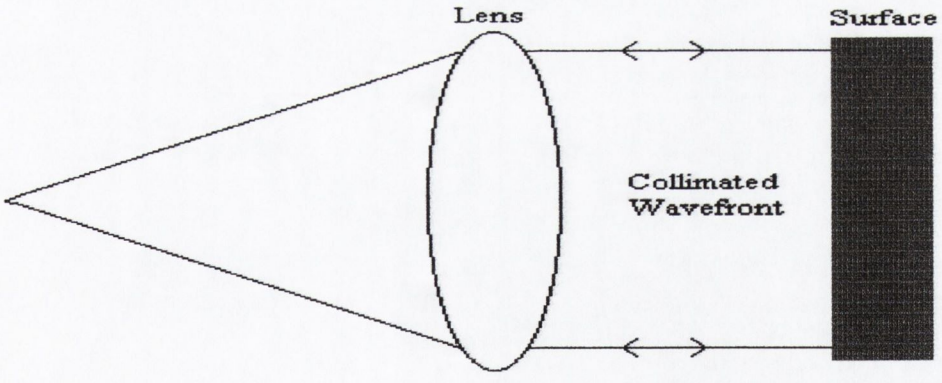

Fig. 2.27 A flat master wavefront used in ESPI contouring for shape measurement.

A collimated beam illuminates the plane surface and the reflected light will converge to the original point of divergence. In other words, if the shape of a surface is to be measured it must be illuminated by a flat master wavefront and if

this same wavefront was used on a optically flat surface all rays reflected from the surface would reach the CCD array with the same phase.

If the Michelson interferometer configuration and collimated light are used, as shown in Figure 2.28 the intensity of the resultant speckle pattern at a point in the image, I_{T1}, formed by the coherent addition of the object and reference fields, is given by

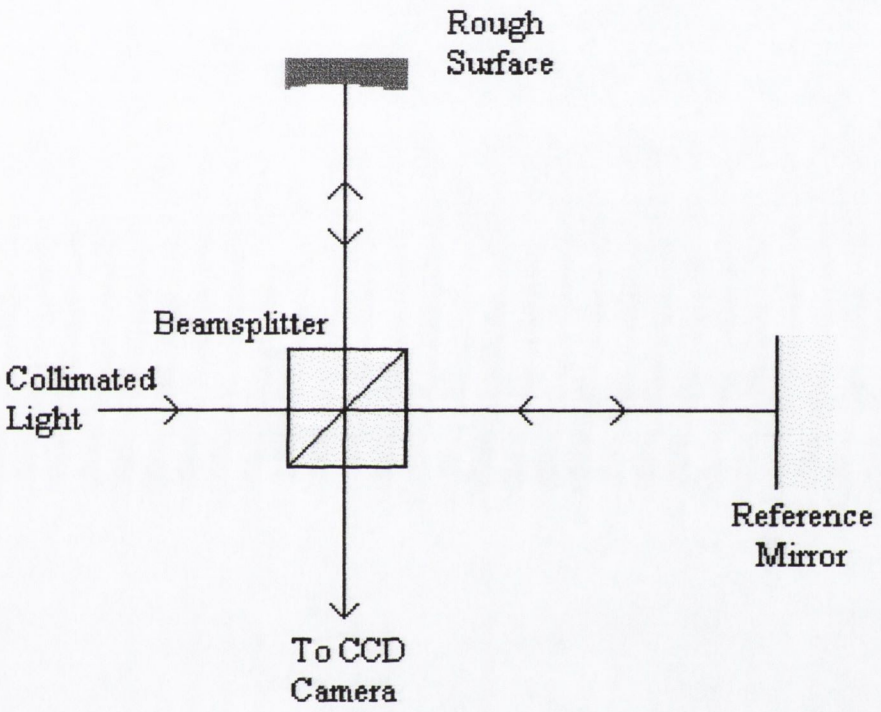

Fig. 2.28 The Michelson Interferometer arrangement used in ESPI contouring.

$$I_{T1} = I_o + I_r + 2\sqrt{I_0 I_1}\cos\phi \qquad \text{Equation 2.76}$$

where I_o and I_r are the intensities of the object and the reference beams respectively and ϕ is the phase difference between the object and reference beams associated with the different optical paths travelled. If the wavelength of the light is changed, a phase change $\Delta\phi$, will result and the intensity is now given by

$$I_{T2} = I_o + I_r + 2\sqrt{I_o I_r}\cos(\phi + \Delta\phi)$$ Equation 2.77

Using the correlation coefficient, $\rho(\Delta\phi)$, of two random variables to correlate between I_{T1} and I_{T2}, it was shown in Section 2.2.1 that,

$$\rho(\Delta\phi) = \frac{1}{2}(1 + \cos\Delta\phi)$$ Equation 2.78

Thus the correlation is unity when $\Delta\phi = 2n\pi$, where n is an integer, and zero when $\Delta\phi = (2n + 1)\pi$. Thus correlation between the two images produces a fringe pattern defining contours of equal phase change. It was also be shown that if the images are subtracted and the result rectified, the resultant intensity I_T, is

$$I = 4\left[I_o I_r \sin^2\left(\phi + \frac{1}{2}\Delta\phi\right)\sin^2\frac{1}{2}\Delta\phi \right]^{1/2}$$ Equation 2.79

Again, when $\Delta\phi = 2n\pi$, I_{t1} and I_{t2} have maximum correlation and so the resultant intensity is zero. Minimum correlation occurs when $\Delta\phi = (2n + 1)\pi$ and the resultant intensity will be a maximum.

Therefore, if the shape of the object surface is identical to the shape of the reference surface, the intensity of the subtracted image is constant across the image because the phase change, caused by the wavelength change, is constant across the image. Figure 2.29 shows a flat illuminating wave, R, and a sloping object surface, O. The object is illuminated by collimated light. The light that has been scattered from a point P has travelled a distance 2d further than the light that would be reflected from an equivalent point on the reference surface.

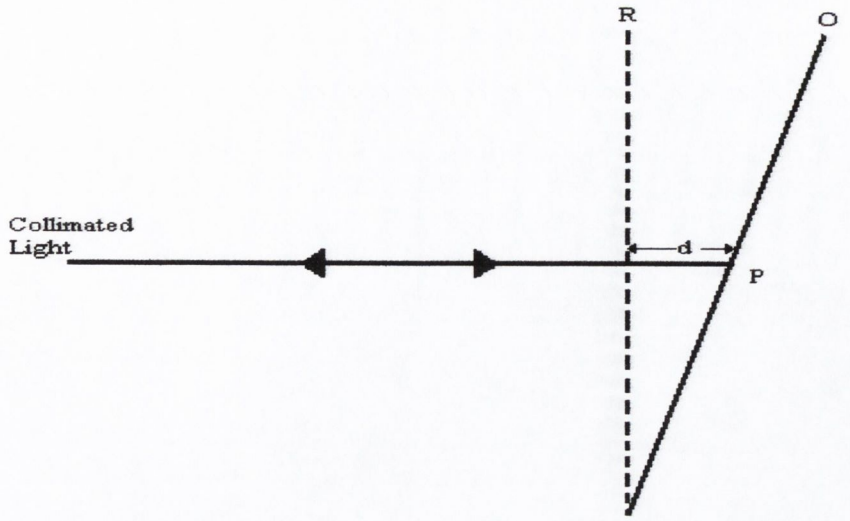

Fig. 2.29 A flat illuminating wavefront, R, is used to measure a sloping surface at O.

The phase difference, $\Delta\phi$ between the two beams caused by the distance d is given by

$$\Delta\phi = 2d\left(\frac{2\pi}{\lambda}\right) \qquad \text{Equation 2.80}$$

Equation 2.77 now becomes

$$I_{T1} = I_o + I_r + 2\sqrt{I_o I_r}\cos(\phi_1 + 4\pi d/\lambda_1) \qquad \text{Equation 2.81}$$

and at λ_2, equation 2.77 becomes

$$I_{T2} = I_o + I_r + 2\sqrt{I_o I_r}\cos(\phi_2 + 4\pi d/\lambda_2) \qquad \text{Equation 2.82}$$

Correlating these two intensity patterns, by subtraction and rectifying produces an intensity pattern given by [70]

$$I_S = \sin^2\left[1/2(\phi_1 - \phi_2) + 2\pi(1/\lambda_2 - 1/\lambda_1)d\right] \qquad \text{Equation 2.83}$$

Thus correlation fringes are obtained when the object surface differs from a flat shape and the fringes occur at intervals, Δz, given by [8]

$$\Delta z = \frac{1}{2(1/\lambda_2 - 1/\lambda_1)} \qquad \text{Equation 2.84}$$

which may be written as

$$\Delta z = \frac{\lambda_1 \lambda_2}{2(\lambda_1 - \lambda_2)} \qquad \text{Equation 2.85}$$

For a range of sensitivities it is necessary to have a selection of wavelengths. To use the optical configuration, shown in Figure 2.28, it is necessary to have a tunable wavelength source. The source needs to have certain characteristics to be used for contouring. Speckle decorrelation occurs if the angle at which the light is incident on the surface changes when the wavelength is changed. Initially an image of the speckle pattern is grabbed when the surface is illuminated with λ_1. As with all ESPI techniques, the intensity change in the speckle pattern is measured and so the speckle pattern must not move. Therefore, when the wavelength is changed to λ_2, the light must be incident on the surface at the exact same angle as it was for λ_1, otherwise the speckles would be displaced. Also, to achieve optimum contrast, the intensity of the light at the two wavelengths must be the same, so upon subtraction, all the background light will be eliminated. Thus an ideal source would be tunable over a large range, for example 100 nm, and the intensity of the light and the angle of illumination should remain constant over that range.

Argon ion lasers have been used to measure the shape of surfaces in these systems [8]. Using the nine lines they offer a range of sensitivities, but the intensity of the light changes, as does the angle of illumination. They are also too big to be used in any portable systems. The use of an argon ion laser in an ESPI contouring system is discussed in Chapter 5. An alternative to using a tunable laser is to use two laser diodes.

The obvious drawback with this system is the limited sensitivity and the extra cost. It is the requirement of a tunable laser that has made the use of this technique so uncommon. ESPI contouring can also be performed using an in-plane system and rotating the angles of illumination. An image of the surface is taken in Figure 2.22, and after the angles of illumination changed by $\Delta\theta$ another image is taken. The first image is then subtracted from the second and the result rectified to produce fringes which represent height contours, Δz, on the surface given by [120]

$$\Delta z = \frac{\lambda}{2\sin\theta\sin\Delta\theta} \qquad \text{Equation 2.86}$$

This technique is commonly used in a variety of different set-ups. However they all involve rotation of at least one component and are therefore prone to mechanical instability. Chapter 5 of this thesis describes an ESPI contouring system which uses a tunable source.

2.3 Fringe Analysis

2.3.1 Fringe Detection

The initial result from any ESPI system is a fringe pattern, also called an interferogram. In many cases a quantitative analysis of these fringes is not necessary, for instance in defect or crack detection. However there are situations where quantitative data are needed, for example stress and strain analysis. The exact meaning of the fringes depends on which ESPI system produced them. Two consecutive fringes in a fringe pattern obtained from an out-of-plane system correspond to a displacement d, along the viewing direction, of $\lambda/(1+\cos\theta)$. The fringes can simply be counted and the total displacement calculated using this sensitivity value. However, it is not possible to obtain proper data from a single pattern, unless the fringe order number n, and the directions of the fringes are known. These can only be determined by observing the fringe pattern develop. Figure 2.30 shows a fringe pattern obtained from an out-of-plane ESPI system.

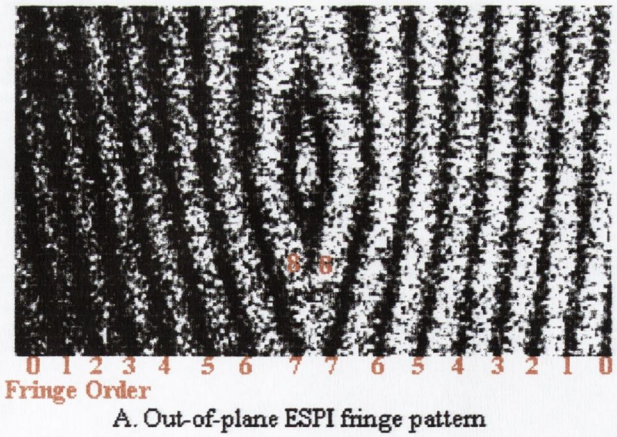

A. Out-of-plane ESPI fringe pattern

Fig. 2.30 An ESPI fringe pattern with the fringe order number marked in red.

The fringe order is marked on the fringes so the total displacement can be calculated by simply multiplying the fringe number by the sensitivity value, d =

$\lambda/(1+\cos\theta)$. In this example the left and right edges of the illuminated area moved very little while the centre moved approximately $8\lambda/(1+\cos\theta)$. This displacement occurred along the z axis but without better analysis there is no way of knowing in which direction. This displacement can then be used to calculate stress and strain values if the dimensions of the surface area are known. It is important to note that the zero order fringe is the area where no movement took place and also there can be multiple fringes of the same order. When the visibility of the fringes starts to deteriorate due to decorrelation or the number of fringes being too great, the fringe pattern can be saved and a new reference can be taken.

This method of analysing the fringes is inaccurate and can only provide information for points located along fringes. Any method of fringe analysis using the intensity of the pattern can not provide a resolution of better than about $2\pi/10$ [8,121]. An automatic fringe analysis is needed if accurate results are to be obtained. This caused many problems in early ESPI systems and a considerable amount of work was done on improving analysis techniques. The introduction of CCD cameras and frame-grabbers to digitize the images helped researchers develop advanced fringe analysis algorithms.

The major difficulty in automatic analysis is in actually identifying the fringes because of the noise inherent in an ESPI fringe pattern. Many different filtering techniques have been introduced and tested with these patterns, but the most commonly used are median filters. Fringe tracking algorithms were introduced to locate the fringe and record the order in which they appeared. This method fails when the fringe pattern is complex or there are holes on the surface. An automatic fringe analysis technique, called phase-shifting [122], that was used previously in conventional interferometry on optically smooth surfaces, was applied to ESPI. This technique is now the most commonly used fringe analysis technique used in EPSI systems, and most commercial systems are supplied with phase-shifting software.

2.3.2 Phase-Shifting

Fringes have a sinusoidal intensity profile, where a full cycle, a dark and a bright fringe, corresponds to a phase change of 2π. The point by point analysis of the phase will lead to the determination of the real displacement of every point on the inspected surface. Phase-shifting is based on the introduction of a temporal phase shift, between the object and reference beams in the interferometer and the resulting effect is a movement of intensity peaks across the pattern. This phase shift is introduced either as calibrated phase steps or as continuous periodic phase modulation. The phase change may be implemented as a displacement of a mirror, a tilt of a glass plate, elongation of an optical fibre, electro-optical modulation, or a refractive index change [121]. Phase shifting techniques are widely used for the retrieval of the phase map of an interferogram and have become integrated into all modern ESPI systems. The main reasons for their success are the high precision of the measurements and the simple experimental arrangement. The result from the phase-shifting algorithm is another fringe pattern with considerably less noise than the original fringe pattern. The fringes are no longer sinusoidal in nature but resemble ramp waves. The value at any point is the phase change caused by the surface displacement.

There are a wide variety of algorithms used to calculate the phase, all of them sharing the ability to eliminate the background terms by simple arithmetic or trigonometric operations on the acquired images. The phase shifts, however, have to be introduced when the speckles are perfectly still, so phase shifting techniques only work when the phase-shifts can be introduced without any mechanical or thermal instability. The most common phase-shifting technique is one in which the phase in one arm of the interferometer is stepped in N equal and controlled steps so that the total phase shift is 2π.

From Equation 2.53, the reference frame is given by,

$$I_A = I_1 + I_2 + 2\sqrt{I_1 I_2}\cos\phi \qquad \text{Equation 2.87}$$

and from equation 2.55 the frame grabbed after there has been an unknown phase shift, $\Delta\phi$, is given by,

$$I_B = I_1 + I_2 + 2\sqrt{I_1 I_2}\cos(\phi + \Delta\phi) \qquad \text{Equation 2.88}$$

Figure 2.31 shows the mathematical simulation of these equations. Line profiles through the speckle patterns show the high frequency speckle "noise". The fringe pattern produced when these patterns are subtracted and rectified is also shown in Figure 2.31C. The line profile through this pattern shows the noise on the fringes, which makes automatic analysis difficult. The points on the profile with zero intensity are the areas of $2n\pi$ phase shift. Applying the phase shifting algorithm will eliminate the noise and produce fringes, which represent the phase change at each point.

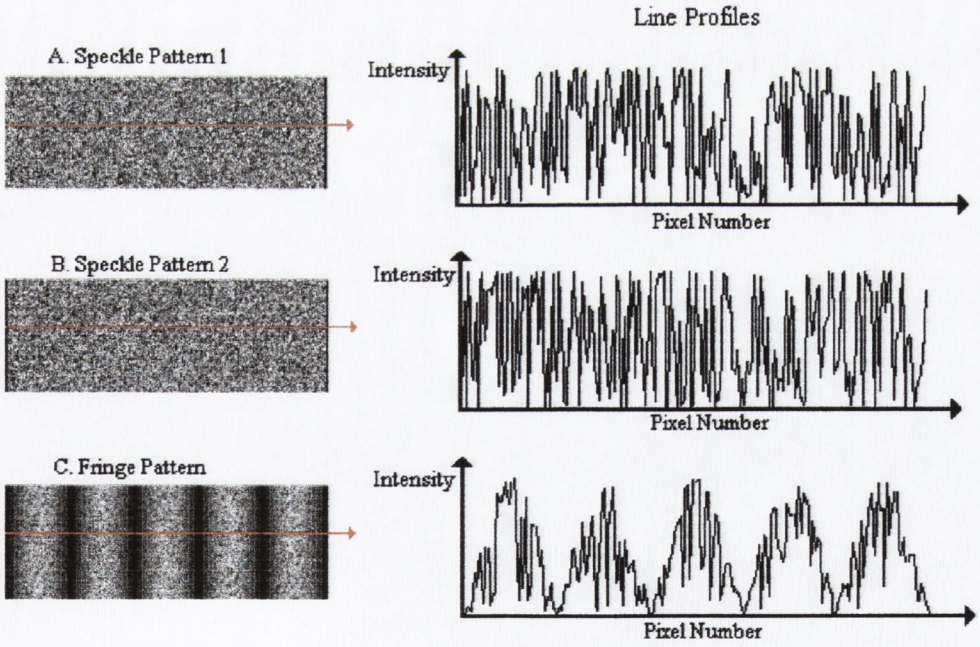

Fig. 2.31 Line profiles through the two speckle patterns and the resulting fringe pattern.

In the simplest method a reference frame is grabbed and then the phase of one beam is stepped N times and at each step, an image is grabbed. By combining the

resulting N+1 images it is possible to solve for ϕ, the phase at each pixel. If N=3, four frames are grabbed $\pi/2$ apart and ϕ can be calculated for every pixel. From Equation 2.87, phase shifts $\pi/2$, π, and $3\pi/2$ produce the following four equations,

$$I_{T1} = I_1 + I_2 + 2\sqrt{I_1 I_2}\cos(\phi)$$

$$I_{T2} = I_1 + I_2 + 2\sqrt{I_1 I_2}\cos(\phi + \pi/2)$$

$$I_{T3} = I_1 + I_2 + 2\sqrt{I_1 I_2}\cos(\phi + \pi)$$

$$I_{T4} = I_1 + I_2 + 2\sqrt{I_1 I_2}\cos(\phi + 3\pi/2)$$

Using the following algorithm,

$$\frac{I_{T4} - I_{T2}}{I_{T1} - I_{T3}}$$ Equation 2.89

results in

$$\frac{I_{T4} - I_{T2}}{I_{T1} - I_{T3}} = \frac{\sin(\phi)}{\cos(\phi)} = \tan\phi$$ Equation 2.90

which leads to,

$$\phi_{(x,y)} = \tan^{-1}\frac{I_{T4(x,y)} - I_{T2(x,y)}}{I_{T1(x,y)} - I_{T3(x,y)}}$$ Equation 2.91

This produces an image in which the intensity value (0-255) at each pixel represents the phase at that pixel in the reference image. However, since the inverse tan function gives values between $-\pi/2$ and $+\pi/2$, the phase cannot be directly evaluated over a 2π interval. This inconsistency can be removed by taking

into account the signs of $(I_{T4(x,y)} - I_{T2(x,y)})$ and $(I_{T1(x,y)} - I_{T3(x,y)})$ which correspond to $\sin[\Delta\phi_{(x,y)}]$ and $\cos[\Delta\phi_{(x,y)}]$, respectively.

The object is then displaced and a new image, described by Equation 2.88, is grabbed. Again, the phase of one beam is stepped N times and at each step, an image is grabbed. By combining the resulting N+1 images and using the same algorithm (Equation 2.89) it is possible to solve for $\phi + \Delta\phi$, where $\Delta\phi$ is the phase change, at each pixel, caused by the surface displacement. The result is another image in which the intensity value (0-255) at each pixel represents the phase (0-2π) at that pixel in the image taken after displacement. The two phase images are then subtracted from one another to produce a resultant image containing the phase information $\Delta\phi$. This image is a fringe pattern where the intensity value (0-255) at each pixel represents the phase change at that pixel caused by the surface displacement.

These fringes are then processed to remove the 2π discontinuities in a process called phase unwrapping. Returning to the mathematical simulation, Figure 2.32 shows the line profiles of the initial ESPI fringes, the wrapped phase fringes and the unwrapped phase map. It is clearly shown in the wrapped phase fringes that the noise has been removed from the initial ESPI fringes. Phase unwrapping is discussed in the next section.

Research into the quality of ESPI fringes demonstrated that remarkable improvements can be achieved by filtering and enhancing the contrast of the speckle interferograms before applying any phase extraction algorithm. It was shown that spatial pre-filtering of ESPI images can increase the resolution up to $2\pi/100$, a value which is typical in conventional interferometry [121]. Therefore using the phase-shifting technique the phase of a point can be evaluated with a typical precision of $2\pi/100$ radians, which is equivalent to one hundredth of the fringe period.

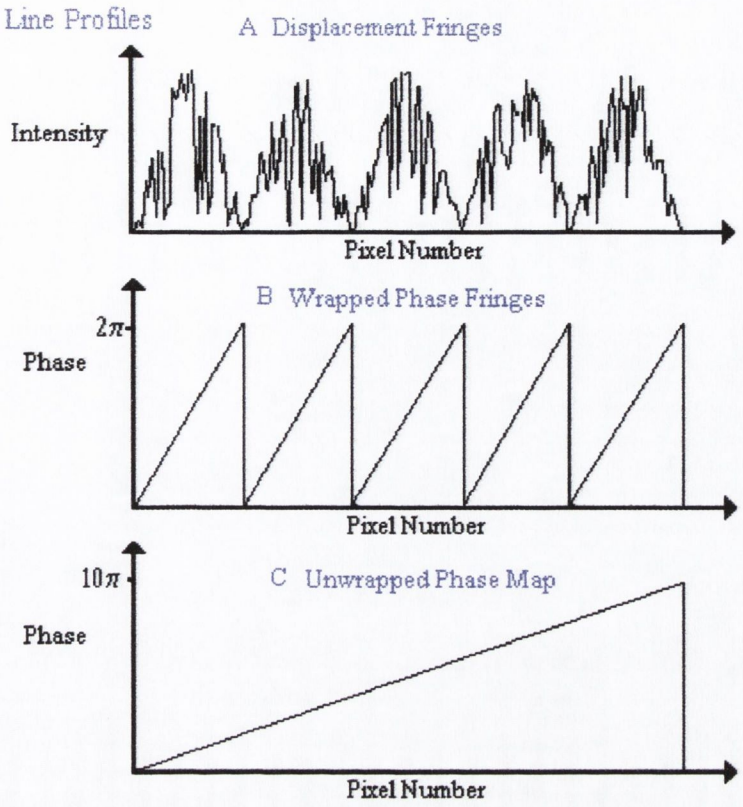

Fig. 3.32 A, comparison of the line profiles though; A, the displacement fringes; B, The wrapped phase fringe and; C, The unwrapped phase map.

The measurement accuracy will be strongly affected by the speckle noise. The technique will also depend on the phase-shifting algorithm used and on the accuracy of each phase-step. The algorithm described is called the "four-bucket" technique because it takes four phase images. There are also two, three and five bucket techniques in use. However, the more images taken, the higher the allowable error in the phase shift. An alternative method called the Carré [123] technique takes four equally spaced phase images, but it is independent of the phase step taken. Therefore once the movement of the phase-shifting device is repeatable this technique is relatively error-free. Errors do occur in phase-shifting because of non-linearities, system errors, and thermal fluctuations and mechanical vibrations. The system errors include the shape of the object and reference wavefronts. It is assumed that a the phase-shift is the same for every point on the surface but this is not true if the angle between the illuminating and reference beams is not constant over the whole surface. When diverging beams are used this

error can be compensated for in the algorithm. The other errors are reduced if the data is taken quickly in a stable environment.

A phase-shifter is a device capable of changing the path length in one arm of the interferometer and so introducing a phase change between the beams. The most commonly used device is a mirror attached to a piezo-electric transducer (PZT) placed in the reference beam. A high-voltage ramp signal is used to move the PZT linearly over a 1 μm range. It is important to note that not all PZTs have a linear response and this should not be assumed in the phase-shifting algorithm without first calibrating the PZT. It there are any non-linearities in the response they can be accounted for using different controlling waveforms. It is advantageous for any ESPI system not to have any moving parts that can be a source of mechanical instability. In a typical dual ESPI systems there are four shutters and two mirrors mounted on PZTs. Besides the extra cost of these devices and the high voltages required, they can all be sources of instability. For this reason the dual in-plane ESPI system described in Chapter 4 has no moving parts and only requires relatively small voltages of approximately 10 V.

Another method of obtaining the wrapped phase map is the Fourier transform technique [124,125]. This method is not used in any of the systems described in this thesis as the use of the Fourier transform fringe analysis method has many disadvantages. The efficiency of the technique depends heavily on the quality of the fringes. The noisy ESPI fringe patterns cause considerable errors in the output of these algorithms. Also the amount of time required for processing and filtering is considerable. At the expense of image pre-processing, filtering and image enhancements, most of these problems can be solved. Now, with faster computer processors and more efficient algorithms these processing times are getting much shorter, and therefore computer time is no longer a disadvantage. However, difficulties can arise with this method near edges and in the presence of fringe pattern discontinuities. This technique is commonly applied to holographic interferometry and fringe projection techniques where the fringe quality is far better.

2.3.3 Phase Unwrapping

The result from the phase shifting algorithm is another fringe pattern called the wrapped phase pattern, with each pixel in this image has a value between 0 and 2π. A procedure called "phase-unwrapping" must be carried out to restore the unknown multiple of 2π to each pixel [126].

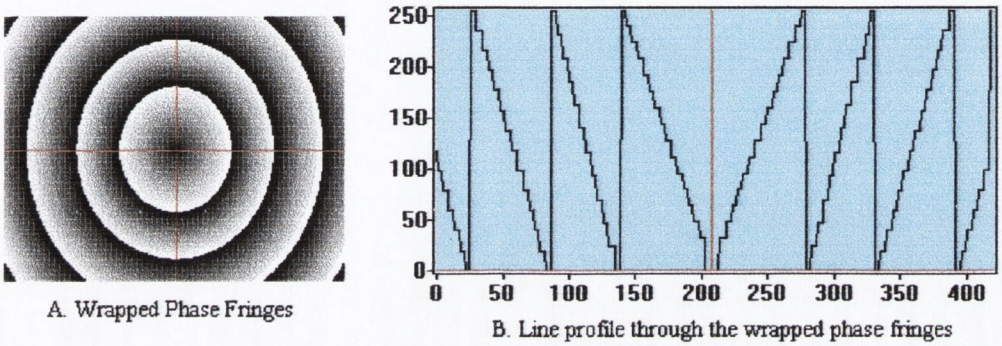

A. Wrapped Phase Fringes

B. Line profile through the wrapped phase fringes

Fig 2.33 A The result of the phase-shifting algorithm is the wrapped phase fringes B A line profile through the fringes shows the 2π discontinuities.

Figure 2.33 shows the fringes now have a sawtooth wave profile but they have retained the fringe order number. The direction of the sawtooth wave provides the information for the direction of the displacement or the slope of the surface. Each phase fringe now corresponds to a phase change when the surface was displaced of $2n\pi$. To remove the 2π discontinuities in the fringe pattern the phase-unwrapping algorithm is used. In principle this procedure can be achieved by comparing the phase difference between adjacent pixels. When the phase difference is greater than π (thresholding), 2π is either added or subtracted from the remaining pixels in the row and the process is then repeated along the columns. Applying this algorithm to the fringe pattern in Figure 2.33A produces the unwrapped phase map in Figure 2.34A. The line profile in Figure 2.34B shows the discontinuities have been removed.

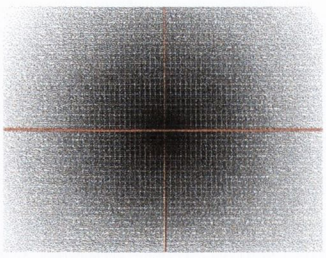

A. Unwrapped Phase Map

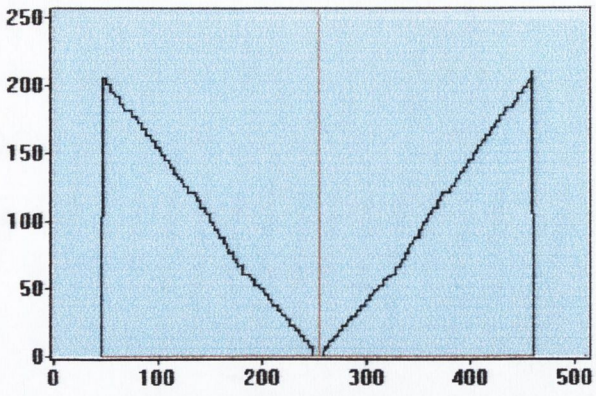

B. Line profile through unwrapped phase map

Fig. 2.34 A Using the unwrapping techniques the 2 π discontinuities can be removed to produce the unwrapped phase map. B .Line profile through the centre of the unwrapped phase map.

Phase unwrapping would be simple if not for the presence of noise and fringe discontinuities. These make the process complex and prone to large errors that are sometimes difficult to avoid. In recent years the development of new unwrapping algorithms has been a key area of research [127]. The inefficiency of the simpler algorithms often provides unreliable results. However the simpler algorithms are computationally efficient requiring relatively little time to unwrap the phase images. The main problem arises from the speckle and electronic noise inherent in the phase images. The algorithm not only has to allow for this high frequency noise but must also be able to cope with phase discontinuities caused by holes or boundaries. Displaced fringes and dislocations seen in complex fringe patterns caused by cracks and abrupt changes in the surface structure can also cause discontinuities. Even though there are many problems associated with phase unwrapping and it is a complex procedure, there are many different algorithms to choose from [127-130]. They vary in their complexity, efficiency and computational time. It is assumed the greater an algorithm's efficiency, the greater its complexity. However, Huntley has developed algorithms that have noise immunity and are not complex [131]. These algorithms are based on the requirement that the unwrapped map should be independent of the direction in which the unwrapping takes place.

Phase unwrapping algorithms also determine the direction and order of the fringes by the direction of the ramp profile of the fringes. The result is an absolute phase map of the phase change that occurred over the whole surface. As the absolute phase change is now known at every point on the surface the geometrical sensitivity term can be used to obtain the actual displacement or contour map. For example, in the out-of-plane system shown in Figure 2.19 the displacement is given by $d = \lambda\Delta\phi / (2\pi(1 + \cos\theta)$. Figure 2.35 shows a typical displacement map calculated from the phase map in Figure 2.34A.

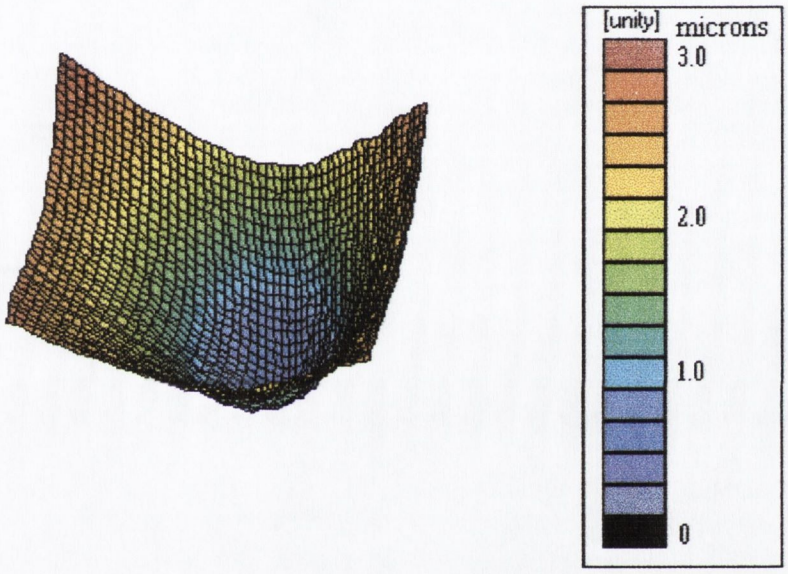

Fig. 2.35 The sensitivity term can be used to produce this displacement map.

In summary, ESPI correlation produces a fringe pattern describing the displacement that occurred or the shape of the surface. The exact meaning of the fringes depends on the optical configuration used. The fringes can be analysed by a fringe detection and counting method. But this is highly inaccurate and a method of determining the phase change at each point on the surface is needed to obtain more accurate results. Two methods of phase determination are possible: Fourier and phase-shifting. Both of these produce wrapped phase maps, or phase fringe patterns describing the phase change, modulus 2π at each point. To remove the 2π discontinuities a phase-unwrapping algorithm is used which determines the direction and order of the fringes by the direction of the ramp profile of the fringes.

Usually at least one mean filter is required to reduce the speckle noise before the unwrapping algorithm can be used. The result from the unwrapping algorithm is an absolute phase map of the phase change that occurred over the whole surface. The displacement map or contour map can be obtained from the unwrapped phase map by simply using the sensitivity equation for the different systems.

The ESPI systems described in this thesis use the four-bucket phase-shifting algorithm described previously and a phase-unwrapping algorithm developed by Ghiglia and Romero [128]. This unwrapping algorithm uses a fast cosine transform and a weighted least square function to allow for phase inconsistencies.

Chapter 3 White Light Interferometer

3.1 Introduction

In this chapter the optical configuration of the white light profiler is described along with the data acquisition and analysis algorithms. The optical configuration is based on existing commercial scanning white light interferometric surface profilers. However, the profiler described here is a full-field technique and therefore profiles without the need for scanning apertures. This allows for a simpler optical set-up and a faster acquisition time. The profiler uses the coherence properties of a white light source, as described in Chapter 2, to build a three-dimensional image of the surface. Three different algorithms were used to analyse the data. Two of these were developed during the course of this research while the other one is used so that these two could be compared to an existing technique used in commercial systems. These algorithms are simple and very efficient, providing good resolution and fast acquisition and analysis, without the use of Fourier transforms or phase-shifting operations. Descriptions of the post-processing filters used to eliminate pixels that do not contain any useful information are also provided.

Problems associated with, and properties of, both the optical set-up and the algorithms are discussed in the practical considerations section. In this section results from experiments carried out to quantify some of the problems inherent in optical profiling are presented. In the results section, surface profiles as measured by the white light interferometer are shown. The profiler was first tested on calibrated optically smooth surfaces. Surfaces of different shapes and roughness were also profiled and the results are presented here. Finally, a discussion of the overall performance of the profiler is given in the conclusions. In this section the profiler's properties and specifications are also compared to the existing commercial systems and the performance of the algorithms is compared with a more commonly used technique. Some of the work described in this chapter was carried out in the European Commission Joint Research Centre.

3.2 Development of White Light Profiler

3.2.1 Optical Configuration

The optical set-up of the white light interferometer, which was designed and built, is shown in Figure 3.1. It is essentially a Michelson interferometer with one of the mirrors replaced by the object whose surface is to be profiled and a 5 x 5 cm cube beamsplitter is used to split the wavefront. The specifications of all the main equipment used in this profiler are given in Appendix A. Initially to align the system the 10 mW helium-neon laser and a mirror in place of the object are used. The light from the laser enters the interferometer along the same optical axis the white light travels. A screen is placed in front of the imaging lens system and the two laser spots are aligned to overlap, by adjusting the tilt of the reference mirror. The monochromatic light is then expanded using a 10x objective lens and split into two spherical wavefronts by the beamsplitter. The two reflected spherical wavefronts are recombined to interfere, producing concentric circular fringes on the screen as described in Chapter 2. The reference mirror is then finely adjusted so as the centre of the fringe pattern is in the centre of the screen.

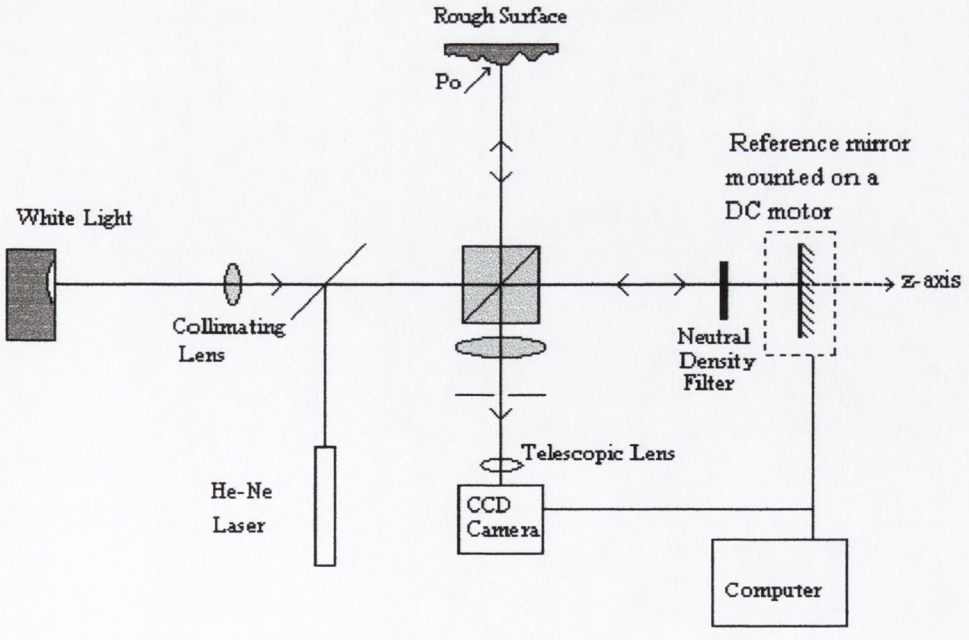

Fig. 3.1 The optical configuration of the white light surface profiler

From the discussion in Chapter 2 it is known that as the optical path difference between the two wavefronts is increased the fringe order will increase and so the fringes will appear to come out from the centre. Similarly, if the path difference is decreased the fringes seem to move into the centre of the pattern. The reference mirror is mounted on a DC motor allowing it to be moved along the z-axis. By observing the direction of the fringe movement, as the reference mirror is moved, the location where the optical path difference is approximately zero is found. Before replacing the other mirror with the object and starting a scan, the helium-neon laser is once again used to ensure that the reference mirror is aligned at every point along the z-axis. The reference mirror is moved through the whole 2.5 cm range of the DC motor and the fringe pattern is used to guarantee that it moves parallel to the z-axis. If it does move parallel to this axis the centre of the fringe pattern should remain in the centre of the screen. The reference mirror is then returned to the point of approximately zero optical path difference.

The helium-neon laser is then switched off and the white light source, an Oriel 75W xenon arc lamp, with a coherence length of approximately 2 μm, is used to obtain white light fringes. If the mirrors are aligned and the wavefronts are perfectly collimated one single fringe should be seen to cover the whole image and every pixel in the image will have the same intensity. As the reference mirror is translated along the z-axis the intensity in every pixel should modulate in the exact same way. The pixel modulation is shown in Figure 3.2.

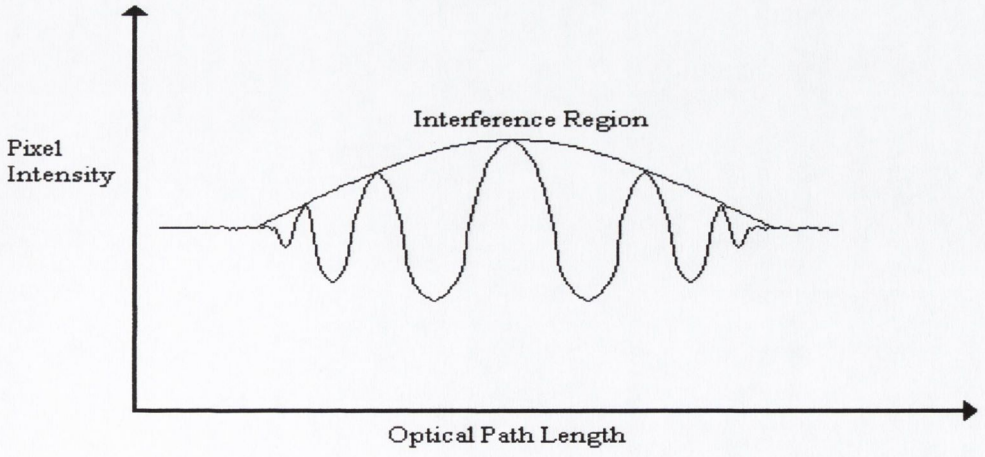

Fig 3.2 Pixel modulation as the reference mirror is moved along the z-axis

The position of the reference mirror along the z-axis is now finely adjusted so that the brightest fringe covers the whole field of view. This is the location of zero optical path difference. The object is then placed in the system and its surface is imaged onto a CCD camera using a telecentric lens system. An aperture, placed at the Fourier plane of the objective lens, is used to vary the intensity and speckle size in the image plane. The aperture also filters out the light that is not reflected straight back along the z-axis. The image is then sent to the frame grabber on board the computer where it is digitised. To achieve maximum contrast a neutral density filter is placed in the path to the reference mirror, so that the reflected intensities are approximately equal.

Before the surface is scanned, the reference mirror is moved a distance away from the beamsplitter such that the optical path length from the beamsplitter to the mirror is greater than the optical path length from the beamsplitter to the furthest away point on the surface. As mentioned in the previous chapter, the profiler utilises the fact that the visibility of the interference pattern decreases rapidly from its maximum at zero optical path difference, to zero at optical path differences greater than the coherence length of the white light source. The interference region occurs in a pixel when the corresponding point on the surface is at a position such that the optical path difference between the reference mirror and that position is less than this coherence length. The reference mirror is brought closer to the beamsplitter and the first point on the surface in which interference will occur will be the position with the lowest surface height. At this position of the mirror, the optical path length from the beamsplitter to the mirror is equal to the optical path length from the beamsplitter to this point on the surface.

During profiling, the reference mirror is moved along the z-axis in steps, controlled by the computer, and frames are grabbed continuously. These frames are quickly analysed by the computer so that at the end of the scan, the interference region has been located for each pixel in terms of the frame number in which it occurred. For instance the interference region could have occurred for the lowest point on the surface in frame 10 and in frame 50 for the highest point. If the reference mirror was moved in 1μm steps, the height difference between these two points is 40 μm.

The accuracy with which the profiler can locate the interference region depends on the coherence length and the reference mirror step. When profiling smooth surfaces the profiler can locate the point of maximum modulation within the interference region and thus increase the resolution. The profiler uses two separate algorithms and corresponding computer programs were written in C++. These algorithms are described in the next section.

The lateral resolution of the profiler depends on the size of the surface to be profiled. The illuminated region of interest is imaged onto a CCD array of 512 x 512 pixels, with each pixel having dimensions of approximately 10 x 10 μm. The maximum surface area is limited by the size of the optics and the collimated wavefront, which has a diameter of 5 cm in this profiler. An area of 2.5 x 2.5 cm imaged onto the array will provide a lateral resolution of approximately 50 μm.

3.2.2 Data Acquisition and Analysis

The first of the two algorithms locates the area of maximum modulation, within the coherence region, for each pixel in the frame. Five buffers, numbered 1 to 5, are used as memory locations for data acquisition. Frames are continuously grabbed as the reference mirror is moved through a predetermined distance. For example, if the scan length was 50 μm, a frame could be grabbed every quarter of a micrometer. Figure 3.3 shows the flow chart for this algorithm.

The buffers used are essentially indexed arrays containing 262,144 elements, where the elements are the intensity values of the 512 x 512 pixels. Initially, the first image grabbed is sent to buffer 1 and a copy of it is sent to buffer 2. The reference mirror is then moved a step forward and a new image is sent to buffer 3. This image is subtracted from the image in buffer 1 and the result is sent to a temporary buffer. Any negative values resulting from this subtraction are given a zero value. If the intensity of any pixel in the temporary buffer is greater than zero it means that the intensity of the corresponding pixel on the first image (buffer 1) is greater than in the second image (buffer 3). The locations of all the pixels whose

intensities are greater than zero are used to replace the intensity values of buffer 1 with the intensity values from buffer 3. In this way buffer 1 now contains the minimum intensity values to occur for each pixel in the frame. The frame number in which the minimum intensity occurs in each pixel is saved in the corresponding pixel in buffer 4.

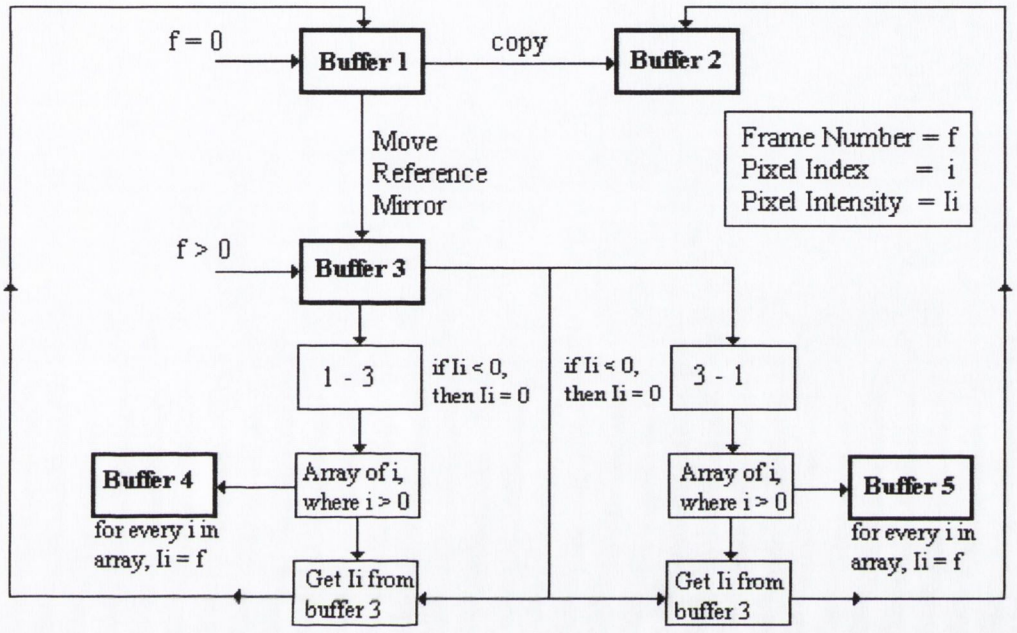

Fig. 3.3 Flow chart of the maximum modulation algorithm.

Similarly, in a separate process buffer 1 is subtracted from buffer 3 and the result from this is used to fill buffer 2 with the maximum intensity values that have occurred. The frame number in which the maximum intensity occurs is recorded in buffer 5. For the rest of the scan the image that is grabbed at each position of the stepper motor is sent to buffer 3. At each step this is compared to buffer 1, by subtraction, so that if any pixel has an intensity value less than the minimum intensity value that has occurred in that pixel in the scan so far, this value replaces the existing minimum value recorded in buffer 1. In the same way, it is compared to buffer 2 so that if any pixel has an intensity value greater than the maximum intensity value that has occurred in that pixel in the scan so far, this value replaces the existing maximum value recorded in buffer 2. Buffers 4 and 5 are used to record the frame numbers in which the minimum and maximum intensities occurred respectively. In this way, at the end of the scan, for each pixel, the lowest

and highest intensities and the frame numbers, at which these intensities occurred, are stored in four memory locations, buffers 1, 2, 4 and 5 respectively.

As the distance travelled by the reference mirror between each frame is precisely controlled, the relative positions of the intensities within the scan are known. The frame numbers in which the minimum intensities occurred can be multiplied by the distance the reference mirror was moving between each step to convert it into relative surface height data. Similarly the frame numbers recorded in buffer 5 can be converted into height data. These frames are then compared with one another to ensure that, for every pixel, the locations of the maximum intensity and the minimum intensity are a distance $\lambda/4$ apart, where λ is the mean wavelength of the source. A movement of $\lambda/4$ corresponds to a change in the optical path length of $\lambda/2$. Any pixel for which the distance is greater than this value is deleted and a neighbouring pixel averaging technique is used to fill in these pixels when the surface is imaged. A simple three-dimensional curve fitting technique is used on the positions of maximum intensity to build an image of the surface.

If the surface is rough, scattering can cause large intensity variations to occur outside the coherence region. When viewing an optically rough surface, at zero optical path difference, the image is similar to a speckle pattern seen in electronic speckle pattern interferometry (ESPI). An alternative algorithm is used on these surfaces which detects continuous modulation, that is, it detects the coherence region for every pixel in the scan. Again, it does this by continuously grabbing and analysing frames.

Figure 3.4 shows the flow chart of this algorithm. At the beginning of the scan an image is grabbed and sent to buffer 1. The reference mirror is then moved two equal steps and at each step a frame is grabbed and sent to buffers 2 and 3, respectively such that frame 1 and 3 are $\lambda/4$ apart. Buffer 1 is then subtracted from buffer 3 and the absolute value of the result is placed in buffer 5. Buffer 5 is then scanned for values greater than a set threshold level. The user inputs this level before the scan and it usually depends on the contrast of the interference pattern. If any pixel has a value greater than this value, it means that modulation has occurred

between the two frames λ/4 apart. This corresponds to a change in optical path difference of λ/2 which is the distance between a peak and a trough in the interference pattern. If modulation did occur in any pixel, it is recorded in this pixel by adding a intensity value of 1 to the same pixel in frame 6. Initially, all pixels in this frame have an intensity value of zero. Before the reference mirror is again stepped a distance of approximately λ/8, the image in buffer 2 is copied into buffer 1 and the image in buffer 3 is copied into buffer 2. After the mirror is moved a new frame is grabbed and sent to buffer 3. In this way buffers 1, 2, and 3 always contain the last three recorded images.

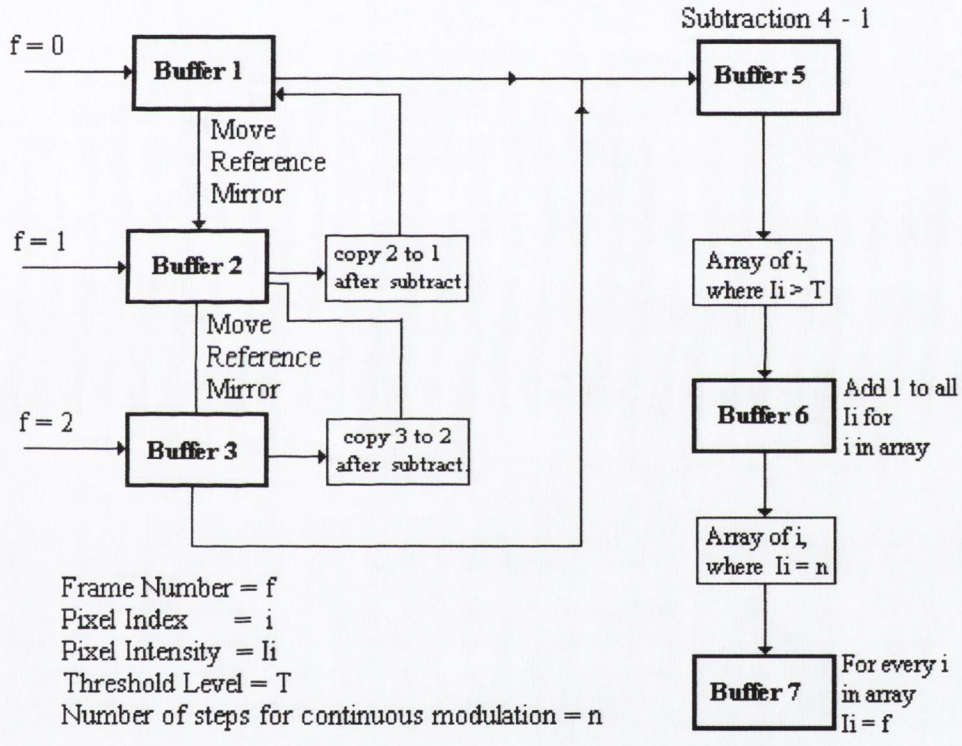

Fig 3.4 Flow chart of continuous modulation algorithm.

A frame is grabbed at each step of the reference mirror for the rest of the scan. As each frame is grabbed, it is compared to the frame that occurred a distance λ/4 before, and if modulation, greater than the set threshold level, has occurred in any pixel an intensity value of 1 is added to the same pixel in buffer 6. Buffer 6 is scanned at each step for any pixel with a value of n, set by the user and dependent on the coherence length and the step size. For any pixel with this value, the frame number in which it was detected is recorded in the same pixel in buffer 7. In this

way, if modulation is recorded, between points $\lambda/4$ apart, for a preset number of consecutive frames (depending on the coherence length and the step size), then the frame number of this frame is sent to a memory location (buffer 7) for that pixel. So at the end of the scan buffer 7 contains the frame numbers in which the continuous modulation was detected for each pixel. It is assumed that this region of continuous modulation is the interference, or coherence, region. As the distance travelled, between consecutive frames is controlled by the computer, the relative position of these frames are known, and can be used to build a three dimensional image of the surface.

The obvious disadvantage of this method compared to the previous algorithm is the poorer resolution. The profiler is now locating the coherence region which has a length of twice the coherence length of the source, l_c. The exact location of the frame within this scan is not known and it depends on the step size, the threshold level and the shape of the interference region. This is discussed in detail in the next section.

When using the first algorithm it is important that the distance the reference mirror moves between each frame is small enough so that both the highest and lowest intensities are recorded. These intensities are a distance $\lambda/2$ apart which corresponds to a movement of the mirror of $\lambda/4$, so this is the maximum step size. However using this step size can result in the loss of relevant data. If the distance between the frames is very small the data recorded gives an accurate description of the signal and so the results will be more accurate. In the second algorithm the step size must be such that at least n number of frames are grabbed within the coherence region. The value of n is set before each scan and will depend on the coherence length of the light source. The step size cannot be too small or else the modulation between consecutive frames will not be greater than the threshold value. Therefore, a step size of $n\lambda/8$ is used ($n = 1,2,3\ldots$), which means the frames that are compared to one another at each step are $n\lambda/4$ apart. These restrictions mean the acquisition time for the second algorithm is less than that for the first, as less frames are needed for a complete scan..

These algorithms work very quickly and use a minimum of memory as the frames are discarded immediately after they are analysed. When using the second program, if a high resolution is not required, the light source can be filtered or replaced by a more coherent source, thus increasing the coherence length and so reducing the number of frames needed for a complete scan, which in turn reduces the acquisition time. The algorithms can be used in conjunction with one another so that the second algorithm detects the interference signal, and once this is located, the first algorithm locates the point of maximum modulation within this signal.

To apply these algorithms computer programs were written in C++, see Appendix B. The programs control the DC motor, on which the reference mirror was mounted, as well as the frame grabber. To perform the subtractions and analysis of the images, look-up tables (LUTs) are used. The programs are very fast, despite the complexity of the algorithms, because there is no need for any multiplications or divisions. The computer can perform the subtractions and the LUTs in near real time.

3.2.3 Vertical Resolution and Errors

When profiling optically smooth surfaces the profiler uses the algorithm that locates the point of maximum modulation and builds an image of the surface using the points of maximum intensity. The optically smooth surfaces mean that the fringe profiles are accurately recorded for each pixel as shown in Figure 3.2. The algorithm locates the lowest and highest intensities, which correspond to the point of maximum modulation as shown in Figure 3.5. Assuming that the whole dynamic range of the CCD camera is used the maximum intensity has a gray level value of approximately 255 and the minimum intensity is near zero.

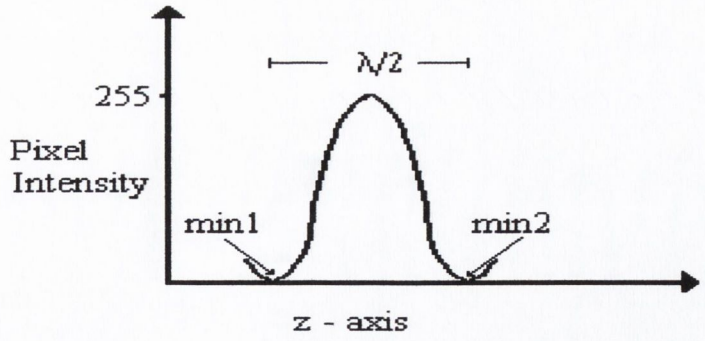

Fig 3.5 Maximum modulation within the interference region

After the scan is completed the profiler checks that the maximum and minimum are a distance λ/4 apart. It does not matter whether min1 or min2, in Figure 3.5, is detected as only the locations of maximum intensity are used to build the three-dimensional image of the surface. The minimum repeatable movement possible with the DC motor is 60 nm and this is used as the step size for this algorithm. Therefore the maximum error in the location of a maximum or minimum intensity is ± 30 nm. Unlike many optical interferometric surface profilers [57] the resolution is not dependent on the range. Assuming two points are spatially resolved, the profiler can distinguish between them so long as the height difference is greater than 60 nm. This profiler has been used successfully on smooth discontinuous surfaces of the type shown in Figure 3.6, where it can measure steps in a range of 60 nm to 2.5 cm with an error of ±30 nm. If the profiler is used to measure a 2 cm step the percentage error is only ±0.0002.

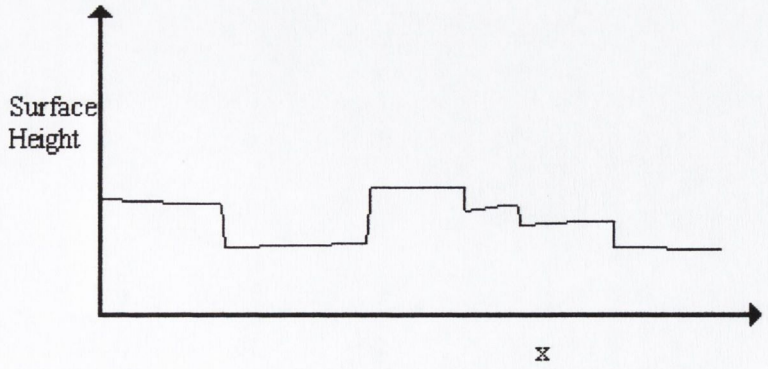

Fig 3.6 A cross-section of an optically smooth discontinuous surface

The use of this algorithm requires the surface to be smooth. When profiling optically rough surfaces the algorithm that detects continuous modulation is used. The profiler is now locating the coherence region which has a length of twice the coherence length of the source, l_c. The modulation threshold is set before each scan so that the algorithms can ignore all the background intensity modulations. Modulation must occur continuously for a certain number of frames before the coherence region is recorded. This number of frames is also set before the scan and is dependent on the coherence length. The step is set as $n\lambda/8$ so as there is one frame between the maximum and minimum intensity frames $n\lambda/4$ apart. The pixel intensity modulation is now uncertain and is different for each pixel. Setting a modulation threshold level high enough to eliminate background modulations can also alter the shape of the measured signal. The algorithm locates a point within the coherence region, which has a length $2l_c$. Therefore there is a maximum error in each location of $\pm l_c$, which corresponds to a movement of the reference mirror of $\pm l_c/2$. The profiler can reliably resolve between height differences of l_c. When the profiler is using this algorithm it has an error in the height readings of approximately ± 1 μm in the range of 2 μm to 2.5 cm.

3.3 Practical Considerations

3.3.1 Optical Configuration

3.3.1.1. Intensity of the light source

The lens system only images light reflected back along the z-axis onto the CCD array of the camera. The aperture at the Fourier plane of the objective lens filters out the rest of the light, allowing only the zero-order through. Therefore, the use of a light source with relatively low output power means the profiler is only suitable for profiling surfaces with a high degree of reflectively. There are problems when profiling curved or sloped surfaces as the amount of light reflected back along the z-axis will be extremely low. There was only one practical problem associated with the use of very high power sources and this was overcome. The reflections from

the internal faces of the cube beam-splitter alone were sufficient to saturate the CCD camera when using a 75-Watt white light source. This problem was overcome by tilting the arm of the interferometer, containing the light source, beam-splitter and reference mirror, relative to the other arm. When using such sources the neutral density filter is also tilted so that the reflections from its surfaces are not directed at the camera. The profiler can now be used on surfaces of relatively low reflectivity. Therefore the use of high power sources is advantageous.

3.3.1.2. Reflected Intensities

The neutral density filter is used to make the intensity of the light reflected from the reference mirror equal to the intensity of the light reflected from the object. This ensures the interference pattern has maximum contrast and the full dynamic range of the camera is used. However, problems arise when profiling curved surfaces because the illuminating beam is uniform and the light intensity reflected from the curved surface varies across the field. For instance, if one part of the surface is normal to the illuminating beam a significant amount of light will be reflected. However if the surface is curved at another point much less light will be reflected from this area along the z-axis. This non-uniform reflected wavefront is recombined with the uniform wavefront reflected from the reference mirror. Therefore the contrast of the interference will vary across the image and in some cases will be undetectable in parts. This means the profiler is not suited to highly curved continuous surfaces, as shown in Figure 3.7A. As the curvature increases at any point the reflected light intensity decreases, thus reducing the contrast. However, it can profile diffusely reflective surfaces which are sloped, as in Figure 3.7B, because the reflected light intensity is approximately the same for all points on the surface. If this amount of light is a small percentage of the illuminating light a suitable neutral density filter is placed in the path of the reference beam to equalize the reflected beam intensities.

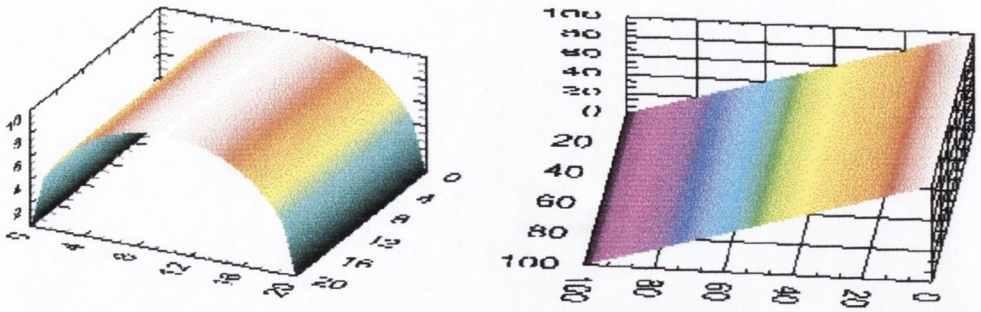

Fig 3.7 The curved surface shown in A causes problems for the profiler while it can easily handle the sloped surface in B.

The problem with profiling a highly curved surface is that if the intensity of the reference beam is reduced to equal the intensity reflected from a curved area of the surface, the light reflected from a flat area would be far greater than the reference wavefront. This means the contrast of the interference in the area of the flat surface will be reduced. Increasing the intensity of the source has the same effect, in that there is still non-uniform contrast in the image.

Figure 3.8 shoes how this variation in the contrast causes errors in the data analysis. It shows results from optically rough curved surfaces as profiled by the white light interferometer. As the illuminating wavefront is collimated, only parts of the surface which are approximately normal to the wavefront, reflect enough light, which upon interfering with the reference beam, produces detectable interference. In these surfaces this area is the top of the peak, with very little light reflected back along the same path from the sloped areas.

As the slope of the surface increases the amount of light reflected decreases and so too does the visibility of the interference pattern. Figure 3.8 shows the profiles of various surfaces as the slope of the surface decreases. These images have been filtered so that areas of the surface where the amount of non-modulating pixels is greater than 75% have been given an intensity value of zero. An averaging filter has been applied to areas where the amount is less than 25%. The percentage of pixels with intensity values of zero is displayed, in Figure 3.8, for each surface.

This shows the limitation of the profiler when applied to highly curved surfaces and why it is better suited to flat discontinuous surfaces.

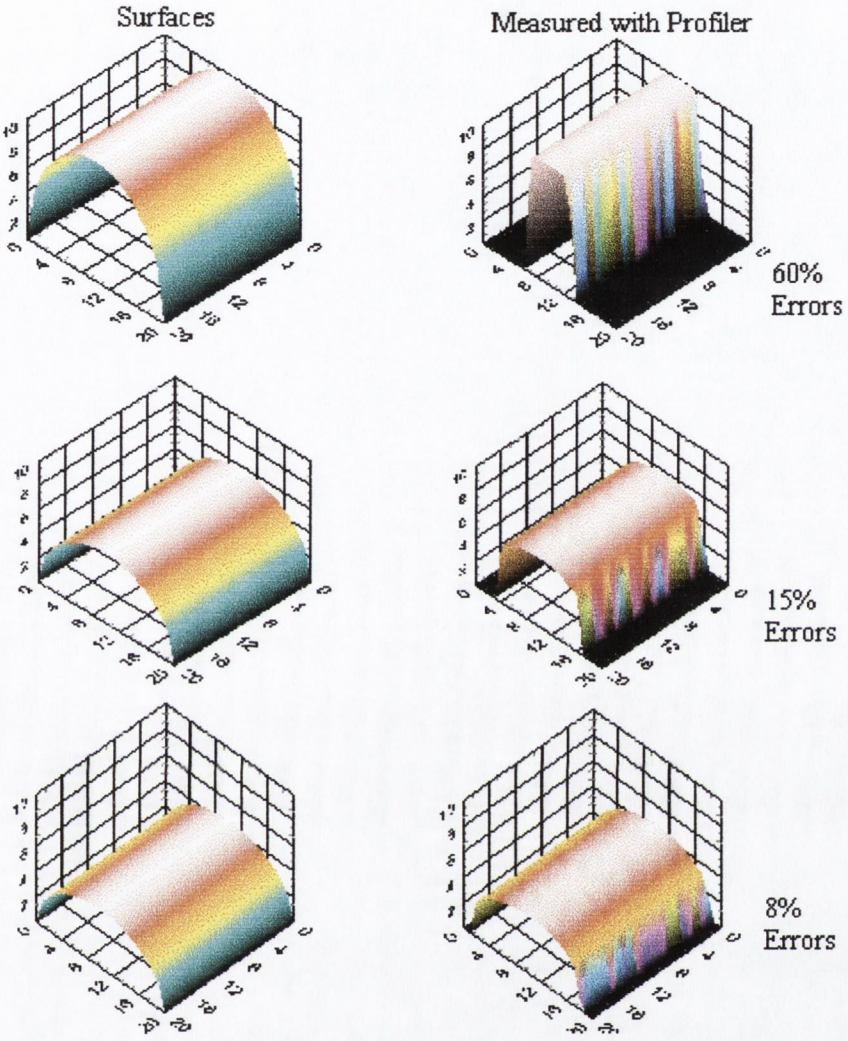

Fig 3.8 Three surfaces of different curvature; As the curvature decreases , the percentage of "bad" pixels decreases.

If a specularly reflective flat surface is placed in the profiler all of the incident light is reflected back towards the CCD camera. However if it is placed at a slope the light is reflected in a direction away from the camera. If a mirror is used as the surface and aligned perfectly normal to the z-axis, at zero optical path difference, one fringe will take up the whole field of view. As the surface is tilted more fringes appear in the image until all the white light fringes can be seen.

If the surface is now profiled it will indeed be profiled as a sloped surface because the point of maximum modulation will be recorded as it travels up the mirror. When the surface is tilted such that the fringes are no longer resolved in the image, the profiler can not measure the surface. In this system, it was found that if the difference in height between the highest and lowest edges of the 2.5 x 2.5 cm specularly reflective flat surface is greater than approximately 2 mm the fringes cannot be resolved and so the surface cannot be profiled. However this is not the case when profiling rough surfaces and provided there is sufficient light scattered back along the illumination direction, the surface may be profiled.

3.3.1.3. Collimation

The effect the temporal coherence length has on the sensitivity and resolution of the system has already been discussed. However, the spatial coherence and the shape of the wavefront play a significant role. It is assumed in the analysis of the results that all the beams in the illuminating wavefront have the same phase and degree of coherence as the corresponding beams in the reference arm. If this is not the case, there will be errors in the readings. These depend on the degree of collimation and the quality of optics. Therefore the use of a point source, such as an arc light source, and high quality collimating optics are required. However, if the shape of the wavefront or the degree with which it deviates from a flat wavefront is known, it can be compensated for in the results. The size of the illuminated area depends on the size of the collimated illuminating beam, which in turn depends on the size of the collimating lens. Large aperture lenses tend to be more prone to optical defects that cause a departure from an ideal lens. The effect is aberrations, such as spherical aberration, coma, astigmatism, field curvature and distortion [81]. To avoid these, a high quality achromatic lens is used to produce a highly collimated wavefront.

3.3.1.4 Neutral Density Filter and Reference Mirror

The optical quality of the neutral density filters used to adjust the reference beam intensity and the reference mirror itself play an important role in the efficiency of

the system. Both the object and the reference beams pass through the other optical components so that they both experience any change caused by poor quality. However only the reference beam passes through the neutral density filter and is incident on the reference mirror. The reference beam is assumed to be perfectly flat and collimated when it interferes with the object beam. If the reference mirror and the neutral density filter are not of high quality this will not be the case. So again, high quality optics are required.

3.3.2 Data Analysis

3.3.2.1. Filtering

When profiling rough surfaces, certain pixels will not modulate, as the reference mirror is moved, due to the shape of the surface as at that point on the surface there is no light reflected back to the camera. If a camera pixel is located at such a dark region, there is no information from the corresponding object point. Post-processing filters are used to eliminate these missing points in the image. Decreasing the size of the speckles can significantly reduce the number of dark pixels. If a number of speckles are imaged onto one pixel, the intensity per pixel will not, on average, be zero. This is achieved by opening the aperture in the imaging lens system. However, the contrast of the interference is decreased and light that is not reflected along the viewing direction is also allowed to interfere on the CCD faceplate. There is a compromise between the contrast and the number of zero intensity pixels.

The initial output of the profiler is a two-dimensional intensity map where the pixel gray level value represents the height of the surface at that point. In the continuous modulation algorithm the values of the gray levels are the frame numbers in which the coherence region was detected. In the other algorithm the peak modulation within the coherence region was located. When using this algorithm, if in any pixel the maximum and minimum intensities are not a distance $\lambda/4$ apart the pixel is initially given an intensity value of zero. Then a neighbouring

pixel averaging technique is used to fill in the surface height information. When profiling smooth surfaces the errors due to the maximum and minimum intensities not being the appropriate distance apart tend to be very small, less than 0.3%.

The majority of errors in the two-dimensional map of rough surfaces are caused by non-modulating pixels. A custom algorithm developed in the European Commission Joint Research Centre, was designed to correct the resulting two-dimensional images of the profiler and is used to filter these images. It detects and corrects pixels whose gray level is very different from its surrounding pixels. The correction is done by a neighbour averaging technique.

Another filter is used to fill in the sloped areas between the flat areas of a surface. Figure 3.9A shows a line profile from an optically smooth stepped surface as measured by a stylus profilometer. Figure 3.9B shows the appropriate cross section through the two dimensional map measured by the white light profiler using the maximum modulation algorithm. The area between the two plateaus contains no information as interference was not detected in the pixels corresponding to that area. This image can be post-processed to fill in this area by simply fitting straight line between the pixels at the edges of the flat areas. This is done in a mathematical package and requires the user's input. Figure 3.9C shows the image after it has been filtered.

Finally there is also a post-processing filter used to change the three-dimensional surface map. If a surface, which is flat with a step on it, is placed into the system at an angle the result will be a three-dimensional image of a sloped surface with a step on it. For instance, Figure 3.10 shows an optically smooth surface with a single step height on it.

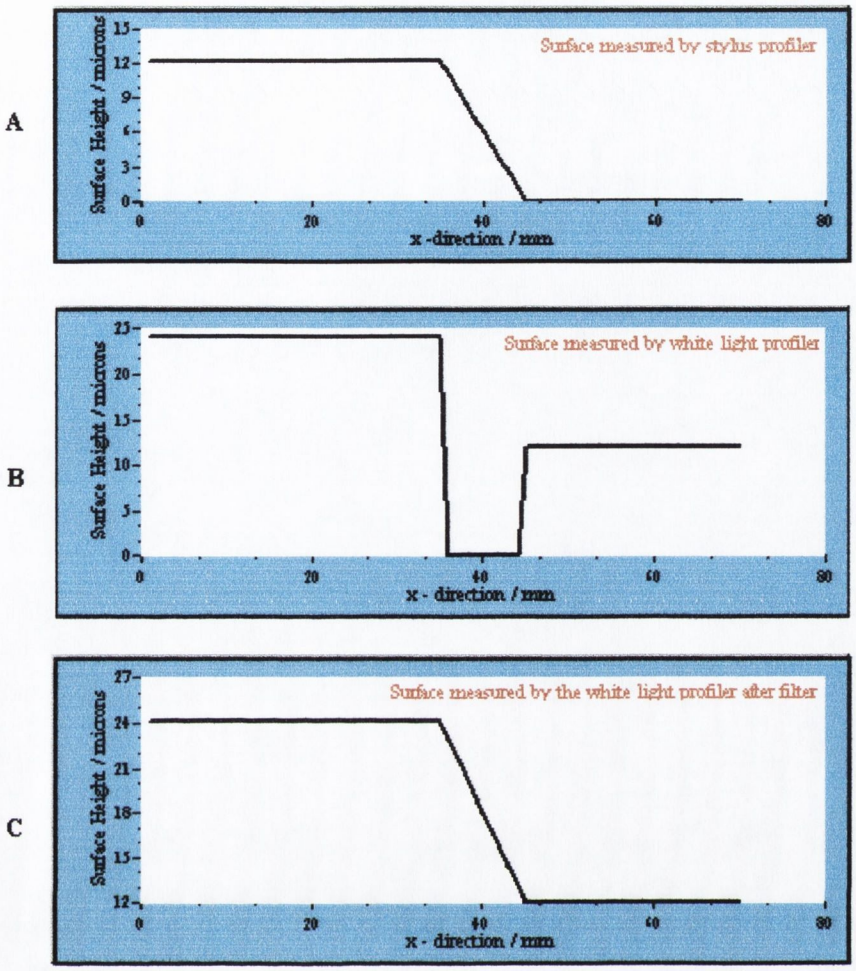

Fig. 3.9 An optically smooth surface with one step; A As measured by a stylus profiler; B as measured by the white light profiler; C After a filter has been applied.

This was placed in the profiler and aligned so that it would be seen as a flat stepped surface. However, as the figure shows, the surface was slightly tilted producing a sloped surface. In this figure this is seen as five steps of 0.06 μm, the step taken by the profiler. This result is then transferred to a image-processing package where it can be filtered to eliminate the slope. This requires the user to place lines across the surface defining points that should be at the same height. The program then alters the surface height accordingly. This obviously requires the users input and some prior knowledge of the surface shape, but this is often the case. Figure 3.10B shows the filtered three-dimensional profile initially measured in Figure 3.10A.

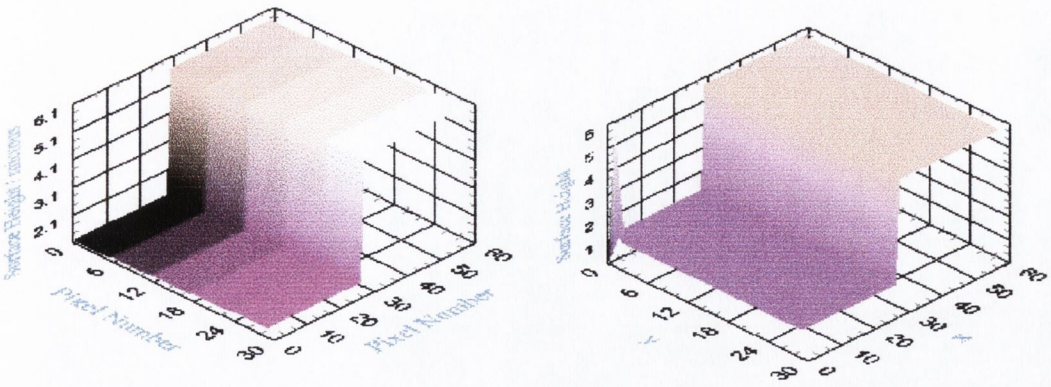

Fig 3.10 An optically flat surface with a step on it, is profiled in the white light system; A. The surface was placed in the system with a slight tilt; B. This can be corrected by removing the slope after in an image-processing package.

3.3.2.2. Sampling

When using the algorithm that detects the maximum modulation within the interference region, the step size is very important. If the step size is too large the modulation signal cannot be recorded accurately. The Nyquist theorem states that the sampling rate should be twice the maximum frequency which would mean a frame every $\lambda/4$, where λ is the mean wavelength. However the use of this theorem is not appropriate here, as the sampled points are not saved so that a curve can be fitted to them. In practice it was found that to obtain the most accurate results with the least errors the smallest step possible should be taken. In the case of this profiler that is 0.06 μm.

When using the program that locates the coherence region the smallest step size is usually taken as this corresponds approximately to $\lambda/8$. This program locates the coherence region by looking for continuous modulation, above a set threshold level, between frames by a subtraction process so if the step is too small the modulation will not be greater than the threshold level. The step size and the starting point are very important in this program and a trial and error process has to be used to find the optimum step unless the mean wavelength is accurately known.

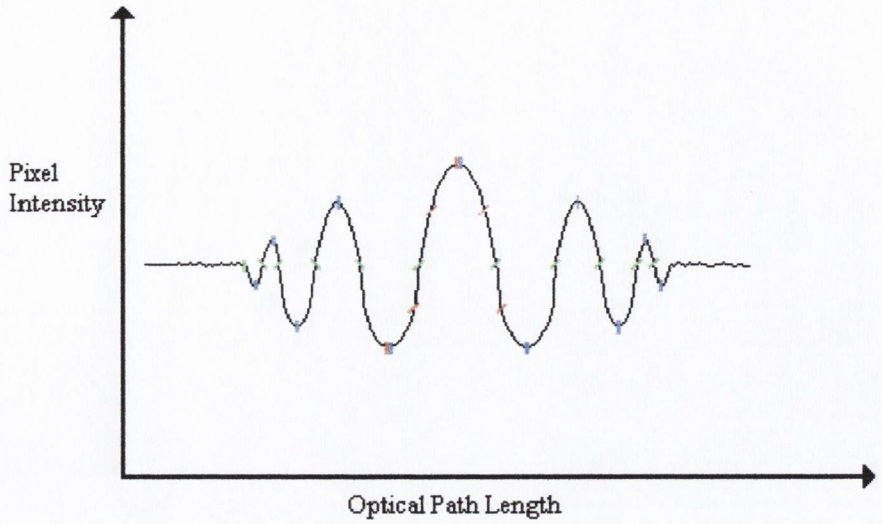

Fig. 3.11 The pixel intensity as a function of the optical path length must be sampled at the correct interval.

In Figure 3.11, if the distance between the sampled points is too small the measured modulation will not be greater than the threshold level. However if the readings are taken at the blue points, an interval of $\lambda/2$, the modulation will be clearly observed. An interval of $\lambda/2$ corresponds to a movement of the reference mirror of $\lambda/4$, where λ is the mean wavelength of the source. This value is known, but to measure the modulation the starting point must be correct. In Figure 3.11 there is also an interval of $\lambda/2$ between the green points and yet the modulation would not be recorded. To allow for this, at any one time three images are taken with an interval of $\lambda/4$ ($\lambda/8$ movement of the reference mirror) between them and the two images $\lambda/2$ apart are compared to one another. Then the reference mirror is moved a distance $\lambda/8$ and another frame is grabbed. This frame, along with the last two in the previous set, form a new set of three frames. For this technique to work well the step of $\lambda/8$ must be taken accurately. When the system is initially set-up and there are two mirrors in the interferometer the mean wavelength can be calculated by measuring the distance between two fringes. If relatively large surface heights are to be measured it is useful to use an interference filter in the system to increase the coherence length of the source. Then it is not appropriate to take a step of $\lambda/8$ as this would mean a large number of frames are taken. To reduce this number and thus the acquisition and analysis time, frames a distance $n\lambda/4$ apart, can be compared to each other. This decreases the number of steps

necessary for a complete scan and this is one of the advantages of this technique over the previous algorithm. Figure 3.12 shows six different results from profiling a flat surface, taking different step sizes each time. A 589 nm interference filter was used to increase the coherence length. The figures quoted are the path changes caused as the reference mirror moved between each frame. The surface was a flat piece of rough aluminum mounted on a black surface. It can be seen from this figure, that a path change of 0.3 μm is correct, which corresponds to approximately $\lambda/2$, when using this light source as the step size will be dependent on the wavelength.

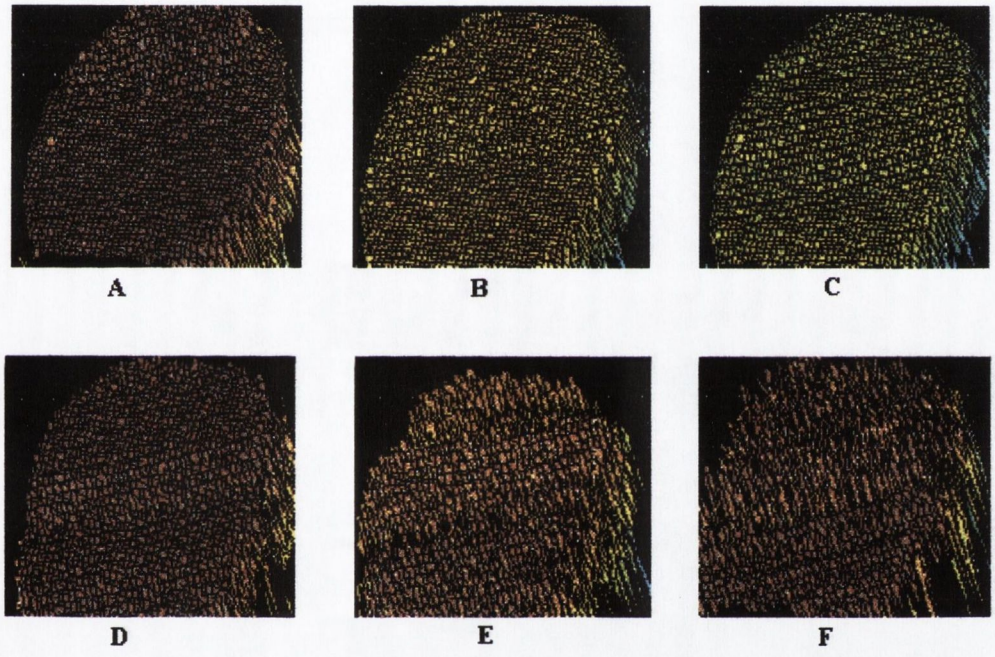

Fig. 3.12 An optically rough flat surface as profiled by the white light interferometer with different path changes taken between each frame grabbed; A 0.06 μm; B 0.18 μm; C 0.3 μm; D 0.42 μm; E 0.54 μm; F 0.66 μm.

3.3.2.3. Threshold

The set threshold level is also very important. If the threshold level is too small, modulation can be recorded even when there is no interference and when it is too high modulation will not be recorded when interference occurs. Figure 3.13 shows six different results from profiling the same surface, using different threshold

levels each time. In Figure 3.13A, modulation occurs in all pixels immediately as the threshold value is zero. As the threshold is increased the number of errors decreases. However, when the value gets too high, errors start occurring because no modulation is recorded in the pixels. A threshold level of approximately 10 (gray levels) should be used to obtain maximum useful information, as shown in Figure 3.13D. This value will depend on the contrast of the interference region, which is dependent on the relative intensities of the beams.

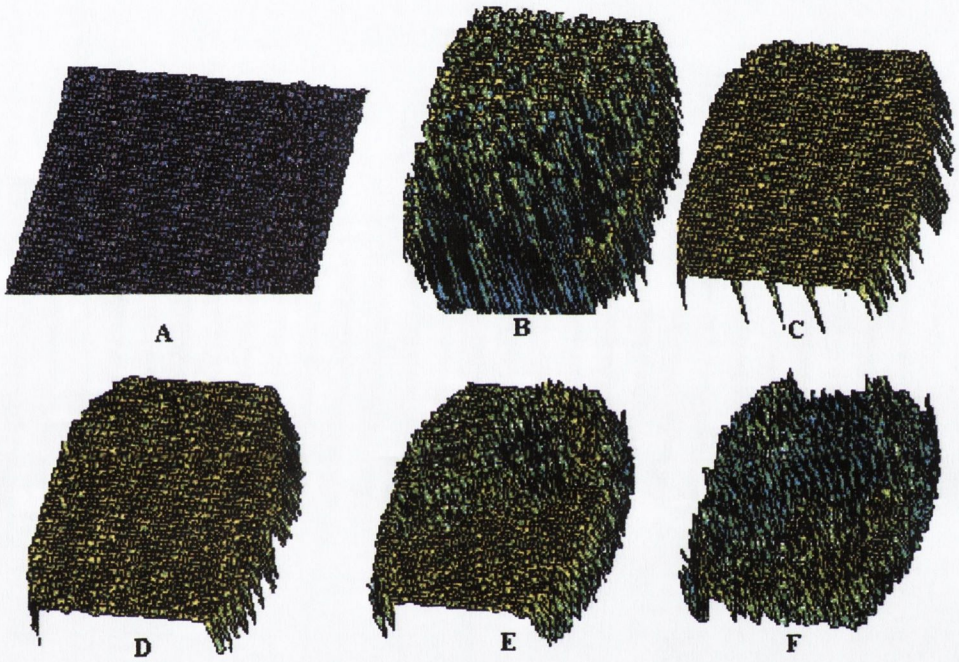

Fig. 3.13 An optically rough flat surface as measured by the white light profiler with different modulation threshold levels, in gray levels; A 0; B 3; C 7; D 10; E 20; F 30.

The user sets the threshold, the step size and the starting point before running the program. There is also the choice of which algorithm to use and the length of the scan. These settings depend on the shape and roughness of the surface, the coherence length and wavelength of the light source, and the required resolution.

3.4 Results

3.4.1 Optical Thickness of Glass and Plastic

As well as measuring the profile of surfaces the white light interferometer can also be used to measure the optical thickness of transparent materials. If the refractive index is known it can be used to measure the actual thickness. Similarly if the thickness is known the profiler can be used to measure the refractive index. Michelson interferometers are commonly used to measure the optical thickness of glass plates in a simple procedure [80]. Manually, this is done by first aligning the interferometer so that white light fringes are observed. The mirrors are carefully aligned so that the central bright or dark fringe covers the whole image. The mirrors of the interferometer are now at zero optical path difference. When the glass plate is placed in one of the arms, the optical path length of that arm increases so the fringes disappear. One of the mirrors is then translated to bring the path difference back to zero and once again get the same fringe covering the image. The distance the mirror must move to do this, is the length the path was increased when the glass was placed in the interferometer. If the mirror moved a distance d, the thickness of the glass plate is simply given by

$$t = d/(n_1 - n_0) \qquad \text{Equation 3.1}$$

where n_1 and n_0 are the refractive indices of the glass and air respectively. In effect this is the same principle as the profiler measuring surface height by locating the peak modulation within the coherence region for different parts of the surface.

With the interferometer aligned, using the two mirrors, a glass microscope cover slide was placed up against one mirror in the system so that it covered the right half of the area of the mirror. When interference fringes are seen on the left of the image, there will be no fringes in the area of the glass because the optical path

difference is greater that l_c in this region. If the reference mirror is translated away from the beamsplitter along the z-axis, at some later stage interference will occur in the region of the glass. This is also what happens when the profiler measures a step height on an optically smooth surface. In that situation, the surface reflects the light that has traveled different path lengths due to the step. In the case of the glass plate, the path length difference is due to the change in refractive index as the light travels through the glass. For this reason it was decided to use this arrangement as an initial test for the profiler.

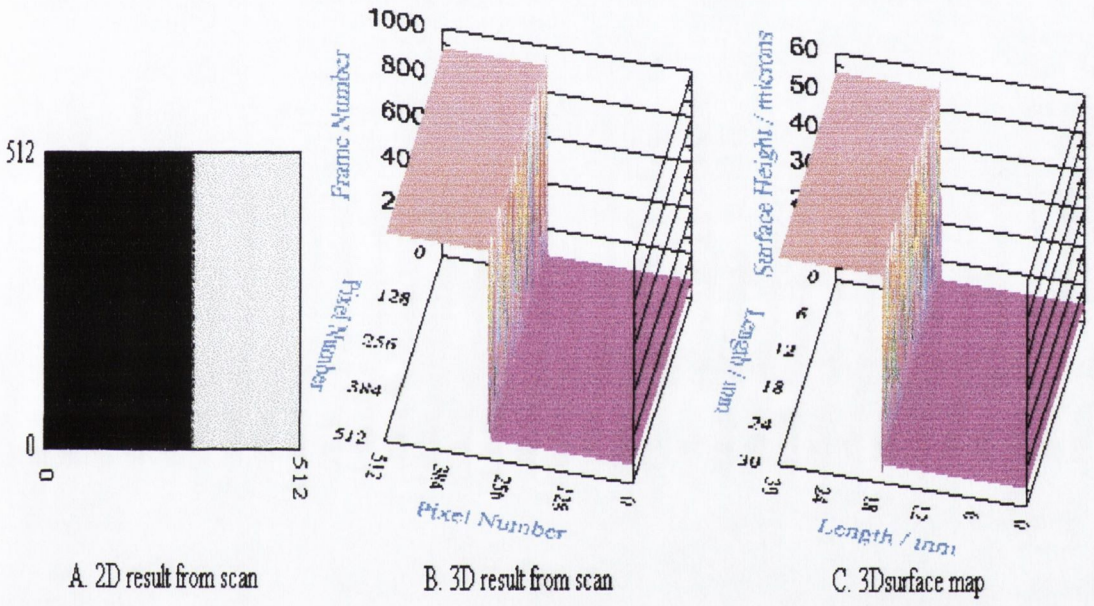

Figure 3.14 Results from a scan of a glass slide on a mirror; A. This is the initial 2D result where the pixel gray level represents the frame in which maximum modulation was detected; B, The is the 3D view of the image in A and again the height is shown in terms of the frame number; C, This is the final 3D result of the scan with the height shown in μm.

The reference mirror was returned to the position of zero optical path difference between the two mirrors. It was then moved closer to the beamsplitter so that no interference was seen in the region of the mirror. The profiler then began to scan using the algorithm that locates the peak modulation within the interference region and the smallest possible size of 0.06 μm was used as the step between each frame. At the end of the scan the result was a two-dimensional image shown in

Figure 3.14A where the gray level represents the frame number in which the maximum modulation was recorded.

It occurred in frame number 83, for the area of the image corresponding to the mirror, and in frame 916 for the area of the glass slide, as shown in Figure 3.14B. The frame grabber has only 8-bit resolution so can only contain pixel gray levels in the range 0 – 255. However when relatively long scans are performed, overflow buffers are used so that it is possible to take more than 255 steps. In this case three overflow buffers were necessary and all four buffers are added together after the scan, in an image-processing package.

Therefore, the optical thickness of the glass cover slide is the height in frames multiplied by the distance moved between each frame, which equals 49.98 ± 0.03 μm, as shown in Figure 3.14C. From Equation 3.1, this corresponds to an actual thickness of 99.96 ± 0.06 μm. It was assumed that the refractive index of the glass was 1.5. The manufacturers quoted the refractive index and thickness at 1.5 and 100 μm respectively. The lateral resolution is dependent on the magnification and in this case a surface area of 2.5 x 2.5 cm was imaged onto a CCD array of approximately 5 x 5 mm. The CCD array is divided into 512 x 512 elements and the area on the object that is imaged onto one single element or pixel, is the lateral resolution of the system. Therefore, in this case the lateral resolution is approximately 50 microns.

This test was repeated with more than one cover slide in the path to simulate multiple surface steps and the profiler produced accurate surface maps. A program was written to calculate the percentage of "bad" pixels, i.e. pixels which do not provide any information and for these tests the number was less than 0.1% and therefore no filtering was necessary.

To further test the profiler and software, a flat transparent plastic slide was placed on a mirror and profiled. Again, instead of profiling the surface of the plastic, its optical thickness was measured with the profiler. It was placed in the white light profiler, as the surface to be profiled, and imaged onto the CCD camera, with the

plastic slide partially covering the mirror. The reference mirror was then translated until there was an optical path difference of zero between the paths to the two mirrors. A 630 nm interference filter was then placed in front of the CCD array, increasing the coherence region to approximately 25 μm. The reference mirror was then slightly tilted so that fringes could be seen in mirror part of the image, as shown in Figure 3.15A.

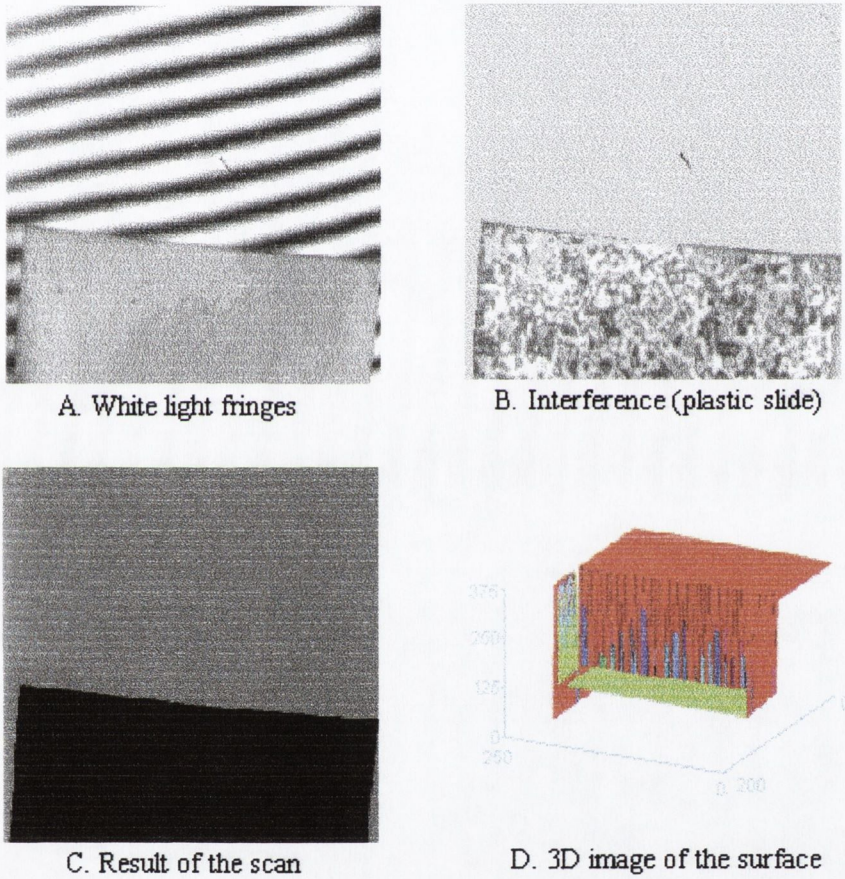

A. White light fringes

B. Interference (plastic slide)

C. Result of the scan

D. 3D image of the surface

Fig 3.15 Images of the plastic slide partially covering the mirror taken at various stages from the white light profiler; A, White light fringes are observed in the mirror region of the image; B, Interference in the plastic slide region of the image; C, The result of a scan where the gray level represents the frame number in which interference occurred for each pixel; D, A three-dimensional image of the surface, with the height shown in terms of the frame number.

The fringes can be clearly seen, as there is a tilt between the two mirrors. This was done purely to show the white light fringes. If the two mirrors were perfectly parallel, fringes would not be seen as a single fringe would cover the field of view. The reference mirror was moved back from the beamsplitter until the interference was seen in the plastic slide part of the image, as shown in Figure 3.15B. This was the location of approximately equal optical path difference between the reference mirror and the mirror behind the plastic slide. The plastic was increasing the optical path length in that area. If the plastic is perfectly homogenous and smooth, white light fringes would again be seen. But as it is not, the fringes are distorted and resemble a speckle pattern.

The reference mirror was then returned to the location of the white light fringes shown in Figure 3.15A. The mirrors were then finely adjusted so that one fringe covered the whole field of view. The mirror was then moved out from the beamsplitter a distance further than the point where the interference occurred in the plastic slide. This was taken as the starting point for the scan. The mean wavelength was now 633 nm so a step size of 1.2 μm was used, which corresponds to approximately $15\lambda/8$. This means the two frames that are compared to one another are a distance $15\lambda/4$ apart. This is an interval of $15\lambda/2$ on the interference signal. A step of this size could be taken on account of the length of the coherence region. Using the software, and after entering appropriate values for the threshold, step size and coherence length, the program was started, using the algorithm that locates the coherence region. The reference mirror moved in steps while the computer grabbed and analysed frames.

First, interference was observed in the plastic slide region of the image, and in a later frame it was observed in the mirror region. When the program was completed, a image of the surface is displayed in which the gray level represents the frame number in which the interference occurred, as explained in the previous section. Figure 3.15C shows this image, which is then transferred to a mathematical package where the frame number can be multiplied by the step size and a three-dimensional image of the surface is plotted. Figure 3.15D shows the

three-dimensional image of the plastic slide, with the height shown in terms of the frame number in which the interference occurred.

The thickness of the plastic slide was measured using vernier calipers to be 0.75 ± 0.01 mm. The reference mirror in the white light profiler moced a distance of 304 ± 12.5 μm. Therefore, from Equation 3.1, the refractive index of the plastic is 1.4 ± 0.02. The percentage of non-modulating pixels in this test increased compared to the last but is still less than 0.5%. This scan had to be performed three times at different starting points before a satisfactory result was obtained. Once a suitable starting point was found the scan was performed 10 times with the same result each time.

These tests showed the software was working efficiently and relatively fast, with an acquisition and analysis rate of about 2 frames per second. The profiler completes a scan of 250 steps is approximately 125 seconds. In other words it can measure the height of the surface at 262,144 points in about 2 minutes. Even though these tests measured the optical thickness of glass and plastic, the speed of the acquisition and analysis is independent of the surface, so the rate of 2 frames per second is the same when actually measuring surface heights.

Calibrated glass plates were then profiled to ensure the profiler was operating correctly and to check the accuracy of the readings. The first surface was a piece of glass with two steps on it of heights 8.7 ± 0.01 μm and 1.6 ± 0.01 μm. Again the optical thickness was profiled, with the glass having a refractive index of 1.5, by placing the glass on a mirror. Figure 3.16A shows the three-dimensional image of the optical thickness of the glass specimen. The maximum modulation algorithm was used on these glass plates and the reference mirror moved a distance of 4.38 ± 0.03 μm and 0.78 ± 0.03 μm for the two steps respectively. Therefore the thickness of the glass works out to be 8.76 ± 0.06 μm and 1.56 ± 0.06 μm.

Errors in pixels in the vicinity of the steps can be seen in Figure 3.15A. Steps that are not perfectly vertical can cause these errors. However in these surfaces the

errors are more likely to be caused by imaging both sides of the step onto one pixel. The effect is an average of the intensities and this type of pixel error is common in all CCD imaging systems. The filters described in the previous section are used to remove these errors. Figure 3.16B shows the result after filtering. The effect of these filters becomes more apparent when profiling actual surfaces and not just measuring the optical path thickness.

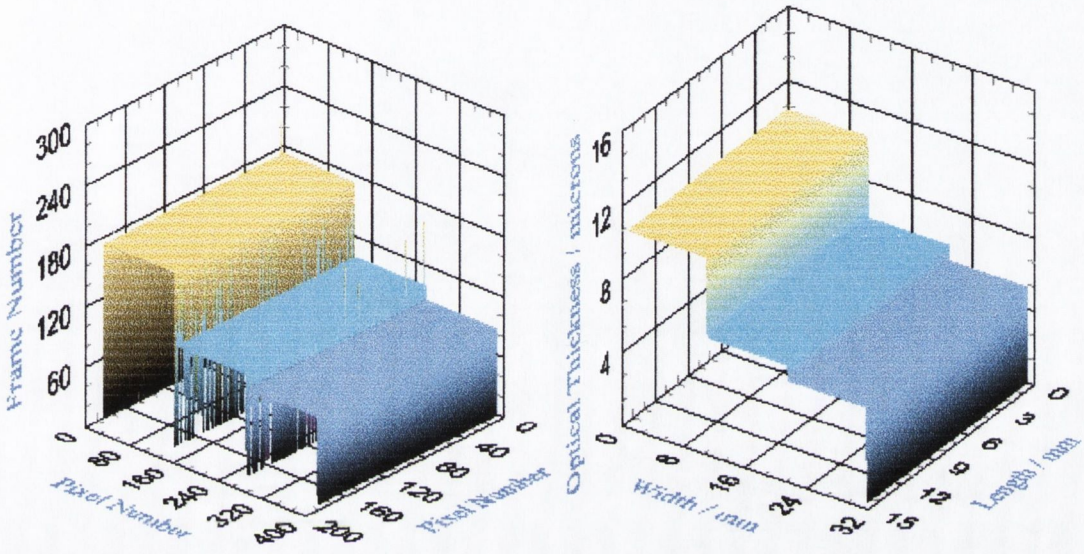

A. 3D image of stepped surface where the height is in frame number

B. 3D height map of the stepped surface

Fig. 3.16 Three-dimensional images of the stepped surface; A, Height is given in frame number in which maximum modulation occurred; B, Actual height map of the surface.

3.4.2 Surface Profiles

3.4.2.1 Optically Smooth Surfaces

The first surfaces to be profiled were silicon surfaces steps, of 0.36 μm, 0.62 μm, 1.18μm and 4.5 μm, supplied by Dublin City University. They were roughly 2 x 2 cm in area and the steps were layers of carbon nitride covering approximately half the surface area. The purpose of the measurements was to ensure that the thickness of the carbon nitride layers remains constant to within 10%. They had

previously been measured using a stylus profilometer but this technique was not really suitable as the stylus technique only takes a single line profile at a time so the surface had to be scanned and there was also concern that the stylus would damage the surface. For these reasons, the non-contact full-field white light interferometric technique was more suitable. The size of the object and the fact that both the silicon and carbon nitride surfaces are specularly reflective made these specimens ideal for this system.

The first surface profiled, with the 0.36 μm step, was placed in the system and scanned using the maximum modulation algorithm without an interference filter. The surfaces were placed in a holder mounted on a translation stage, which could be controlled manually. As the step size is so small relative to the minimum step of the reference mirror, 0.06 μm, it was ensured before the scan that the maximum intensity fringe would be sampled in the silicon area of the surface. Then if the carbon nitride layer was indeed 0.36 μm this fringe should appear in this part of the surface six frames later.

The reference mirror was then moved away from the beamsplitter by 1.2 μm and the scan was started. As expected the profiler located the interference region in the silicon area of the surface in frame 20 and in frame 26 for the carbon nitride region. The result is shown in Figure 3.17A before a filter has been applied. In the area of the step there was a large percentage of errors. From a visual examination of the surface it was clear that the step was sloped.

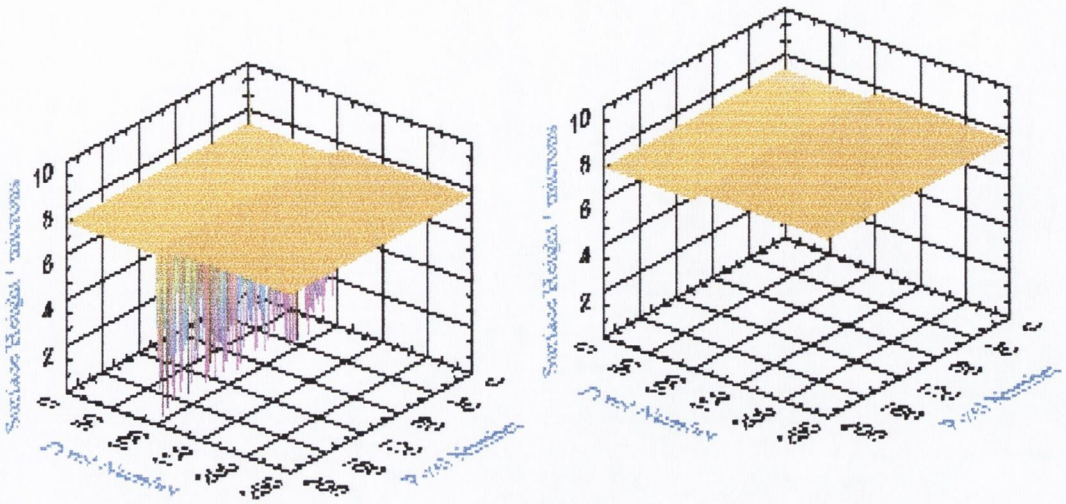

A. The unfiltered image of a step on silicon

B. The filtered image of the step

Fig. 3.17 A step profile of 0.36 μm on a silicon surface; A. Unfiltered and B. Filtered.

Under microscope examination the area of the slope was found to be very rough. This caused errors in this area but these were filtered out and Figure 3.17B shows the filtered three-dimensional image. The profiler measured the height of the carbon nitride layer to be 0.36 ± 0.03 μm and the layer thickness remained constant over the surface.

Using the same procedure the two other surfaces were profiled and the results are shown in Figures 3.18, 3.19 and 3.20. The steps heights were measured as 0.6 μm, 1.2 μm and 4.2 μm, all with an error of ± 0.03 μm.

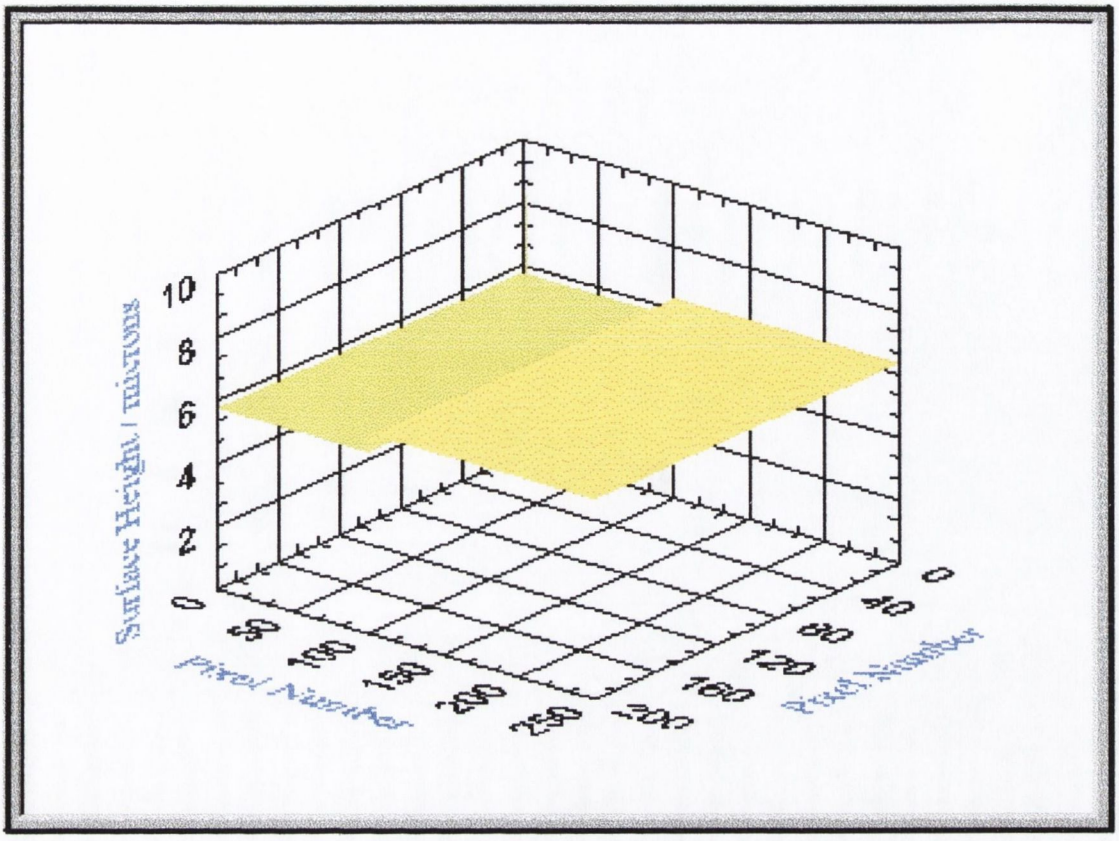

Fig. 3.18 Surface profile of a 0.6 μm step height.

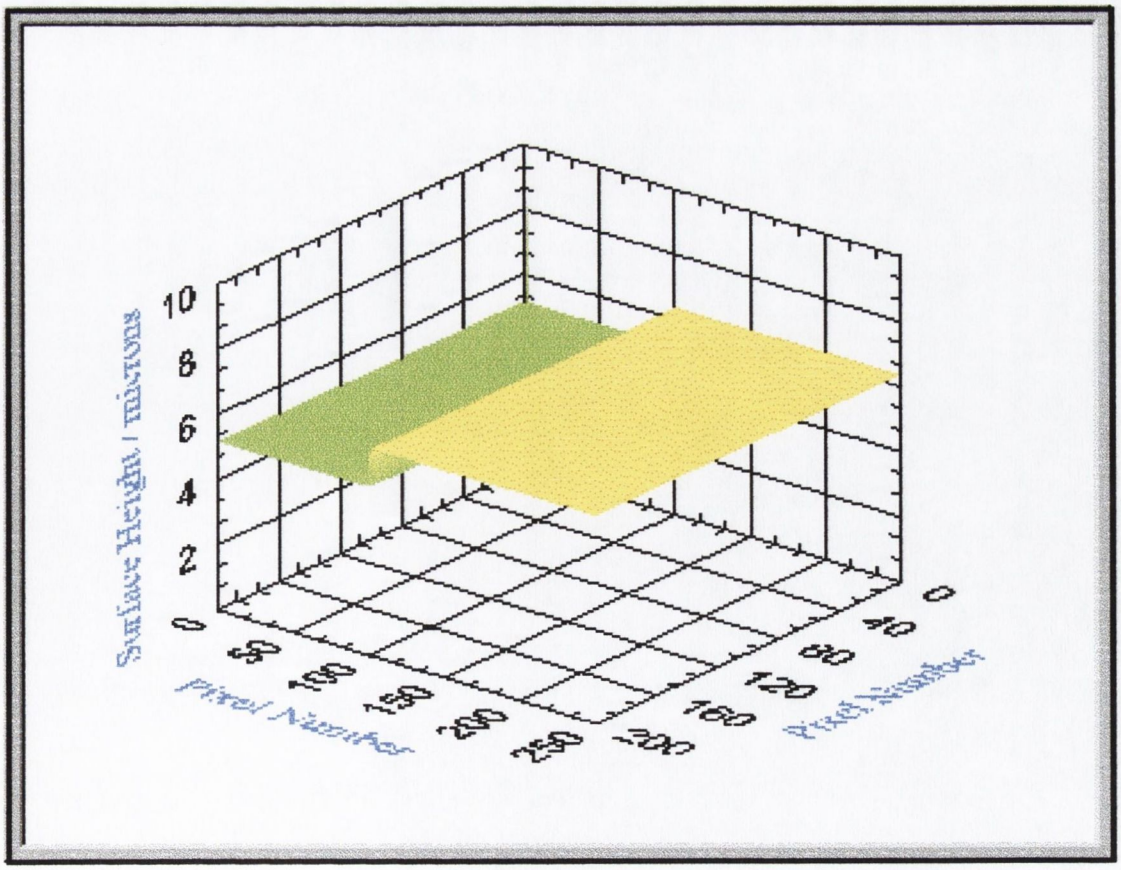

Fig. 3.19 Surface profiler of a 1.2 μm step height

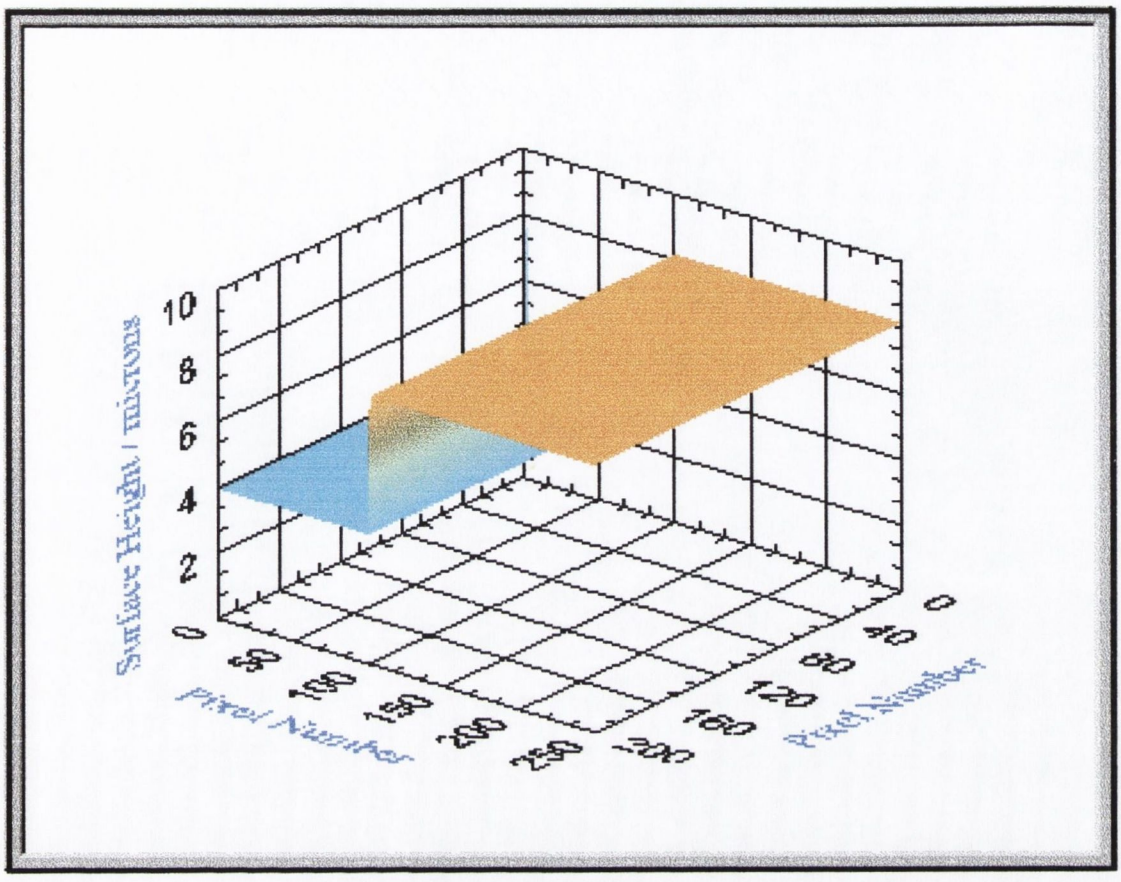

Fig. 3.20 Surface profile of a 4.2 μm step height

3.4.2.2 Optically Rough Surfaces

The profiler was then tested on rough aluminium surfaces using the continuous modulation algorithm. In all the results given so far very high contrast interference was imaged onto the CCD camera. When a rough surface is used the fringes become distorted because of the slight changes in surface height at each point. This means that the reflected beams from these different surface heights arrive at the CCD array with different phases. On the array they interfere with a reference beam that has a constant phase across the image.

This results in a different resultant intensity at each point. If the optical path difference between the reference mirror and all points on the surface is less than the coherence length, the image will now look like a speckle pattern, as described in Chapter 2. The major difference between this speckle pattern and the speckle pattern used in ESPI is that when the reference beam is taken away the speckle

pattern no longer exists. However, this system can now also be used to do electronic speckle pattern interferometry, even with a white light source and this is discussed in Chapter 5. Figure 3.21 shows the image of an optically rough surface at a path difference of less than the coherence length. The speckle pattern can be seen on the surface.

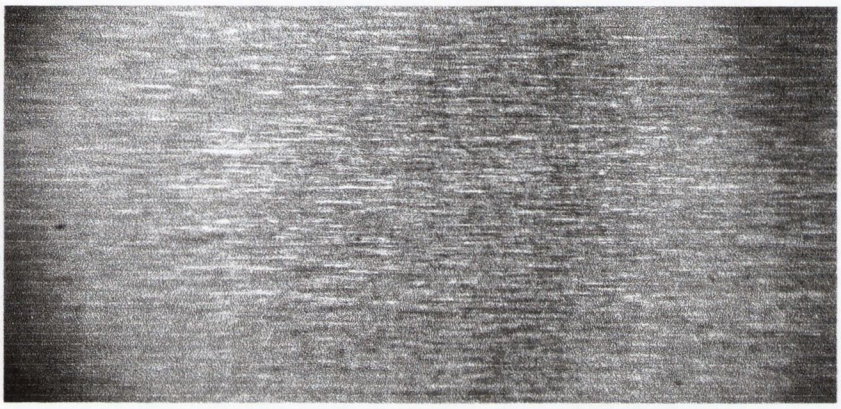

Fig 3.21 A white light speckle pattern on a aluminium surface.

To check, first, that the interference region would indeed be recorded using the continuous modulation algorithm, a flat piece of aluminium was placed on a mirror and profiled in the system. The aluminium only took up about one quarter of the image area and a 630 nm interference filter was used to increase the coherence length. The reference mirror was moved past the interference region for the mirror and stopped short of the interference region for the aluminium. As the objective of this experiment was not to measure the height of the sample, but to check if the interference region would be recorded, this position was set as the starting point for the scan. Before the scan was started the reference mirror was moved forward so that the interference could be visibly seen in the image of the aluminium. In this position the pixel intensities are examined to check the contrast. The contrast was relatively high so a threshold level of 20 was set. The step taken was 1.2 μm, which corresponds to $15\lambda/8$ as the mean wavelength was now 630 nm. If the algorithm worked correctly it would only see modulation in the aluminium area of the image. Figure 3.22 shows the unfiltered three-dimensional result from the scan.

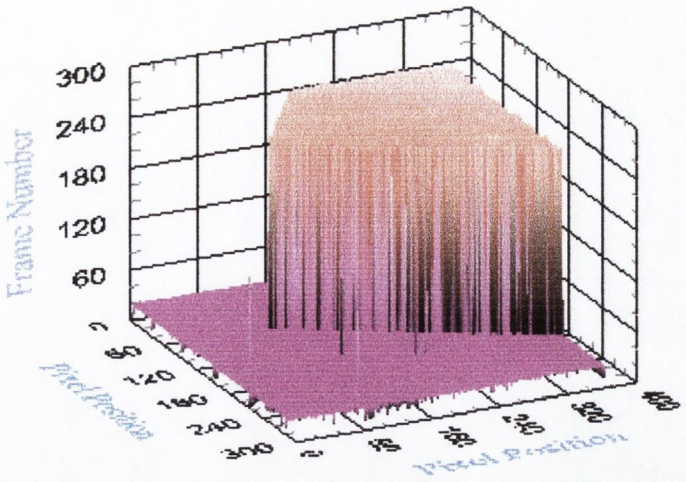

Fig. 3.22 The 3D profile of an aluminium sample which was used to test the continuous modulation algorithm.

The profiler had recorded the interference region using this algorithm with a significant number of errors around the edges of the sample but again the percentage of bad pixels in the aluminium area is less than 5%.

To measure a step height, an aluminium plate with a step of 500 μm of its surface was placed into the system. The surface was rubbed with emery paper to ensure it was very rough and the 630 nm interference filter was again placed in front of the CCD array to increase the coherence length to approximately 25 μm. After a few scans using different threshold levels and step sizes, the optimum settings were found to be a threshold of 10 and a step size of 1.2 μm. The surface was then scanned and the result in shown in Figure 3.23. It can be clearly seen that the number of errors has increased compared to the smooth surfaces. Figure 3.24 shows the image after it has been filtered.

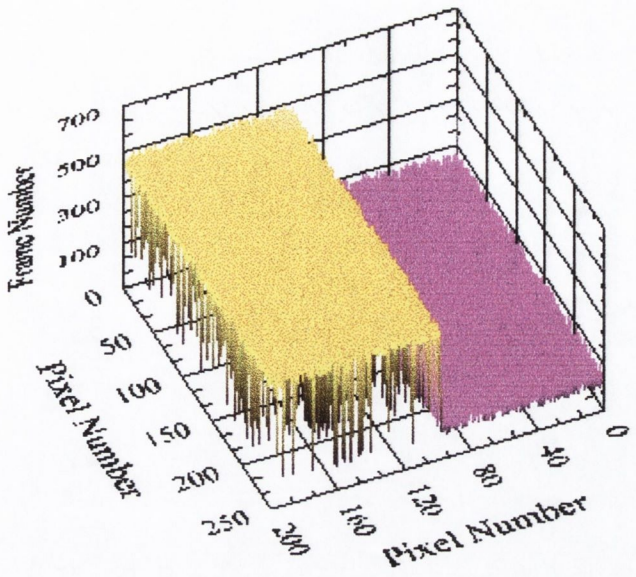

Fig.3.23 The unfiltered 3D profile of the aluminium step with the height given in terms of the frame number in which continuous modulation was recorded.

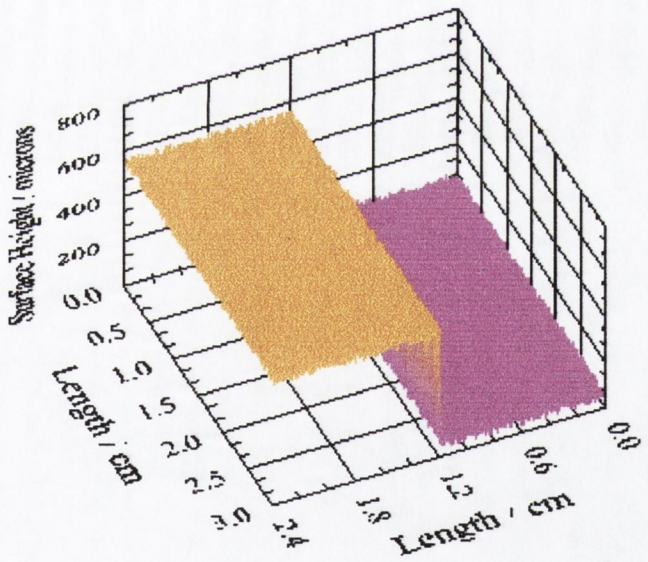

Fig. 3.24 The filtered 3D profile of the aluminium step with the surface height given in micrometers.

As mentioned in the previous section the profiler can measure the slope of surfaces placed in the system at a tilt, so long as the surface is diffusely reflective. Figure 3.25 shows the unfiltered profile of a flat steel bar that has been sprayed with matt white paint. The bar was tilted such that the difference in height between the lowest and highest points on the surface was 2 cm. The percentage of

errors is relatively large in this result, with about 15% of the total number of pixels containing no useful information.

Figure 3.26 is a filtered profile of part of an aluminium cantilever beam, again placed in at a tilt. This surface had a trench running along the length of it, in which an optical fiber is placed when measuring the deflection of the beam. The fiber was not in the trench during the profiling but the trench is not well resolved. The width of the trench was approximately 150 μm and an area of 5 x 5 cm was imaged onto the CCD camera. Therefore, the lateral resolution was approximately 100 μm, which meant that at best, the trench could be one pixel wide. However, it is more probable that the light reflected from the trench will contribute to pixels already receiving light from the area around the trench. In Figure 3.26, the trench is barely seen as a discontinuity in the surface contours.

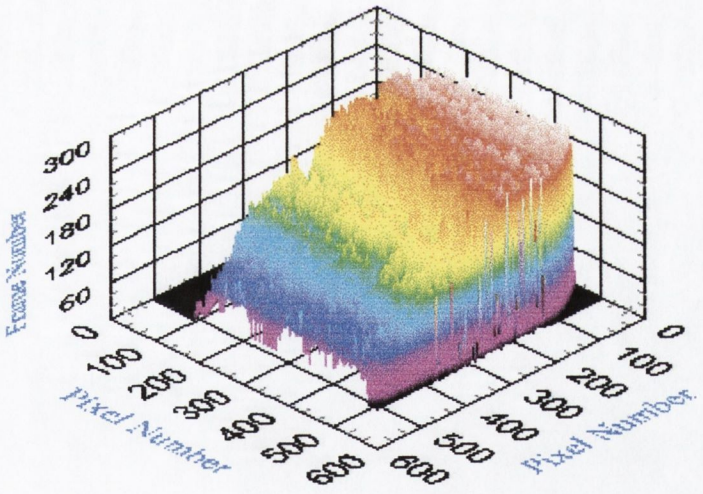

Fig. 3.25 The surface profile of a flat steel bar placed in the system at an angle.

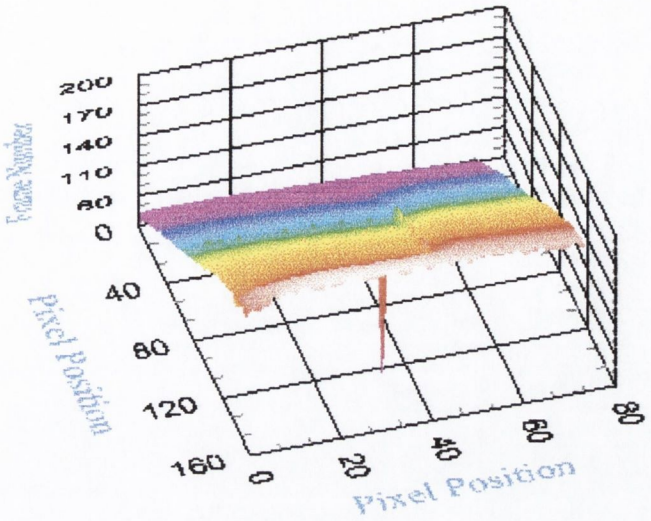

Fig 3.26 The surface profile of a section of an aluminium bar which has a trench for an optical fiber running down the middle.

The remaining figures show surface profiles of coins as measured by the white light profiler. Optical profilers have been used in America and Australia to accurately measure the shape of coins and the moulds used to make the coins for the national mints [132]. Again, the advantages of using an optical technique are non-contact and full-field measurements. Coins are relatively rough surfaces with many variations in curvature across the surface. When the profiler was first developed it was not capable of measuring the profile of the whole surface area of a coin, as it was extremely difficult to align so that high contrast, white light speckle could be seen covering the whole surface. It was at this time that Figure 3.27 was taken, showing a profile of the letter P from a ten pence Irish coin. After continuous development and optimisation the system was eventually capable of profiling whole surfaces. This was made possible by building the system so that the surfaces were always correctly aligned. This was due to the use of Spindler and Hoyer macrobench holders which could all be aligned independently and then fixed in that position. Figures 3.28, 3.29 and 3.30 show the profiles of an Indian coin, a Canadian coin and a German coin respectively.

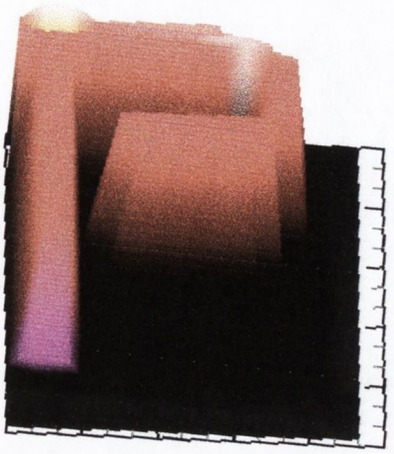

Fig 3.27 The surface profile of the letter P taken from an Irish 10 pence coin.

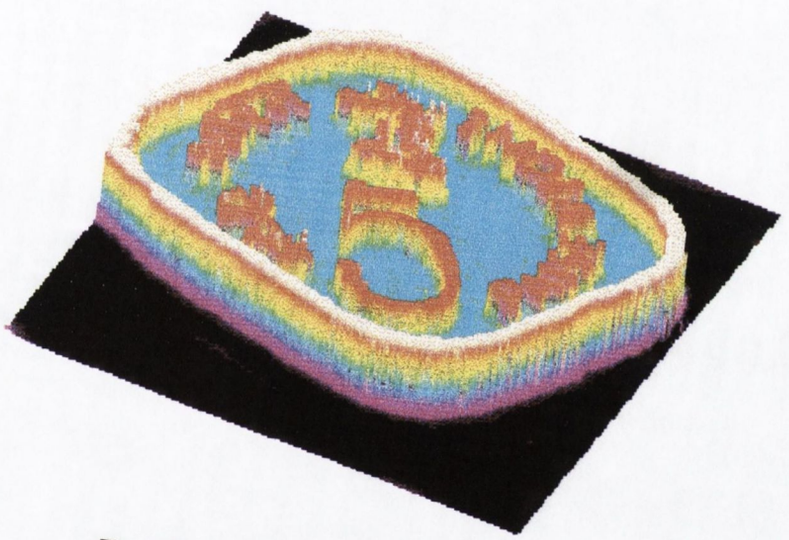

Fig. 3.28 The surface profile of an Indian coin.

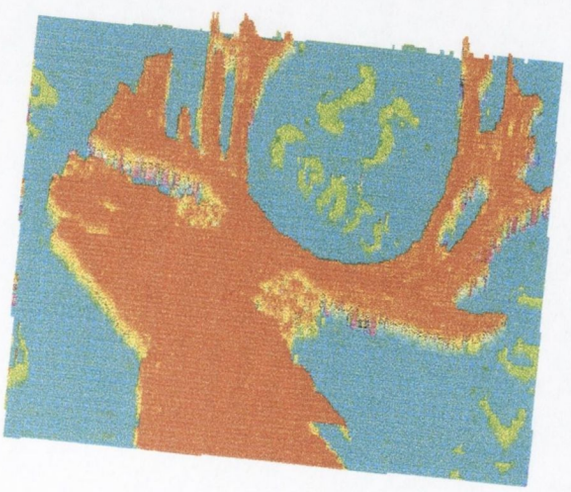

Fig. 3.29 The surface profile of a Canadian coin.

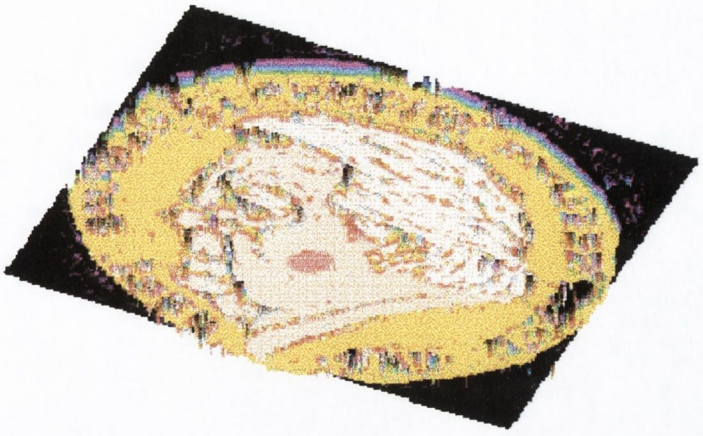

Fig. 3.30 The surface profile of a German coin.

3.5 Conclusion

The white light interferometric system described is a very efficient optical profiler. It utilizes the short coherence length of the white light source to produce surface profiles with a resolution of 0.06 μm when profiling smooth surfaces and approximately 1-2 μm when measuring height variations on rough surfaces. Its range is only limited by how far the reference mirror can move, which is about 5 cm in this system. The algorithms, which were designed, deal with the vast amount of data in a fast and simple manner enabling images of 512 x 512 pixels to be analysed efficiently. The optical configuration has been designed for optimum performance with almost perfect collimation and filtering at the Fourier plane of the telescope objective lens.

The profiler has been tested on various surfaces with good results. Once all the practical considerations have been taken into account the system can be used on most surfaces. The only problems are associated with surfaces that have a low reflectivity or large variations in curvature. Typical optical profilers measure phase and so are unable to measure step heights of greater than λ. This system's unlimited range and the fact that it does not measure phase, so step heights greater than λ do not introduce errors, give this system a distinct advantage over other optical profilers. Furthermore, the fact that the profiler has a high resolution when

profiling optically smooth surfaces makes it the ideal technique for profiling smooth stepped surfaces. However, the efficiency of the system does decrease as the surfaces get rougher and more convoluted. Even so, the system has still proved effective at profiling rough surfaces and is ideal when a resolution better than l_c is not required where l_c is the coherence length of the light source.

The error in the vertical height data is ± 0.03 μm when measuring optically smooth surfaces and $\pm\frac{1}{2}l_c$ when measuring rough surfaces. To locate the point of maximum modulation with an accuracy of ±0.03 μm, a frame must be taken at every 0.06 μm step of the reference mirror. To locate the coherence region any step of $n\lambda/8$ can be taken, so long as there is a sufficient number of steps taken within the coherence region itself. Therefore, if a high resolution is not needed, an interference filter can be placed in front of the CCD camera, increasing the coherence length to allow a relatively large step size to be used. This results in fewer frames taken for a scan, which means a faster acquisition time. Whether the maximum modulation or the continuous modulation algorithm is being used, the frame acquisition and analysis rate is approximately 2.5 Hz. This means in two seconds, five 512 x 512 frames can be acquired and analysed. This rate is doubled if an image of 256 x 256 pixels is taken.

The phase-shifting algorithm, described in Chapter 2, was utilized so it could be compared to the developed algorithms. This algorithm has a higher resolution that the two algorithms described in this chapter but is much slower. To obtain and analyse the three phase-shifted images took just under three seconds. These were obtained by moving the reference mirror that was now mounted on a PZT, which was then mounted on the DC motor. When profiling rough surfaces this algorithm proved inefficient compared to the simpler continuous modulation algorithm.

In order to evaluate the performance of the profiler it was compared to two commercial white light optical surface profilers. Table 3.1 shows the primary specifications of the Zygo Maxim GP Surface Profiler [133], the WYKO NT2000 Surface Profiler [15] and the profiler described in this chapter. The two commercial profilers are both microscopic systems as so can only look at small

areas at any one time. However the table shows they have very high vertical resolution compared to the full-field profiler.

	Maxim GP	NT 2000	New Profiler
Vertical Resolution (smooth surfaces)	0.01 nm	0.1 nm	0.06 μm
Maximum Step Height	<1 mm	185 μm	2.5 cm (limited by maximum linear travel of motor)
Errors in Height Readings	< 3% @ 10 μm < 1.5 % @ μm < 1.0% @ 150 nm	0.01 nm	0.03 μm
Field of View (Max)	2.82 x 2.11 mm	8.2 x 6.1 mm	5 x 5 cm

Table 3.1 The main properties of two commercial systems and the profiler described in this thesis.

They also have a higher lateral resolution because of the greater magnification. However both the commercial techniques are limited to use on surfaces with roughness values of less than 10 μm Ra, whereas the new profiler can be used on surfaces of any roughness value. While there are many applications that require sub-nanometer resolution, such as integrated circuit inspection, there are many others where this type of resolution is not required and a larger range would be essential. Table 3.1 highlights the difference in the ranges of these profilers, showing the large range of the full-field technique.

Some typical applications of the profiler described here are gauge length measurement, thickness of multiple thin films, and silicon plate inspection. After the paper presented in Reading [134] and the Optical Engineering publication [135], a research group in Oxford have decided to use this technique to measure the distance between silicon plates. These plates are incased in glass so only optical techniques can be used. As the distance between the plates is in the region of 1 cm and the maximum allowable error is a couple of micrometers, the optical profiler described here is ideal.

Chapter 4 Dual In-plane ESPI system

4.1 Introduction

Electronic speckle pattern interferometry offers high sensitivity and accurate surface displacement measurements. The technique can measure separately both in-plane and out-of-plane displacements. It is a non-contact method and can be used as for non-destructive testing of materials. Under a known load, the surface displacement data can be analysed to produce strain data, from which the mechanical properties of the material, such as Young's modulus, may be calculated. The technique has a high sensitivity and unlike the conventional strain gauge method, it is a full-field technique that provides data over the whole surface area. However even with these advantages it has not been readily accepted into industry. The reasons for this include bulky and fragile optical configurations that are very sensitive to vibration and mechanical noise. It usually requires an experienced optical physicist or engineer to operate the systems and analyse the data. The use of high-powered lasers has also curtailed the industrial use of the ESPI technique because of the potential dangers to users.

The objective of the research described in this chapter was to develop an industrial prototype of an advanced dual in-plane ESPI system. The system would be portable, compact and robust, and capable of producing quantitative displacement data. To produce this quantitative data, phase shifting devices would be incorporated into the system. The interferometer would make efficient use of the illumination available without the use of shutters. As the goal of the research was to develop a device that could be incorporated easily into industry, only low voltage devices were used without the need for bulky or expensive electronics.

The development also included the design of advanced software that would not only control the ESPI system, including the phase shifting and image acquisition, but also analyse the data to produce displacement data. The ultimate aim of the

research was to produce a system that could be taken into an industrial environment and used in-situ, to produce accurate data. The research was supported by the European Commission DGXIII under contract CSA96112 and the software was written in the European Commission Joint Research Centre.

This chapter follows the development of the ESPI system from the first laboratory system to the final industrial prototype. The first system did not incorporate any phase shifting devices and so could only produce qualitative results. Even so, it was taken to the Department of Structural Engineering in Torino Polytechnic and used successfully to measure crack propagation through clay components. The results of these tests are presented here.

The final system fulfilled all the requirements and is described in detail along with a description of the control software. Initial tests of this device involved calibration of the fringe sensitivity along with quantitative measurements of surface displacements. This system is very innovative and has no moving parts. Instead it uses electro-optic devices for both phase-shifting and switching between horizontal and vertical in-plane sensitivity. The ability of the electro-optic device to change the polarisation of the laser light forms the basis of this switch. The electro-optic devices are liquid crystal layers cemented between optically flat glass plates. An electric field can be set up across the layer by applying a voltage to electrodes deposited on the inner faces of the glass plates. The speckle interferometry system incorporates two of the liquid crystal devices to facilitate phase shifting.

The control software is also advanced, not only controlling the system but also being capable of controlling loading machines and producing displacement versus load graphs. Extensive tests were carried out with this system and the displacement data obtained were compared to data obtained from strain gauges. Finally the system was used to measure the surface displacements of steel bars under tensile forces. These results are presented along with the wrapped phase fringes, unwrapped phase maps and colour coded displacement maps.

4.2 Development of Prototype

4.2.1 Initial System

The purpose of developing this first system was to become familiar with the ESPI technique, especially its capabilities and limitations. Before an advanced system could be designed it was necessary to investigate the performance of other systems available commercially or described in papers. After this was done and areas of potential improvements identified, work began on an initial design. The first system would not include any phase shifting devices as it was important first to develop an initial design of a dual in-plane ESPI system which was sturdy and reliable. After this had been accomplished a more complicated system could be designed. From the outset the goals were to develop a small compact and robust system.

This system is sensitive to both horizontal (x) and vertical (y) in-plane displacements. For this complete in-plane analysis the object under inspection is illuminated from four directions, lying in two perpendicular planes. When using the four illumination beams, because the speckle fields produced by the two beam pairs must be distinguished, the interferometer is restricted to sequential recording of the two interferograms. The first interferogram, or resultant speckle pattern, is obtained when the two beams in the horizontal plane (x-z) illuminate the object and then another is taken when these two beams are switched off and the two in the y-z plane are switched on. The corresponding interferograms both relate, pixel by pixel, to the same points on the object surface.

The optical configuration used to split the beam into two pairs of beams in orthogonal planes is shown in Figure 4.1. A 532 nm laser with a long coherence length was used. The system used three beamsplitters and three mirrors to split the laser beam into four beams, two in the x-z plane and two in the y-z plane. To stop all beams illuminating the object at any one time two manually controlled shutters

were used. The beams were then expanded, using microscope objectives, and directed onto the object surface. All the optical components, used to divide the beam into four beams, were mounted in hollow aluminium cubes (12 x 12 cm). These were attached tightly together and connected to steel railing making this part of the system very compact and sturdy. Two circular plane mirrors, M6 and M7 in Figure 4.2, with diameters of 5 cm are attached to the extremities of the railing so that two of the illumination beams exiting the aluminium blocks were incident on these mirrors. This railing was attached at right angles to another railing of the same size, which was placed horizontally on the optical table, as shown in Figure 4.2. Two more railings were attached to either end of the horizontal railing and a circular plane mirror was attached to each of these so that the two other illumination beams were incident on the mirrors. The railings allowed the four circular mirrors, which directed the light onto the surface, to be moved, if necessary. Illumination angles were set at 30 degrees from the surface normal.

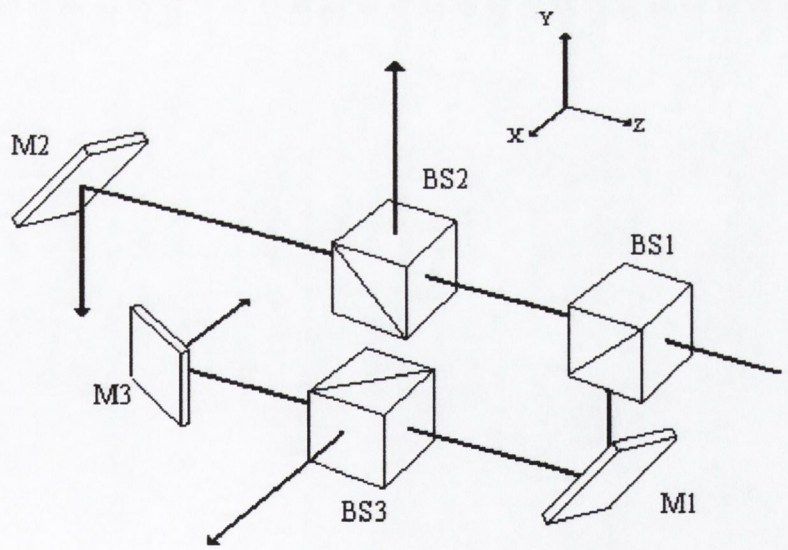

Fig. 4.1 The optical configuration of the beamsplitter used to produce two illuminating beams in orthogonal planes.

The speckle interference patterns are imaged by the CCD camera and the image is then sent to the frame store on board the computer. A reference frame is grabbed

for both planes of illumination, before deformation of the object. During deformation frames are continuously grabbed and subtracted from the reference frame and the fringes are displayed on the monitor. In this way it was possible to watch the fringes form and change. If, at any time, the number of fringes on the screen was too large a new reference frame could be grabbed. However, as the shutters were manually controlled there was no synchronization between the switching and the image acquisition. When using this system, a complete test was carried out measuring the displacement in the x-direction. The test was then repeated to measure the displacement in the y direction.

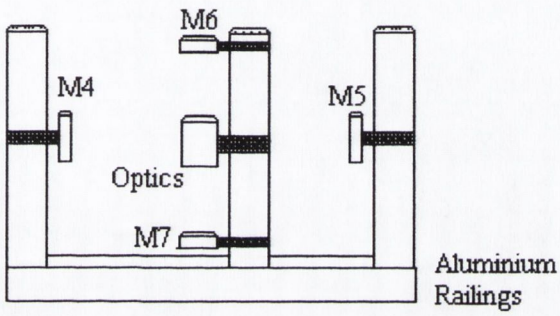

Fig. 4.2 The structural support on the ESPI system

Figure 4.3 shows a typical fringe pattern produced by this in-plane ESPI system. A metal plate was illuminated in the y-z plane and a reference frame was grabbed. A point source of heat was connected to the right side of the plate and frames were grabbed continuously and subtracted from the reference frame. This fringe pattern was taken after the heat had been applied for one minute. Consecutive fringes represent relative displacements of approximately 0.5 μm, from Equation 2.74 in Chapter 2.

Therefore, there was a displacement of approximately 2.25 μm, about 4.5 fringes, between the top and bottom on the right side. On the left side, the displacement between the top and bottom is only about half this, just over two fringes. So, as expected the displacement in the y direction is greater in the area of the applied heat.

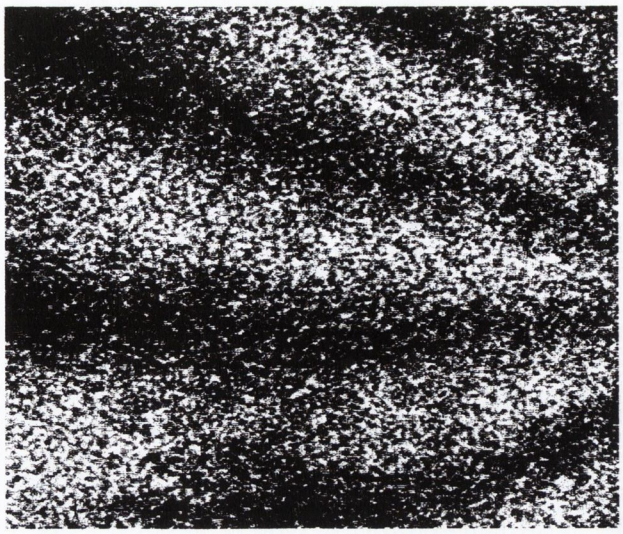

Fig. 4.3 Fringe pattern caused by heating a metal plate.

Figures 4.4 and 4.5 show the displacement fringes caused by compression of two different bricks. The loading was carried out using a Hounsfield loading machine that was controlled by software written in LabVIEW. Details of this program are included in Appendix B. Figure 4.4 shows vertical fringes depicting surface displacements in the x direction. Figure 4.5 shows horizontal fringes representing surface displacements in the y-direction. The displacement caused by the deformation can be measured from these interferograms and from this information the surface strain can be calculated. As mentioned previously, there is no mechanism in this pre-prototype system for automatic analysis of the interferograms.

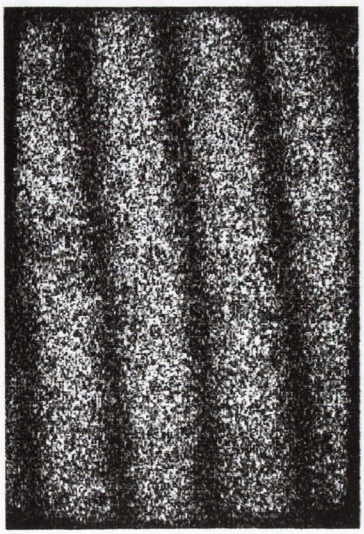

Fig. 4.4 Vertical fringes.

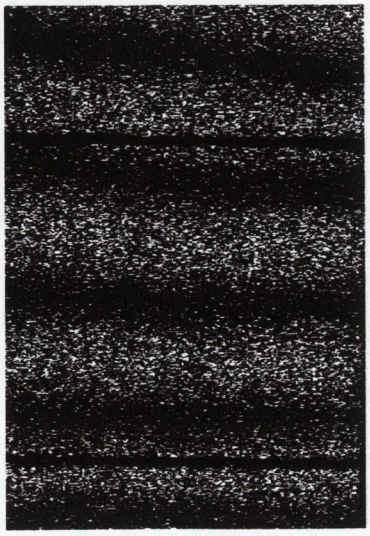

Fig. 4.5 Horizontal Fringes.

The system was taken to Torino Polytechnic and used to measure concrete blocks and clay materials obtained from blocks used to manufacture composite floors. It was tested in a very noisy environment as there were continuous creep and fatigue tests being carried out, in the same work area, on very large-scale concrete structures. The system was unable to measure the horizontal displacements when a concrete block was compressed or when a three-point bending test was carried out on the clay material. The reason for this was the fact that the horizontal mirrors, which were mounted on the two outside railings, were mechanically unstable. During the test their instability led to mechanical noise which caused very poor fringe contrast. An alternative ESPI system for detecting horizontal displacement was built on site, which worked very well and produced high contrast fringe patterns. To reduce the mechanical noise the newly designed system used only one of the vertical railings. The outer railings were discarded and the mirrors were instead mounted to the cubes attached to the central railing. The other optical components were also attached to this frame making the system smaller and more robust.

Because the optics of the system are mounted on just one railing it is easier to adjust the height when using different size test samples. If the height of the original system had to be adjusted, the mirrors and the laser also had to be adjusted which meant realigning the system every time. With the new system the laser remains bolted to the table and a beam-steering device is used to adjust the height of the illuminating light if the system height must be altered. The system can also be placed much closer to the surface, thereby allowing an increased angle between the illuminating beams and the surface normal and thus increasing the sensitivity of the system. The system still used the 532 nm laser.

The analysed results of the Torino tests are presented in Section 4.3 of this chapter. These results produced valuable information for the manufacturers of the clay components and the significance of the results is also outlined. The system was still far from being a tool that could easily be adapted into industry. It was still too big and bulky and had proved to be mechanically unstable. It also

required an experienced user to operate and analyse the data. There was no automatic control of the illumination switching or any mechanism for phase shifting. However the development of this system lead to the identification of areas where improvements, not just to this system, but to the more commonly used configurations, could be made. Early on, it was realised that the optimum solution would have no moving parts, be small and very compact, free from mechanical variations, use only low voltage devices, be easy to use and relatively cheap, and make efficient use of the laser power. The optimized system would also have advanced control software so that there is very little user input. There is no system available commercially or described in the literature that fulfils every one of these requirements. It was with this in mind that the optimised and innovative system was designed.

4.2.2 Advanced System

The optical set-up of the final ESPI system is essentially two separate interferometers, one of which gives sensitivity to in-plane displacement in the horizontal direction and one of which gives sensitivity to in-plane displacement in the vertical direction. The ESPITest software described in the next section of this chapter switches between the two in synchronism with the frames grabbed, thus giving the required dual in-plane sensitivity. Each interferometer consists of two beams emerging from a beam splitter, which are expanded, collimated and directed towards the object so that they overlap in the object plane and have an angle of 60° between them. The illuminated object is imaged by a CCD camera, which is connected to a frame grabber on board a computer. The beams originate from a common point behind the CCD camera and the two beams in each illumination geometry have a common axis of symmetry. A laser diode, with wavelength 852nm and a maximum output power of 150 mW is used as the light source. As well as having the advantage of its wavelength being near the peak of a CCD array's sensitivity, the diode laser is compact and portable. The beam produced by the laser is elliptical and diverging, but customized collimating and correcting optics produce a 4mm diameter collimated beam. The reflectivity of

different objects will vary a great deal so independent control of the intensity of light striking the object is necessary if the imaging system is to work efficiently. It is possible to control the laser power by varying the drive current to the laser diode. There is also an 852 nm filter in front of the imaging lens system so background light does not reach the CCD array.

The beam splitting unit consists of a polarising beam splitter with a quarter wave plate and a mirror placed in the transmitted beam path. This produces two beams, spatially separated by 180 degrees, with the same plane of polarisation. The ratio of intensities of the two beams depends on the plane of polarisation of the incident light beam. In Figure 4.6, light polarised parallel to the z-axis will be transmitted and light polarised parallel to the x-axis will be reflected. The optic axis of the quarter wave plate is aligned at 45 degrees to the plane of polarisation of the horizontally polarised laser beam, converting it into left-circularly-polarised light. The addition of this quarter wave plate (QWP 1) and the mirror (mirror 1) in the transmitted beam rotate the plane of polarisation of the transmitted light through 90°, (back to being parallel with the x axis) so that it is now reflected by the polarising beam splitter.

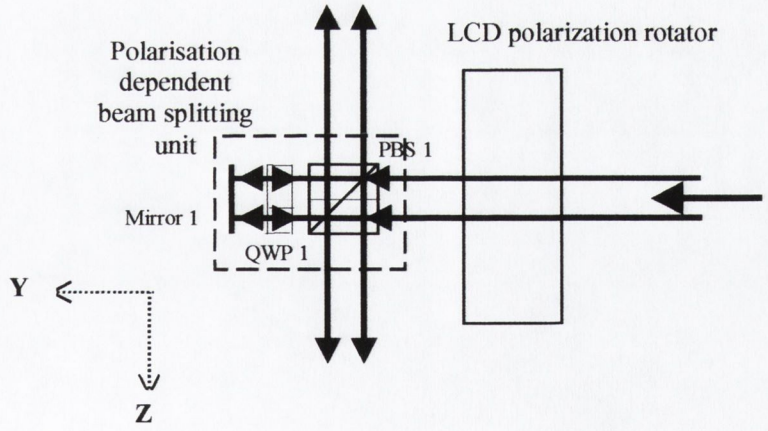

Fig. 4.6 The optical switch using the liquid crystal

A device that could be controlled by the software, which can control the plane of polarisation of the laser light was needed, so that the illumination beams could be controlled. As polarisation and retardance were obviously going to play an

important role in the optical configuration of the system and the choice of polarisation rotator, extensive research was carried out into polarisation and related areas. Detailed descriptions of both polarisation and retarders are given in Appendix C. Also software was written which analyses the polarisation state of the output from a retarder. The user inputs data about the incident light and the retarder itself and the program outputs the polarisation state of the output. A description of this software and the program are also given in Appendix C.

Electro-optic devices are ideal for switching because there are no moving parts and liquid crystals, in particular, do not require high voltages. A liquid crystal polarisation rotator was chosen to rotate the plane of polarisation so it could be used in conjunction with one of the beam splitting units described above to form an optical switch. Before the device was chosen for use in the system, extensive testing of the liquid crystal rotator was performed. These tests were carried out to characterise the behaviour of the device and to determine its suitability for use in an ESPI system. A detailed description of this liquid crystal device and the results of the testing, along with the reasons it was chosen, are given in Chapter 6.

This liquid crystal device, driven by an audio frequency square wave, causes the plane of polarisation to be rotated through 90^0, on software command. Depending on the square wave amplitude, the beam is either plane polarised parallel to the x-axis or parallel to the z-axis and is thus directed into one of the two possible beam paths (for x and y sensitivity). In each path, after the beam emerges from the optical switch it is split by an identical beam splitting unit. However, in this case a permanent 50/50 split of the beam power is required so there is no need for the liquid crystal polarisation rotator. A 50/50 split is ensured if the plane of polarisation of the light incident on the beam splitter makes a 45^o angle with the vertical axis of the beam splitter.

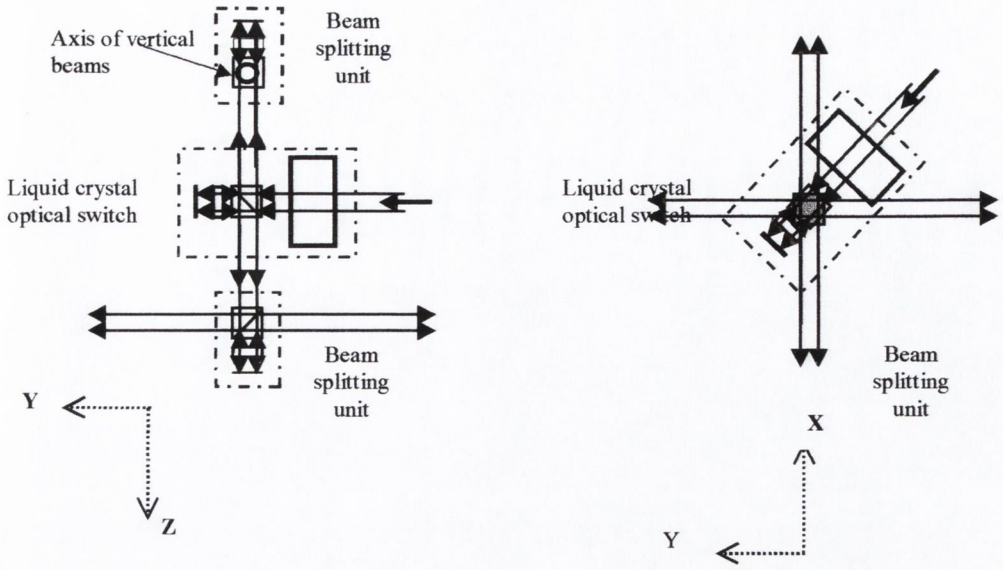

Figure 4.7 Beam directing optics.

This could be achieved by using a half wave plate to rotate the plane of polarisation of each beam to the required angle, but it is equally convenient to physically rotate the optical switch (all the optics shown in Figure 4.6) through 45° in the x-y plane as shown in Figure 4.7. Since the beam cross sections are circular, this has no effect other than the desired rotation of the planes of polarisation of the emerging beams with respect to the beam splitters that follow. This option has the added advantage that the laser can be mounted between two of the arms of the interferometer rather than in line with one of them, allowing for a more compact design. One of the beam splitting units is oriented so that the beams produced are parallel to the y-axis, the other so that the beams produced are parallel to the x-axis.

Plano-concave lenses are used to expand each beam, which is then collimated by 75mm diameter, 60° off axis, diamond turned, paraboloidal mirrors. These mirrors also direct the beams towards the object. This is shown in Figure 4.8 for the vertical axis illumination system. The collimation allows a surface area of 5cm by 5cm to be illuminated. If a bigger area of illumination is needed the paraboloidal mirrors can be replaced by plane mirrors. In this way diverging beams will illuminate the object surface. The components are mounted using a rigid structural support.

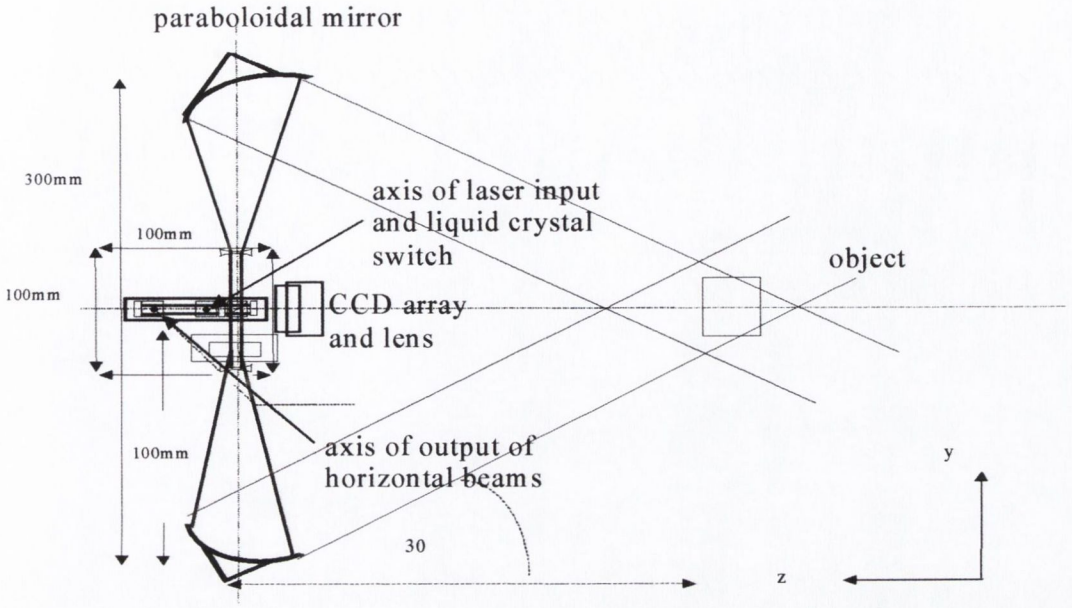

Figure 4.8 Beam expansion and directing optics.

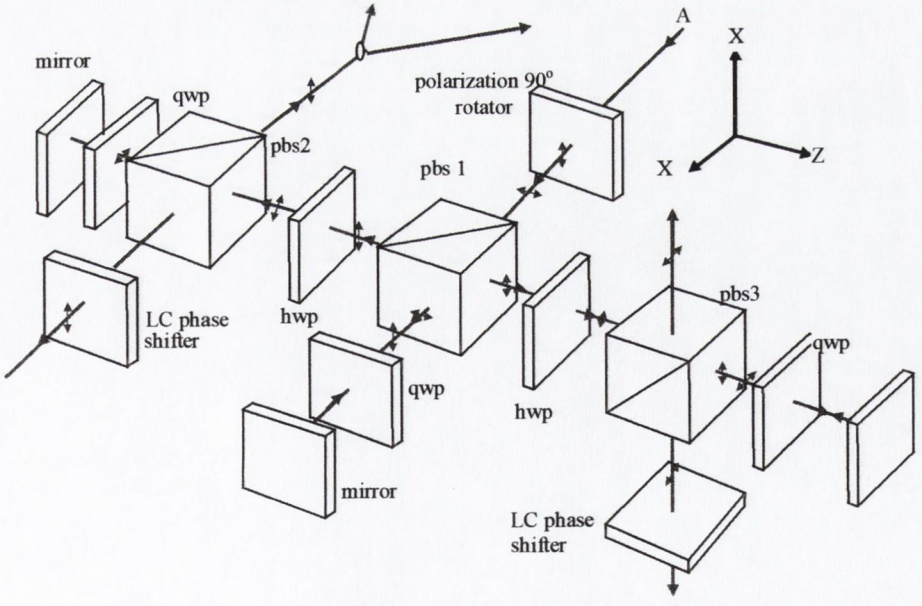

Fig 4.9 Three-dimensional diagram of beam directing optics

The role of each component can be explained using the schematic diagram shown in Figure 4.9. The diagram is merely intended to show clearly how the system works and thus the laser axis is shown lying in the y-z plane and not at 45^0 to it, and as is actually the case the half wave plates on either side of pbs1 are not used. All optical faces, with the exception of the mirrors, are antireflection coated at 852 nm. The expanded, collimated beam is initially plane polarised parallel to the x-axis and has a diameter of about 4 mm. The beam enters, at point A, the liquid crystal polarisation rotator, which causes the plane of polarisation to be rotated through 90^0 on software command.

The beam reflected by pbs1 is split into two orthogonal plane polarised beams by another polarising beam-splitter (pbs2). A combination of quarter wave plate and plane mirror returns the beam transmitted by pbs2, to pbs2, but now plane polarised parallel to the x axis, so that it is reflected at pbs2 and is in alignment with the beam previously reflected by pbs2 and is in the same vertically plane polarised state (parallel to x axis). These two beams are expanded by short focal length concave lenses and collimated as shown in Figure 4.8, by the off-axis parabolic mirrors and illuminate the surface for sensitivity in the y direction.

For sensitivity in the x direction, an identical optical configuration is used. When the light incident on pbs1 is horizontally polarised with respect to the beamsplitter it is initially transmitted by the beamsplitter but is reflected back vertically polarised so it is reflected towards pbs3. The light is now plane polarised at 45 degrees to pbs3 so 50% of it is reflected. The other 50% is transmitted through the beamsplitter, through the quarter wave plate and reflected at the mirror. The beam arriving back at pbs3 is polarised parallel to the y axis, so that it is reflected at pbs3 and is in alignment with the beam previously reflected by pbs3. These two beams are expanded by short focal length lenses and collimated by the off-axis paraboloidal mirrors to provide illumination of the surface, for sensitivity in the x direction.

To facilitate phase shifting, a device capable of changing the optical path length of one of the interferometer arms is needed. The use of a PZT is not ideal as any

moving part can cause instability. Also attaching the large paraboloidal mirrors to a PZT and ensuring mechanical stability would be quite difficult as they are large and relatively heavy. It was decided to use liquid crystal devices to change the optical path length. These devices operate at relatively low voltages, 0 to 10 volts, and are easily incorporated into the optical configuration. Again, extensive testing of these devices was performed and results of these tests are given in Chapter 6.

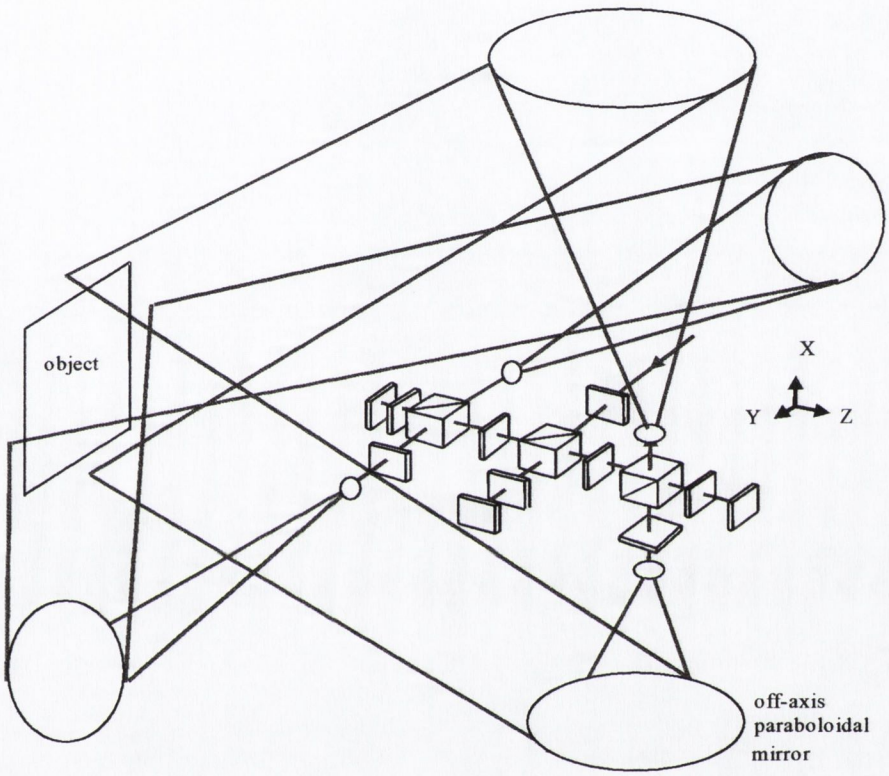

Fig 4.10 Complete optical configuration.

Before one of the beams in figure 4.9 is expanded it first passes through the liquid crystal phase modulator. This device provides up to 2π phase shift, again under software control.

From Figure 4.10 it can be seen that the system is capable of providing sensitivity in x and y directions alternately, as the switching voltage applied to the liquid crystal polarisation rotator is changed. All of the laser power is directed alternately into each illumination geometry.

4.2.2 Initial Results

Figure 4.11 shows six fringe patterns obtained as the voltage across the liquid crystal phase-shifting device was increased. The surface of a disk was illuminated in the x-z plane and after a controlled in-plane rotation of the disk the first fringe pattern was obtained. The voltage across the liquid crystal, in one arm of the interferometer, was then increased in controlled steps. The phase change experienced by the beam in that arm can be seen in the six fringe patterns shown in Figure 4.11. As described in Chapter 6, there is a non-linear relationship between the voltage and the phase change. This can be compensated for in the software so that the four phase shifted images $\pi/2$ apart can be accurately taken.

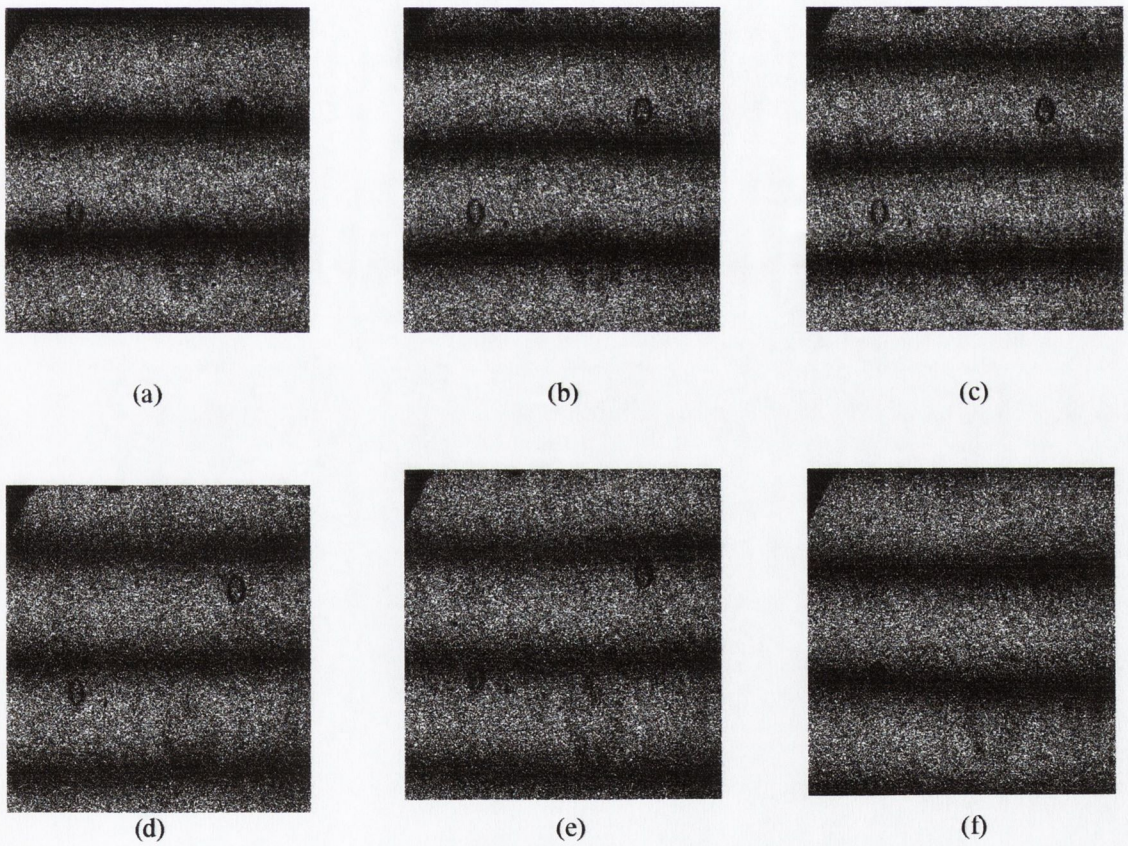

Fig. 4.11 Fringe patterns taken while the voltage across the liquid crystal phase-shifter was increased : (a) 0.0 V, (b) 1.2 V, (c) 1.8 V, (d) 2.0 V, (e) 3.4 V, (f) 4.2 V

So long as the liquid crystal phase shifters have been accurately calibrated it is not necessary to calibrate them before each test. However as the effects of time on these devices are not known, it is recommended that they be calibrated as often as possible.

The interferogram, in Figure 4.12, shows fringes representing displacement in the x direction. The object under investigation was again a rotating disk. The software gives the user the option to either observe the formation and progression of the displacement fringes or the wrapped phase map. Updating of the wrapped phase maps is, of course, slower on account of the time needed to calculate the phase.

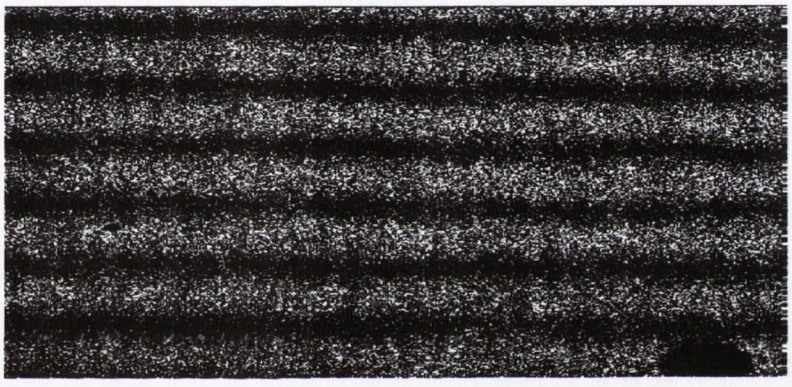

Fig. 4.12 Fringe pattern representing the displacement of a surface along the x-axis.

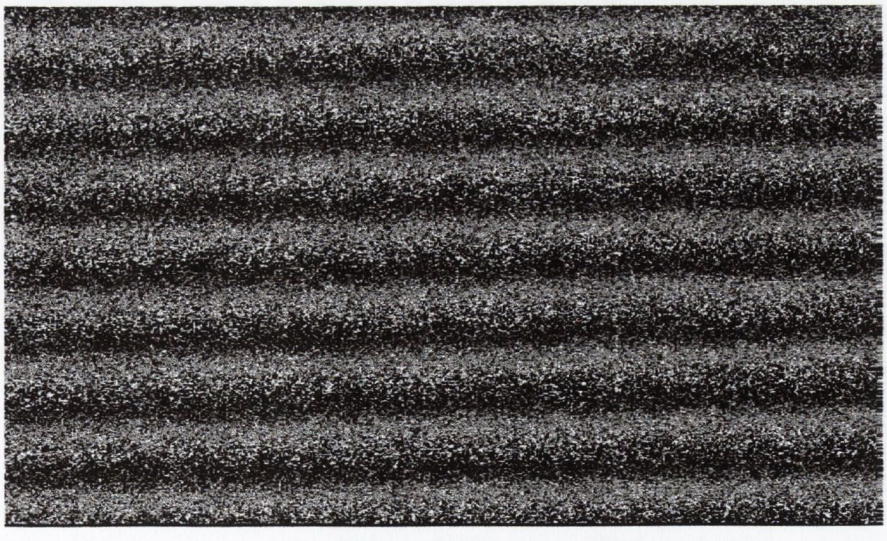

Fig 4.13 Wrapped phase fringes

However, an update rate of 2 Hz is typically achieved with an image size of 768 x

512 using a 266 MHz computer with a PCI frame grabber. Using the same rotating disk with a different displacement, the wrapped phase map shown in Figure 4.13 was obtained. Figure 4.14 shows the wrapped and unwrapped phase images obtained from a three-point bend test of a section of a high-density polyethylene prismatic bar with holes. A region is defined so that the holes are not interpreted as discontinuities in the wrapped phase fringes by the unwrapping algorithm.

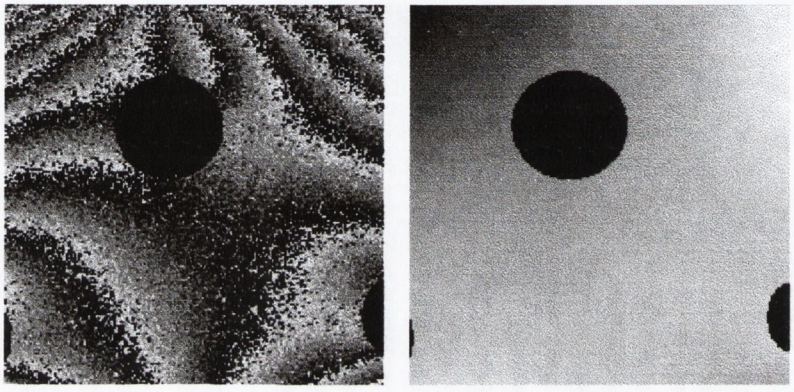

Fig. 4.14 The wrapped and unwrapped phase images obtained from a three-point bend test of a section of a high density polyethylene prismatic bar with holes.

The user also has the option of performing ESPI in a single plane or in both planes. In both planes the software will continuously change the voltage across the liquid crystal switch. As the object is illuminated in each plane, a frame is grabbed and subtracted from the reference frame recorded originally in that plane. The user can observe the two displacement fringe patterns form and change on the computer screen. Therefore, the system can measure the surface displacements of both the x and y components with a delay of a frame between each frame grabbed in each plane. For instance as a frame is grabbed every 40 ms then the y data in Figure 4.15 would have been obtained 40 ms after the x data in the same figure.

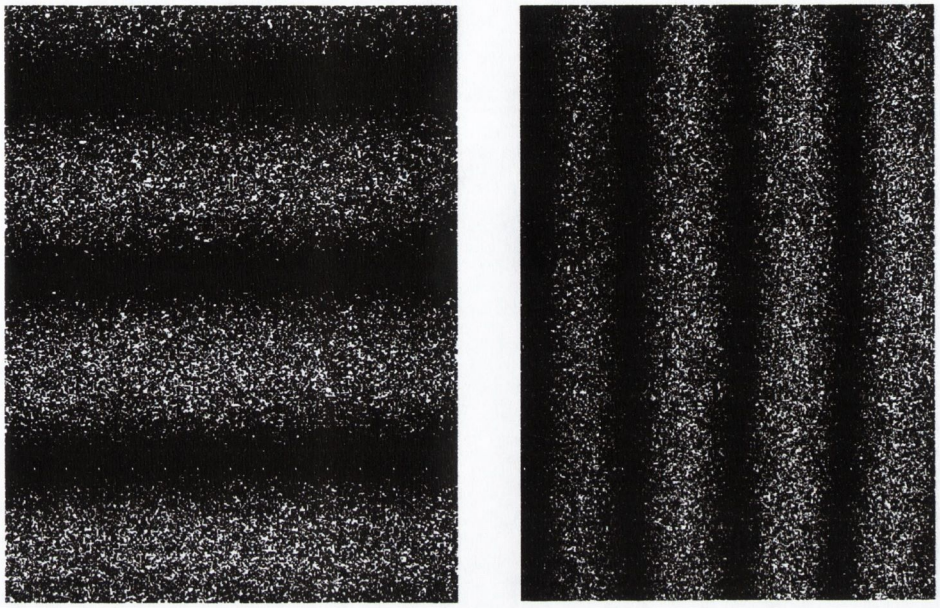

(a) (b)

Fig. .4.15 Displacement fringe in both the x (a) and y (b) direction.

The system was constructed using both Spindler and Hoyer macrobench and microbench, as shown in Figure 4.16A. The dimensions of the system are 50 cm x 50 cm, which is larger than was first anticipated. The reason for the long arms and the use of the bulky macrobench was the need for collimation and the weight of the laser diode (including the Peltier cooler and collimating optics). Illuminating the object with collimated light ensured the phase change sensitivity remained constant across the surface. However to collimate the beams, the relatively large and heavy parabolic off-axis mirrors were needed. These mirrors had to be placed a certain distance away from the expanding lens, defined by their focal length. This meant the interferometer arms had to be quite long. Another disadvantage of using these mirrors was the fixed working distance. If the surface was placed at a different distances the mirrors had to be rotated and the light was no longer collimated. As described in Chapter 2, the error due to not collimating the illumination beams is negligible if the object is viewed and illuminated from a relatively long distance, typically 1 meter. Even if the surface has to be placed very close to the system the error caused by the change in sensitivity across the

field of view can easily be compensated for in the software, so long as the angles of illumination and divergence are known. Therefore it was decided to replace the collimating mirrors with small, 20 x 5 mm, front surface mirrors. These could be placed much closer to the expanding lenses making the system much smaller. It also eliminated the need for the Spindler & Hoyer macrobench. Instead the whole system was now built with microbench.

It was found that during routine testing the 150 mW laser was never operated at its maximum output. In fact it was almost always operated at its lowest output of approximately 50 mW. For this reason it was replaced with a smaller 50 mW laser, which was far more compact and could easily be connected to the system using microbench. Figure 4.16B shows the final system constructed entirely with microbench and having dimensions 25 x 25 cm. Apart from the mirrors and laser the rest of the system is identical to the system shown in Figure 4.16A. However, because this system is smaller and more compact it is much more stable and can easily be attached to loading devices. Using diverging beams for illumination means the measurable surface area and the phase change sensitivity are not limited. The angle of illumination can be easily changed and the working distance easily altered.

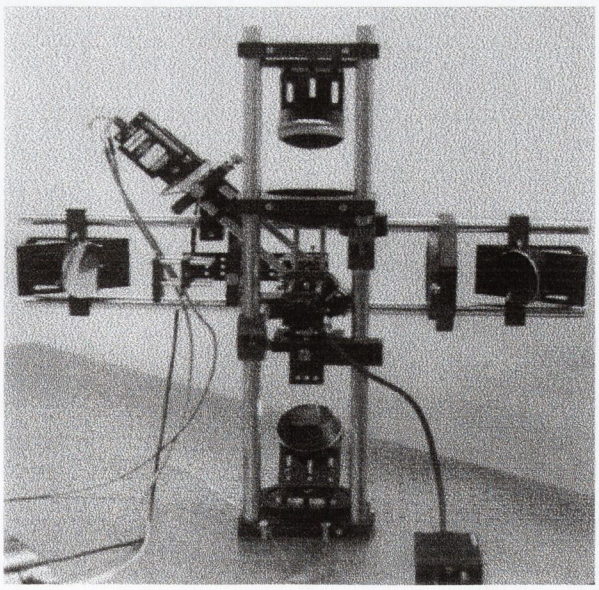

Fig 4.16A First fully automated dual in–plane ESPI system (50 cm by 50 cm).

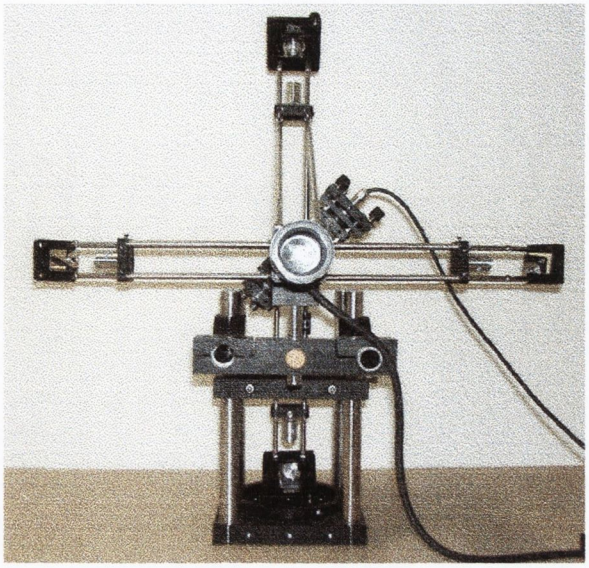

Fig. 4.16B Final fully automated dual in-plane ESPI system (25 cm x 25 cm).

4.2.4 Calibration

To calibrate the system, the angle of illumination was set at approximately 30 degrees, as measured trigonometrically. A flat circular disk was then illuminated and a known area of the disk was imaged onto the CCD camera. The disk was mounted on an Oriel rotation stage that could be rotated in steps of 22.4 arc seconds. When the disk was illuminated in the x-z plane and rotated, the ESPI system measured the surface displacements in the x-direction. Similarly when it was illuminated in the y-z plane the system measured the displacement in the y-direction.

The disk rotates about its central axis making it suitable for calibration of the in-plane displacement. Any rotation causes in-plane displacements that vary across the surface in an easily predictable manner and give rise to simple straight line fringes. As in Figure 4.15, the fringes representing the displacement in the x-direction are horizontal straight line fringes and the vertical fringes represent the displacement in the y-direction.

Figure 4.17 shows a schematic of the rotating disk along with the equations used to calculate the x and y displacements caused by a rotation. When the disk is rotated the ESPI system calculates the in-plane displacements in both the x and y directions across the whole surface. The result is a two-dimensional displacement map where the gray level represents the displacement at each point on the surface.

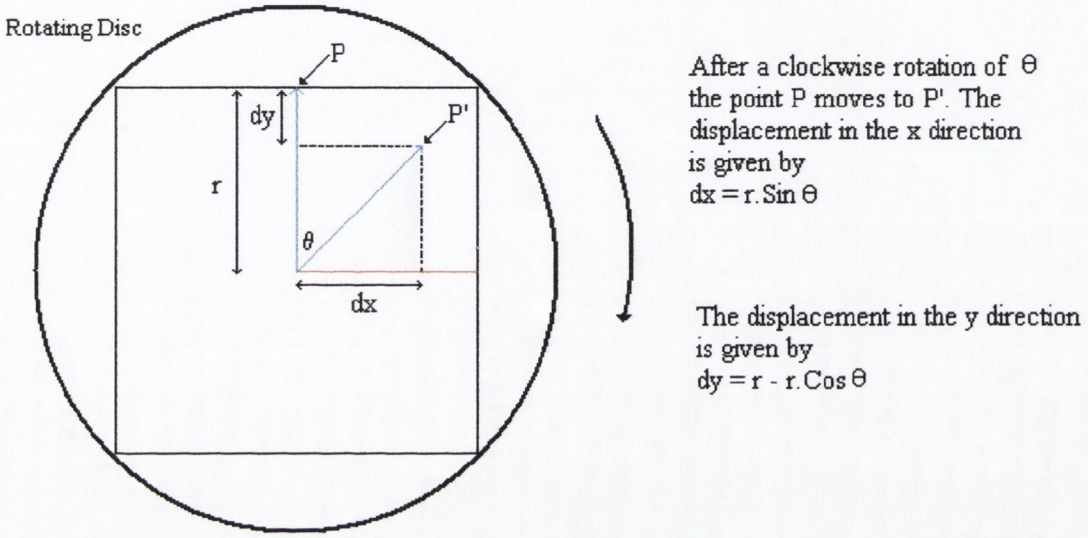

Fig. 4.17 The rotating disk used to calibrate the system.

The displacement in the x direction, as obtained by the ESPI system, was taken at ten equally spaced points along the blue line, shown in Figure 4.17. At these points, the displacements are also calculated using the equations in Figure 4.17. Table 4.1 shows the results of this experiment and the results are graphed in Figure 4.18. It is assumed that the error in calculating the displacement using the equations in Figure 4.17 is very small as the rotation was precisely controlled and the positions along the red and blue lines were accurately measured with a vernier calipers. However, the error in measuring the angle of illumination is significantly greater as this is much more difficult to measure accurately. Therefore, if the error between the displacements as measured by the ESPI system and the equations is calculated it can be used to correct the value for angle of illumination. Table 4.1 shows the displacement data calculated by the ESPI system if the angle is corrected. It was assumed that the illumination angle was set at 30 degrees, but if

an angle of 30.6 degrees is used the percentage error between the new measured values and the calculated value is extremely small. This was repeated for the y displacements and the value for the illumination angle in the y-z plane was also corrected to 29.4 degrees. These results are also shown in Table 4.1. The fringes patterns or phase maps from the system can now be accurately converted to displacement maps using the new angles of illumination.

x – Displacement / μm			X – Displacement / μm		
Calculated From rotation stage readings	ESPI Illumination angle = 30°	Corrected Illumination angle = 30.6°	Calculated From rotation stage readings	ESPI Illumination angle = 30°	Corrected Illumination angle = 29.4°
0	0	0	0	0	0
0.43	0.44	0.43	0.43	0.45	0.44
0.86	0.88	0.87	0.86	0.87	0.86
1.29	1.30	1.28	1.29	1.33	1.31
1.72	1.77	1.74	1.72	1.74	1.71
2.15	2.19	2.16	2.15	2.16	2.13
2.57	2.60	2.55	2.57	2.63	2.57
3.00	3.06	3.00	3.00	3.07	3.00
3.43	3.53	3.46	3.43	3.51	3.45
3.86	3.92	3.85	3.86	3.92	3.85
4.29	4.35	4.27	4.29	4.36	4.48

Table 4.1 Results from calibration of ESPI system

The system was now capable of providing accurate quantitative surface displacement data. It was then used for both qualitative and quantitative measurements. Qualitative measurements were performed to locate defects and cracks. Quantitative measurements provide strain data for the calculation of mechanical properties. The next section describes the overall operation and performance of the system including the software and phase shifting. The results section presents results obtained at different stages of the development.

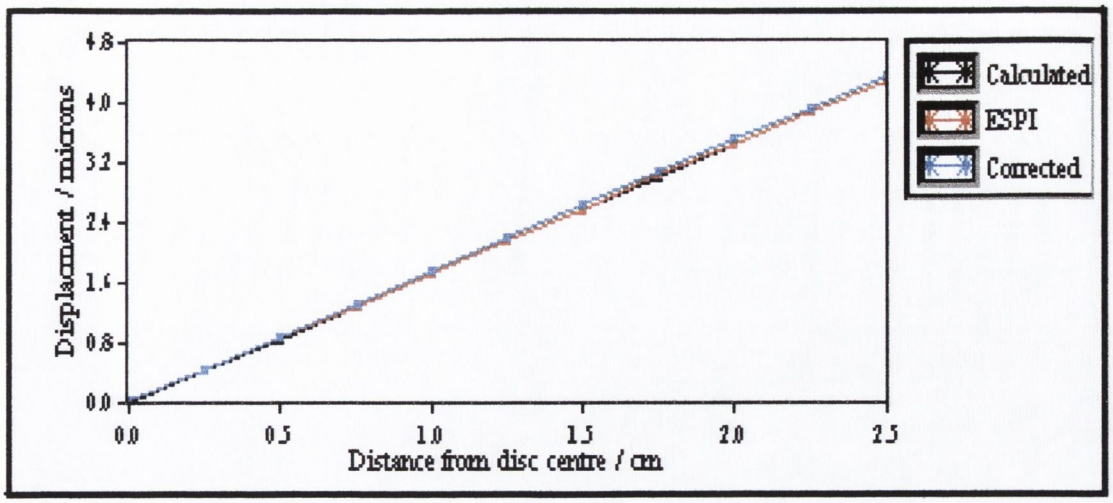

Fig 4.18 Graph of the x displacement as a function of distance from the centre.

4.3 System Operation

4.3.1 Software

The ESPI system is controlled by software called ESPITest, which was specifically designed to control the system described in this chapter. However, ESPITest can be used to control any interferometry system that uses low voltage switching and phase shifting devices, a standard CCD camera and framegrabber. It is a Windows NT based software package for acquisition, measurement, control and post-processing for electronic speckle pattern interferometry. The software was also designed to control the deformation using standard loading machines. As one of the objectives of the research was to develop a system that could be easily adapted into other scientific and industrial areas, the software was designed so that it required very little user input.

The program is made up of smaller sub-programs, each with a particular task. For instance, one sub-program communicates with the frame grabber. The program was designed this way so that different frame grabbers could be incorporated into the software later by just re-writing certain sub-programs or drivers. When the software package is started, two property windows and a toolbar appear in the

main application window, as in Figure 4.19. The toolbar contains the icons for opening and saving graphics files along with tools for activating the property windows. The uppermost property window, "Calibration & Settings", shown in Figure 4.19, contains all the controls necessary for the calibration and settings of the various measurement devices, including the frame grabber and the analog output board used to control the optical switch and the phase shifters. From this property window it is also possible to set the size of the acquired image and to use median filters. The other window, called the "Video Acquisition" window, contains the controls for image acquisition, ESPI subtraction, wrapped phase map calculation and displaying the results.

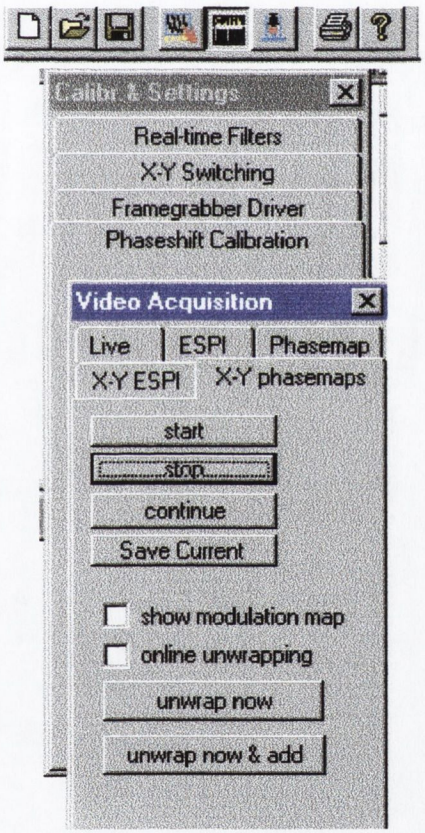

Fig 4.19 The two property windows and the toolbar used in the ESPITest software to control the ESPI system.

A Data Translation framegrabber board is used to acquire and digitise the analog signals from the CCD camera. The software acquires the digitised images and performs the subtraction and rectification and displays the fringe pattern on the computer monitor. When the phase shifting devices are incorporated into the

system, the software uses the phase shifting algorithm, described in Chapter 2, to calculate the wrapped phase maps. It then uses an unwrapping algorithm to unwrap this data and convert it to displacement data. At any stage, the images can be saved in bitmap format or filters can be applied to increase the fringe contrast or image brightness.

A National Instruments D/A board is used to control both the phase shifters and the polarisation switch. Using the Calibration & Settings property window the user inputs the two values for the operating voltages of the polarisation switch. The user can also input the calibration data of the phase shifters. However, the software can calibrate the devices if needed. In this case, the two phase shifting devices must be calibrated separately and when the system is fully operational. This is done initially when an image of the surface, illuminated in one plane by the two symmetrical beams, is being acquired.

A triangular waveform is then applied to the phase shifting device so that the path difference between the beams is changed. Each pixel in the image will modulate in a sinusoidal way as the phase changes between the illuminating beams. The software records the intensities of 16 pixels in the image and plots the intensities as a function of the applied voltage. If the device has a linear response the plotted intensities should have a sinusoidal shape, as in Figure 4.20. A sin wave is fit to the data so that the voltage corresponding to a phase change of 2π can be obtained. Once this voltage has been determined, it is simply divided by four to calculate the voltage required to change the phase by $\pi/4$. This process assumes a linear response and so it is limited to certain phase shifting devices.

It can be clearly seen in Figure 4.20 that only some of the pixels will modulate in the predicted manner. As the image as inherently noisy, the program ignores the four worst fit data plots. It then weights the other 12 according to how closely each signal resembles a sine wave. Figure 4.20 shows the calibration curves obtained when the image is illuminated in the x-z plane. The voltage corresponding to 2π, as calculated by the software is displayed on the right, along with other parameters the user can set. If the user does not agree with the

calculated voltage the green and red vertical cursors can be used to select a new voltage. Figure 4.21 shows the calibration obtained in the y-z plane.

Before the system is ready to be used other important parameters must be set. The speeds of the phase shifters and polarisation rotator are limited by their response times. So long as these are known the user can set appropriate delays or acquisition rates. For instance if the rotator has a maximum switching rate of 2 Hz, then this is the maximum rate at which the x and y data can be acquired.

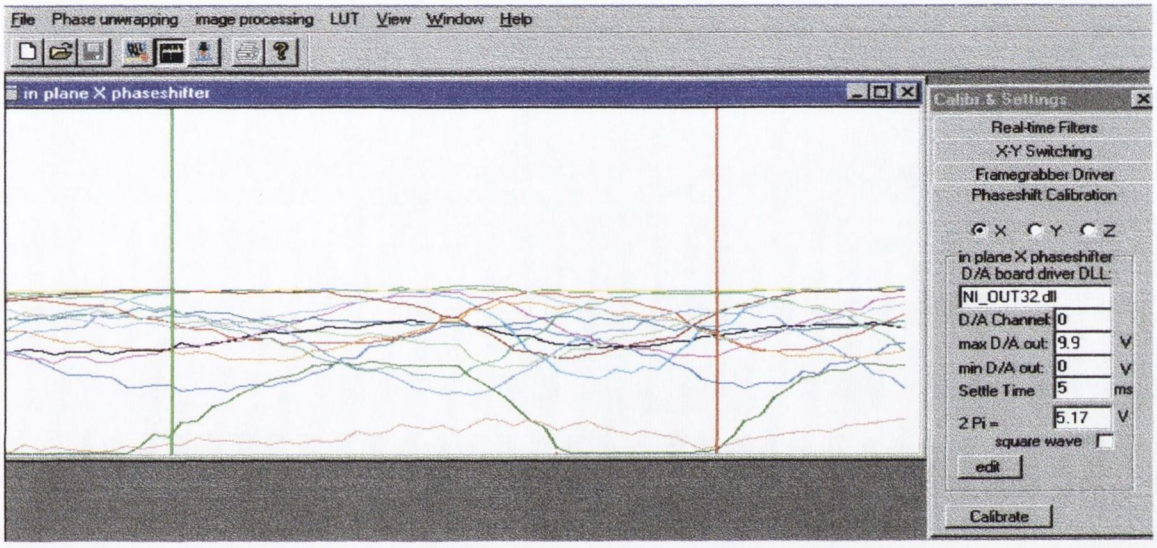

Fig. 4.20 The calibration curves of the phase shifter in the x-z plane.

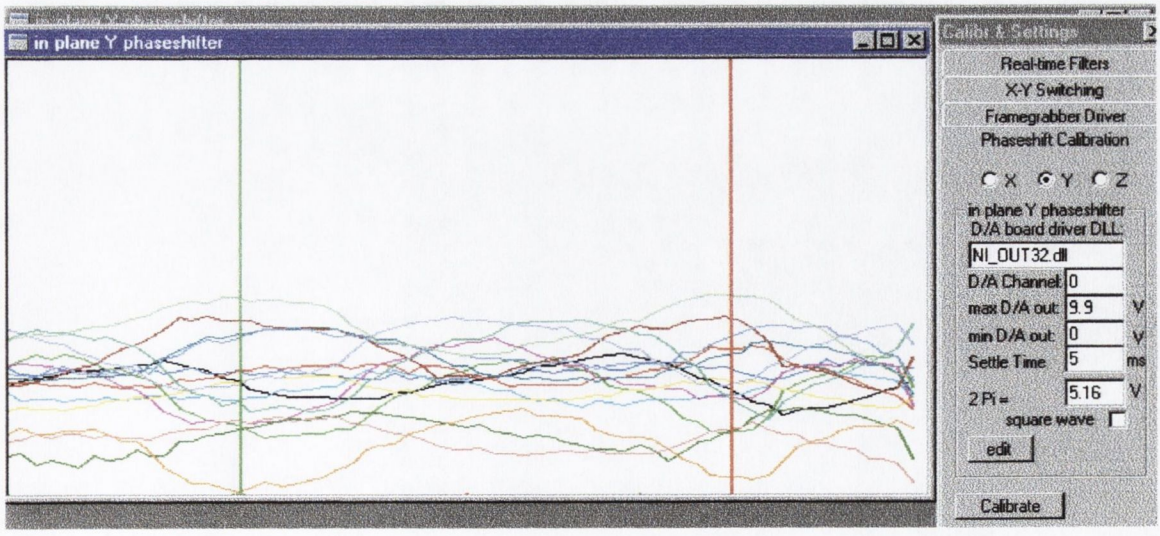

Fig. 4.21 The calibration curves of the phase shifter in the y-z plane.

The system is now ready and can be operated in a number of modes. The first choice the user has is to acquire either displacement fringes or wrapped phase maps. If qualitative tests are to be performed, for instance for crack or defect detection, then it is only necessary to observe the displacement fringes. In this case, the software does not control the phase shifters and only performs the subtraction and rectification. It is sometimes only necessary to measure the displacement in one direction, for example when the strain in one direction only is required. The user has three choices; illuminate in the x-z plane and measure the displacement in the x-direction; illuminate in the y-z plane and measure the displacement in the y-direction; or switching between the two planes. If only one plane is used, the software applies the appropriate voltage to the polarisation rotator and if two planes are needed, it switches between the two. It is possible to view displacement fringes in real-time (25 Hz). However the acquisition time is greatly increased if the wrapped phase maps are calculated.

When quantitative data are necessary, the software takes four images, in each illumination plane, as it shifts the phase by 0, $\pi/2$, π and $3\pi/2$. It uses these images to work out the subsequent phase change caused by a deformation of the object and displays the data as wrapped phase fringes. It can take up to 0.5 seconds to calculate the wrapped phase in a 512 x 512 image. However the computer then unwraps these fringes to produce a high resolution phase map that may be analysed to display the displacement map. As the software is Windows based it is possible to open multiple windows, for example to observe the fringe patterns corresponding to both the x and y displacements. Figure 4.22 shows the ESPITest window displaying the wrapped phase fringes of both the x and y sensitivities, the calibration data of the phase shifter in the x-z plane and the live image.

4.3.2 Summary of System Operation

The system described in this chapter is a reliable, robust and portable dual in-plane ESPI system. The stability requirements for this system are the same as they are for all typical ESPI systems that are measuring displacement of a fraction of the wavelength. However, the sources of instability have been reduced in this

system. It has no moving parts as it uses liquid crystal devices for both switching between illumination planes and phase-shifting. Initial work showed that the devices had proven to be both efficient and effective, but extensive quantitative tests of the switching speeds, reliability and repeatability are described in Chapter 6.

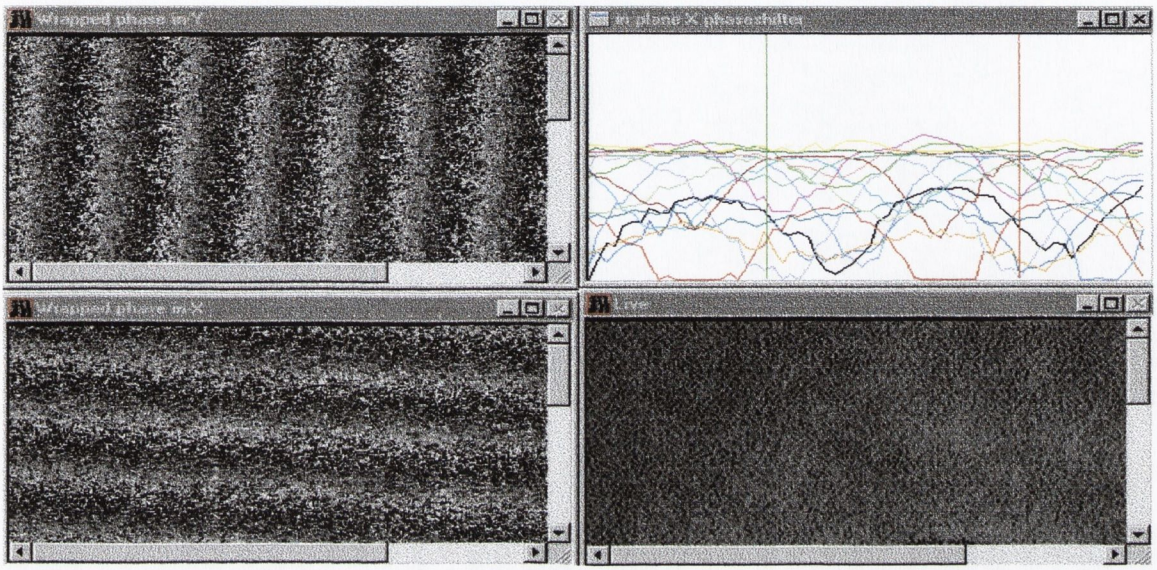

Fig 4.22 The ESPITest window showing the phase maps of the x and y displacements, the calibration data of the phase shifter in the x-z plane and the live image.

The strong structural support means the system is mechanically stable. The ESPI system is controlled by advanced software which performs all the analysis and calibration of the phase-shifting devices. The system, controlled by this software, has proved to be very reliable in the tests carried out to date. When measuring time dependent loads, the dual in-plane ESPI systems, which measure both the x and y plane components simultaneously, have a distinct advantage. However, these systems require either two cameras or two lasers. Also, unless parallel processing is used the wrapped phase maps will have to be calculated sequentially. There is a loss of data with this system in each plane when data is being recorded in the other plane. However with the fast switching speed, this loss is minimal. Also in any ESPI system which uses phase-shifting algorithms, the speed of the data acquisition is limited by the time needed to calculate the wrapped phase maps. As described in Chapter 6, the liquid crystal devices are also under continual development to improve their performance further.

4.4 Measurement of Crack Propagation in Clay Components

4.4.1 Crack mechanics

Unexpected failure of building materials has occurred throughout the structural engineering world. A number of these failures have been due to poor design. However, pre-existing flaws in materials can initiate cracks that grow and lead to fracture, which causes many failures. The field of study known as fracture mechanics deals with the factors that cause these defects and the effect they have on the mechanical properties of the material. Fracture mechanics is extremely broad, including applications in engineering, studies in applied mechanics, including elasticity and plasticity, and materials science, including fracture processes, fracture criteria and crack propagation [24].

Fracture is concerned with the initiation and propagation of a crack, or cracks, in the material until the extent of cracking is such that the component or structure can no longer sustain the applied load. It is generally accepted that initiation of a crack is relatively difficult to guard against in the design phase and, in fact, most components or structures will contain some crack-like flaws by the time manufacturing is completed in spite of rigorous inspection procedures. It is therefore necessary to design for non-propagation or, at worst, controlled propagation [16].

By examination of the damaged zone surrounding a crack propagating through a specimen, it is possible to obtain information about the mechanical characteristics of the material [136]. In the last few years, more and more attention has been devoted to improving the knowledge of mechanical characteristics of the clay components used in manufacturing beam-block concrete floors, used in civil constructions. In particular, attention has been paid to the determination of fracture energy and the stress-strain relationships that influence the ductility characteristics of clay materials. As regards fracture energy, it is necessary to evaluate the dimensions of the fracture process zone during crack propagation

[137] and to establish as accurately as possible both the critical crack-opening displacements and the strain map surrounding the propagating crack.

While classical laboratory tests, like the use of strain gauges in the three-point bend test, allow only the determination of the mean value of the fracture energy [24], optical methods make it possible to map the strain field around the crack [138]. Consequently, it is possible to measure with sufficient accuracy, the damage surrounding the crack propagation zone and critical crack opening at the crack mouth. In this way, the local value for the fracture energy, that is the energy required to propagate the crack tip can be obtained.

As stated previously, the ESPI technique has high sensitivity and allows a full-field analysis of the inspected area without any need for physical contact with the surface. ESPI can sometimes provide more or different information where other techniques fail or cannot be applied. As described in this section, ESPI has been used successfully to measure the deformations surrounding cracks propagating through clay specimens. The aim of the test was the characterisation of clay materials obtained from blocks used to manufacture composite floors.

The method involves inducing an excitation force, in this case a mechanical pressure, using a three-point bending test to create measurable deformation displacements on the surface of the object. As mentioned in Chapter 2, the fringe patterns obtained by ESPI are graphically descriptive of the qualitative behaviour of the surface under evaluation. The spacing of the fringes is inversely proportional to the displacement and the fringes are aligned perpendicularly to the direction of the displacement. Therefore full-field strain distributions can be derived, and crack formation and propagation in structures can be easily observed. This definitely makes ESPI a suitable technique for the characterisation of these clay materials.

As the ESPI system at this stage did not incorporate any mechanism for phase shifting the fringe patterns were qualitative and quantitative interpretation was done manually. However, with high-speed computers, the fringes can be quickly

processed using semi-automatic fringe analysis. This section presents the results of the tests carried out at the Structural Engineering Department of the Politecnico di Torino (Italy).

4.4.2 Experimental Technique

The pre-notched specimens were examined for the purpose of determining the displacement map and deformations surrounding the propagating crack. The ESPI technique was applied to three notched specimens with notch depths of 0.1h, 0.3h, 0.5h, where h is the height of the samples, see Figure 4.23. The pre-notched specimens were tested in crack mouth opening displacement (CMOD) controlled condition [139], by the three point bending method, based on the same principles suggested by RILEM recommendation for concrete specimens [140].

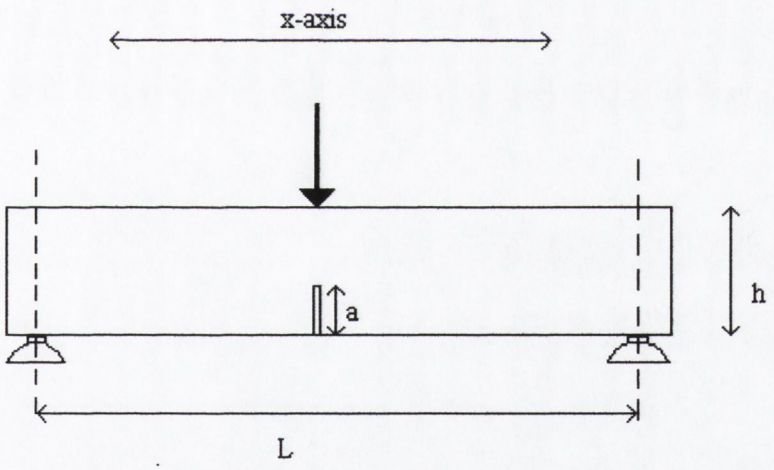

Fig. 4.23 Three point bending set-up and geometry of the pre-notched specimens.

The vertical displacements of the specimen were measured by means of three pairs of displacement transducers with 1 mm of maximum measuring range. As the damaged zone produced by the crack propagation was restricted to a small part surrounding the middle region of the specimen, the CCD camera was imaged on an area of 60 mm^2 around the specimen's midpoint.

The specimens had a length L = 230 mm, a height h = 40 mm and thickness s of 8 mm. The three notch lengths, a, were consequently equal to 4, 12, and 20 mm, respectively.

As stated at the beginning of this chapter the system taken to Torino proved to be too unstable to reliably measure the horizontal displacement. An alternative system, shown in Figure 4.24A was built on site, which worked very well and produced high quality fringe patterns. To reduce the mechanical noise the new system was designed to be sensitive only to horizontal in-plane displacements, which eliminated the need for the railings. The mirrors were instead mounted to the small optical table, which was attached to the loading device. The rest of the equipment was also secured to this table making the system smaller and more robust.

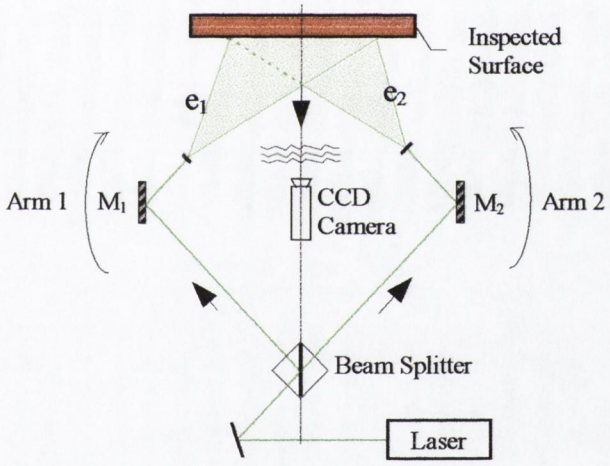

Fig. 4.24A ESPI optical setup used for the experiment.

The system could also be placed much closer to the surface, thereby increasing the angle between the illuminating beams and the surface normal and thus increasing the sensitivity of the system. The illumination angle was approximately 26 degrees, so consecutive bright or dark fringes correspond to a real in-plane displacement of 594 nm.

Figure 4.24B shows a photograph of the optical and mechanical systems with the illumination beams shown as the green dotted lines. The red lines are the points of contact in the three point bend test. The loading device exerts a downward force at the reference point, shown by the yellow arrow.

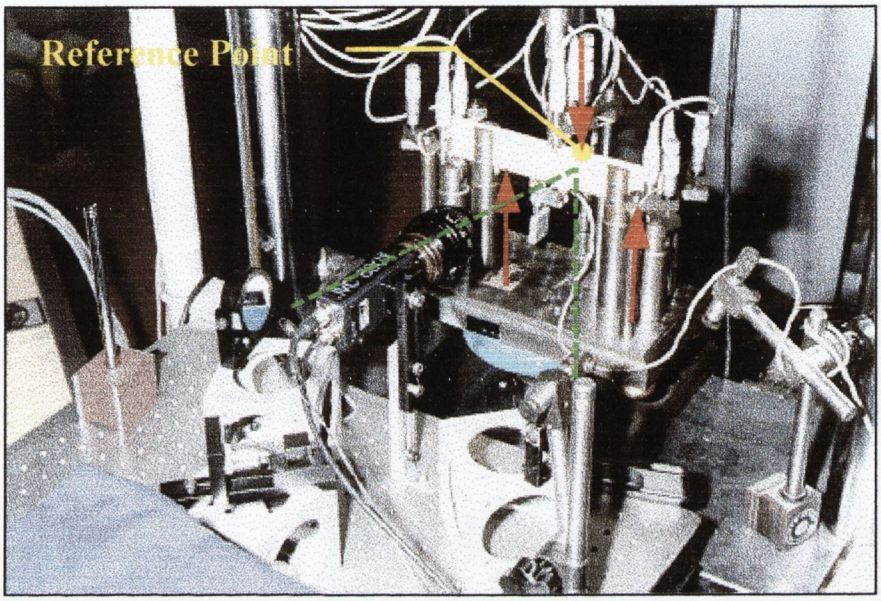

Fig. 4.24B The loading device, the three-point bending test and the installed ESPI system.

The speckle patterns were imaged by the CCD camera and the image was then sent to the frame grabber on-board the computer. A reference frame was grabbed before any deformation of the object. During deformation, frames were continuously grabbed and subtracted from the reference frame and the fringes were displayed on the monitor. In this way it was possible to watch the fringes form and change. There was no mechanism in the system to allow for phase shifting and only qualitative results could be obtained from this system.

As the deformations in the specimen continued, the visibility of the fringes decreased, as the number of fringes became too great. For this reason, when the number of fringes was too high, an updating of the reference image was necessary. Each test took about 20 to 30 minutes so in order to record the entire fringe formation and movement, each test was recorded using a video recorder. This meant that the fringes could be analysed after the tests were complete. For all specimens the maps of the horizontal in-plane displacements were obtained.

4.4.3 Fringe Patterns

The in-plane displacements can be predicted and hence the expected fringe patterns. The green arrows in Figure 4.25 show the displacements. Each resulting in-plane displacement can be decomposed into its horizontal and vertical components. The diagram on the right shows the predicted horizontal components of in-plane displacement at various locations on the surface.

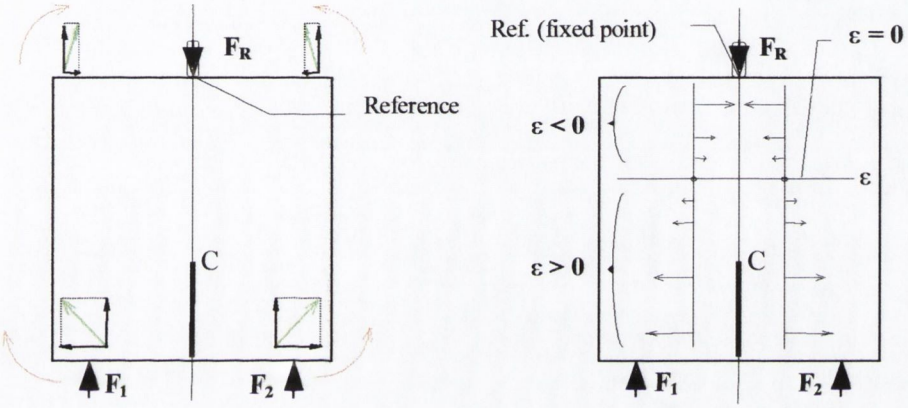

Fig. 4.25 Forces (F_1, F_2, F_R) on the E_03 sample and the resulting horizontal in-plane displacements.

It can be seen from the figure that the strain (ε) map will contain three different zones of positive, zero, negative strain. The forces F_1, F_2 and F_R separate both sides of the notch, widening the notch mouth. After a few minutes a crack appears at the tip of the notch C, called the junction point. The fringe pattern can be inferred, taking into account that the ESPI system was only measuring the horizontal component, as shown in Figure 4.26A. This is confirmed by the measured fringe pattern shown in Fig. 4.26B. The crack propagates upwards as the loading continues, until the sample completely breaks. As shown in Figure 4.26A, right in the middle, between the crack tip, C, and the reference point, a zero horizontal strain zone moves along with the crack.

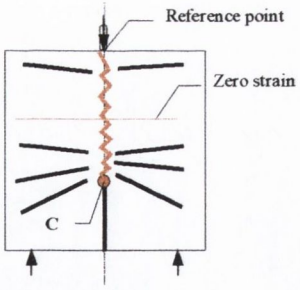

Fig.4.26A Supposed fringe pattern.

Fig. 4.26B Measured fringe pattern.

Keeping in mind that there is a 594 nm displacement between successive fringes (bright or dark), it is possible by calculating the total number of fringes produced during a measurement session, to evaluate the total horizontal in-plane displacement at each point on the sample surface. Figures 4.27, 4.28 and 4.29 show three fringe patterns obtained at different stages of the loading from the clay samples with the 4 mm, 12 mm and 20 mm notch respectively. The crack tip is seen in the patterns as the point towards which the fringes converge. In the first pattern on the left the crack has only begun to grow and it travels up along the specimen as shown in the second pattern. The third pattern shown in each figure was taken just before the specimen completely broke. The fringe analysis procedure and the results are presented in the next section.

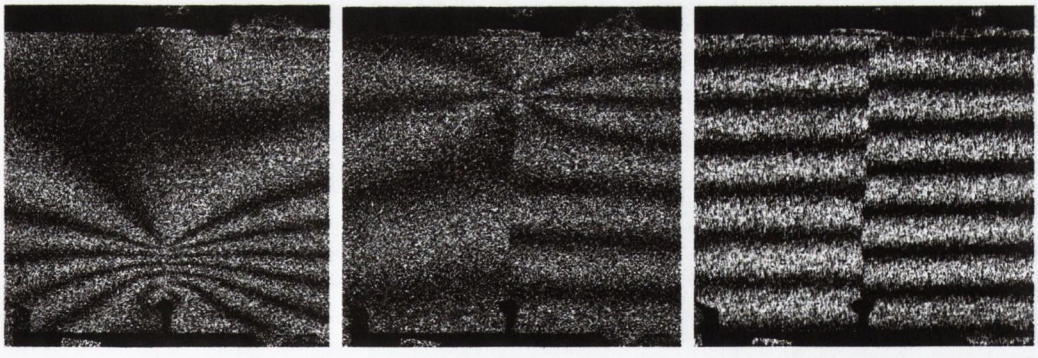

Fig. 4.27 Propagation of the crack in the 4 mm notch sample.

Fig. 4.28 Propagation of the crack in the 12 mm notch sample.

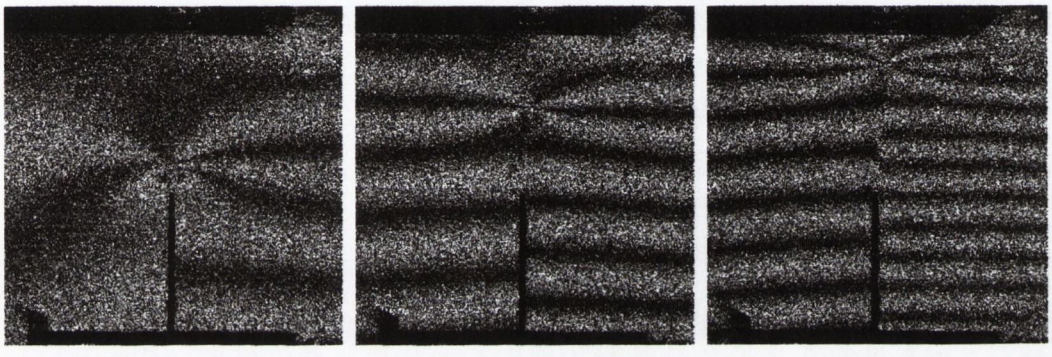

Fig. 4.29 Propagation of the crack in the 20 mm notch sample.

4.4.3 Data Analysis

4.4.3.1 Overview of Data Acquisition

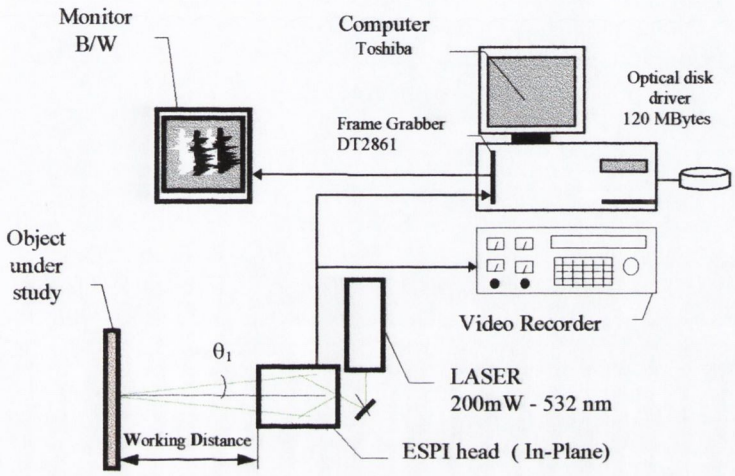

Fig. 4.30 General measurement configuration.

Figure 4.30 shows the general setup of the data acquisition and storage. During the measurements, the interferograms produced by the ESPI system are continuously recorded on a video recorder. As already mentioned in section 4.4.2, an updating of the reference image was performed when the fringe contrast degraded or when the number of fringes was too high. Before each update, the current interferograms were digitised by the frame grabber and saved in 512 x 512 pixels bitmap format on the local optical disk of the PC. A typical experiment that took about 30 minutes produced approximately 15 updates. Figure 4.31 shows a photograph of all the acquisition and storage equipment as well as the loading device.

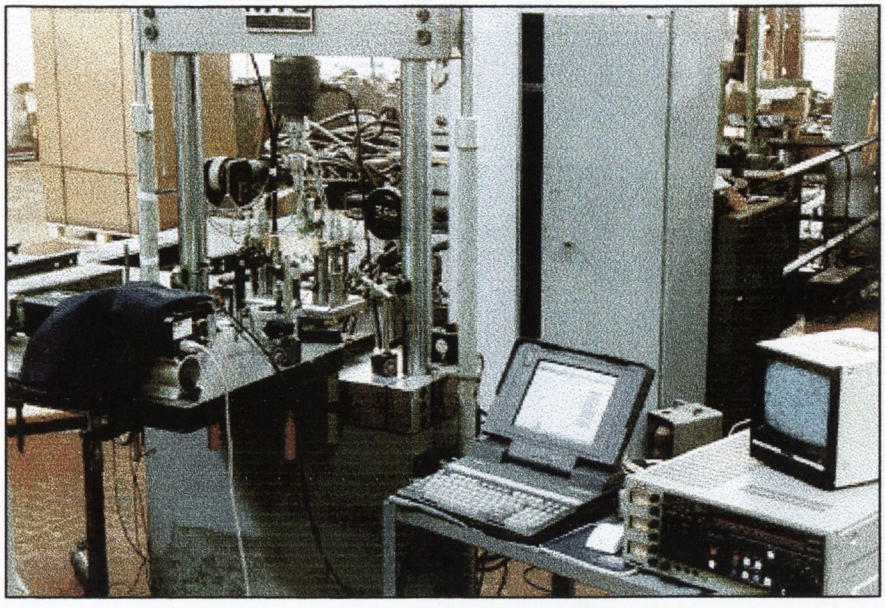

Fig. 4.31 General overview.

To calculate the total horizontal in-plane displacement, it is necessary to sum all the accumulated fringes throughout the whole experiment from crack initiation right up to when the sample breaks. The fringe counting was manually carried out by superimposing a transparent grid onto the fringe pattern. This is explained in the next section. The sum of the accumulated fringes was then graphed, to show the strain maps and the final two-dimensional horizontal displacement maps.

4.4.3.2 Grid

Inherent in the digitisation process is a geometric deformation in which the interferogram (monitor) vertical and horizontal distances are proportional to the real measured object dimensions. Geometric correction is then an important step in the fringe analysis process.

The fringe summation process uses a grid and the image of a square object grabbed with the CCD camera is a rectangle. For the square object, the real geometric ratio between equals 1/1, while the displayed geometric ratio shows a height equal to 3/2 times the width. This is important when placing a grid over the interferograms, especially if the grid is superposed over the monitor or a hardcopy of the fringe pattern. In these tests a hardcopy of the 15 (approximately) fringe

patterns, taken before a new reference was grabbed, were printed. A transparent grid was placed over these patterns so that the displacements at particular points on the surface could be calculated.

The manufacturers of the clay components were interested in selected positions lying on a grid spacing of 5 mm along the clay sample height and a grid spacing of 5, 10, 20, 40 mm symmetrically aligned on either side of the notch. As only 30 mm, either side of the notch, of the clay sample width was imaged, only the first three aligned points are visible as sketched in Figure 4.32.

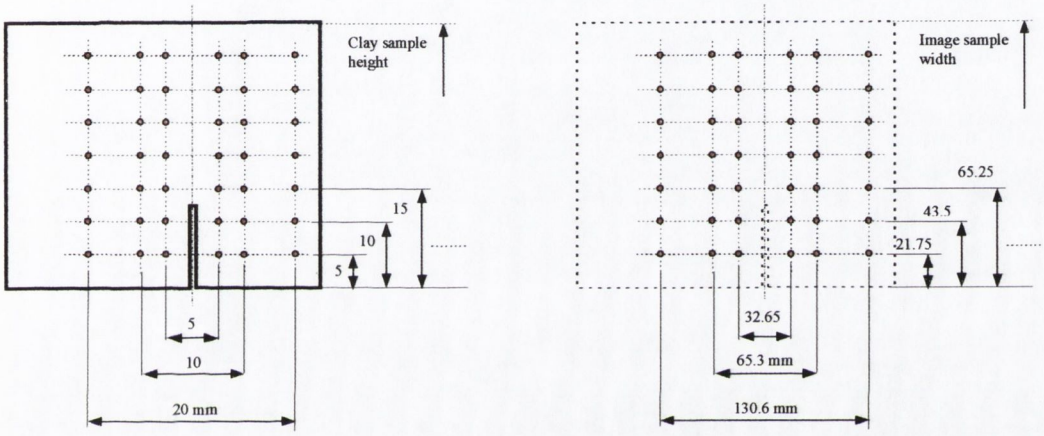

Fig. 4.32 Clay component dimension (left) and Grid dimensions (right).

4.4.3.3 Fringe Summation Process

Figure 4.33 shows the interferogram with the superimposed grid. Using the red points the summation of the fringes can easily be performed, starting from the red bar. The fringes are counted counter clock wise to the corresponding point on the other side of the notch. They are counted around the crack tip and fringes in the negative strain area are not considered. The number of fringes represents the distance between the two corresponding points, namely the horizontal component of the crack mouth opening. Table 4.2 shows the number of fringes between the positions shown on the interferogram.

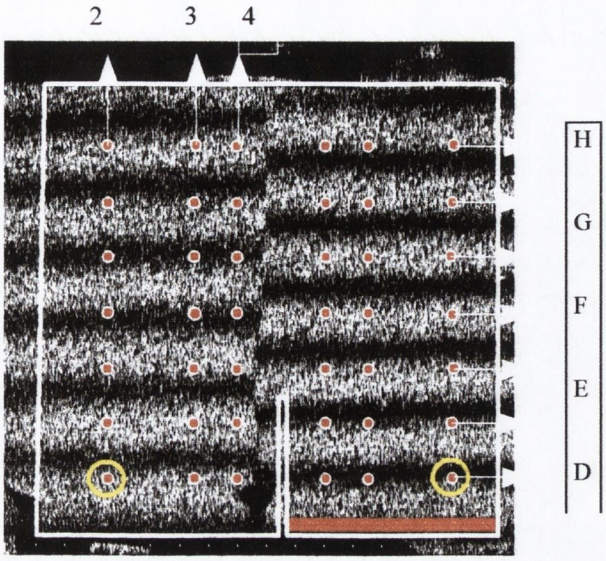

Fig.4.33 Interferogram sample superimposed by a grid.

#	B	C	D	E	F	G	H
2	12	10.25	8.75	6.75	5.25	3.25	1.75
3	12.25	10.5	9	7	5.5	3.5	1.75
4	12.25	10.5	9	7	5.5	3.5	2

Table 4.2 The fringe number between the points of interest on the sample.

Note that in the negative strain zone, a negative sign must be used with the values. Furthermore, the crack is propagating from the bottom to the top of the interferogram and so progressively repels the negative strain zone to the top until the sample fully breaks. The fringe numbers from each interferogram are recorded in sub-tables (about 15 per sample), and are then added to one another yielding the total fringe numbers reflecting the in-plane horizontal displacement component, as shown in Table 4.3.

	B	C	D	E	F	G	H
2	175.85	150.1	125.3	99.55	73.25	47.05	19.95
3	177.75	151.5	125.9	100.35	74.2	47.6	19.95

4	178.75	152.2	126.8	101.15	74.9	49.05	19.6

Table 4.3 Total fringe count for the 4 mm notch clay sample.

From Table 4.3, 175.85 fringes appeared in the spatial distance between the point B2 and its symmetrical counterpart (yellow circles in Figure 4.33) on the other side of the notch axis. From the total fringe number it is possible to calculate the displacement that occurred between those points in the surface. This provides the horizontal in-plane displacement around the crack mouth.

4.4.3.4 Total Horizontal In-Plane Displacement

Each successive bright or dark fringe corresponds to a real in-plane displacement of 594 nm. Table 4.4 shows the total horizontal component of displacement, expressed in μm, for the clay sample with the 4 mm notch.

μm	B	C	D	E	F	G	H
2	104.45	89.16	74.43	59.13	43.51	28.21	11.85
3	105.58	89.99	74.78	59.61	44.07	28.27	11.85
4	106.18	90.41	75.32	60.08	44.49	29.14	11.64

Table 4.5 The total horizontal in-plane displacement, in μm, for the 4 mm notch clay sample.

The same method was applied to the other two clay samples with the 12 mm and 20 mm notches.. Table 4.5 and 4.6 show their respective total horizontal in-plane displacements.

μm	B	C	D	E	F	G	H
2	98.8	83.6	70.4	55.2	39.5	25.4	10.2
3	99.3	84.1	70.9	55.1	38.7	24.7	10.2
4	99.6	84.2	71.2	55.5	39.0	24.9	10.2

Table 4.5 The total horizontal in-plane displacement, in μm, for the 12 mm notch clay sample

μm	B	C	D	E	F	G	H
2	103.5	87.7	73.4	58.2	43.5	29.1	12.7
3	103.5	87.4	73.1	58.1	43.7	29.0	12.8
4	103.5	87.4	73.1	58.9	44.7	29.4	11.9

Table 4.6 The total horizontal in-plane displacement, in μm, for the 20 mm notch clay sample

In the next section, together with the data taken from the mechanical transducers of the loading device, the displacement versus load diagrams are computed and plotted to extract useful information about the mechanical characteristics of the clay samples.

4.4.3.5 The Fracture

In beam-block concrete floors used in civil constructions both concrete and clay blocks can contribute to the strength of the whole structure. In addition, both components should guarantee a sufficient elasticity to be considered collaborating in the structural behaviour of the floor. Clay blocks usually show a higher compressive strength and a lower ultimate elongation compared to those shown by concrete blocks [140].

As regards fracture energy and its possible dependence on the structure size and the testing method, it is necessary to evaluate the dimension of the fracture process zone, shown in Figure 4.34, during crack propagation. It is also necessary to establish as accurately as possible both the critical crack-opening displacements and the strain map surrounding the propagating crack.

As shown in the last section, the ESPI technique makes it possible to map the strain field around the crack, and consequently to measure, with sufficient

accuracy, the displacement surrounding the crack propagation zone and the critical crack opening at the crack mouth. In this way the local value for the fracture energy, i.e. the energy required to propagate the crack tip over a unit length, can be obtained.

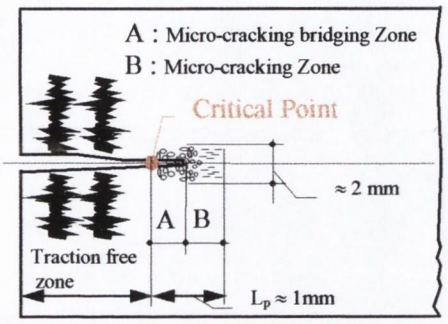

Fig. 4.34 Fracture process zone.

The results obtained by the application of the ESPI technique (Tables 4.3, 4.4, 4.5) can be exploited for determining the crack mouth opening displacement (CMOD) and the displacement and deformation fields in the crack propagation zone. Even though clay material is characterised by very limited strains at initial crack propagation, the high sensitivity of the ESPI system led to some interesting results that allowed quantitative analysis of the cracking phenomenon.

The purpose of the experimental programme, in progress at the Department of Structural Engineering of the Politecnico di Torino, was the characterisation of various clay mixtures used to manufacture blocks employed in composite floor structures (beam-block floor systems) and, in particular, the determination of their fracture energy.

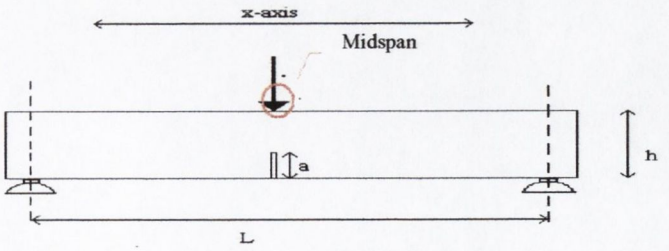

Fig. 4.35 The midspan point of the clay sample in the three-point bend test.

Figure 4.35 shows the midspan point of a clay sample in the three-point bend test. Using mechanical displacement transducers the vertical displacements were measured at this point. Figures 4.36 A, B and C show the three load-deflection curves recorded at midspan of the 4 mm, 12 mm, and 20 mm notch clay samples respectively. On onset of the cracking process, the three point bending device automatically starts the unload procedure.

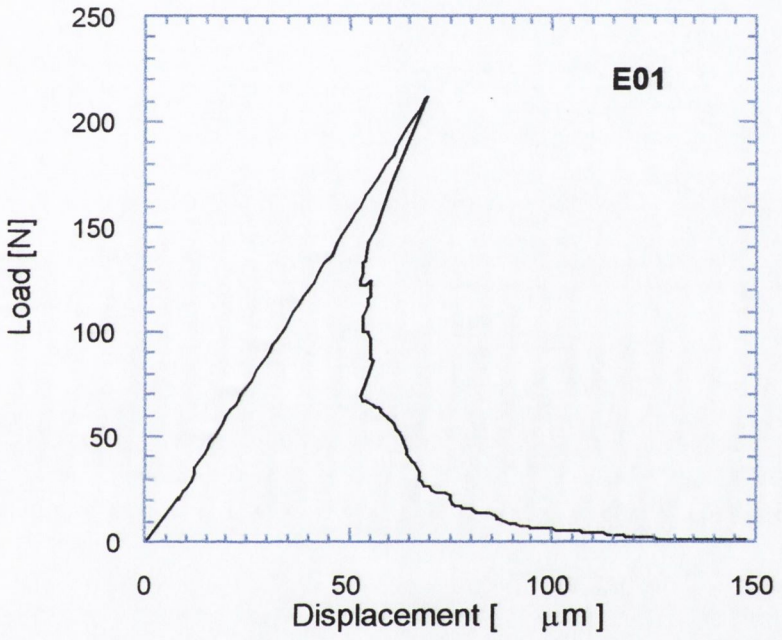

Fig. 4.36A Load-midspan deflection of the specimen with the 4 mm notch.

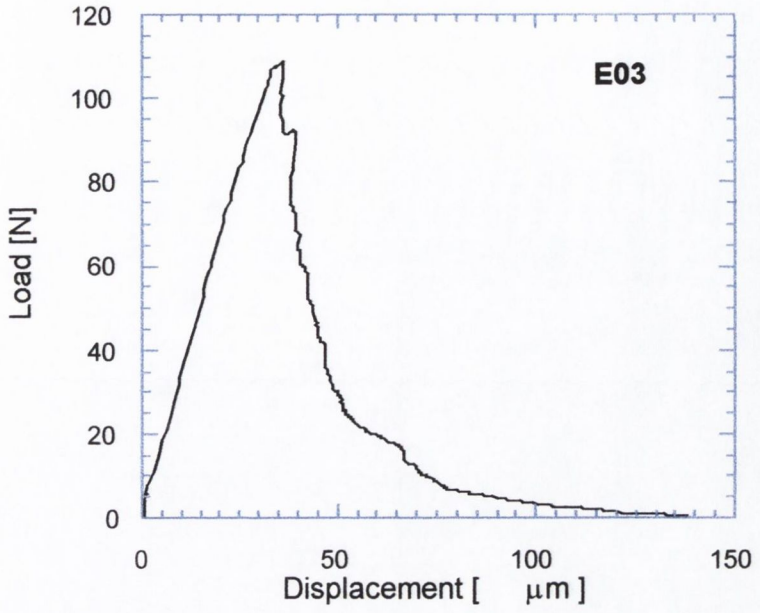

Fig. 4.36B : Load-midspan deflection of the specimen with the 12 mm notch.

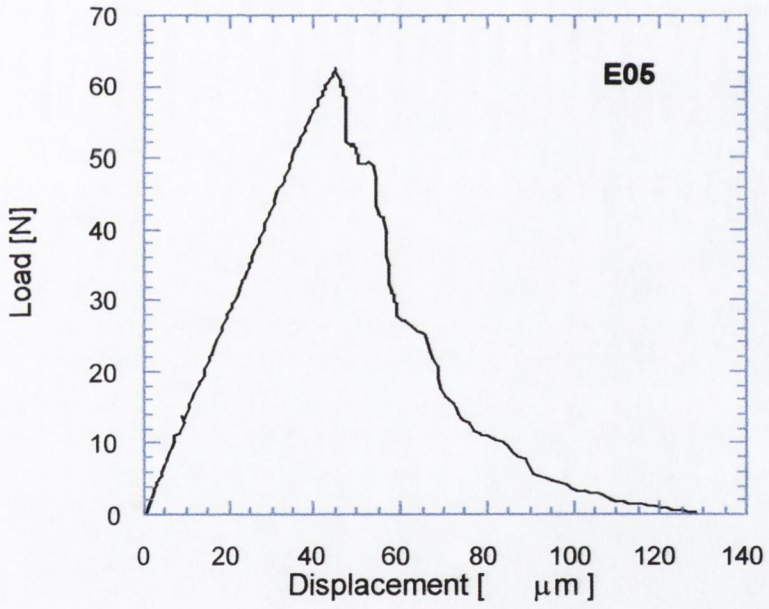

Fig. 4.36C : Load-midspan deflection of the specimen with the 20 mm notch

4.4.3.6 Mean Strains

As shown previously, the calculations of the relative horizontal displacements and mean strains were performed with reference to a grid of points located on the intersections of four vertical lines, and seven horizontal lines (level B, C, D, E, F,

G, H) spaced 5 mm apart. The four vertical lines (lines 1, 2, 3, 4) were spaced 40, 20, 10 and 5 mm respectively, symmetrically about the notch for all specimens.

In Figure 4.37 the load versus time curve is plotted for the specimen with the 20 mm notch. In the same figure the three mean strain versus time curves taken from Table 4.5, for the three lengths, D2 = 20 mm, D3 = 10 mm, D4 = 5 mm, at level D (approximately at notch tip level) are also plotted.

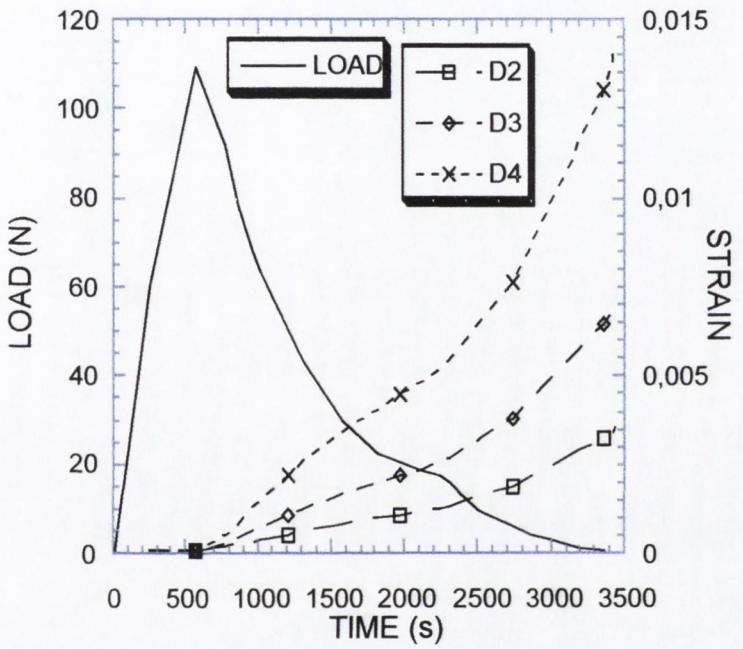

Fig. 4.37 Load versus time curve and mean strain versus time curves on three lengths at level D. (D2=20 mm; D3=10 mm; D4=5 mm).

From this figure, it is clear that :

a) The mean strain changes considerably for each length and, as expected, the maximum value occurred for the point nearest the notch (5-mm). It is worth noting that the maximum calculated change in length Δl ($\Delta l = \varepsilon l$, where ε is the strain) is approximately the same for the lengths and sufficiently small for considering the two sides of the propagating crack to be already traction free. This means that the strain localisation occurs close to the crack and that the damage is not extensive around it.

b) The slopes of the strain curves show an abrupt increase (particularly visible for the curves D3 and D4) located approximately at the same time as the peak load. This reveals the coalescence of micro-cracks into major cracks at the onset of crack propagation in the notch tip region and a consequent local decrease in flexural stiffness.

In Figure 4.38, also for the specimen with the 20 mm notch, the load versus time curve, is plotted together with the mean strain (Table 4.6) versus time curves, at the length of 5 mm about the midspan at the seven levels from B to H.

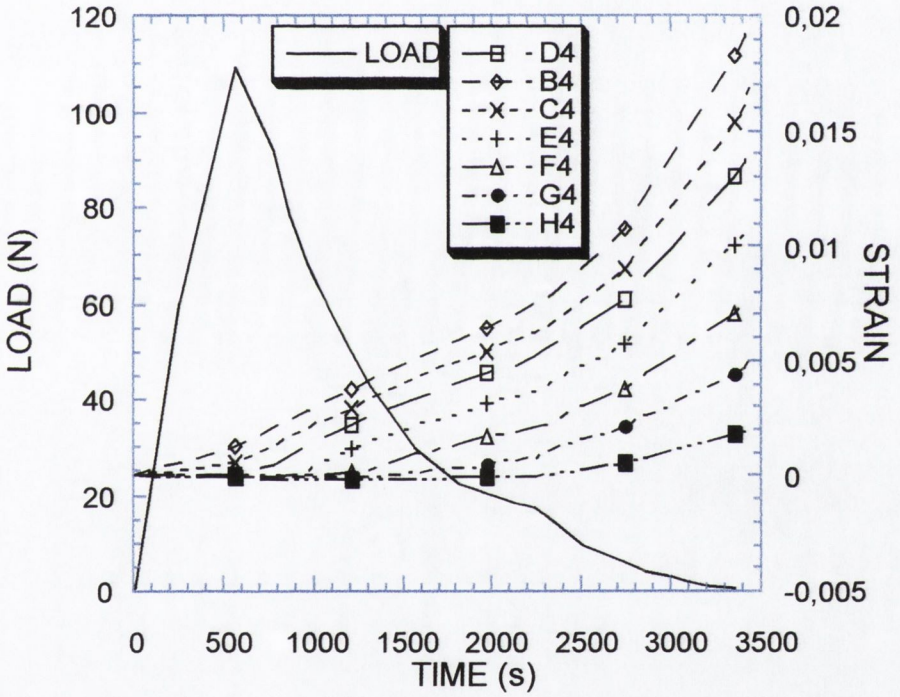

Fig. 4.38 Load versus time curve and mean strain versus time curves at levels from B to H (lengths B4=C4=D4=E4=F4=G4=H4= 5 mm).

In this case, compared to that of Fig. 4.37, it is only possible to point out the presence of the abrupt increase in the curve D4, again approximately occurring at the same time as the peak load, while the other curves show an increase when the crack tip crosses the correspondent level.

The high sensitivity of the interferometric method in determining the displacements of one point (of the order of magnitude of 1 μm), allows results to be obtained with an accuracy not obtainable using several other techniques such as strain gauges and displacement transducers.

The method can also be usefully applied in combination with other traditional experimental procedures as demonstrated in this particular case, in which ESPI technique was combined with the three point bending test for determining the fracture energy of the material.

4.4.3.7 Summary

The high sensitivity of the ESPI instrument makes it possible to measure displacements on the micrometer scale. The horizontal component of the in-plane displacement was measured successfully with high accuracy in three clay specimens with different notch lengths.

Despite the usual environmental vibrations, high contrast fringe patterns were obtained. This permitted in-situ measurements and the recording of the whole process, from start to crack initiation, crack propagation and eventually to sample breaking up. However the next step, namely fringe pattern processing and analysis was somewhat time consuming, as the system was not yet fully automated. A table of total horizontal in-plane displacements of selected points around the crack was obtained and was used by the structural engineers in the assessment of the real behaviour of the clay material.

Essentially the method allows the retrieval of information about the cracking process and reveals the very small strains that are involved at crack propagation and surround the crack during its propagation up to failure. In addition it was possible to follow, with sufficient accuracy, the crack tip position as a function of load and then to obtain information on the local fracture energy of this material, whose characterisation is assuming more and more importance in practical applications.

4.5 Displacement and Strain Measurement

4.5.1 Loading Method

When phase shifting is not possible and the fringe counting method is used in-plane ESPI is sensitive to displacements of approximately 0.4 μm. This is calculated using illumination angle of 30 degrees, a wavelength of 780 nm and presuming that half a fringe spacing can be resolved. Therefore, even without phase shifting, it is ideal for measuring strain, over a length of 1 m, in the range 0 to 10 microstrain. This section presents results from experiments to measure strain in aluminium and concrete. These tests were performed before the phase shifting had been incorporated into the ESPI system, at about the same time that the extensive testing of the liquid crystal devices was carried out. Measurements were made on loaded samples using both strain gauges and simple ESPI fringe analysis in order to check the performance of the new ESPI system.

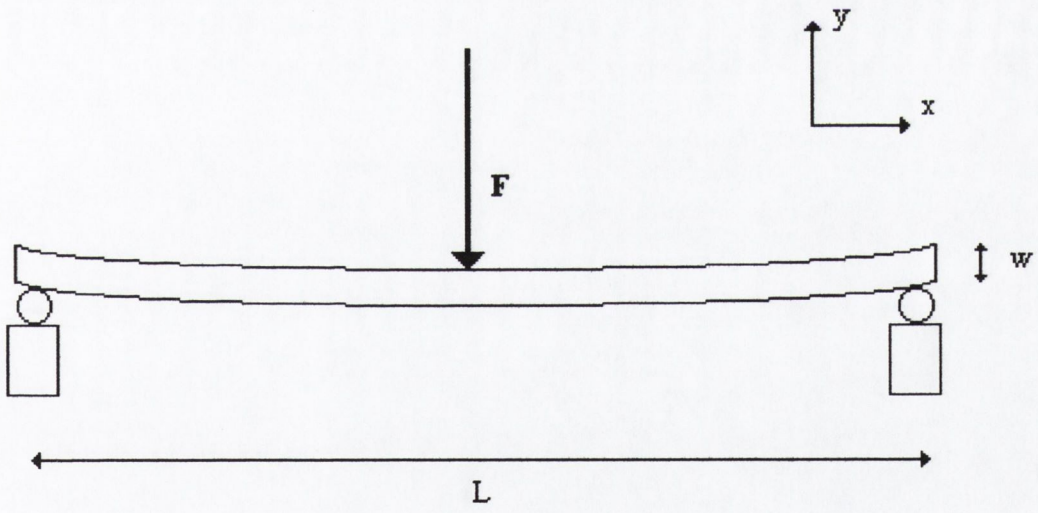

Figure 4.39 The three-point bend test set-up.

As in any ESPI technique it was necessary to use a sample loading method that could be implemented with negligible vibration or in-plane rigid body motion. The method chosen was again a three-point bending test. An aluminium sample, which was in the form of a rectangular bar with dimension 0.635 m x 0.022 m x 0.085 m, was horizontally supported near its two ends with the load applied in the

centre from above, as shown in Figure 4.39. As the ESPI system had no phase shifting facility, the technique depended on the ability to obtain fringes of sufficiently high contrast. Theoretically if the bar is homogeneous and the ends are free to move, the strain map (x component) should look something like Figure 4.40. There is a zero strain line running through the centre of the bar and maximum negative and positive strains at the top and bottom respectively. Preliminary calculations showed that with the available loads, strains of less than 20 microstrain were to be expected. As the ESPI system was restricted to viewing maximum surface areas of about 10 cm^2, a strain in the x direction of 20 microstrain is only a change in length of 2 μm over 10 cm. This is the maximum change in length and only corresponds to, approximately, two and a half fringes.

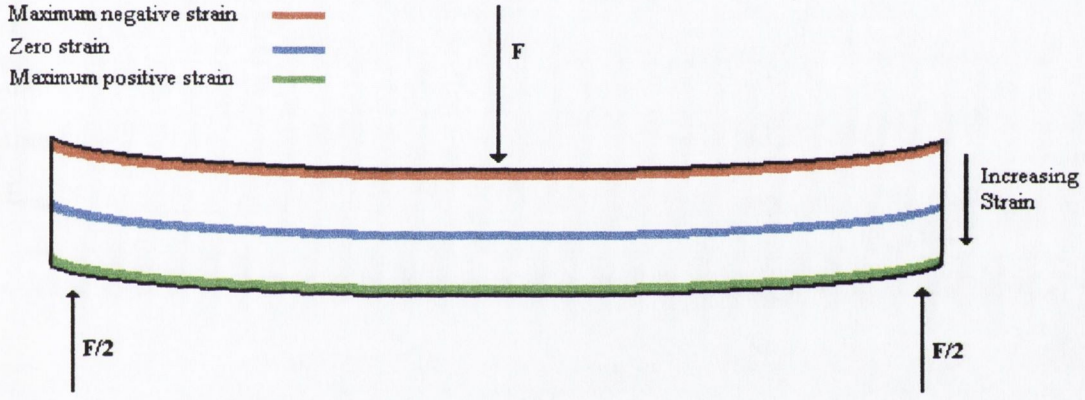

Fig. 4.40 The strain distribution in a sample under an ideal three point bend test.

Also, the loading device did not make it possible to perform an ideal three-point bend test. As the ends were not free to move, horizontal forces were introduced that dramatically alter the strain map. The strain along the top of the bar (red line in Figure 4.39) will increase from zero at the ends to a maximum at the centre. It was decided that the ESPI system would be used to measure the y-component of displacement, as this would produce vertical fringes that could be easily analysed. The strain in the x direction can be worked out from the measured y component and this can then be compared to the value obtained from the gauge. A strain gauge was fixed to the midpoint, of the bar at the top, and at the very end of the bar, to measure the strain in the x-direction.

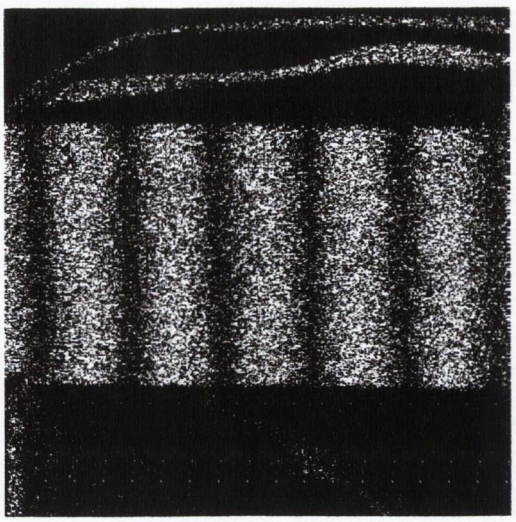

Fig. 4.41 ESPI fringe pattern obtained from the aluminium bar.

The bar in Figure 4.39 was illuminated by two beams lying in the y-z plane, making an angle of 30 degrees with the z-axis. The z-axis is normal to the face of the sample and is directed towards the viewer. The bar was then loaded to produce ESPI fringes representing the displacement in the y direction.

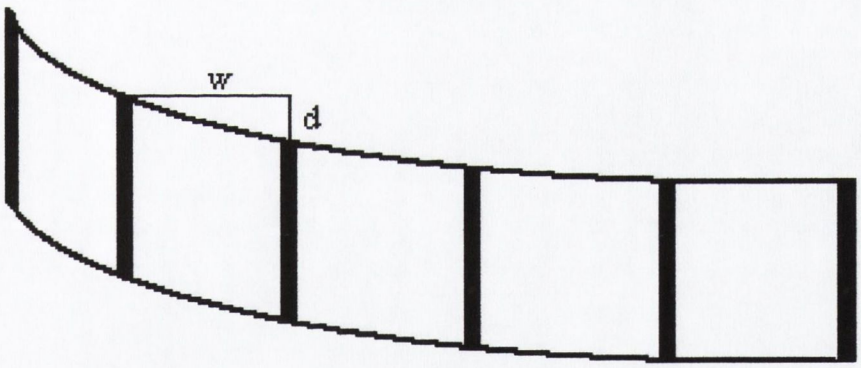

Figure 4.42 The sag geometry used to calculate the change in length in the x direction.

4.5.2 Fringe Analysis

Figure 4.41 shows a typical fringe pattern obtained from part of the bar. Figure 4.42 shows the geometry used to work out the sag of the bar at any point. Once this has been obtained, the change in the length in the x-direction from the end of

the bar to the midpoint can easily be obtained. This calculated value of strain was then compared to the strain value as measured by the strain gauge. In Figure 4.42 the value of d is simply the fringe sensitivity term and the value of w is easily measured using a vernier callipers. The slope of the bar between the two fringes under the load can be obtained. Then length of w is then subtracted from the length of the curved line to produce a value for the change in length in the x direction.

This approach introduces an error due to the bar being curved and not having a constant slope. However this error is significantly reduced if the slope is worked out for each fringe spacing. The changes in length between each fringe spacing can then be added together to give a total value of the change in length over the whole length. This analysis was performed as the load on the sample was increased and a value for strain calculated at intervals in the loading process. These values were then compared to the strain measured using the strain gauge. The theoretical strain was also calculated and used for comparison. A brief description of the theory and formulae used to perform this calculation are given in Appendix D.

Table 4.7 shows the results obtained from the aluminium bar, where SG1 and SG2 are the strain gauges at the end and midpoint of the bar respectively. It is important to note that the strain gauge SG2 provides a value for strain at the midpoint of the bar while the ESPI technique provides a value averaged over the longer length of the bar than the strain gauge measures over. This accounts for the discrepancies in the values of the ESPI and strain gauge readings and the reason for the measured ESPI readings closely following the theoretical results, which are also averaged over the length. If the error in the fringe count is considered the other measurement errors are negligible. The error in the calculated strain is then equal to $\pm$ 0.3 μstrain.

In an ideal test the strain along the top of the bar is constant, but this is very rarely achieved unless a sophisticated loading device is used, as in the previous section. To achieve a constant strain value across the top of the bar the ends of the bar

must be free to move, which was not the case in this experiment. It can be clearly seen from SG1 that the strain across the top of the bar is not constant. Therefore the value of strain increased towards the midpoint with the maximum value at the midpoint and the minimum at the ends.

Load (N)	**SG1** (μstrain)	**SG2** (μstrain)	**ESPI** (μstrain)	**Theory** (μstrain)
13	1	3	**3.0**	**3.0**
18	1	5	**4.2**	**3.9**
22	2	6	**5.2**	**5.0**
27	2	8	**6.4**	**6.0**
31	2	9	**7.5**	**7.0**
36	3	10	**8.5**	**8.0**
40	3	12	**9.5**	**8.8**
45	4	14	**10.7**	**9.8**
49	3	15	**12.1**	**10.8**
54	4	16	**12.6**	**11.8**
58	4	17	**13.7**	**12.8**
62	4	19	**15.5**	**13.7**
49	3	15	**12.1**	**10.8**
36	3	11	**9.0**	**8.0**
13	2	7	**6.0**	**5.0**

Table 4.7 Results from the three-point bend tests on an aluminium beam.

The test was repeated with a concrete slab again under the three-point bend test. The concrete mix was 3:1 sand to cement and the dimensions were 82 cm x 10 cm x 5 cm. From the fringe data at three different loads, the results in Table 4.8 were obtained. The values of Young's modulus of elasticity obtained from the fringe data are within the expected range of 20 – 30 GNm^{-2}.

load (N)	**ESPI** (μstrain)	**Calculated E** GNm^{-2}
27	**3.1**	**29**
45	**5.9**	**25**
72	**10.1**	**23**

Table 4.8 Results from the three-point bend tests on the concrete slab.

4.5.3 Summary

The ESPI technique has been successfully used to measure strain in an aluminium bar and in a concrete slab. In an ideal three-point bend test the strain over across the top of the bar is constant and only one strain gauge is needed. However, when the strain is not constant many strain gauges are required to map the strain field. ESPI, on the other hand, can map the change in length over the whole length. The technique was also used to measure the Young's modulus of elasticity of a concrete slab and again the results were within the expected range.

4.6 Quantitative Results from Phase Shifting

4.6.1 Calibration of phase-shifters

When the system was fully operational it was used to measure the in-plane displacements in both the x and y directions of the surface of a steel bar under tensile strain. A photograph of the tensile rig used in these tests is shown in Figure 4.43, along with a schematic of one of the steel bars in Figure 4.44. Unfortunately there was no transducer attached to the loading device to measure the applied force. However the purpose of these experiments was to test the phase shifting capabilities of the system along with the unwrapping procedure. When the sample was mounted into the loading device and securely fixed, a hand-pump was used to control the tensile force. Unfortunately the device was not capable of supplying a sufficient force to significantly stretch an ordinary steel bar. However it could stretch the steel bars with notches at their midpoints. One of these bars was

mounted in the loading device and an increasing force was slowly applied until the maximum force was reached.

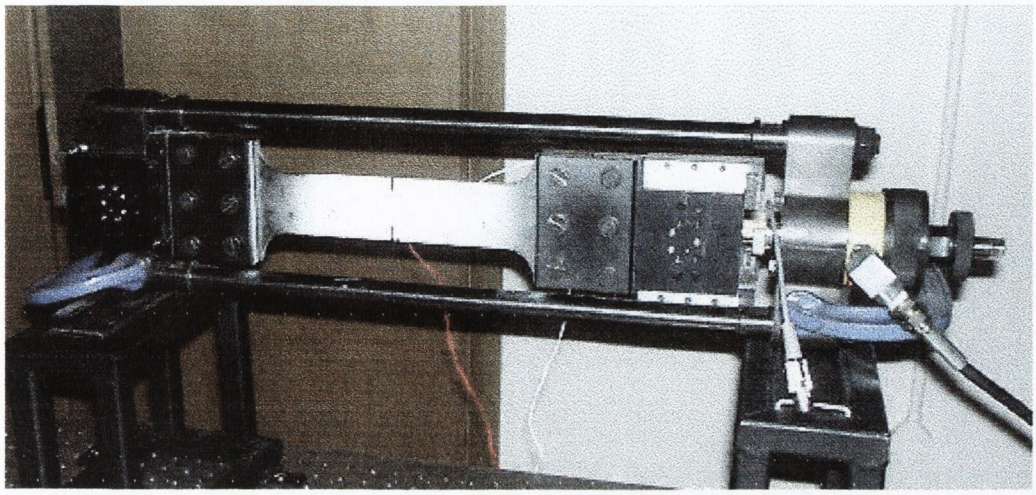

Fig. 4.43 The loading device capable of applying a tensile force.

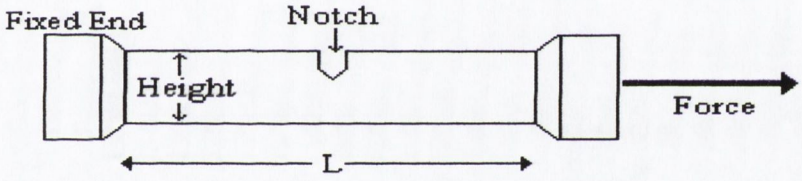

Fig 4.44 Steel bar with notch.

The ESPI system was placed in front of the device and the midpoint point of the bar was imaged onto the CCD camera. The dimensions of the imaged surface and of the notch depth and width were measured as shown in Figure 4.45. Appropriate voltages and delay-time values for the liquid crystal rotator were entered into the software. The surface was then alternately illuminated in the x-z and y-z planes and the displacement fringes were obtained, as shown in Figure 4.46. As in the previous sections these fringes can be analysed by simply counting the fringes between two fixed points and using the fringe sensitivity term to calculate the relative displacement. From these displacements it is possible to calculate the strain in both directions. However there is a relatively large error associated with this technique.

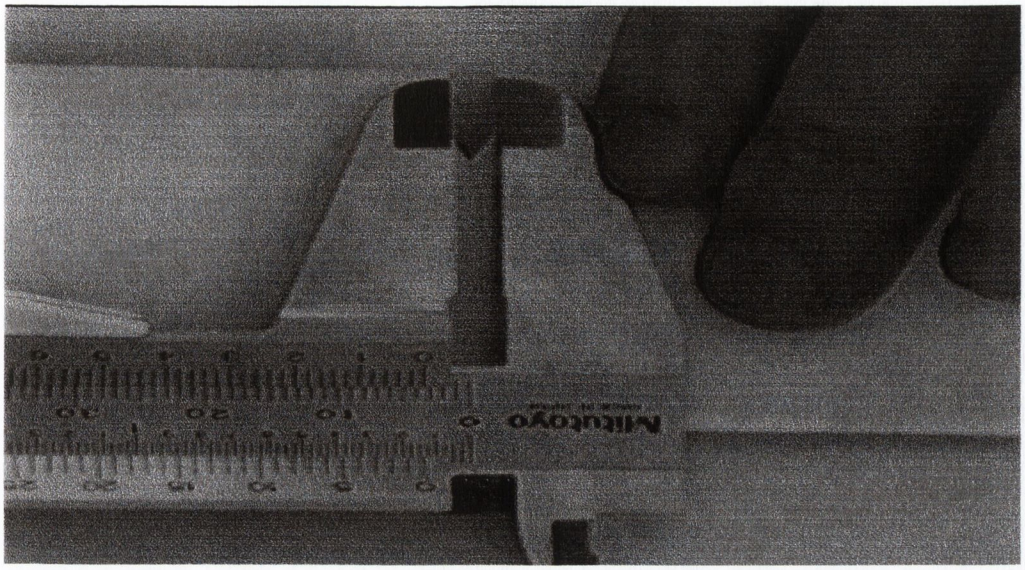

Fig. 4.45 The dimensions of the notch in the steel bar.

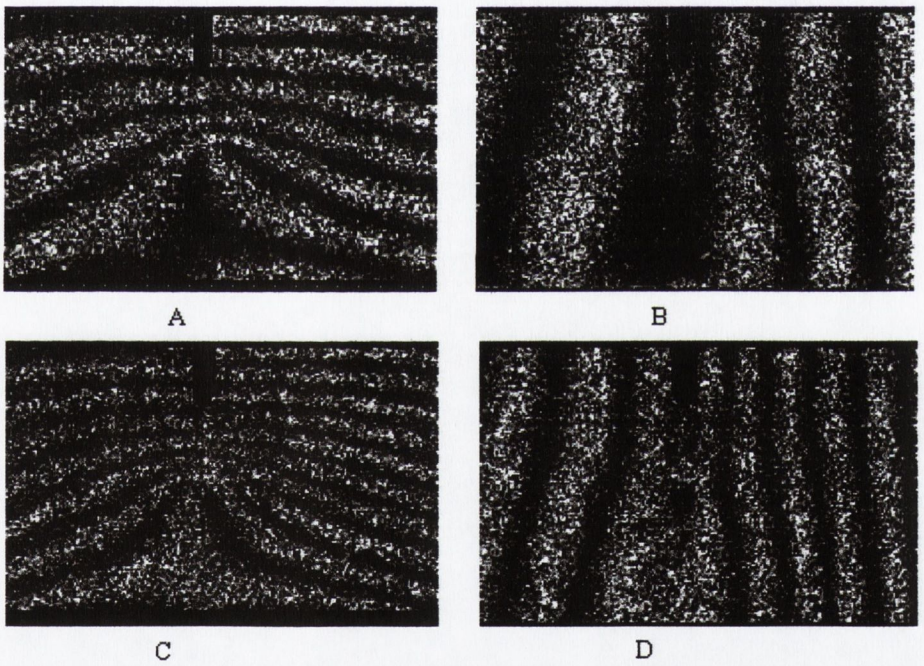

Fig. 4.46 ESPI displacement fringes; A and C represent displacements in the x direction while B and D represent displacements in the y direction.

The test was repeated using the liquid crystal phase shifters to calculate the phase maps as described in previous sections. The surface was again alternately illuminated in the x-z and y-z planes, only this time the wrapped phase fringes were calculated when the maximum force was applied. Figure 4.47 shows wrapped maps representing the change in phase (modulo 2π) caused by the bar stretching, in both the x and y directions. Using the ESPITest software,

unwrapped phase maps were produced from the wrapped phase maps. Two of the unwrapped phase maps are shown in Figure 4.48.

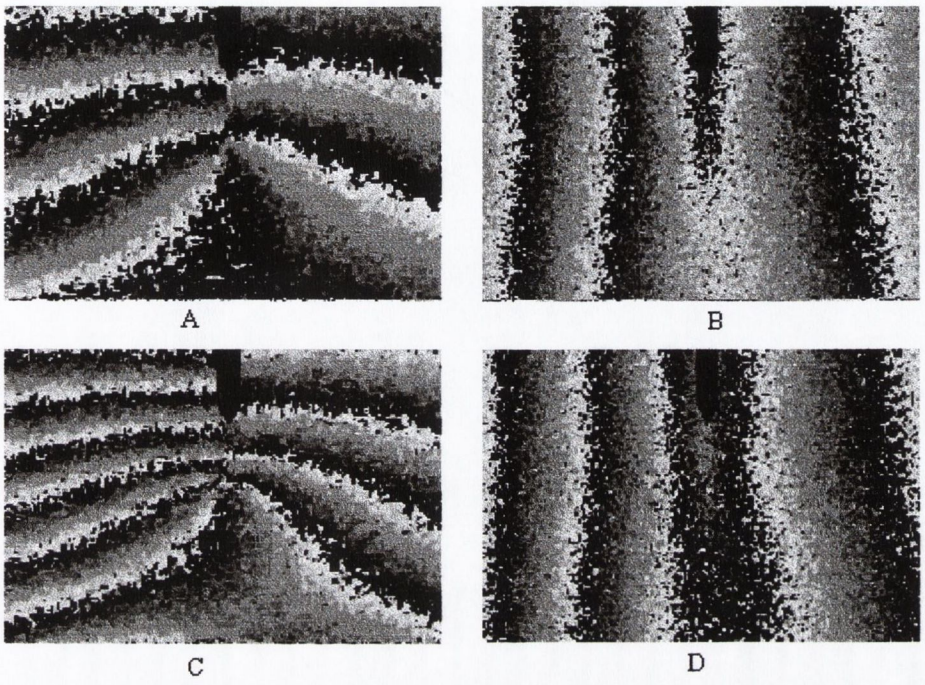

Fig. 4.47 Wrapped phase fringes; A and C represent displacements in the x direction while B and D represent displacements in the y direction.

A gray level of 255 in the wrapped phase fringe pattern represents a phase shift of 2π and in the unwrapped image the phase shift represented by a gray level of 255 depends on the number of 2π phase shifts in the wrapped phase pattern.

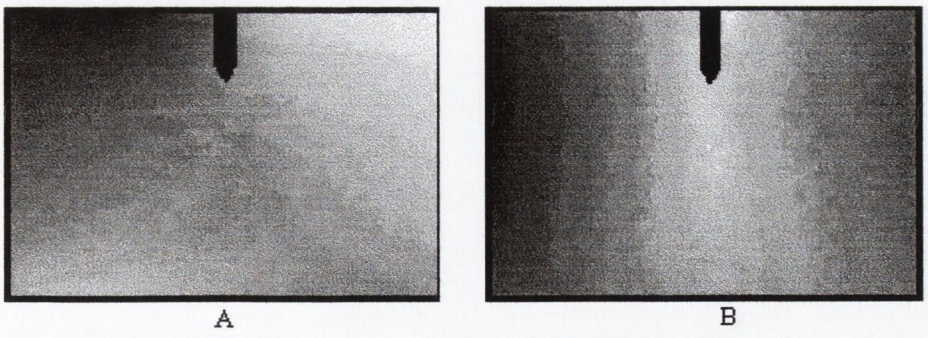

Fig 4.48 The unwrapped phase maps showing the phase change in the; A x direction and; B y direction.

This can be easily obtained from visual examination of the wrapped phase fringe pattern. The displacement maps can then be displayed on a three dimensional graph where the height represents the displacement. The displacements are calculated using the phase sensitivity term, which in the case of an in-plane ESPI system, is given by

$\Delta\phi = \pi\lambda / d\mathrm{Sin}\theta$ Equation 4.1

where $\Delta\phi$ is the change in phase, θ is the illumination angle, λ is the wavelength of the light source and d is the displacement.

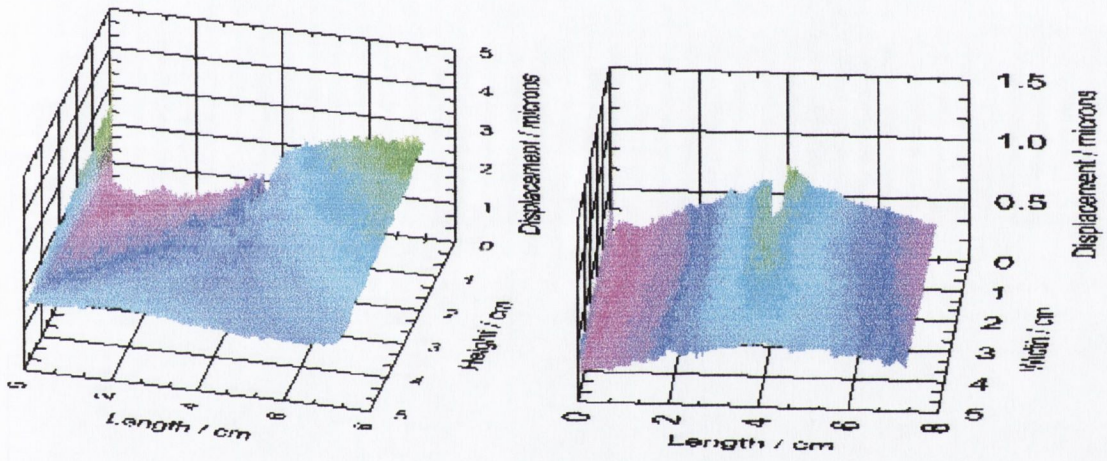

Fig 4.49 The three-dimensional surface displacement maps in both the x and y directions.

Figure 4.49 shows the colour coded three dimensional displacement maps of both the x and y displacements. To calculate the strain in either direction the displacement maps can be differentiated over the length (x-direction) or height (y-direction). Figure 4.50 shows the x direction displacement map with four marked horizontal lines and Figure 4.51 shows the displacement plotted along these lines. Along line A, the displacement is greater on the right of the notch as this is the side the force was pulling, with, as expected, the biggest difference at the very top of the bar. Further down the bar the difference between the displacements on the

left and right of the midpoint decrease until they are approximately equal. It is also noted that the four plotted lines intersect in the location of the notch.

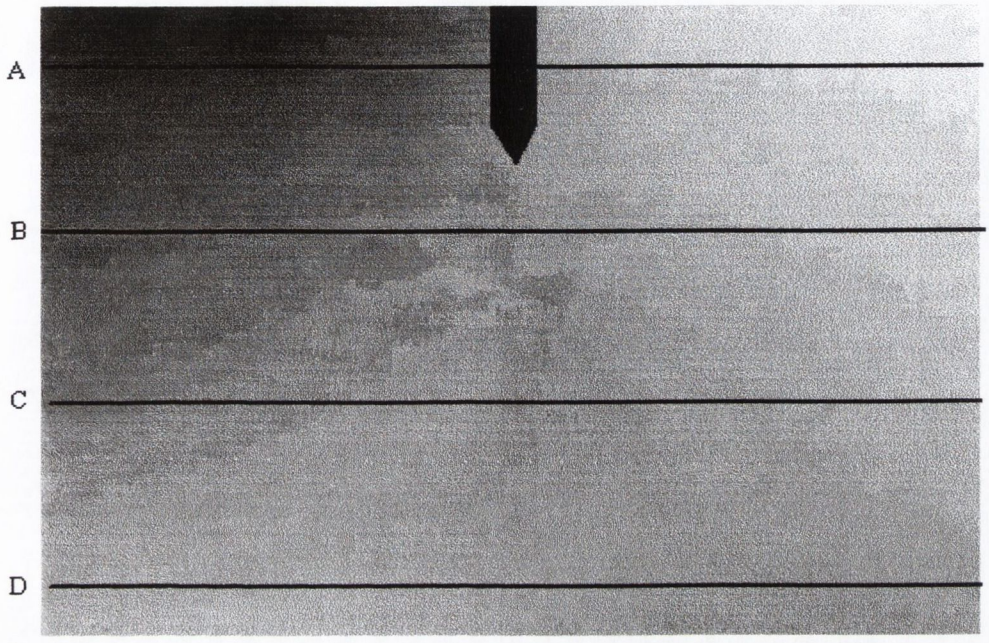

Fig. 4.50 The displacement map if the x component of in-plane displacement.

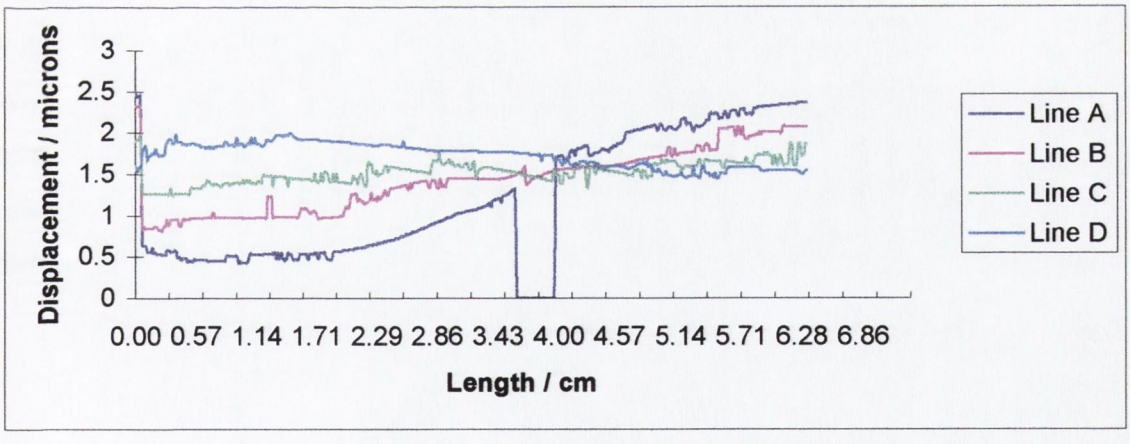

Fig. 4.51 Displacements in the x direction, shown at four different heights on the surface of the steel bar.

It can be seen from taking lines across the surface that the strain is greatest near the notch tip. This can be seen in data plotted by the Line A, in Figure 4.51, as the area with a maximum slope. By taking more plots through this region, as in Figure

4.52, and differentiating, the strain can be calculated. From this data the strain at the area of the notch is approximately 23 μstrain, with the value decreasing as the distance from the notch increases.

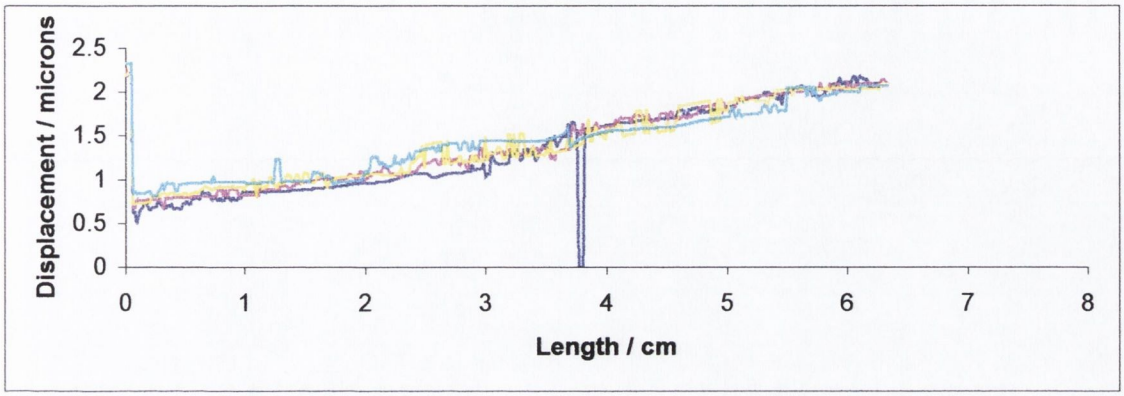

Fig. 4.52 Displacements in the x direction shown for four different heights around the notch tip.

Visual examination of the displacement map in the y direction shows there to be very little strain in that direction. Again, the only area where the strain is significant is in the area of the notch. The fact that there is very little strain in the y direction can be clearly seen from Figure 4.53, in which the displacement in the y direction along four lines across the length of the surface are plotted. The lines were taken at distances of 2 cm, 3 cm, 4.5 cm and 5.5 cm away from the left edge of the surface, for points A, B, C and D respectively. As the slopes of the plots are relatively constant and equal to zero, the strain is approximately zero in the y direction.

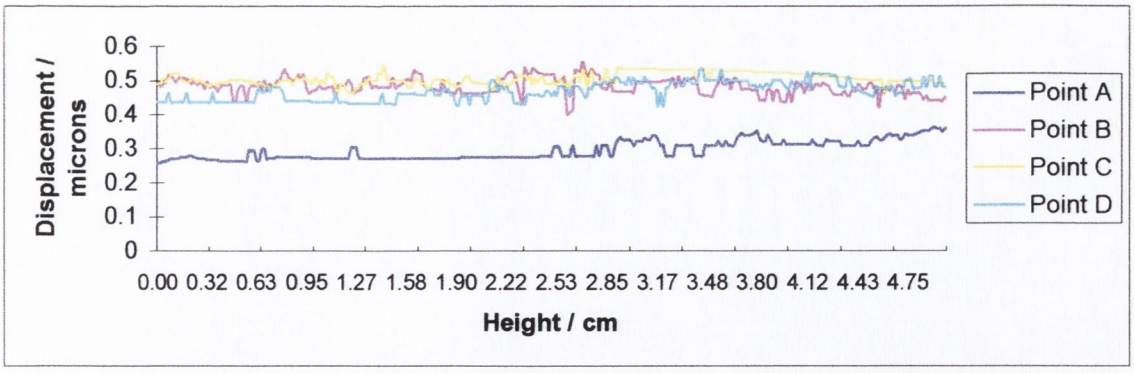

Fig. 4.53 Displacements in the y direction shown of four different lines across the surface length.

The tests were repeated on a steel bar with a notch at the top and another at the bottom. Again the maximum force was exerted on the sample and the wrapped phase map was obtained as shown in Figure 4.54. The maximum displacement in the x direction is less than it was for the single notch sample, as the same force is now opening two notches instead of one. There was also less displacement in the y direction, so only the x direction wrapped phase map is shown.

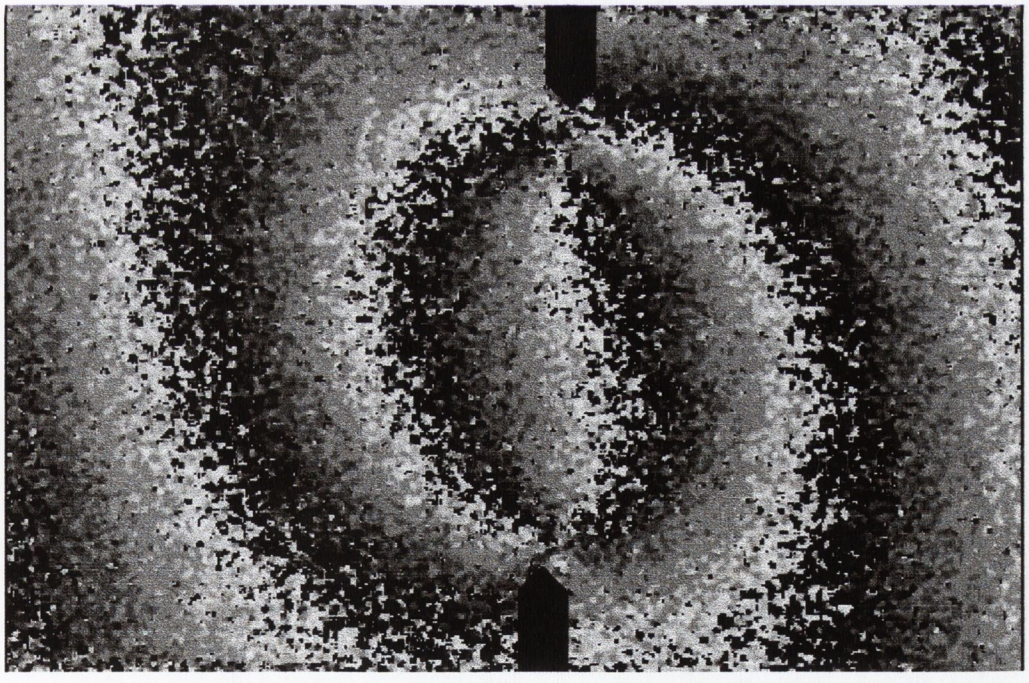

Fig. 4.54 The x direction wrapped phase fringe pattern from a steel bar with two notches.

Again the ESPITest software was used to unwrap this image to produce the absolute phase map. This in turn is converted into the three-dimensional

displacement map shown in Figure 4.55. By comparing the surface displacement maps of the samples, the effect of the second notch can be clearly seen. The displacement across the length of the bar is more uniform, as the effect of one of the notches is cancelled by the other notch. This can be observed in Figure 4.56, where the displacements along four lines at different heights in the sample are plotted. The data were acquired at 0.8 cm. 1.8 cm, 3.5 cm and 4.5 cm from the bottom of the sample for the plots; points A, B, C and D respectively.

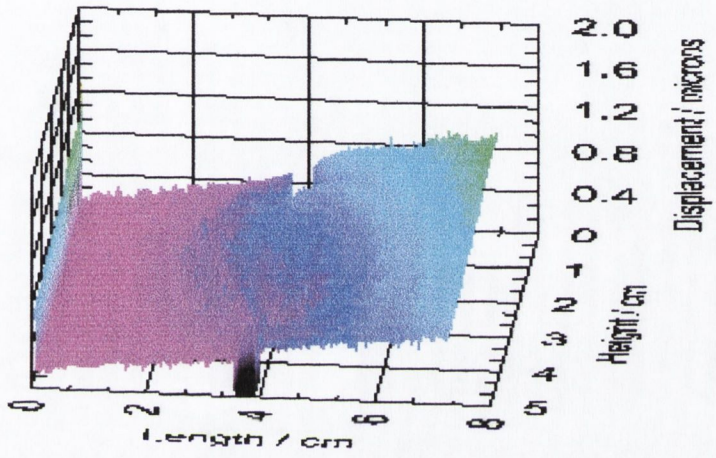

Fig. 4.54 The three dimensional displacement map.

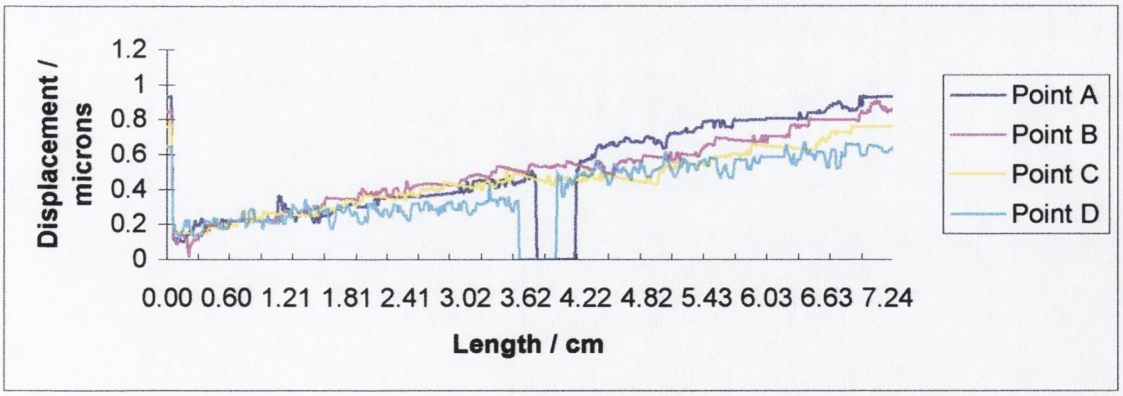

Fig 4.55 Displacements in the x direction shown for four different lines across the surface height.

From Figure 4.55, the slopes of the plots are relatively constant showing a constant strain across the surface. As the lines taken across the length of the

surface move away from the bottom of the surface there is a slight increase in the strain, from approximately 8.5 μstrain near the bottom to approximately 11.5 at the top.

4.7 Discussion

The ESPI technique can measure surface displacements of less that one micrometer and using phase shifting procedures the resolution can be improved to less than 50 nm. The technique is full-field and requires no contact with the surface. Unlike conventional mechanical techniques, such as strain gauges, it can provide information over the whole surface. Also, unlike strain gauges it can be used to measure the relative displacement between two points on the surface, for example on either side of a notch. It can be used qualitatively to detect cracks and defects in real time, as ESPI subtraction fringe patterns can be produced at a rate of 25 Hz. For quantitative measurements the fringes must be analysed. This can be simply done by counting the number of fringes and multiplying by the sensitivity term. This term depends on the wavelength of the light and the geometric optical configuration and ESPI systems can be configured to be sensitive to displacements in only one direction. To analyse the data completely, phase shifting is used to produce wrapped phase fringe patterns, which describe the phase change caused by the surface displacement. These are then processed to produce unwrapped phase maps, which can be converted to displacement maps using the phase sensitivity term.

In this chapter a dual ESPI system capable of measuring the displacement in both the x and y directions is described. This dual in-plane ESPI system has proven to be very effective at measuring surface displacements perpendicular to the direction of viewing. The system can measure the displacement in both the x and y directions and from these components one can calculate the resultant in-plane displacement. The innovative optical configuration has no moving parts but is still capable of switching all the available laser power from one illumination plane to the orthogonal plane using a liquid crystal polarisation rotator as the basis of the

optical switch. The system also incorporates two liquid crystal phase shifting devices to allow for phase shifting. Each illumination plane contains one of these devices, which is capable of providing a 2π phase shift.

The optical components and the liquid crystal are small enough to be held in Spindler & Hoyer microbench. This allows the system to be very compact and stable. A 50 mW laser diode with a wavelength of 780 nm is used as the light source. This is also easily attached to the microbench making the whole system portable and robust.

The system has been used to measure displacements in various materials, including clay, aluminium, concrete, brick and steel. It has been used for crack detection as well as for quantitative displacement measurements using the phase-shifting and phase unwrapping procedures. The easy-to-use ESPITest software allows total control over the system and post processing and filtering of the captured images. The system takes approximately 500 ms to calculate the phase map of a 512 x 512 image. As the liquid crystal switch allows the illumination beams to be switched at 2 Hz, the system is capable of producing both the x and y phase maps on the screen at a rate of 2 Hz. It is also possible to unwrap these images during acquisition, but this slows down the process considerably and it is recommended to unwrap only after the test is completed.

Overall, the objective of this research, i.e. to develop an industrial prototype of an advanced dual in-plane ESPI system, has been accomplished. The system design is presently being investigated by Ettemeyer [113], one the largest European manufacturers of commercial ESPI system, with the objective of developing it into a commercial ESPI system. The system is portable, compact and robust, and capable of producing quantitative displacement data. The interferometer makes very efficient use of the illumination available without the use of shutters. Only low voltage devices are used without the need for bulky or expensive electronics. The ESPI system can be taken into an industrial environment and used in-situ, by anyone to produce accurate and useful data.

Chapter 5 Dual Electronic Speckle Pattern Contouring / White Light Interferometer

5.1 Introduction

This chapter describes the work carried out in the European Commission Joint Research Centre during a four month period. The objective of the work was to develop an optical instrument that is capable of measuring the shape of objects of various shapes and sizes. These objects were mainly bio-medical implants and other medical devices. The maximum surface area was about 5 x 5 cm which made the surfaces ideal for profiling with the white light interferometer described in Chapter 3. This white light interferometric profiler is ideal for profiling smooth discontinuous surfaces. However, as it was shown, as the curvature and roughness of the surface increase the efficiency of the profiler decreases. Also, sub-micrometer accuracy was now needed even when profiling rough surfaces, which is not possible with this system. Due to the limited time available, it was decided that only existing equipment and software would be used. As well as the existing white light profiler there was also the ESPITest software, described in the previous chapter, and tunable wavelength sources available. For this reason, the feasibility of using the white light profiler as an ESPI contouring system was investigated. White light interferometry is the ideal technique when profiling smooth and discontinuous surfaces while ESPI contouring is ideal for profiling rough and continuous surfaces. The versatility and resolution of this dual system, would make it an efficient surface profiler, which is not limited to use on any particular surface finish and with a relatively unlimited range.

To begin with the optical configuration was unchanged and a high quality interference filter was placed in front of the CCD array. This increased the coherence length of the white light in the interferometer to approximately 50 μm. A flat aluminum plate was placed in the system at optical path difference of zero, producing a speckle pattern that could be seen over the whole image. This speckle

is not strictly the same as the speckle described in Chapter 2 as it is not produced by the reflections from the rough surface alone. In Chapter 2 it was shown how one speckle is produced in an image by the interference of light waves reflected from an area of the surface. The size of this speckle depends on the aperture of the imaging lens. In this system the aperture in the Fourier plane of the objective lens only allows light from one resolution area on the surface to reach the CCD array and this interferes with the light from the reference beam. The object wavefront in the image plane contains waves with different phases due to the variations in height across the rough surface. This wavefront interferes with the plane reference wavefront to produce an image whose intensity at any point depends on the relative phase between the two wavefronts at that point. This results in variations in intensity across the image producing the speckle pattern, that behaves exactly the same as the resultant speckle pattern in an ESPI system.

As mentioned in Chapter 2 a Michelson interferometer can also be used for out-of-plane ESPI, usually with a monochromatic source, and ESPI contouring using a tunable wavelength source. Initially the ESPITest software was used to obtain out-of-plane ESPI fringes using a white light source with the interference filter, by pressing on the aluminum plate from the back. This was done to ensure it would be possible to do any ESPI in this interferometer. Obviously, if the plate is displaced so that the optical path difference between the arms of the interferometer is greater than 50 μm decorrelation occurs. Alternatively the helium-neon laser used to align the system can be used to produce ESPI fringes. However this laser had a relatively low output power. To use the system as a dual optical profiler both the white light source and a laser source for ESPI contouring must be available. It was decided to replace the helium-neon laser with a laser suitable for ESPI contouring. In this way the new laser could still be used for aligning the system.

If we use the Michelson interferometer configuration and collimated light, and the wavelength of the light is changed, at any point in the image there will be a phase change $\Delta\phi$, so long as the surface is not at zero optical path difference. This phase change causes a change in the intensity at that point. From Chapter 2, the result of

correlating the intensity of the two images is unity when $\Delta\phi = 2n\pi$, where n is zero or any integer, and zero when $\Delta\phi = (2n + 1)\pi$. Thus correlating the two images produces a fringe pattern defining contours of equal phase change. The fringes represent the difference in shape between the two reflected wavefronts. Therefore, if the shape of the object surface is identical to the shape of the reference surface, the intensity of the subtracted image is constant across the image because the phase change, caused by the wavelength change, is constant across the image. Thus correlation fringes are obtained when the object surface differs from a flat shape and the fringes occur at intervals, Δz, given by

$$\Delta z = \lambda_1\lambda_2 / [2(\lambda_1 - \lambda_2)] \qquad \text{Equation 5.1}$$

Altering the difference between the two wavelengths can vary the fringe sensitivity. The greater the change in wavelength, the greater the sensitivity. The correlation is performed by subtracting the image taken at λ_2 from the image at λ_1 and the result is rectified to produce the fringe pattern.

ESPI contouring depends on the ability to change the wavelength of the light source. To do this, systems have used two laser diodes to change between two set wavelengths [141]. However the system is then limited to only one sensitivity which may not always be adequate. An ideal source would have a range of wavelengths to allow different sensitivities to be chosen. For the ESPI contouring system described here, three options were investigated; an argon ion laser with an intra-cavity prism; an argon ion laser and an acousto-optic filter; and a titanium-doped-sapphire laser pumped by an argon ion laser.

5.2 Development of Optical System

5.2.1 Variable Wavelength Source

5.2.1.1 Argon Ion Laser

A Spectra-Physics Stabilite 2016 Argon Ion laser was used. The specifications of this laser are given in Appendix A. The maximum output intensity of the laser was approximately 7 Watts with all lines on. With an intra-cavity prism in the laser it is possible to select one of the nine wavelengths, given in Table 5.1, by rotating the vertical adjustment at the back of the laser. Each line was selected in turn and using a spectrum analyser and a power meter, its wavelength and maximum power output were measured, as shown in Table 5.1. The laser beam was directed, using mirrors into the system. Table 5.2 shows values of the contouring sensitivity, Δz, for a number of different wavelength changes, using Equation 5.1.

	Wavelength nm	Output Power Watts
1	514.5	2.25
2	501.7	0.6
3	496.5	0.75
4	488.0	1.95
5	476.5	0.7
6	472.7	0.3
7	465.8.	0.2
8	457.9	0.4
9	454.5	0.2

Table 5.1 Output power of Argon Ion Laser

Theoretically, the system could now contour with this range of sensitivities. To obtain maximum fringe contrast, in ESPI contouring, it is important that the average intensity does not change between the frames grabbed at the two wavelengths. It can be seen from Table 5.1 that the intensity varies considerably between lines. To overcome this, the power of the laser had to be adjusted as each wavelength was selected. Initially a frame is grabbed at one wavelength and all subsequent frames are subtracted from this image and the rectified result displayed on the monitor. This displayed image stays totally black (zero gray level) until the wavelength is changed because the speckle pattern is unchanged. The wavelength is then changed to obtain fringes and the laser power is adjusted until the fringes have a good visibility.

Another problem associated with this technique was the way in which the lines were selected. In ESPI contouring it is very important that the light at both wavelengths travels down exactly the same path making the same angle with the surface. Even small shifts away from this axis when changing the wavelength leads to speckle decorrelation due to a movement of the speckle pattern. Therefore, when λ_2 is selected it must not only have the same power as the λ_1, but it must also travel along the same axis. This proved extremely hard to achieve by manually rotating the prism. To help reduce this alignment problem a optical fiber coupler was attached to the laser, the other end of which was connected to the system. This helped the alignment, as the light would only couple efficiently into the fiber when the light was directed at a certain angle.

λ_1 / nm	λ_2 / nm	Δz / μm
454.5	457.9	30
496.5	501.7	24
465.8	472.7	16
488.0	496.5	14
501.7	514.5	10
572.7	488.0	7.5

488	514.5	5
454.5	514.5	2.3

Table 5.2 Contouring Sensitivities for different argon laser lines

However, because the only available optical fibre was designed for 532 nm, the output power of the lower wavelengths were significantly diminished after travelling through the fibre. In order to get sufficient laser light through the fibre, for these lines, the power of the laser had to be increased to a level at which it was in danger of damaging the fibre. Therefore only the three longest wavelengths could be used. For these reasons this technique proved limited and even though contour fringes could be obtained, it was not an ideal solution.

5.2.1.2 Argon Ion Laser and Acousto-Optic Filter

Acousto-optical devices use the refraction and diffraction effects observed when light passes through a transparent material at right angles to a high frequency sound field propagating in the same medium. The associated pressure wave creates a periodic refractive index variation inside the medium with the effect that the light wave is incident normally on a stationary phase grating. The period of the grating depends on the frequency of the sound wave, so by modulating this frequency it is possible to modulate the period of the grating. Acousto-optic Bragg cells are solid state optical tunable filters with which the wavelength of the diffracted light is selected by application of a corresponding radio-frequency wave. The intra-cavity prism was removed from the argon-ion laser so that it emitted all nine lines at once. If this beam is incident normally on the acousto-optic filter, it is possible to select each line in turn by applying a pressure wave to the filter of the appropriate frequency. A window in the casing of the filter only allows the first order diffracted light through. The diffraction efficiency, i.e. the percentage of the light diffracted into the first order beam, can also be controlled by the amplitude of the pressure wave. A Gooch & Housego Limited, Model TF575 was used. The specifications of this device are shown in Appendix A.

A LabVIEW program was written to control the frequency and amplitude of the pressure wave across the acousto-optic filter. The computer program sends commands, via the serial port to a command module. This module translates the serial code into another digital code which it sends to a radio-frequency generator. This generates a sinusoidal wave of appropriate frequency and amplitude, depending on the command from the computer. This is then amplified before it is sent to a piezoelectric transducer connected to the acousto-optic material. With the intra-cavity prism back in the argon ion laser, each of the nine lines was manually selected in turn, by rotating the prism. At each wavelength, the output light was incident on the acousto-optic filter as shown in Figure 5.1, and the intensity of the diffracted light measured with a power meter. The readings were then sent to the computer via an A/D board and analysed using the same LabVIEW program.

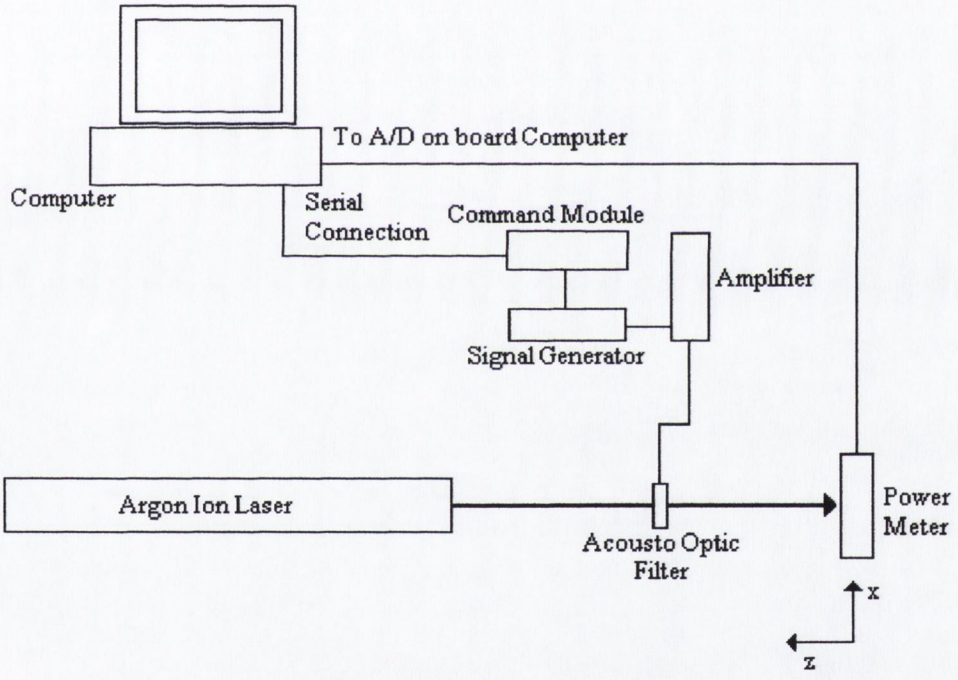

Fig. 5.1 Diagram of acousto-optical tunable filter control circuit.

The frequency of the sound wave across the device was then scanned to find the frequency at which the laser output was diffracted out of the filter. Figure 5.2 shows the output power of the light diffracted from the filter, when the 514.5 nm line was incident on the filter, as the frequency of the sound wave was varied. This was repeated for all nine lines and similar graphs for each line are given in Appendix E. Figure 5.3 shows a graph of the wavelength of the light versus the

frequency applied to the acousto-optic filter, for all nine lines of the argon laser. By controlling the frequency and amplitude of the sound wave across the tunable filter, it was now possible to control the wavelength and power of the light.

The prism was taken out of the laser cavity so all nine lines were incident on the filter. Using the LabVIEW program, it was possible to efficiently select each of the nine lines and control the power. It was therefore possible to use all the range of sensitivities, provided by the laser, in the ESPI contouring system. The problem of manual control had been eliminated, as had the problem with fluctuating output power. However, there was one significant problem. There was a slight change in the diffraction angle as the wavelength was changed. This caused decorrelation in the speckle pattern due to the shift in the illuminating wavefront. To overcome this problem, the filter was mounted on a rotating stand.

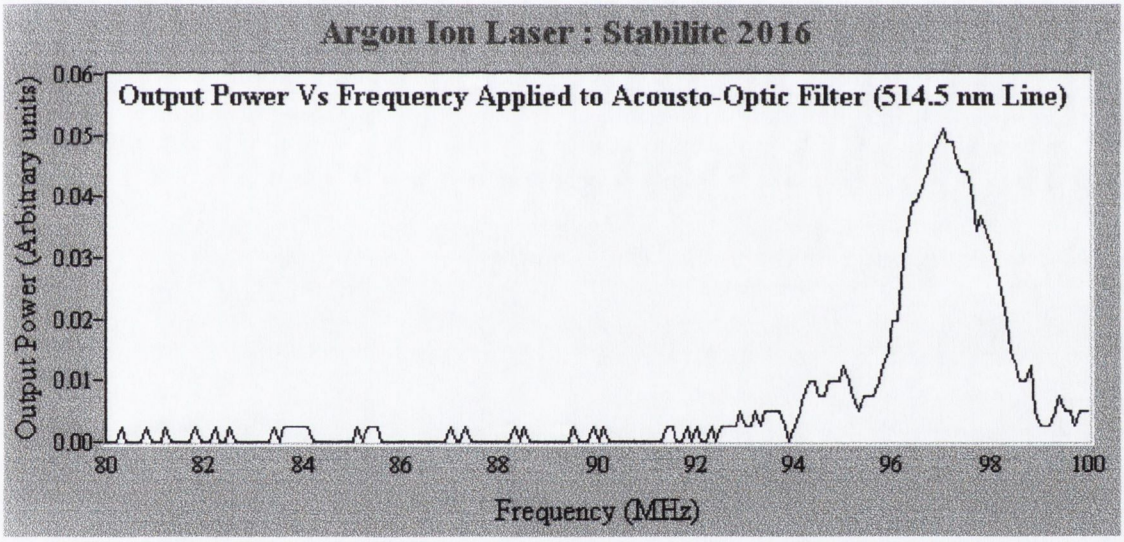

Fig. 5.2 Graph of output power versus frequency for the 514.4 nm argon line.

The filter could now be rotated slightly around the x-axis, see Figure 5.1, and so the direction of the diffracted beam could be controlled. Rotating the filter to find the right diffraction angle proved difficult even though the rotation was small. Changing the incident angle changed the diffraction efficiency of the filter and so changes the output power. It was possible to change the angle and still get ESPI correlation fringes but this technique was still not ideal because it again required

manual control. It did have the advantage, however, of been able to select all the nine lines of the laser and control the power.

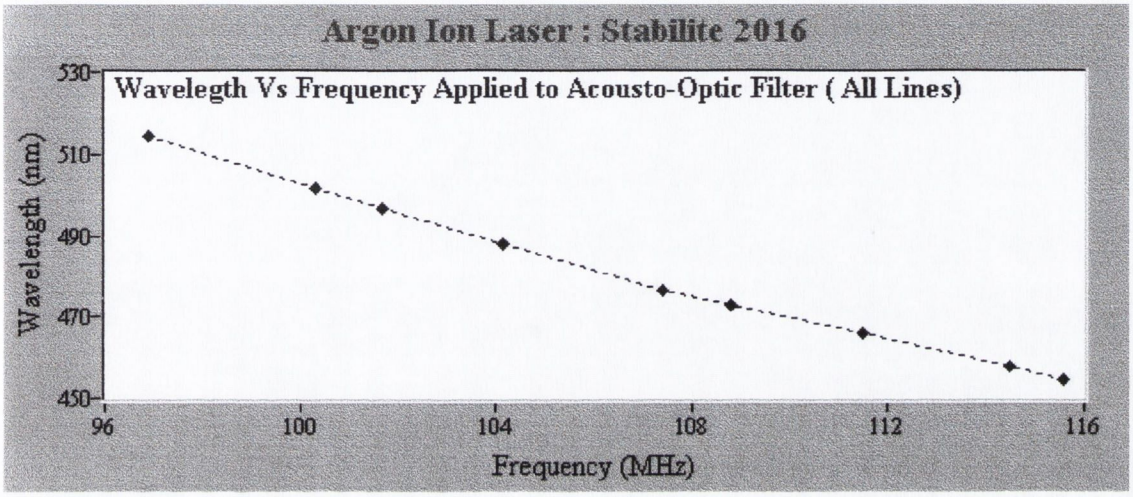

Fig .5.3 Graph of wavelength versus the frequency of the sound wave applied to the tunable filter.

5.2.1.3 Titanium doped Sapphire Laser

The ideal solution to all the problems was found using a titanium-doped-sapphire laser. A Ti:Sapphire crystal is a solid state laser medium capable of laser action over a broad range of near infrared wavelengths. A Spectra-Physics, Model 3900S, CW Ti:Sapphire laser was used, the specifications are given in Appendix A. It was pumped using the argon ion laser with all lines emitted. When the argon ion output power is approximately 7 W, the output power of the Ti:Sapphire laser is approximately 750 mW. To achieve maximum output power the pump light must be focused to a narrow line within the Ti:Sapphire rod, which is several millimeters in diameter. A four-mirror cavity is used to allow this narrow focusing, as shown in Figure 5.4.

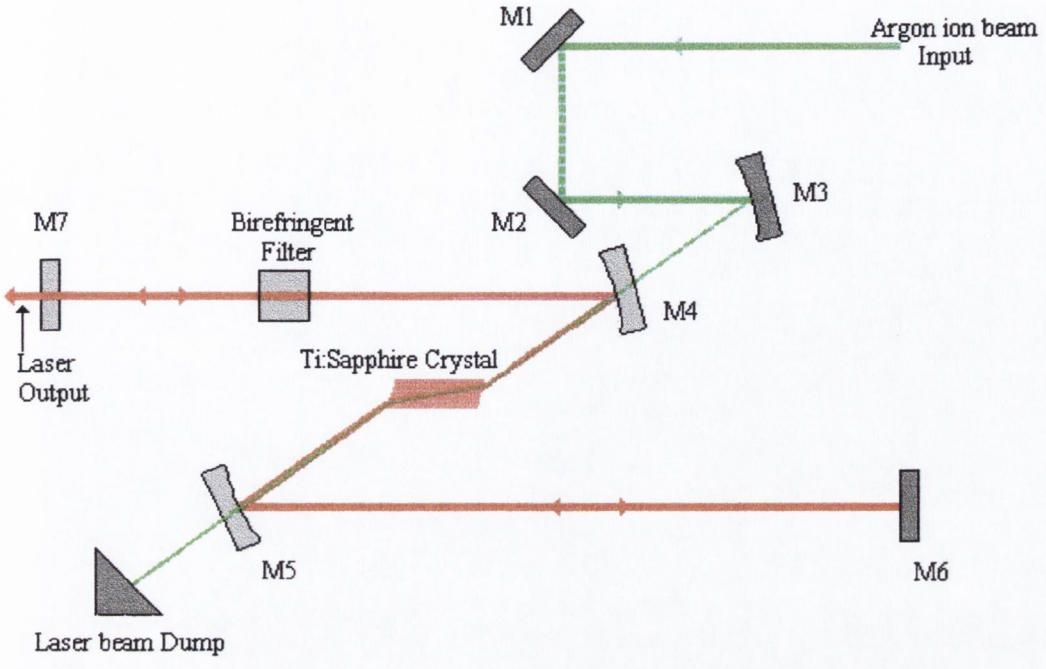

Fig. 5.4 The optical arrangement of the Ti:Sapphire laser including the z-cavity.

A birefringent filter consisting of three crystalline quartz plates is placed in the z-cavity of the laser. This is used to tune over the wavelength range 700 to 850 nm. After the laser was aligned the wavelength of the output was measured using a spectrum analyser. The birefringent filter is adjusted by rotating the micrometer at the top of the laser. Using the spectrum analyser the reading on the micrometer was calibrated for the wavelength range. Figure 5.5 shows the calibration graph. By using this graph it is possible to select any wavelength between 700 and 850 nm with a sensitivity of 0.5 nm.

The output power was then measured as a function of wavelength. Figure 5.6 shows the results of these measurements. As mentioned previously, it is important to keep the power constant when changing the wavelength in ESPI contouring. Therefore the wavelength range selected for ESPI contouring was from 760 to 830 nm. This enables a continuous range of contouring sensitivities, from Equation 5.1, of approximately 4.5 μm to 6 mm.

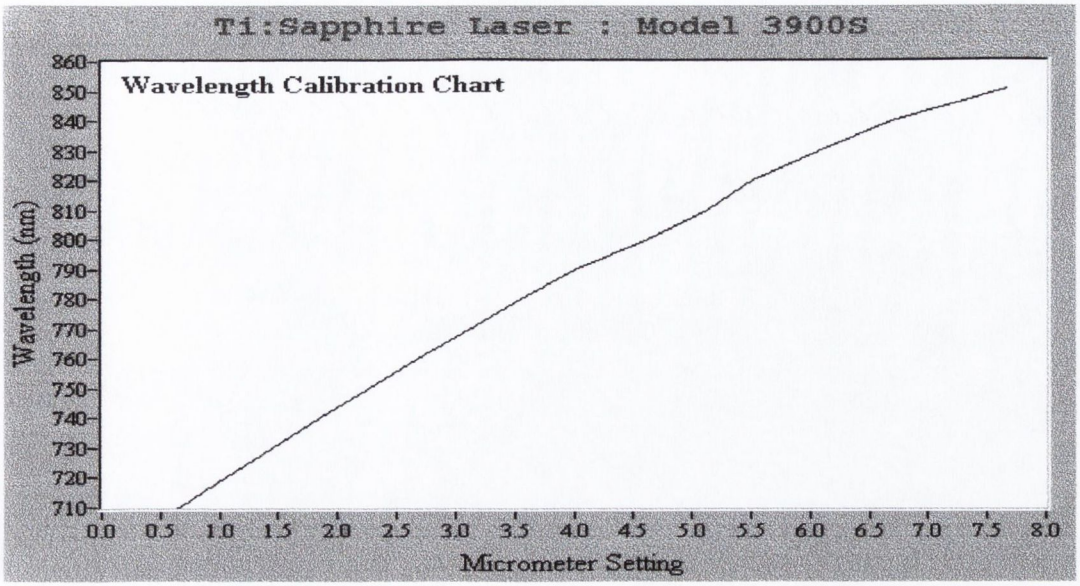

Fig. 5.5 Calibration chart for the micrometer on the Ti:Sapphire laser.

As the wavelength changes, the output beam does not change direction making this source ideal for ESPI contouring. The power does not fluctuate as the wavelength changes and selecting the different wavelengths is repeatable to 0.5 nm. Using the Michelson interferometer the coherence length was also measured over the range. It was measured at greater than 10 cm over the range of 760 to 830 nm, which was more than adequate for our purposes as the optical arrangement would always ensure that the surface is placed in at nearly zero optical path difference.

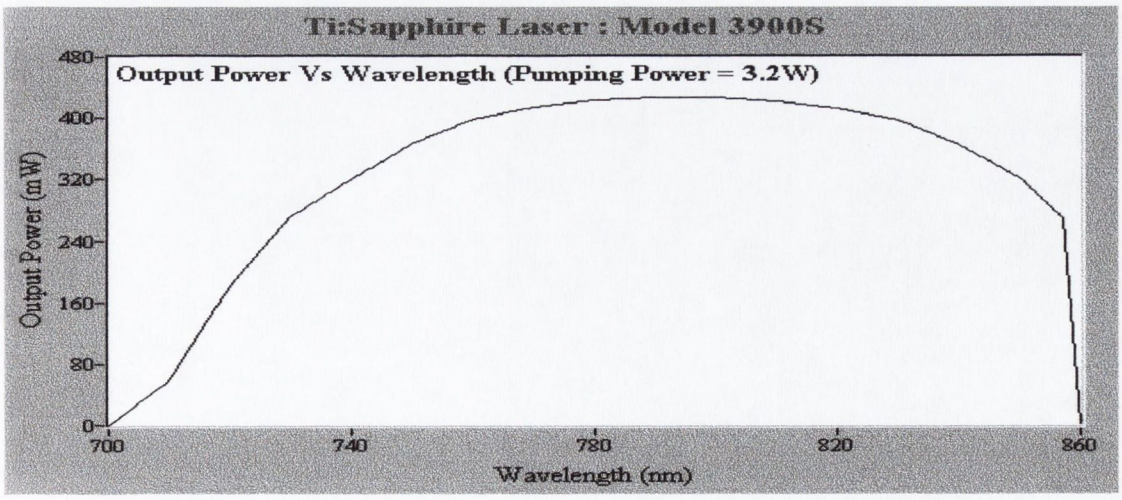

Fig. 5.6 Graph of output power of the Ti:Sapphire laser versus wavelength.

5.2.2 Optical Setup

An optical setup for ESPI contouring was designed which is almost identical to the white light profiling interferometer. The only difference is the light source, as the white light profiler has a white light source and a helium-neon laser, both of which are unsuitable as sources for a contouring system. To produce ESPI contour fringes a variable wavelength coherent source is used. In the white light profiler the helium-neon laser is used for alignment purposes only. Therefore it can be replaced with the Ti:Sapphire laser which can also be used for alignment. This optical system, as shown in Figure 5.7, can now be used for both white light profiling and ESPI contouring. A microscope objective lens is added to the system to produce a diverging beam from the laser, which is then collimated using the same collimating lens used by the white light source. In the contouring system, the CCD camera grabs an image of the surface to be profiled. Frames are then grabbed and subtracted from the initial image in real-time (25 Hz) and the result rectified. This is displayed on the computer monitor so that when the wavelength is changed fringe patterns are displayed, representing contours of the shape of the surface, as described in Chapter 2. All the optical components used in the white light profiler are again used in the ESPI contouring system.

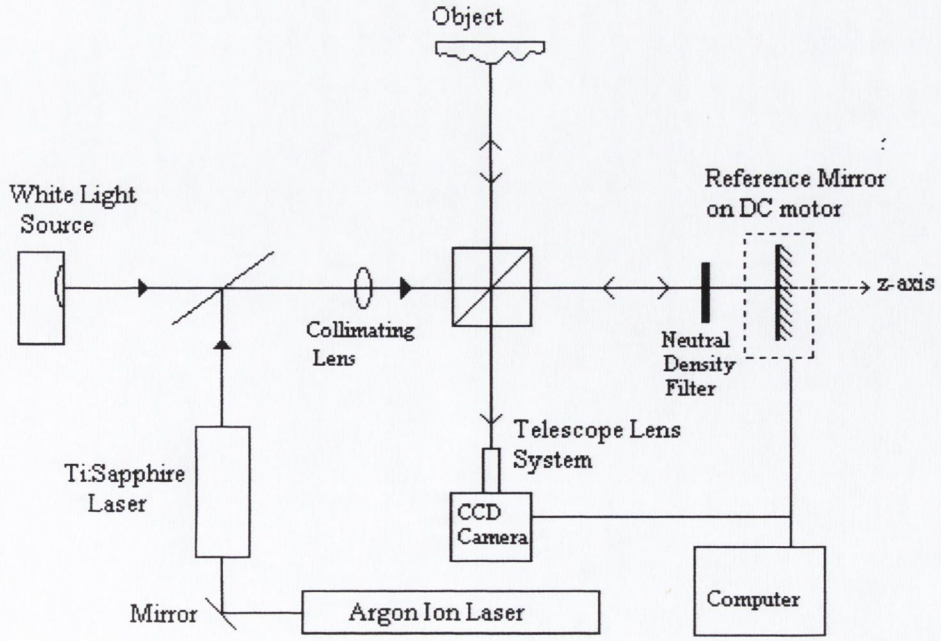

Fig. 5.7 The schematic of the optical arrangement of the dual white light profiling / ESPI contouring system.

5.3 Results

5.3.1 Analysis

Optically smooth surfaces can now be profiled with an accuracy of ± 0.06 μm using the white light technique. Optically rough surfaces can be measured using the ESPI contouring technique. The initial result from any ESPI system is a fringe pattern that, in this case, maps points of equal surface height. To obtain maximum sensitivity, the largest possible wavelength change must be used. Two adjacent fringes in the pattern produced when changing from 760 nm to 830 nm represent two areas on the surface that have a height difference of approximately 4.5 μm. However, as was mentioned in Chapter 2, to produce good correlation fringes, the speckles must not move and the speckle size must not change when the wavelength is changed. As the speckle size is dependent on the wavelength, given by the following equation

$$d_{sp} = \frac{2.4\,\lambda v}{a} \qquad \text{Equation 5.2}$$

the speckle size will always change as the wavelength changes. In Equation 5.2, a is the aperture of the imaging system and v is the distance from the lens to the image plane. So long as the change in size does not affect the intensity in each pixel of the CCD array, it will have no effect on the correlation fringes. From Equation 5.2, it can be seen that a change of 70 nm produces a change in the speckle size of almost 10 %. When this happens it is no longer possible to effectively correlate the intensities of two speckle patterns, taken before and after the change in wavelength, due to an actual change in the shape of the speckle pattern. If the wavelength is increased, the shape of the pattern changes because of the decrease in the number of speckles, due to the increase in speckle size. This change causes decorrelation in the fringes which is seen as a drop in the visibility

of the fringes. Even if these fringes could be obtained and analysed the sensitivity is not adequate. The difference in phase between neighbouring fringes is 2π which corresponds to a height difference of 4.5 μm. With visual examination the sensitivity is, at best, one tenth of a fringe which is 450 nm. However, even this resolution is hard to achieve due to the speckle noise. Applying a phase-shifting algorithm eliminates both these problems.

The phase-shifting technique is described in Chapter 2 and Chapter 4, where it is applied to an in-plane ESPI system. The phase-shifting algorithm used in that system can also be used here. This involves taking one image at the first wavelength and four images at the next wavelength with a $\pi/2$ phase shift between these four. The algorithm then works out the change in phase due to the change in wavelength. The result of the phase-shifting algorithm is the wrapped phase fringes that can be unwrapped using an appropriate algorithm. Then, the following equation is used

$$\Delta\phi = 2\Delta z\left(\frac{2\pi}{\lambda}\right) \qquad \text{Equation 5.3}$$

to produce a surface contour map. Using the phase shifting algorithm not only eliminates the high frequency speckle noise, but also allows a resolution of at least $2\pi/100$.

It is also possible to make a small change in the wavelength and produce a low sensitivity wrapped phase fringe pattern. Then another small change can be made to again produce a similar wrapped fringe pattern. These two wrapped phase fringe patterns can then be added together to produce a high sensitivity wrapped phase map. For example Figure 5.8A shows a wrapped phase fringe pattern obtained when the wavelength was changed from 760 nm to 765 nm. Figure 5.8B shows the fringe pattern obtained when the wavelength was changed from 760 nm to 770 nm. The sensitivities of these two changes are approximately 58 μm and 30 μm respectively. when the wavelength change was taken from 760 nm to 765 nm

and then from 765 nm to 770 nm and the two phase map were added (modulus 256) together, Figure 5.8C was produced. This pattern is the approximately the same as the pattern in Figure 5.8B, showing it is possible to make multiple wavelength changes and add the resulting wrapped phase maps instead of making just one large change. This solution eliminates the problem associated with decorrelation when a large change in wavelength is made. It is now possible to change the wavelength from 760 nm to 830 nm, in steps and produce a resultant wrapped phase map with a sensitivity of $2\pi/100$, which corresponds to a height difference of 45 nm.

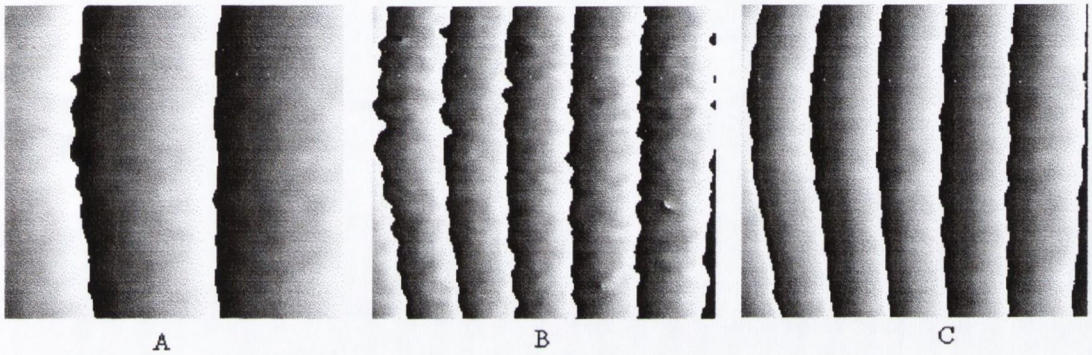

Fig. 5.8 A Phase map obtained when the wavelength was change from 760 nm to 765 nm; B Phase map obtained when the wavelength was changed from 760 nm to 770 nm; C Phase map obtained after the addition modulus 256 of two phase maps obtained when the wavelength was changed from 760 nm to 765 nm and from 765 nm to 770 nm.

In the in-plane system described in the previous chapter, a liquid crystal device was used to introduce the phase shift. The ESPITest software controls a National Instruments data acquisition board which is capable of outputting a voltage of 0 – 10 V. This voltage can be amplified using external electronics so that it can control a piezeo-electric transducer (PZT). The reference mirror can be mounted on the PZT allowing the computer program to control the phase-shift. By moving the reference mirror in calibrated steps it was possible to perform the phase-shifting algorithm and so produce the wrapped phase maps. These could be then unwrapped using the ESPITest software.

As in the white light technique, the spatial or lateral resolution is dependent on the size of the illuminated area imaged onto the CCD array. Using the maximum object size of 5 x 5 cm, allowed a spatial resolution of 100 μm.

5.3.2 Surface Contours

The dual system has been developed for a future project in the European Commission Joint Research Centre, so the objective of the following tests was to check that the system could indeed measure different types of surfaces. It was not an original objective to produce wrapped phase maps by the use of the phase-shifting algorithm. Instead it had to be ensured that the system could indeed produce ESPI fringe patterns that described the shape of the surface. Once the system was producing these fringe pattern the phase shifting could be easily introduced later, in the same way that phase shifting is incorporated into any ESPI system.

The contouring system was mainly tested on rough surfaces which were sloped with respect to the illuminating wavefront. The first test was to measure sloping surfaces whose slope was known. After that various materials with different surface finishes and reflectivities were examined. Once it was ensured that the fringes could indeed be interpreted using equation 5.3, different shaped surfaces were measured. Phase shifting was introduced into the system in time to allow a few wrapped phase-maps to be produced. The first phase maps obtained are shown above in Figure 5.8.

The surface was imaged onto the CCD camera and the first frame was grabbed and recorded. All subsequent frames were subtracted from the first frame in succession. This meant it was possible to watch the fringes form and change as the wavelength was changed. The wavelength could be changed by as much as 70nm without the intensity changing. Therefore, a fringe sensitivity of 4.5 μm was possible. As mentioned previously, to get a better resolution, the full wavelength range of the titanium sapphire laser could be used. In this case a sensitivity of 2

μm is possible. If this change in wavelength was taken in one step, decorrelation would occur due to the change in wavelength causing a major change in the speckle size. When using phase-shifting techniques, this can be overcome by taking any number of steps between 700 and 850 nm. At each step the phase map can be calculated. Then the whole set of phase maps can be added together to produce a high resolution contour map. This method also means the intensity differences at each wavelength are not important as between small changes of wavelength there is little change in the intensity.

To verify the technique by obtaining quantitative results, a sloping surface that measured 10 cm by 15 cm was profiled, as shown in Figure 5.9A. The dimensions and degree of slope were measured prior to contouring. The wavelength was changed by 0.5 nm between the two frames producing a sensitivity, Δz, of approximately 600 μm. Figure 5.9B shows the resulting fringe pattern. As there are approximately 13 fringes in the image, the value of d, from Figure 5.8A, calculated using the fringe pattern is 7.2 mm. Using a vernier calipers to measure the dimensions shown in the diagram, d was measured at 7.1 mm

These calculations do not take into account errors but it is obvious there are significant errors in the fringe counting method and other errors associated with the accuracy with which the wavelength can be changed using the micrometer. These tests were, however, only to prove the feasibility of using the technique in the white light interferometric setup. If real quantitative results were needed phase-shifting algorithms could be used to improve the sensitivity and resolution and thus reduce the errors. This test was repeated using different surfaces and slopes and five typical results are shown in Table 5.3. The values of d, were measured with the vernier calipers but with an error of $\pm$ 0.05 mm as it was difficult to measure accurately to the points on the surface which corresponded to the edges of the image. The error in wavelength of the light, due to the accuracy to which the micrometer could be read, produces an error in the fringe sensitivity of approximately $\pm$ 200 nm.

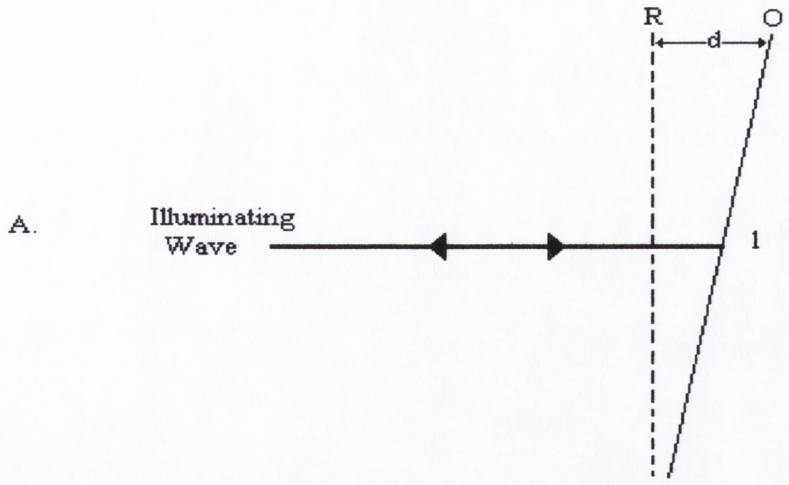

B.

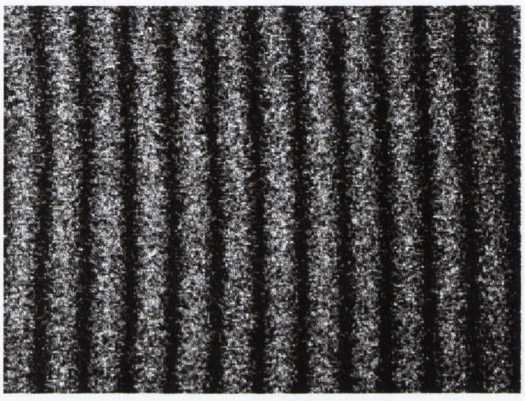

Fig 5.9 A. An optically rough surface mounted in the system as a slope to the x-y plane; B. The resulting ESPI contouring fringe pattern.

Vernier Calipers Reading / mm	d, as measured by ESPI / mm
4.2	3.9
10.3	10.1
13.4	13.8
16.6	16.7
20.0	19.1

Table 5.3 The values of d as measured by a vernier calipers and ESPI contouring

Figure 5.10 show the difference in fringe quality when using the different light sources described in the previous section. Using two lines of the argon ion laser, 496.5 nm and 501.7 nm, images A, B and C were produced. Image A was produced by changing from 496.5 to 501.7 and B was obtained by changing back

from 501.7 to 496.5. The wavelength was changed by rotating the prism in the argon ion cavity. As this proved difficult to precisely control, image C was taken to try and repeat image A. All three images contain approximately seven fringes, thus representing the same slope, with a fringe sensitivity of 24 μm. The fringe contrast is varying over the image on account of the intensity changes produced when changing the wavelength.

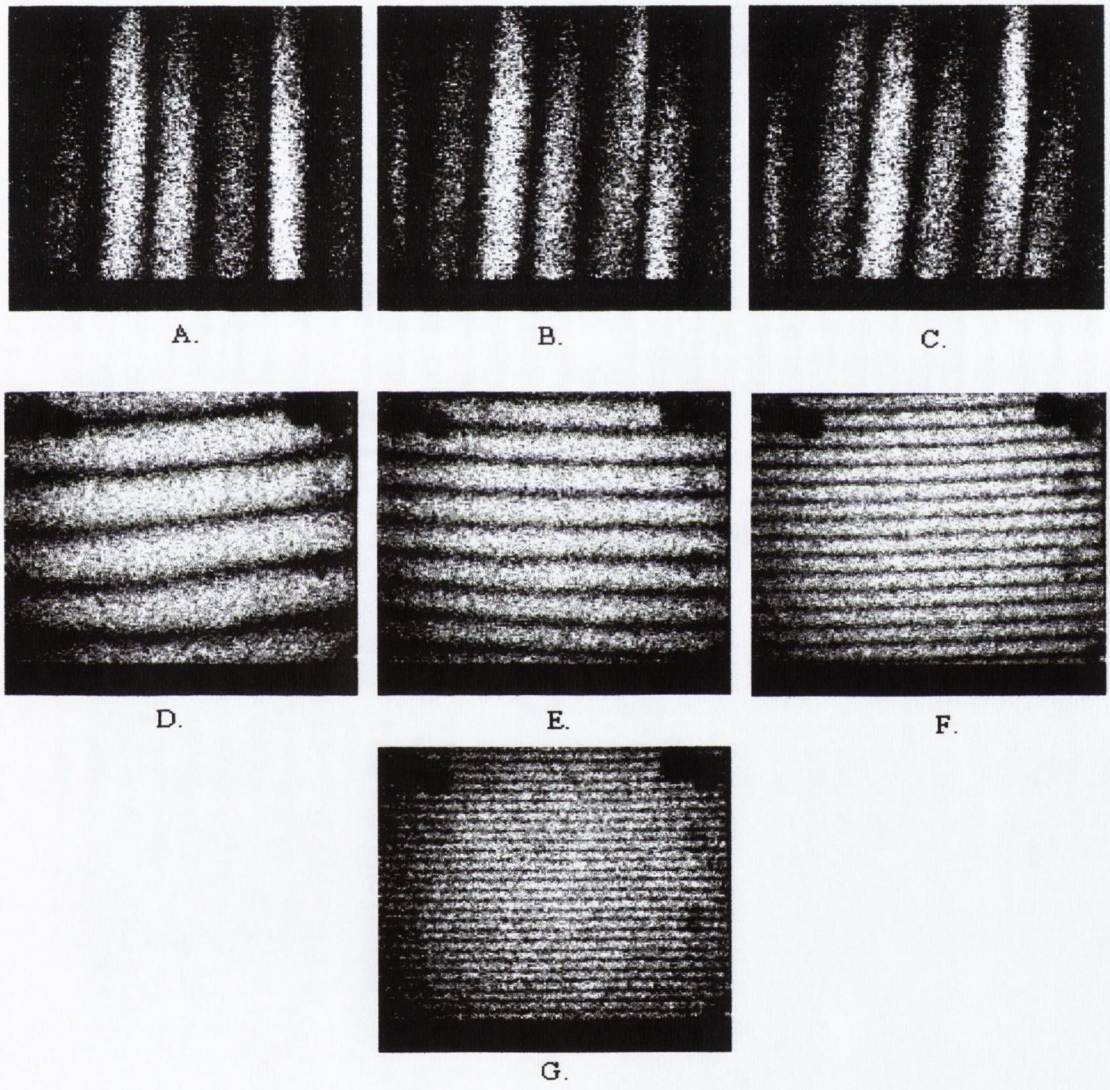

Fig. 5.10 ESPI contour fringe pattern taken from sloped surfaces; A, B, and C using the argon ion laser and D, E, F and G using the Ti:Sapphire laser.

This meant that images with more than seven or eight fringes, had very poor quality fringes. Images D, E, F and G were produced using the Ti:Sapphire laser. The ability to continuously tune the wavelength provided a continuous range of

sensitivities. The fringe quality is now visibly better, allowing for more than twenty fringes to be counted in image G.

The fringe patterns shown in Figure 5.11 were obtained from a curved surface. The yellow line represents a peak on the surface and the blue line is a trough. The wavelength of the light was only varied by 1 nm to obtain the fringes in the second image. This corresponds to a fringe sensitivity of approximately 300 μm. The fringes can be analysed simply by counting the number of fringes so long as the dimensions of the surface are known.

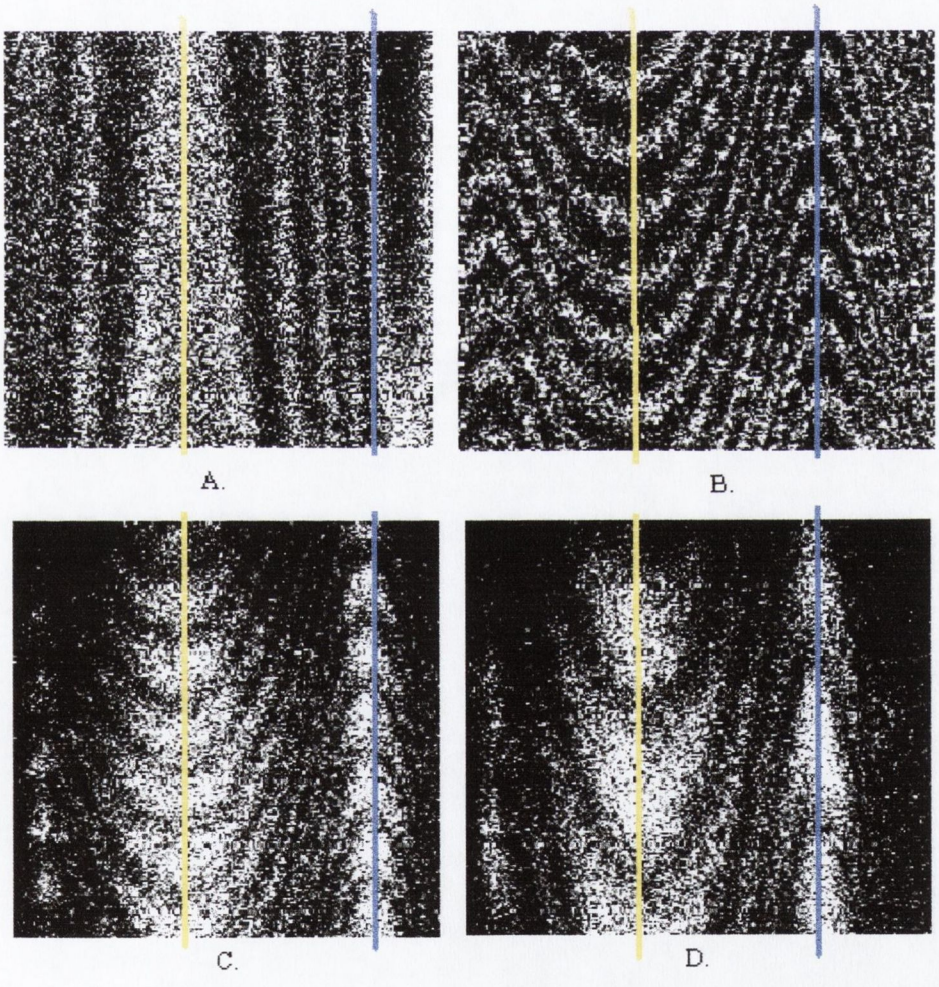

Fig. 5.11 ESPI contour fringe patterns from a curved surface.

However another major disadvantage of not using the phase-shifting technique is that there is no way of knowing which way the surface is sloped. Without prior knowledge of the surface or at least the ability to view the fringes as they form,

there is no way of knowing from the fringe pattern alone which way the surface is sloping. If the source has a continuously tunable range such as the titanium-sapphire laser the direction of the slope can be ascertained by the direction in which the fringes move as the wavelength is changed. When the wavelength is increased the fringes move up a slope, towards the viewing direction (positive z direction). When the wavelength is decreased they move down the slope. If a discontinuous tunable source is used, such as the argon ion laser, then the fringe pattern appears immediately when the wavelength is changed and there is no way of knowing the direction of the slope.

Phase-shifting eliminates this problem as the direction of the sawtooth waveform, that represents the profile of the phase fringes, automatically provides the direction of the slope. Figure 5.12A shows a typical wrapped phase fringe pattern obtained from a sloped surface. Figure 5.12A also shows a line profile taken through the fringe pattern. If this was obtained from an increase in the wavelength, the sawtooth wave travels up the slope. In other words, the ramp in the waveform is pointing towards the viewing direction. Figure 5.12B shows the unwrapped phase map of this image and the line profile.

This clearly shows the slope of the surface and the steepness. Thus using phase-shifting eliminates the need for prior knowledge of the surface or the need to view the fringes form.

The phase shift was introduced by calibrated movements of the reference mirror. Figure 5.13 shows the wrapped phase map, the unwrapped phase map and the surface contour map obtained from a highly curved rough surface. The wavelength was changed from 760 nm to 761 nm, so that a phase shift of 2π was produced between two points whose surface height difference was 290 μm. Thus the distance from the trough to the peak is approximately 2 mm.

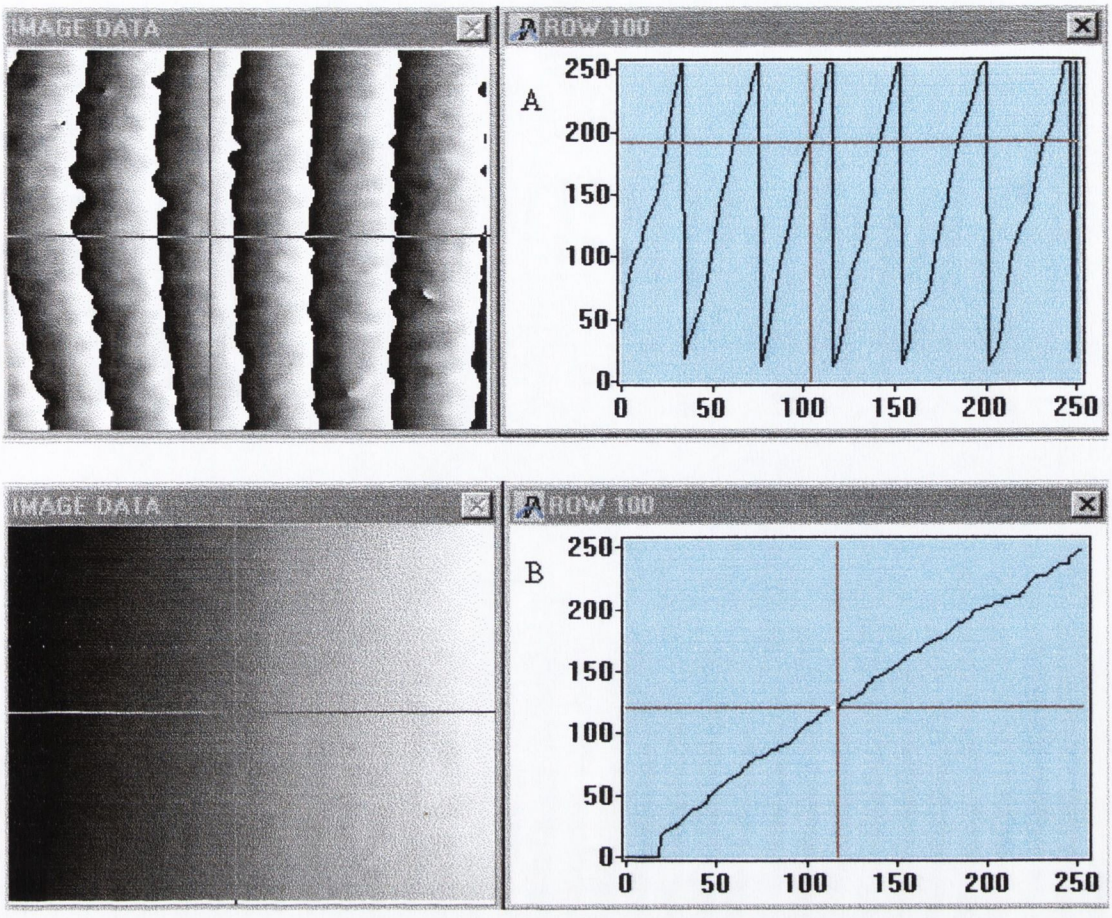

Fig 5.12 A. Wrapped phase fringes and a line profile and ; B. Unwrapped phase map and a line profile

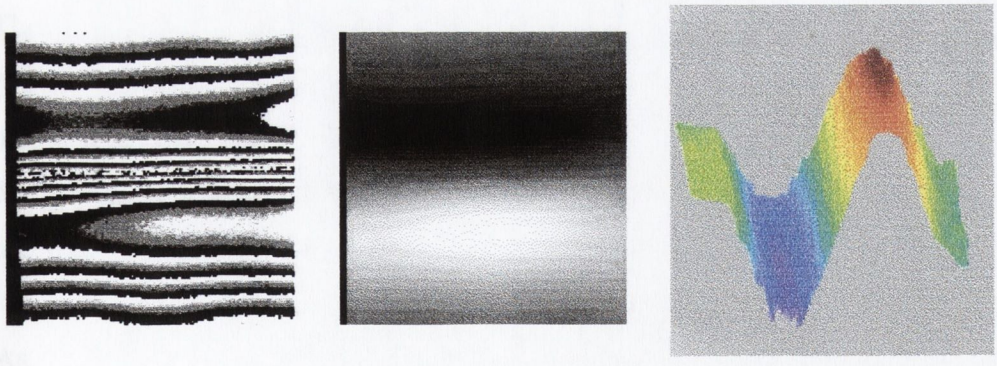

A B C

Fig. 5.13 A The wrapped phase fringes; B The unwrapped phase map and; C The surface contour map.

It was now possible to make small wavelength changes and add the resulting wrapped phase maps. In this way, the whole wavelength range of the titanium sapphire laser can be used to allow a very high sensitivity. Alternatively a very small step can be taken allowing relatively large surface height variations to be measured. Figure 5.14 shows the contour map of a pit in an aluminum plate which has a maximum depth of 5.2 mm.

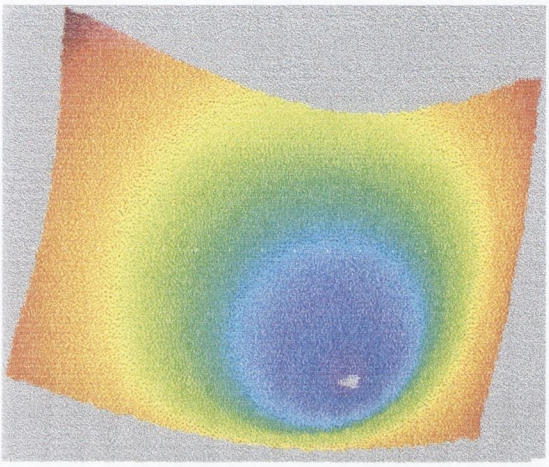

Fig. 5.14 A pit on an aluminum surface.

5.3.3 Comparison of ESPI contouring and white light profiler

The final feasibility test involved measuring the shape of a highly curved optically rough surface. The surface is shown in Figure 5.15A, as measured using a mechanical device. It has a maximum height of 16 mm, with dimensions of 52 x 60 mm. This was placed in the system and was first profiled using the white light technique.

As expected the white light profiler had difficulty in profiling areas of the surface other than those illuminated at an angle near normal. The resulting three-dimensional image is shown in Figure 5.15B. The same surface was then measured using the ESPI contouring technique and much more of the surface was measured, as shown in Figure 5.15C. There are only significant errors around the very edges of the object and this is due to the bad illumination in those areas.

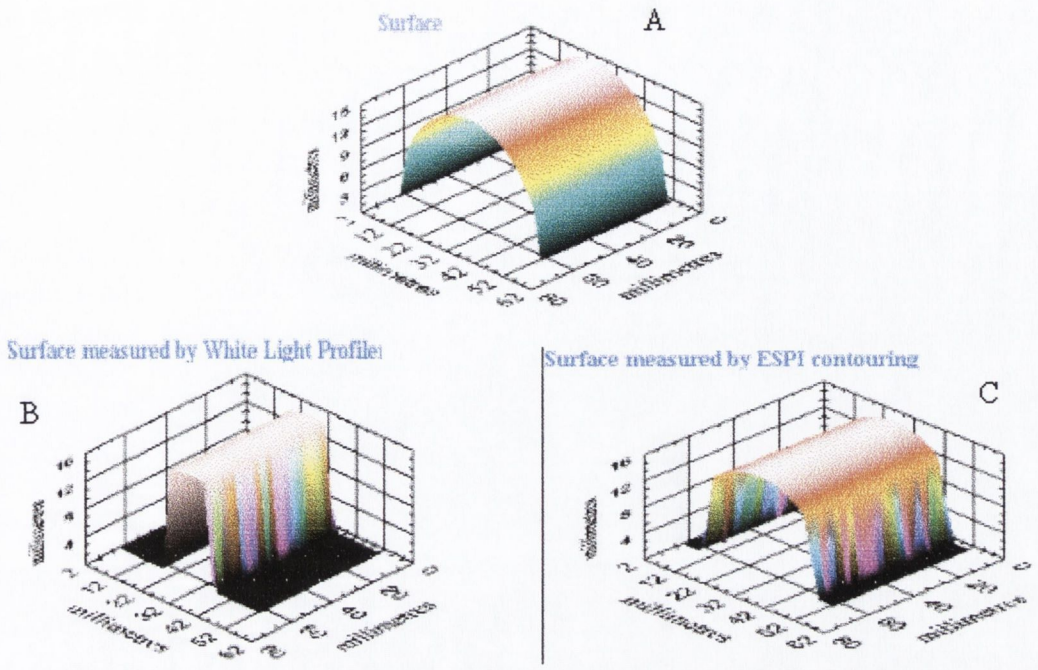

Fig. 5.15 A. A curved surface placed in the surface and measured by; B The white light technique and; C The ESPI contouring technique.

5.4 Conclusion

As mentioned in Chapter 3, the white light interferometric technique is ideally suited to discontinuous smooth surfaces while rough and curved surfaces cause significant errors. The ESPI contouring technique requires a speckle pattern to work and is therefore more suited to profiling rough surfaces. It was for this reason that the ESPI contouring system was added to the white light profilometer. This dual profiler can efficiently profile both rough and smooth surfaces. The ESPI technique is capable, when using phase-shifting algorithms, of measuring rough surfaces with a high resolution. The system also has the ability to measure out-of-plane displacement. For some applications it would be advantageous to profile the surface before carrying out deformation tests. In this case, it is then possible to map the measured surface displacements onto the profile of the surface.

In order to investigate the feasibility of such a system, an ESPI contouring system was designed. The optical configuration of the white light profiler is used for the contouring system, as the collimated light ensures that the fringes represent surface contours. ESPI contouring by wavelength modulation was developed over twenty years ago. However, it is not a very commonly used technique as it is also possible to do ESPI contouring by changing the illumination angle and wavelength modulation was not very practical. However, ESPI contouring by wavelength modulation offers two great advantages of typical contouring systems, in that it has no moving parts and using an appropriate source the sensitivity can be continuously changed over a large range. Moving parts in any ESPI system can lead to errors associated with instability. As ESPI systems measure phase, stability is essential and any moving part is a potential source of mechanical instability.

With the developments in laser technology over the last few and the emergence of tunable laser diodes, ESPI contouring by wavelength modulation is once again becoming an attractive way of measuring shape. Tunable laser diodes, with adequate output intensities, are still expensive and usually operate in the mid-infra-red region, beyond the sensitivity of the CCD camera, but it is only a matter of time before higher power tunable laser diodes with wavelengths compatible with CCD cameras become widely available.

It was with this in mind, that the ESPI contouring technique was combined with the white light system to produce an efficient and relatively unlimited surface profiler. Three possibilities were investigated as variable wavelength sources for this system; an argon ion laser; an argon ion laser with acousto-optic filter; and a Ti:Sapphire laser. While all three options were successful the Ti:Sapphire proved to be the most successful. The wavelength could be changed with a range of 700 nm to 850 nm with a resolution of 0.5 nm. The intensity of the light across this range varied very little and the direction of the emitted light remains unchanged.

This source was used in the ESPI contouring system and various measurements were taken. The system worked well and produced high quality fringe patterns. The dual surface profiling system was now complete and working efficiently. In

the future, when they become widely available, tunable laser diodes can replace the Ti:Sapphire laser in the system making the system a portable and robust optical surface profiler.

The dual system is capable of profiling both optically rough and smooth surfaces. It has a resolution of 0.06 μm when profiling optically smooth surfaces and as low as 0.045 μm when measuring optically rough surfaces. Using phase shifting a resolution of one hundredth of a fringe spacing is possible, which corresponds to $2\pi/100$. If the wavelength is changed from 760 nm to 830 nm, a fringe spacing is equal to a height difference of 4.5 μm. Therefore the maximum possible height resolution is 0.045 μm. The wavelength change must of course be taken in steps and the calculated phase maps added together. The smallest possible change in wavelength is 0.5 nm, which corresponds to a height difference of approximately 0.6 mm. The exact number of fringes that can be resolved depends on the contrast of the fringes, but is typically 50. After this number the fringe thickness is comparable to the speckle size and as mentioned in Chapter 2, this significantly reduces the fringe visibility. If twenty fringes are obtained when the wavelength was changed by 0.5 nm, the corresponding height difference is 12 cm Obviously in this case the resolution is only 6 μm.

The versatility, range and resolution make this system ideal for profiling almost any surface. With the introduction of a tunable laser diode the system becomes very compact and simple. As the same optical components, camera and frame grabber are used for both techniques, the system is a relatively inexpensive tool for shape measurement.

Chapter 6 Characterisation of Liquid Crystal modulators for use in active interferometers

6.1 Introduction

In Chapter 4 it was proposed to use liquid crystal elements as switching and phase-shifting devices in the dual in-plane Electronic Speckle Pattern Interferometer. In particular, it is intended that these devices replace typical piezoelectric elements that tend to be large in size and usually require high driving voltages and power. Nematic liquid crystals consist of molecules that are randomly positioned with respect to one another yet tend to be orientated along the same direction. This bias in molecular orientation results in pronounced anisotropy of the crystal layers thus making it optically birefringent. The degree of alignment of the crystal molecules can be varied by applying an electric field that controls the amount of retardation associated with the fast and slow axes of the device. Such a device, therefore, can be used as a polarisation controller or a phase-shifter, depending on the polarisation state of the light and the relative orientation of the crystal.

This chapter describes the basic physics of liquid crystals and how they can be employed as either polarisation rotating or phase-shifting devices. An extensive experimental investigation was carried out in order to study the behaviour of these particular LC-devices and to characterise their performance particularly with respect to their sensitivity, linearity, range and response time. The objective was to see if these devices could replace the more traditional devices used in interferometry.

The two principal requirements of most modern dual-path, multi-axis interferometers used for optical metrology are efficient use of the illumination available from the light source and some means to phase-shift the reference wavefront to facilitate quantitative measurement. A polarisation based optical

switch can be used to switch all the available light from one measuring axis to the other without significant loss. This optical switch usually consists of an electro-optic polarisation rotator that controls the polarisation state of the source, combined with fixed polarisers incorporated in the optical scheme.

Phase-shifting is usually achieved by the inclusion of a piezoelectric element that moves a mirror located in the optical path of the reference wavefront when a voltage is applied. However, PZT devices often require high voltages and power therefore driving electronics can be bulky and expensive. An alternative to PZT phase-shifters is to use liquid crystal devices, as described in this investigation. In general, the phase-shifting devices must be capable of introducing a phase-shift of at least 2π and the polarisation rotator must be able to rotate the plane of linearly polarised light by at least 90 degrees. Also, for both switching and phase-shifting devices, fast response times, low voltage operation, easy handling and mounting, good stability, high optical transmittance, high efficiency and low cost are all desirable.

An electro-optic modulator is a device that has a variable birefringence in response to an applied voltage across the material. Electro-optic modulators which utilize the Pockels effect [142] may be classified as either longitudinal or transverse, as shown in Figure 6.1. The Pockels effect is a term used for the linear electro-optic effects in crystals. In longitudinal modulators, the electric field is parallel to the direction of light propagation; hence transparent electrodes are required. Transverse modulators operate with the electric field perpendicular to the direction of light propagation, thus avoiding placing the electrodes in the path of the light. There are many materials, both solid and liquid, that exhibit the electro-optic effect, but only a relatively small number have proved useful for practical applications.

One particular material, lithium niobate ($LiNbO_3$) has been in use as an electro-optical modulator for many years [143]. There are many publications detailing its properties and applications as a modulator [144]. The use of liquid crystals as

optical modulators, on the other hand, is new. There are many different types of liquid crystal exhibiting a wide range of properties.

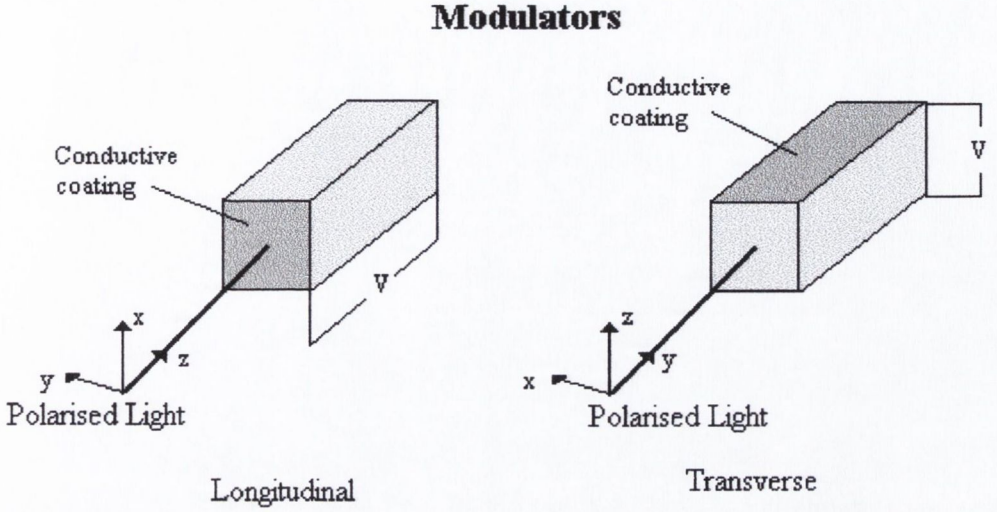

Fig. 6.1 Electro-optical modulators

Liquid crystals have some obvious advantages over the lithium niobate crystals. Firstly, they use lower operating voltages. This is important since it is possible to control liquid crystal devices using a D/A card in the computer without the need for an external amplifier. Low voltages also make the systems safer and therefore more attractive to industry. The atomic structure of the lithium niobate crystal devices available render them unsuitable for phase shifting, as shown in Figure 6.2. It is not possible to send linear polarised light into the material and change the phase without changing the polarisation of the output light. In the arrangement shown in Figure 6.2, as the voltage is increased the optical axis rotates in a different plane to the plane of polarisation of the light. This means the plane polarised light will be separated into two orthogonal components along the fast and slow axes which will travel at different speeds. This causes a phase change between the components that in turn causes a change in polarisation of the resultant of the components of the emergent light.

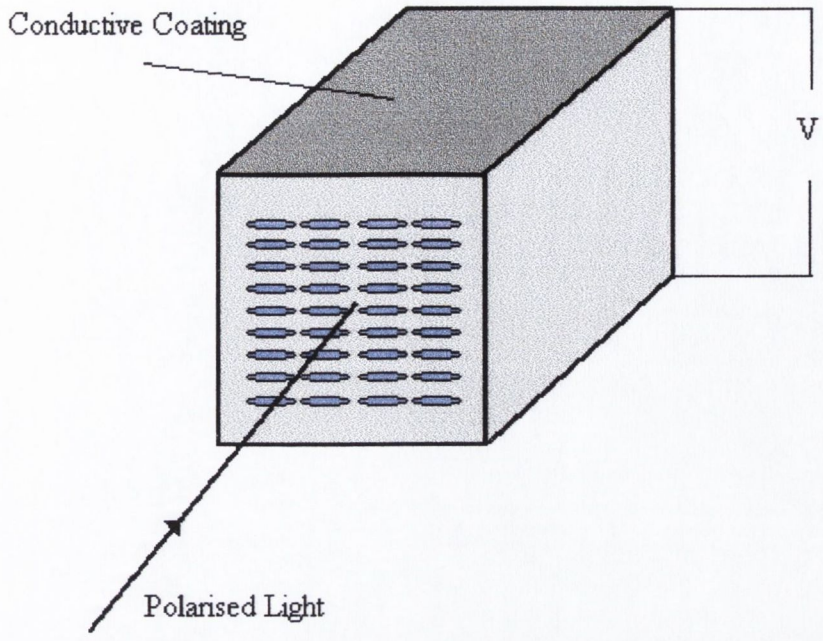

Fig. 6.2 Molecular arrangement of the Lithium Niobate crystal.

The molecular arrangement of the liquid crystals can easily be arranged to make phase-shifting possible without changing the polarisation. The devices can also be manufactured to have a large aperture making it possible to view the object through them, if necessary. The lithium niobate crystals, however, are usually cut in the manner shown in Figure 6.1, making the viewing angle so small as to prevent viewing an object through them. Another important consideration in selecting one of these two types of optical modulator is that liquid crystals are much cheaper and easier to produce than lithium niobate crystals.

6.2 Liquid Crystal devices

6.2.1 Liquid Crystals

This section provides an introduction to liquid crystals and their principal molecular and optical properties. It describes the different types of liquid crystals and the processes involved in making a liquid crystal device for use in the ESPI system. A thorough understanding of these properties is essential as there are

many types of liquid crystal material, with varying properties, and the choice of material for the interferometric devices is important.

The study of liquid crystals began in 1888 when an Austrian botanist named Friedrich Reinitzer discovered a state between liquid and solid [145]. Crystalline materials demonstrate long range periodic order in three dimensions. An isotropic liquid on the other hand, has no orientational order. Substances that are not as ordered as a crystal, yet have some degree of alignment are called liquid crystals. Liquid crystal materials have unusual properties and generally have several common characteristics. Among these are a rod-like molecular structure, rigidness of the long axis and strong dipoles.

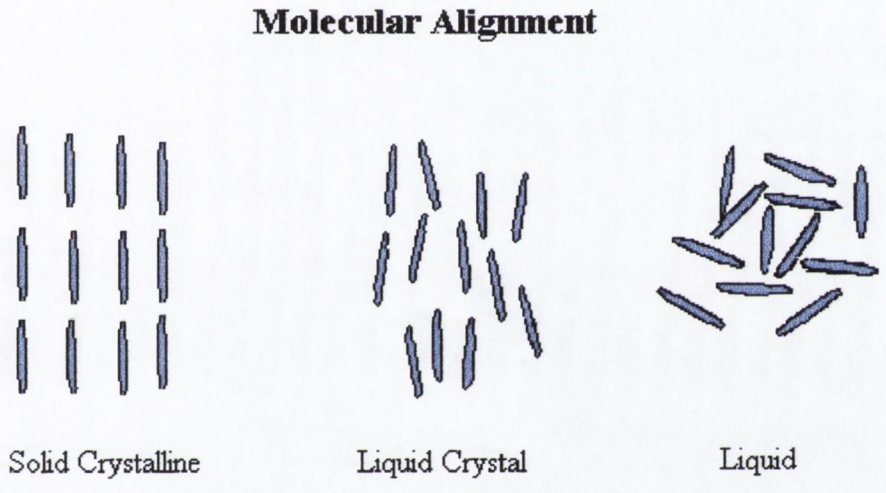

Fig 6.3 The molecular alignment of three states.

The distinguishing characteristic of the liquid crystalline state is the tendency of the molecules to point along a common axis, called a director. This is in contrast to molecules in the liquid phase, which have no intrinsic order. In the crystalline state, molecules are highly ordered but have little translational freedom. Thus the characteristic molecular orientation of the liquid crystal state is between the traditional solid and liquid phases. Figure 6.3 shows the average alignment of the molecules for each phase.

To quantify just how much order is present in a material an order parameter (dS) is defined. The order parameter is given as follows [146]:

$$dS = \left\langle \tfrac{1}{2}\left(3\mathrm{Cos}^2\theta - 1\right)\right\rangle$$ Equation 6.1

where θ is the angle between the director and the long axis of each molecule, as shown in Figure 6.4. The brackets denote an average over all of the molecules in the sample. In an isotropic liquid, the average is zero. For a perfect crystal, the order parameter evaluates to one. Typical values for the order parameter of a liquid crystal range between 0.3 and 0.9, with the exact value a function of temperature, as a result of kinetic molecular motion.

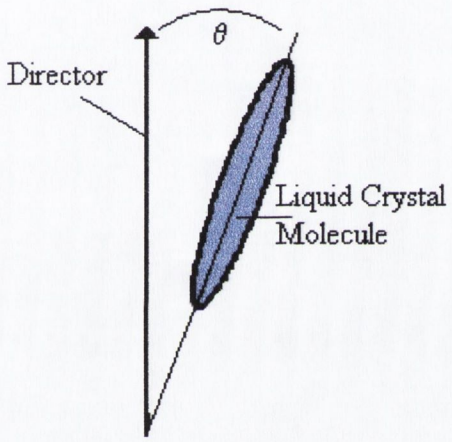

Fig. 6.4 The order parameter defines the degree of order in the material

The tendency of the liquid crystal molecules to point along the director makes the materials highly anisotropic, meaning that the properties of the material depend on the direction in which they are measured.

Most liquid crystal compounds exhibit polymorphism, a condition in which more than one phase is observed in the liquid crystalline state. Depending upon the amount of order in the material, the term mesophase is used to describe the subphases of liquid crystalline materials. Mesophases are formed by changing the amount of order in the material, either by imposing order in only one or two

dimensions, or by allowing the molecules to have a degree of translational motion. We can characterize the different phases, or states, using the following three parameters to describe their molecular structure; positional order; bond orientational order; and molecular orientational order. Each of these parameters describes the extent to which the liquid crystal sample is ordered. Positional order refers to the extent to which an average molecule or group of molecules shows translational symmetry (i.e. how they move together). Bond orientational order describes how the molecules are packed in a two dimensional system, as well as the orientation of a bond joining nearest neighbour centres of mass. Molecular orientation is a measure of the tendency of the molecules to align along the director. It is important to know the effects these parameters have on the properties of the material when choosing a liquid crystal material for a particular purpose.

Certain materials with a solid crystalline state can be transformed into an isotropic liquid. Depending on the detailed molecular structure, the system may pass through one or more liquid crystal mesophases before it is transformed into the isotropic liquid. Transitions to these intermediate states may be brought about by purely thermal processes (thermotropic mesomorphism) or by the influence of solvents (lyotropic mesomorphism). The liquid crystals used in this research were thermotropic. The vast majority of thermotropic liquid crystals are composed of rod-like molecules and are classified into three types: nematic, cholesteric and smectic.

Figure 6.5 shows the molecular structure of the nematic liquid crystal phase, characterised by molecules that have no positional order but tend to be aligned in the same direction (along the director). As mentioned above, liquid crystals are anisotropic materials, and the physical properties of the system vary with the number of molecules aligning with the director. If this number is large, the material is very anisotropic. Similarly, if it is small, the material is almost isotropic. As the temperature of a nematic liquid crystal is increased the material changes to an isotropic liquid.

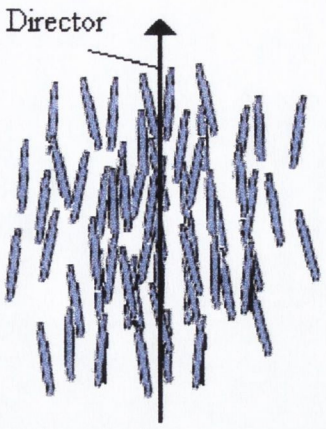

Nematic Liquid Crystal

Fig. 6.5 The molecular alignment of the nematic liquid crystal phase.

A special class of nematic liquid crystals is called chiral nematic, twisted nematic or cholesteric. Chiral refers to the unique ability to selectively reflect one component of circularly polarised light. The cholesteric phase, shown in Figure 6.6, is typically composed of nematic molecules containing a chiral center which produces intermolecular forces that favour alignment between molecules at a slight angle to one another. This leads to the formation of a structure which can be visualized as a stack of very thin 2-D nematic-like layers with the director in each layer twisted with respect to those above and below. In this structure, the directors actually form in a continuous helical pattern about the layer normal. An important characteristic of the cholesteric mesophase is the pitch. The pitch, p, is defined as the distance it takes for the director to rotate one full turn in the helix.

Liquid crystals can be used in a variety of applications because external perturbation can cause significant changes in the macroscopic properties of the liquid crystal layer. Both electric and magnetic fields can be used to induce these changes.

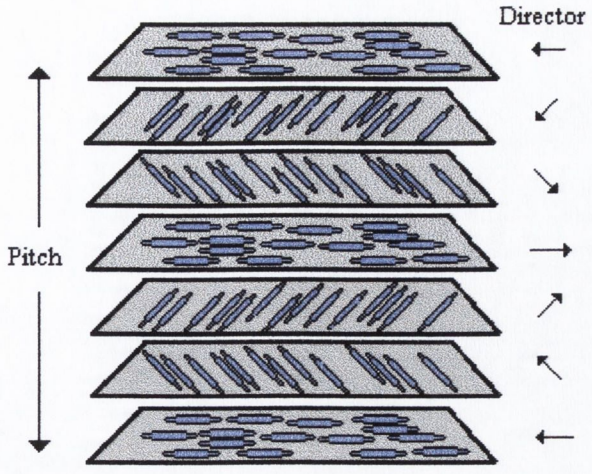

Fig. 6.6 The molecular alignment of the cholesteric liquid crystal phase.

The response of liquid crystal molecules to an electric field is the major characteristic utilized in practical applications, for instance liquid crystal displays. The ability of the director to align along an external field is caused by the electric nature of the molecules. Permanent electric dipoles result when one end of the molecule has a net positive charge while the other end has a net negative charge. When an external electric field is applied to the liquid crystal, the dipole molecules tend to orient themselves along the direction of the field.

In the absence of an external field, the director of a liquid crystal is free to point in any direction. The energy required to deform a liquid crystal is so small that even the slightest perturbation, caused by a dust particle or a surface inhomogeneity can distort the structure quite profoundly. Liquid crystal layers are usually held between two glass plates. Layers in which the molecules are aligned perpendicular to the surface of the plates (homeotropic structure) or parallel to them (homogenous or planar structure) can be prepared by suitable prior treatment of the glass plates. It is possible to force the director to point in a specific direction by introducing an outside agent to the system. For example, the glass plates used to hold and observe liquid crystals may be specially treated so that the molecules near the surface align themselves in a certain direction. A typical special treatment performed on the glass plates employed to align the liquid crystal is a polymer

coating. The surface is rubbed with a cloth to create a series of grooves. The liquid crystal molecules align themselves such that their longitudinal axes are parallel to the grooves.

The competition between orientation produced by this surface anchoring and by electric field effects is exploited in the liquid crystal devices used in the ESPI system. Consider the case in which liquid crystal molecules are aligned parallel to the surface of the glass plates and an electric field is applied perpendicular to the cell. At first, as the electric field increases in magnitude, no change in alignment occurs. However at a threshold magnitude of electric field, deformation occurs. Deformation occurs where the director changes its orientation. The occurrence of such a change from an aligned to a deformed state is called a Freedericksz transition [147]. This is fundamental to the operation of many liquid crystal devices because the director orientation, and thus the properties, can be controlled easily by the application of a field.

Due to their anisotropic nature, liquid crystals are birefringent. In the case of a liquid crystal, light polarised parallel to the director experiences a different refractive index than light polarised perpendicular to the director. When polarised light enters a birefringent material, at an angle other than parallel to the fast or slow axes, it is broken up into the fast and slow components. Because the two components travel at different velocities, they become out of phase. When the waves are recombined as they exit the material the polarisation state has changed because of the total phase difference. The birefringence of a material is characterised by the difference in the indices of refraction for the slow and fast axis. For a typical nematic liquid crystal, this difference may be between 0.1 and 0.2. The thickness of the sample is another important parameter because the phase shift accumulates as the light propagates through the birefringent material. Any polarisation state can be produced with the right combination of the birefringence and thickness parameters. In a typical liquid crystal, the birefringence and thickness are not constant over the entire sample. This means that some areas appear light and others dark when viewed between two crossed polarisers. The

schlieren texture, as this particular arrangement is known [148], is characteristic of the nematic phase.

6.2 Liquid Crystal modulators

6.2.1 Phase retarder

These devices are constructed using optically flat fused silica windows coated with transparent conductive indium tin oxide (ITO), which offers maximum transmission from 450-1800 nm. A thin dielectric layer is then applied and gently rubbed, creating parallel micro-grooves for the molecular alignment. Two such windows are then carefully aligned and spaced 10 microns apart. The cavity is filled with birefringent liquid crystal material and electrical contacts for the ITO films are attached using conductive paint. The glass plates are held in a circular Perspex holder with a diameter of just under 30 mm. The devices were prepared by Fedor Vladimirov at the State Optical Institute, St. Petersburg, Russia. Figure 6.7 shows a photograph of two phase-shifting devices.

Fig. 6.7 Photograph of two liquid crystal devices.

The material, which is a mixture of 6 or 7 nematic compounds, was made by NOIPIK (Moscow) and the exact composition and components is unavailable. The optical anisotropy, or the difference between the slow and fast axis refractive indices, is 0.1315 and the dielectric anisotropy + 4.4.

Figure 6.8A shows the molecular orientation of the material between the glass plates. As mentioned previously, liquid crystals are birefringent materials, whose effective birefringence can be controlled by varying the applied voltage. When polarised light enters the liquid crystal material its two orthogonal components travel at different velocities resulting in a phase change occurring between them. When they emerge from the material and recombine, the resulting polarisation state has changed due to this phase change. An external electric field can cause significant changes in the properties of a liquid crystal material. The molecules have the ability to align along an external field if a voltage is applied across the liquid crystal.

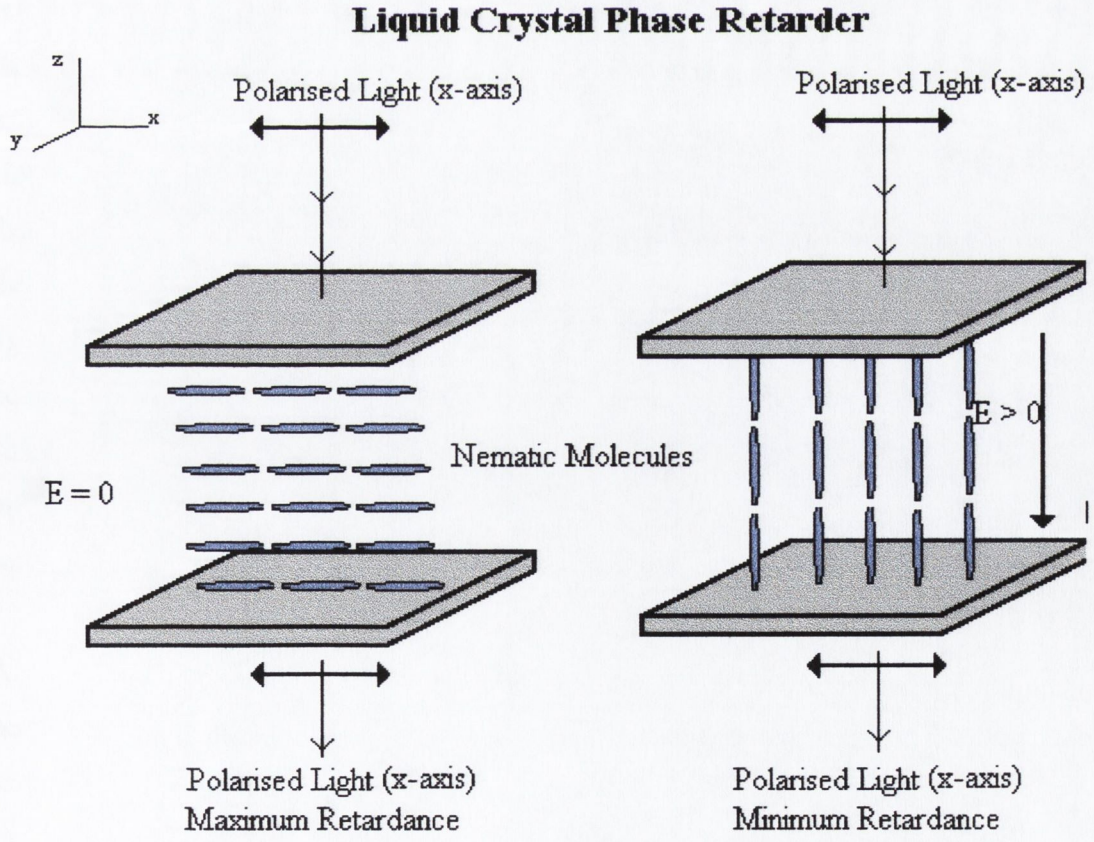

Fig. 6.8 The molecules are aligned parallel with the surface at zero volts and perpendicular at some voltage greater than zero.

By changing the molecular alignment, the amount of retardation can be controlled. In this way, if linearly polarised light is incident on a liquid crystal layer, the polarisation state of the emerging light can be controlled by applying a voltage across the layer. The director of the molecules is the slow axis of the device. If the light entering the device is linearly polarised in the same direction as the slow axis (director) the light travels through the material experiencing a certain refractive index. When a voltage is applied across the liquid crystal layer, the molecules rotate parallel to the electric field, as shown in Figure 6.8b. As the voltage increases the effective value of the refractive index decreases causing a reduction in retardance. Therefore at zero volts, the light experiences the highest refractive index, which decreases, as the electric field increases, until a minimum where the molecules can rotate no further. This happens when the molecules at the surface are unable to rotate freely because they are pinned by the glass plates. This surface pinning causes a residual retardance even at high voltages.

It is important to note that the slow axis of the devices rotates in the same plane as that of the plane polarised light, unlike the molecular orientation shown in Figure 6.2. Therefore the light exiting the device experiences a change in phase but no change in polarisation. This shows how important the molecular orientation and the electric field direction are to the overall effect of the device. For example, if the electric field is in the direction shown in Figure 6.2, the polarisation of the light exiting changes as the voltage is increased. Even though the plane of polarisation is aligned in the same direction as the slow axis, as the voltage changes so too does the orientation of the slow axis. Therefore the light is broken into its slow and fast axis components. This can form the basis of the polarisation rotator.

As the applied voltage controls the phase-shift induced in the beam, the devices need to be calibrated before being used as phase-shifters. This calibration is explained in the experimental section of the chapter. The liquid crystal devices can be optimised to have response times that are compatible with the framing rate of the CCD camera (40 ms) and frame-grabber, thus making them ideal for ESPI.

6.2.2 Polarisation rotator

The polarisation rotator forms the basis of the optical switch. The rotator is held in the same way as the phase-shifter shown in Figure 6.7. A twisted nematic liquid crystal layer and a polymer coating are sandwiched between two glass plates. The polymer coating has the purpose of aligning the molecules near the surface in a certain direction. Two electrodes are attached to the glass plates using conductive paint and the plates are placed in a Perspex holder. The layer is the same thickness as the phase-shifter, 10 microns, and the same nematic material, although in a twisted nematic phase, is used.

The molecular orientation of the liquid crystal material is shown in Figure 6.9. The surfaces of the transparent electrodes in contact with the liquid crystal material are coated with a thin layer of polymer, which has been rubbed or brushed in one direction. The molecules orient with their long axes parallel to this direction. The glass plates are arranged so the molecules adjacent to the top electrode are oriented at a right angle to those at the bottom. In the absence of an electric field, the nematic director undergoes a smooth 90 degree twist within the cell (hence the name "twisted" nematic liquid crystal). The molecular orientation is therefore different in the polarisation rotator than in the phase-shifter. Again, the light entering the device is aligned plane polarised in the same plane as the slow axis (director) at the top of the cell. The twisted arrangement of the LC molecules within the cell then acts as an optical wave guide and rotates the plane of polarisation by a quarter turn (90 degrees) so that the light which exits is plane polarised 90 degrees to the original light entering the device.

When a voltage is applied to the electrodes, the liquid crystal molecules tend to align with the resulting electric field and the optical wave guiding property of the cell is lost, as shown on the right in Figure 6.9. This allows the light to travel through the material without rotating the plane of polarisation. When the electric field is turned off, the molecules relax back to their twisted state and the plane of

polarisation is rotated again. Therefore, by switching the applied voltage from 0 volts to approximately 10 volts, it is possible to switch between vertically and horizontally plane-polarised light.

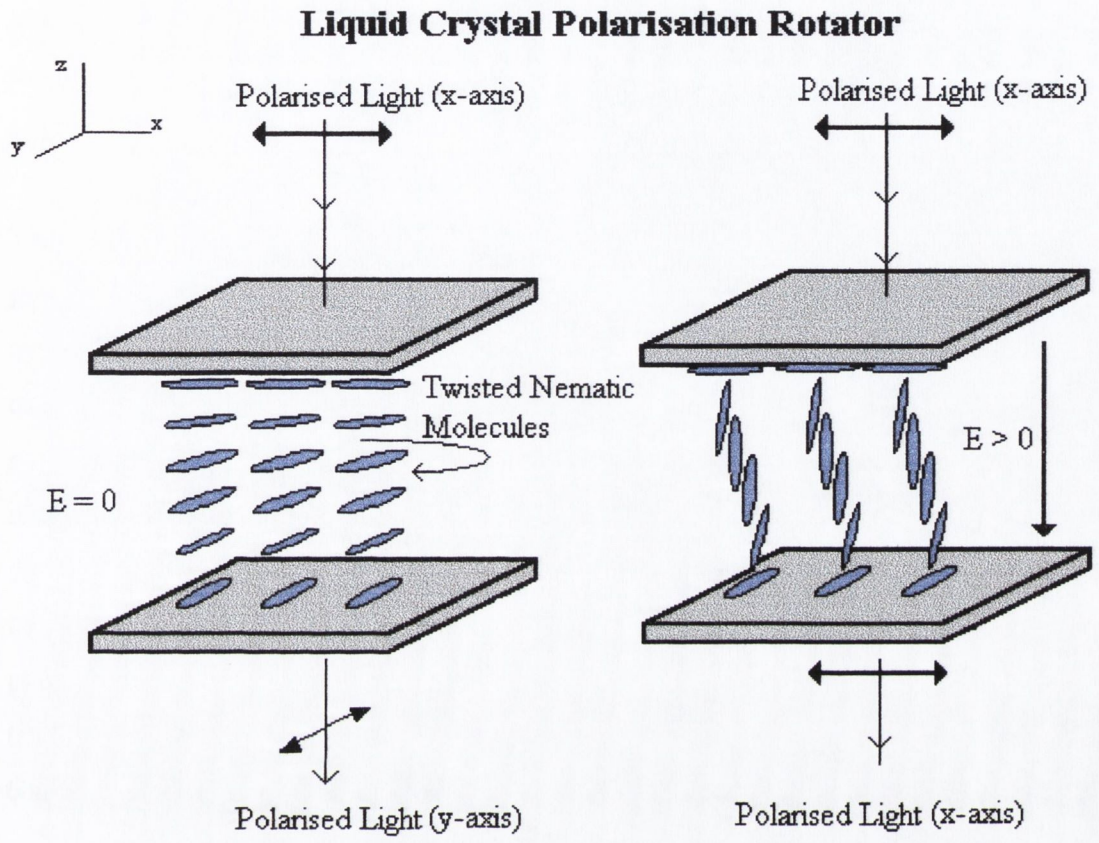

Fig 6.9 At zero volts, the molecular alignment guides the linearly polarised light so that it is rotated by 90 degrees when exiting the device. When a voltage is applied the alignment of the crystals changes so that it no longer guides the light and the polarisation remains unchanged.

6.2.3 Operation

The liquid crystal phase shifters are placed in the path of the laser beam and aligned so that the director is in the same plane as the plane of polarisation of the linearly polarised light. A voltage can be applied to the liquid crystal layer using copper electrodes and the conductive paint. An AC waveform, with no DC component, of approximately 1kHz is applied across the layer. A square wave is used to prevent ionic build-up caused if a DC voltage is placed across the layer [149]. The peak-to-peak voltage of the square wave determines the phase shift

produced by the device. This voltage can be modulated by a triangular wave to produce a continuous phase modulation. The devices had to be calibrated and the frequency response obtained as this information is needed if the devices are to be used in the interferometer to produce a phase shift of 2π. The experiments described in the next section were performed to characterise the devices accurately.

The liquid polarisation rotator is also aligned so that the director is in the same plane as the plane of polarisation of the linearly polarised light. The voltage is applied in the same way and must also be a square wave to prevent damage to the device. At zero volts peak-to peak the plane of polarisation of the laser light is rotated through 90 degrees. At a higher voltage the molecular alignment no longer rotates the plane of polarisation and the plane of polarisation is unchanged. If this device is to be used in the ESPI system it is essential to know the voltage required to distort the helical molecular arrangement so that it doesn't rotate the plane of polarisation. It is also important to know at what frequency the device can perform this rotation. The experiments described in the next section were carried out for this purpose.

6.3 Experimental characterisation of Liquid Crystal modulators

6.3.1 Phase-shifter

An active Michelson interferometer was used to characterise the performance of the liquid crystal phase-shifting device. This approach allowed the direct measurement of any change in optical path length induced by the LC-device when placed in one arm of the interferometer, in real-time. Before any measurements could be made on an LC-device, however, it was necessary to calibrate the interferometer and to ensure that its frequency response was uniform over the range of interest. In preliminary laboratory testing the typical response time of the LC-devices was estimated at roughly 0.2 to 0.8 seconds. A measurement bandwidth of 0-100 Hz was chosen which seemed more than adequate. The configuration used to calibrate the active interferometer system is shown in Figure 6.10.

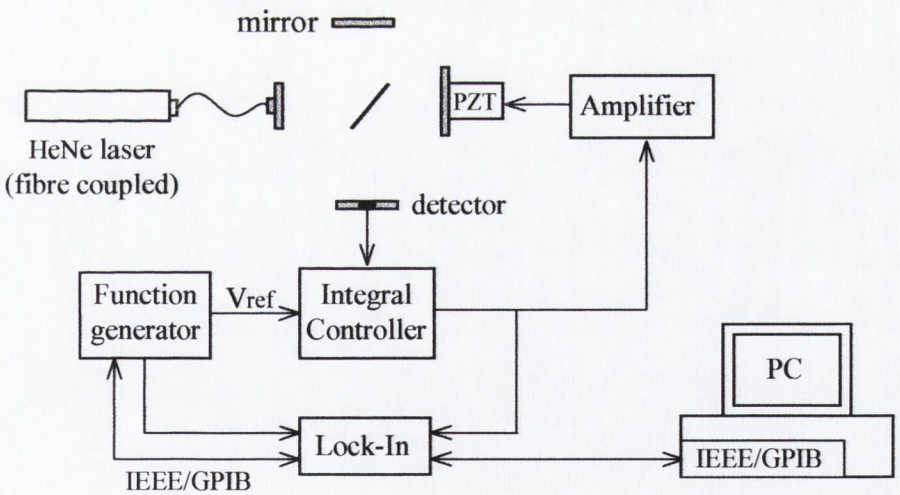

Fig. 6.10 Active Michelson interferometer scheme used to calibrate the piezoelectric phase-shifter.

The system consists of a standard Michelson interferometer utilising a 10 mW helium-neon source and a PZT actuator to move one of the mirrors. The light source was coupled to a single-mode optical fibre to guide light easily into the interferometer and a pig-tailed micro-lens package was used as a collimator. A standard analogue integral controller was used which, once active, locked the PZT-driven arm of the interferometer to an operating point controlled by a reference voltage (V_{ref}). The reference voltage was output from a digital signal generator and either a DC or AC signal could be used to control the system. A lock-in amplifier was used to monitor the feedback voltage from the I-controller to the PZT amplifier, using the driving signal from the function generator as a reference. The initialisation, setup and operation of the lock-in amplifier and signal generator were controlled via IEEE/GPIB communication from a PC. This PC, running a LabView program, was also used for A/D data acquisition. The calibration of the system consisted of two steps. Firstly, with the control system disabled, a triangular waveform voltage was supplied to the PZT amplifier and the signal from the photo-detector recorded. From this measurement signal, the sensitivity of change in optical path length (i.e. phase) to feedback voltage could be obtained, as described below. Secondly, with the control system active, a sine-sweep signal (1 to 100 Hz) produced by the function generator was input to the I-controller as the reference voltage. During the sweep, the lock-in amplifier was used to measure the amplitude of the feedback voltage to the PZT amplifier. The gain of the I-controller was adjusted until the response of the system was constant over the selected frequency range (i.e. 0 to 100 Hz).

The setup used to measure directly the phase-shifting response of the LC-device is shown in Figure 6.11. The value of the quadrature voltage is obtained from the calibration of the PZT. As seen in Chapter 2 the intensity at the detector should modulate in time in a sinusoidal wave, as the reference mirror is moved. This is assuming the reference mirror moves uniformly in time, which depends on the PZT having a linear response to the triangular waveform used for calibration. The light intensity at the detector is measured as a voltage, which will also have a sinusoidal shape.

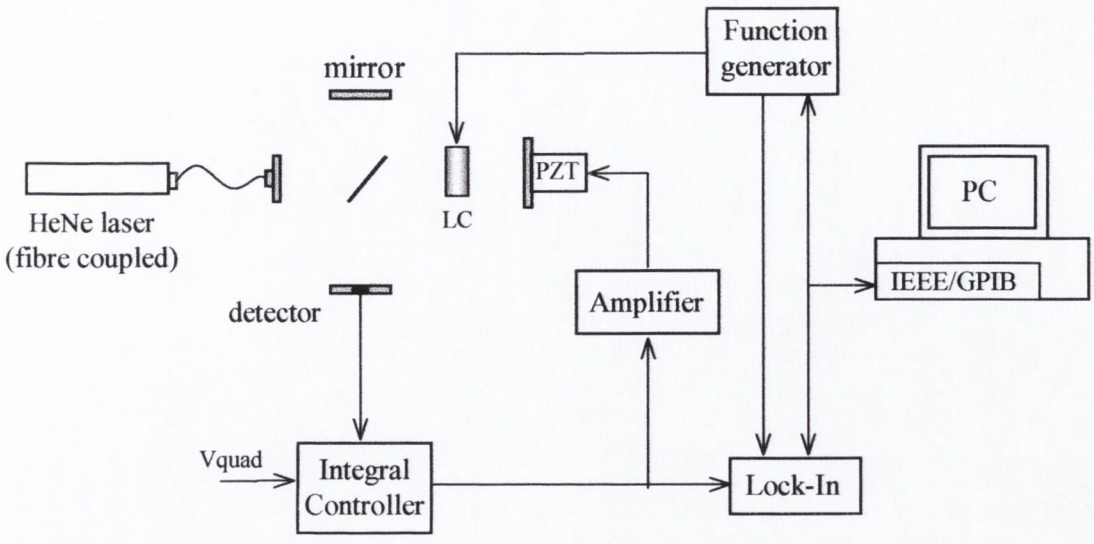

Fig 6.11 Michelson interferometer with active compensation used to measure the response of the Liquid Crystal (LC) phase-shifter.

The quadrature voltage is any voltage that when applied to the PZT produces a voltage at the detector that is half way between a peak and a trough on the sinusoidal waveform. Setting this voltage as the reference voltage allows the interferometer to have maximum sensitivity and a linear response.

The phase shifting liquid crystal device is placed in the arm of the interferometer with the mirror mounted on the PZT. A square wave voltage is applied to the device from a function generator. Again the integral-controller compares the reference voltage to the voltage from the detector and send a feedback voltage to the amplifier of the PZT. A lock-in amplifier is used to monitor the feedback voltage with the signal from the function generator as a reference. The PC using the LabVIEW program controls the settings of the function generator. It also acquires the data from the lock-in amplifier.

As described in the previous section, a square wave voltage must be applied to the LC devices. It is the peak-to-peak voltage that determines the retardance. To calibrate the devices this peak-to-peak voltage was modulated with a triangular waveform so that the peak-to-peak voltage would modulate between 0 and 10 volts. The modulation waveform, which was sent to the function generator from the PC, again using the LabVIEW program, had a relatively long period of ten

seconds. This was to ensure the experiment was performed well within the frequency bandwidth of the device. As the modulated square wave changes the retardance of the liquid crystal the optical path length in that arm of the interferometer changes. This change in phase difference between the arms of the interferometer produces a change in intensity at the detector, which is measured as a change in voltage by the I-controller. The I-controller then outputs a voltage to the amplifier of the PZT to move the mirror so that the detected voltage again equals the reference voltage. In this way, a movement of the mirror compensates for the change in path length caused by the liquid crystal device so that the path length does not change. As the peak-to-peak voltage is changing slowly the response time of the active interferometer is more than adequate to keep up with the changes. By measuring the feedback voltage from the I-controller to the PZT amplifier, the change in optical path length, i.e. phase, caused by the liquid crystal can also be measured.

In the same way that the frequency response of the PZT was measured the response of the liquid crystal phase-shifter was obtained. The sine-sweep signal (1 to 100 Hz) modulated the square wave across the device so that the peak to peak voltage modulated from 0 to 10 volts and the frequency of this modulation swept from 0 to 100 hertz. Again, by acquiring the feedback signal from the I-controller to the PZT amplifier, the response of the liquid crystal device to the sine-sweep signal can be measured. The step response of the device was also measured by changing the peak-to-peak voltage between two fixed values.

From the results of the calibration and the frequency response experiments, information can be acquired about the performance of the phase-shifting device, particularly with respect to its sensitivity, linearity, range and response time. This information is vital if the device was to be used in the dual in-plane ESPI system described in the Chapter 4. The device must be able to produce a phase shift of at least 2π, but greater than this is desirable. For automatic calibration of the 2π phase shift the software assumes a linear response from the phase-shifting device as it sweeps the voltage. If it does not have a linear response there will be an error in the phase map resulting from the phase shifting algorithm. Of course, the non-linearity

can be accounted for in the software so long as the response is accurately known. The response time is also important because, as discussed in Chapter 2, it is advantageous to acquire the four phase-shifted images in as short a time as possible. Otherwise the device can only be used in a very stable environment.

6.2.2 Polarisation rotator

The two most important properties of the liquid crystal polarisation rotator are its switching speed and extinction ratio. The purpose of these experiments was to establish if this device could be used in the dual in-plane ESPI system as the basis of an optical switch. The device must be able to rotate the plane of polarisation of linearly polarised light by 90 degrees. An unexpanded laser beam from a 10-mW laser diode was directed through the device and was incident on a polarising beam splitter. The intensities of both the transmitted (horizontally polarised) and reflected (vertically polarised) components were measured. The intensities of these components were first measured without the liquid crystal rotator in the setup.

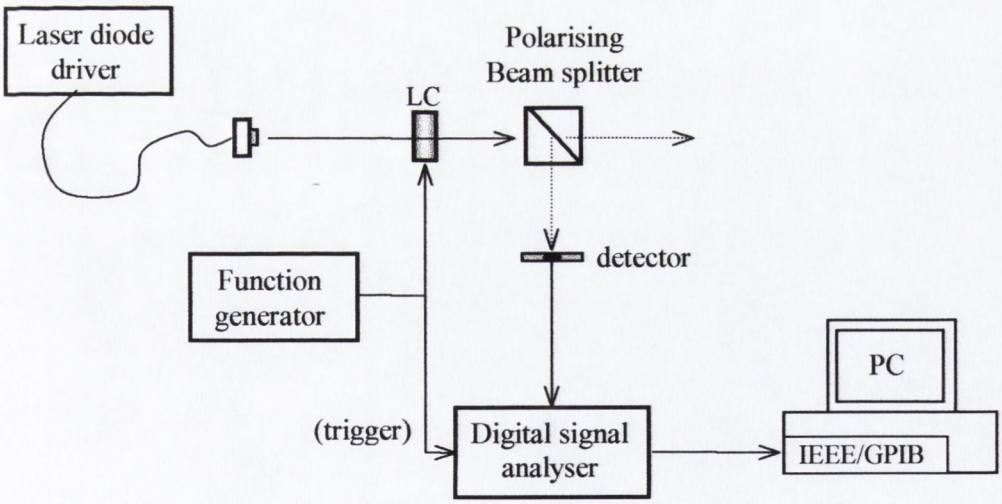

Fig. 6.12 Experimental setup used to measure response time of the Liquid Crystal (LC) polarisation rotator.

The laser was rotated so that the horizontal component was at its minimum intensity. The liquid crystal device was then placed in the system and aligned so that, at zero volts across the device, the intensity of the vertical component was now at its minimum. The peak-to-peak voltage of the square wave across the device was increased from 0 to 20 volts and the intensity in each component measured at intervals of 0.1 volt. From this data the extinction ratio can be calculated at each voltage. The operating voltages are 0 volts, where the intensity of the horizontal component is at a maximum and some voltage, greater than zero, where the intensity of vertical component it at a maximum. This voltage could be obtained from this data.

Once the operating voltage were ascertained, the speed at which the device was capable of switching when the voltage across it changed, could be obtained by measuring the device's step response. As shown in Figure 6.12, a photo-detector was placed in the setup to measure the vertically polarised component of the light transmitted through the device and reflected at the beamsplitter. At zero volts this intensity was at a minimum and was at a maximum at the second operating voltage. By measuring the intensity of this beam as the peak-to-peak voltage alternated between the two set voltages the step response was obtained. From this information the maximum speed at which the device could rotate the plane of polarisation of the light was obtained. Again, this information is vital if the device was to be used in the in-plane ESPI system where a high extinction ratio and fast switching speeds are needed.

6.4 Results

6.4.1 Calibration of the piezo-electric transducer

Figure 6.13 shows the calibration curve of the piezo-electric actuator used to translate the mirror. The piezo drive voltage shown in the figure is the voltage that was sent to the amplifier. As this voltage increased the mirror was moved forward thus shortening the optical path in that arm of the interferometer. This change in path length caused a change in the phase different between the two arms, which in turn caused a change in intensity at the detector. The detector measured intensity at one point in the interference pattern as the mirror moved fringes across that point. The output voltage of the detector, shown in the Figure 6.13 represents the fringe intensity. When the voltage is decreasing the fringes obviously move in the opposite direction, hence the discontinuities in the measured voltage. From the theory in Chapter 2, it is known that the measured intensity should have a sinusoidal profile if the mirror is moved at a constant velocity. This depends on the PZT having a linear response to the drive voltage. Figure 6.13 shows that the detector voltage has a sinusoidal shape and a sine waveform can be fitted to the data. From this data it was possible to choose a quadrature point as explained in the previous section. The red line in the figure shows one such point.

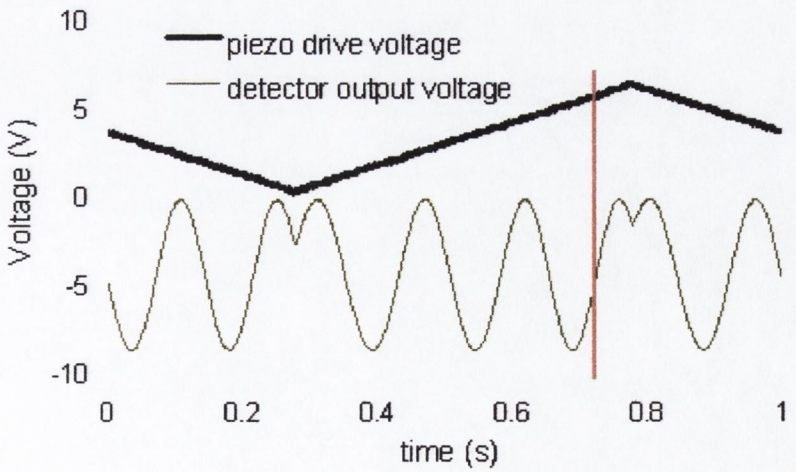

Fig. 6.13 Calibration of piezo-electric phase-shifter.

The system's response was acquired by applying a sine-sweep signal (0 – 100 Hz) to the I-controller as the reference voltage. During the sweep the lock-in amplifier measured the amplitude of the feedback voltage to the PZT amplifier using the sweep signal as a reference. Figure 6.14 shows the graph of the normalised feedback voltage against the frequency of the sweep signal. It can be seen from the graph that over the frequency range of interest, i.e. 0 – 100 Hz, the voltage is relatively constant. This means the systems response is more than adequate to follow any modulation in the optical path length so long as the frequency of the modulation is somewhere between 0 – 100 Hz.

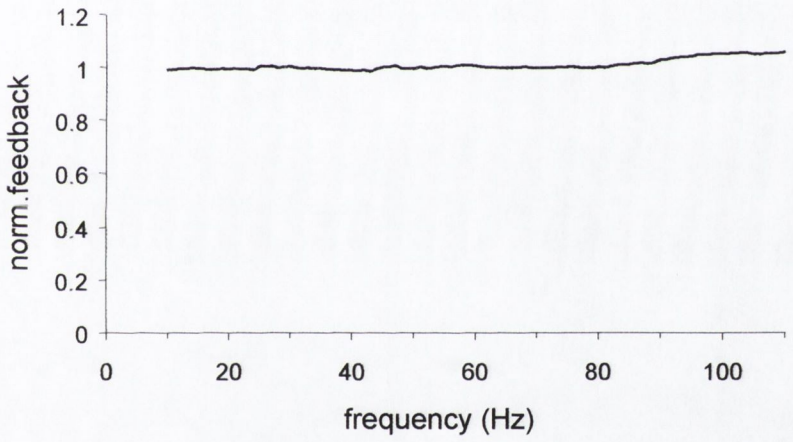

Fig. 6.14 Frequency response of Integral-control loop with PZT phase-shifter.

From these experiments it was now known that the active interferometer using the PZT actuator had a linear response and so could be used to calibrate the liquid crystal devices. It can also be used to measure the frequency response of the liquid crystal devices because of its relatively large bandwidth.

6.4.2 Phase retarder

Figure 6.15 shows the calibration curve for the liquid crystal phase shifter. The graph shows the amplitude of the triangular signal used to modulate the peak-to-

peak voltage of the 1 kHz square wave applied to the device. As in the PZT calibration graph, the voltage from the detector is measured as a function of the voltage applied to the liquid crystal. In contrast to the PZT graph, the response of the liquid crystal is not linear. The peak-to-peak voltage was modulated from 0 to 10 volts with a period of approximately 10 seconds. It is obvious from the results that a sinusoidal waveform cannot be fitted to the measured detector voltage. As mentioned previously it is desirable to have a linear response. The graph shows a change in the phase of approximately 6π. However since these tests were performed in a Michelson interferometer the light travelled through the device twice. Figure 6.16 shows the absolute phase change produced by the liquid crystal device when the peak-to-peak voltage is modulated from 0 – 10 volts.

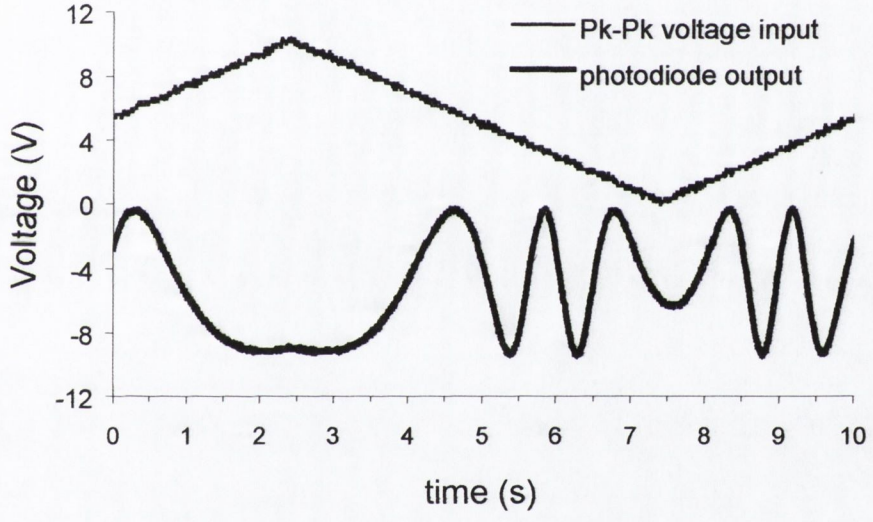

Fig. 6.15 Phase-shifting response of LC-device as a function of applied voltage.

From the graph, a phase change of almost 3.5π is possible. This is more than adequate for use as a phase-shifter to allow for the use of phase shifting algorithms as only a total phase change of 2π is necessary. However, the non-linearity of the response would have to be compensated for in the phase shifting calibration algorithm. The graph shown in Figure 6.15 can be used for this purpose.

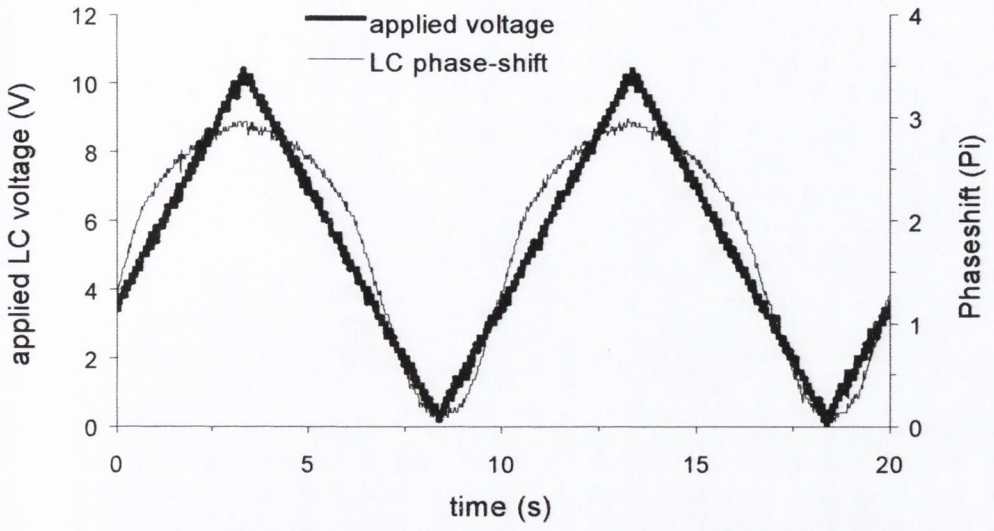

Fig. 6.16 Absolute phase response of LCD-shifter in range 0 to 10 voltage pk-pk.

As before, the frequency response is measured by applying a sine-sweep signal to modulate the amplitude of the voltage across the liquid crystal device. The feedback voltage is then measured as the signal sweeps from 0 to 10 volts and is compared to the reference signal (sine-sweep signal). If the optical path length is modulating in the same way as the sine wave this voltage will remain constant. If the liquid crystal device cannot keep up with the modulating sine wave the feedback voltage will decrease. However this technique requires the device to have a linear response to the sine wave. From Figure 6.15, it can be seen that from 1 to 2 volts the response is relatively linear. To check this, a sine wave of 1 Hz was used to modulate, from 1 to 2 volts, the peak-to-peak amplitude of the 1kHz square wave. The feedback voltage from the I-controller to the PZT amplifier was then measured. Figure 6.17 shows the fast Fourier transform (FFT) of the measured signal. There is a maximum peak at 1 Hz showing the signal is predominately a sine wave of this frequency. The secondary peak as 2 Hz is relatively low and can thus be ignored. This shows the response is quite linear in the range from 1 to 2 volts and so this range was used for the frequency response measurements.

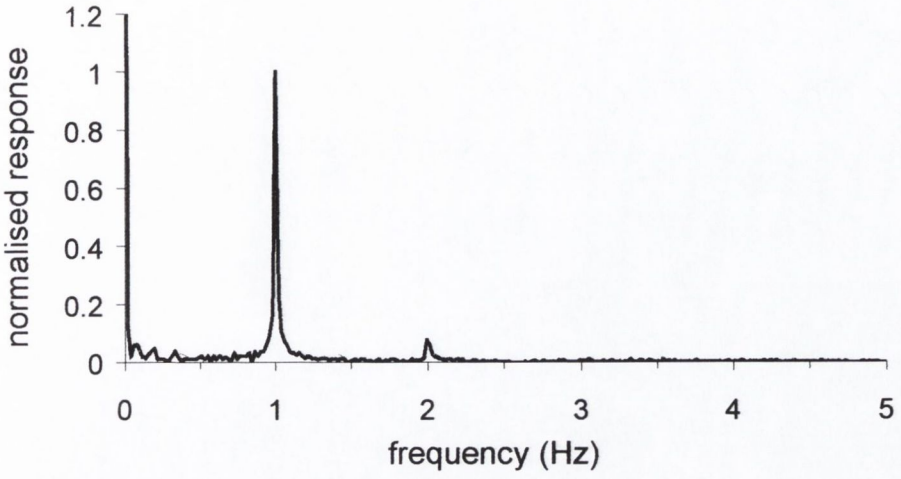

Fig. 6.17 Normalised FFT of LC phase-shifter response with 0.8 V (Pk-Pk) at 1 Hz excitation frequency.

The frequency response of the liquid crystal was measured by applying a sine-sweep signal, sweeping from 0 to 20 Hz and measuring the voltage from the lock-in amplifier as it compared the sine signal modulating the peak-to-peak voltage and the feedback voltage from the I-controller. Figure 6.18 shows the normalised response of the phase shifter in this range. At 1 to 2 Hz the liquid crystal can modulate the optical path length by accurately following the sine wave, but as the frequency of the sine wave increases the device can no longer keep up with it and the feedback voltage drops significantly. This means that the devices are relatively slow only allowing modulations of less than 2 Hz. This is a significant disadvantage if the devices are to be used as phase shifters, because it is important that the four phase images can be taken as quickly as possible. To produce four images $\pi/2$ apart, three steps are needed which would take approximately 1.5 seconds with these devices. This limits their use to stable environments.

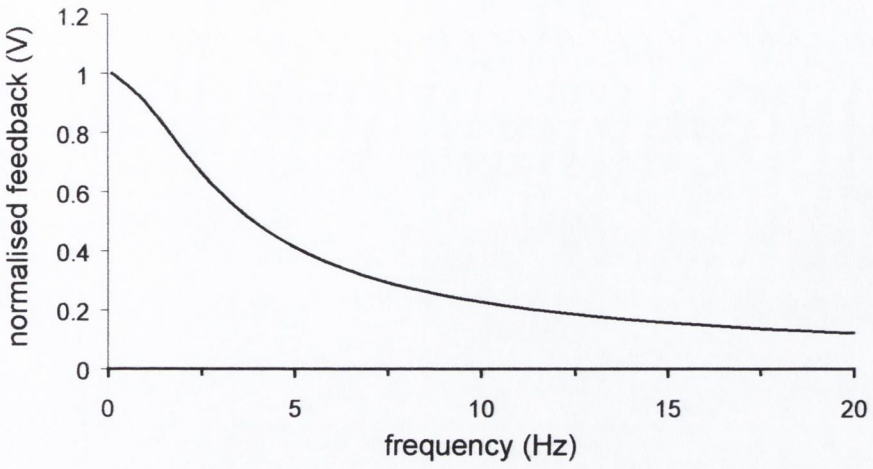

Fig. 6.18 Frequency response of LC phase-shifter in 0 to 20 Hz range.

The final test carried out was to measure the rise and fall times of the device's step response. This is important, as the four phase images will be taken by applying three steps in the peak-to-peak voltage across the device. It was found that the speed at which the device responded depended on the magnitude of the voltage change. The greater the change in voltage the faster the response. Figure 6.19 shows a typical rise and fall response curve as the peak-to-peak amplitude across the device was changed from 0 to 2 volts. The peak-to-peak amplitude was modulated at 100 mHz. The results showed the fall time was considerably longer than the rise time.

For phase shifting the voltage would be stepped up three up times after which it would be returned to its original value, so therefore both the rise and fall times are important. From the data it was ascertained that the maximum fall time was approximately 0.5 seconds. It was therefore concluded that if these devices were used for phase shifting in the ESPI system, an interval of at least 0.5 seconds between the phase images would be necessary. The results also showed the devices to have good stability and repeatability over 1000 seconds.

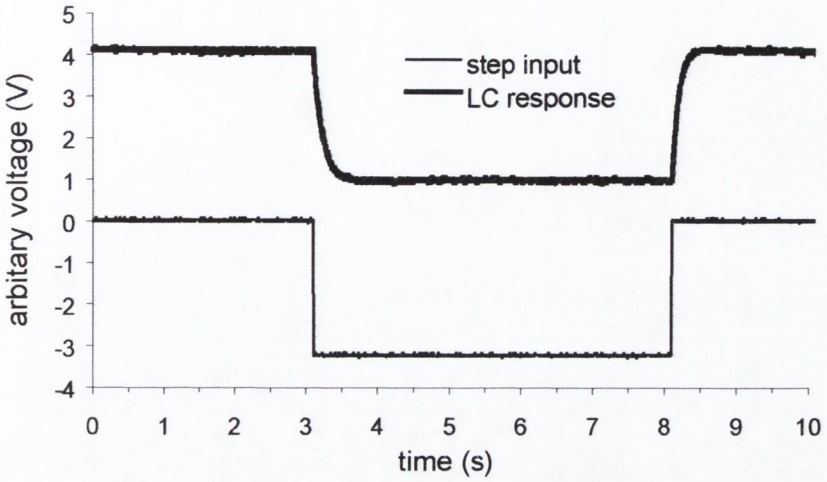

Fig. 6.19 Step response of LC phase-shifter.

This concluded the tests on the liquid crystal phase shifters. They can be operated at relatively low voltages, easily produced by a D/A card on-board a computer. The phase shifts were stable and repeatable and an absolute phase shift of greater than 3π is possible. However the fact that the phase shift response to the applied voltage is not linear has to be compensated for in the phase shifting algorithm used by the ESPI software. Another disadvantage is the relatively slow response time, which limits their use to stable environments. It was decided that the advantages far outweighed the disadvantages and the devices would be used in the ESPI system. At the same time research was carried out into improving the devices by the use of a different liquid crystal material. This is discussed in the conclusion section at the end of this chapter.

6.4.3 Polarisation rotator

From the theory of nematic liquid crystals it was known that at zero volts the twisted nematic devices would rotate the plane of polarisation of the laser light by 90 degrees. The first experiment was carried out to find the second voltage at

which the plane of polarisation was left unchanged. Figure 6.20 shows the graph of the intensities of the vertically and horizontally polarised components of the light transmitted through the liquid crystal polarisation rotator as the peak-to-peak voltage across the device was increased from 0 to 20 volts. The voltage was increased very slowly by increments of 0.1 volts, with a time delay of 1 second between each increment. This was to ensure the liquid crystal device had responded fully. At zero volts the intensity of the vertical is at a minimum and the horizontal component is at a maximum. When the voltage is greater than 3 volts the situation is reversed with the vertical component now at a maximum. As expected from the tests on the liquid crystal the response in again non-linear. However in this case this is of no importance, and only the extinction ratio and the response time are of concern. From the data shown in the graph the extinction ratio was calculated to be approximately 100:1 at both zero volts and at 10 volts. The operating voltages were chosen at 0 and 10 volts. The peak to peak voltage could now be switched between these two voltages so that the transmitted light could be either vertically or horizontally plane polarised. The next test was to find out how fast the device could be switched and still rotate the plane of polarisation.

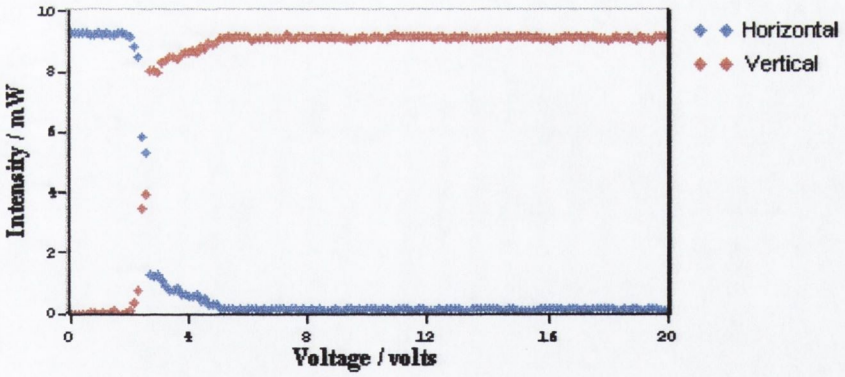

Fig. 6.20 Graph of the intensities of the orthogonal linear polarisation components of the light transmitted through the liquid crystal polarisation rotator, as a function of voltage.

The response time of the liquid crystal polarisation rotator was found to be faster than the response of the phase-shifters but also dependent on the change in voltage. Figure 6.21 shows the device's response to a modulating peak-to peak voltage from 0 to 10 volts. Again, the fall time is greater than the rise time as would be expected. This is because the applied voltage causes an electric field across the

liquid crystal layer, which forces the molecules to align in the direction of the field. When the voltage is removed the molecules relax back into the original states. It takes 0.2 seconds for the device to achieve an extinction ratio of 100:1 when the voltage is changed from 10 to 0 volts. Only 0.12 seconds is required when the voltage is increased again to achieve the extinction ratio of 100:1.

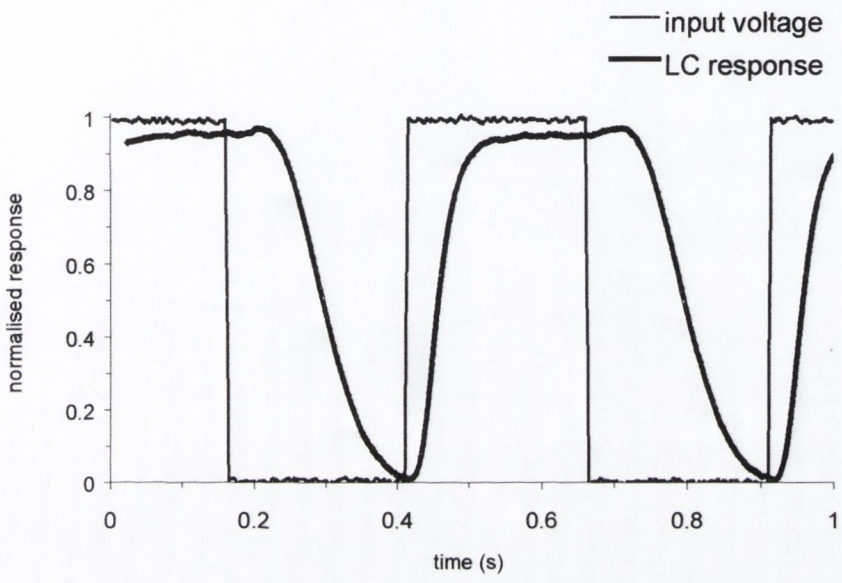

Fig. 6.21 LC-switch response to step input of 0 to 10V Pk-Pk.

If the peak-to-peak voltage is modulated between 0 and 20 volts the rise time changes, as in Figure 6.22. There is a slight increase in the fall time but it is negligible. This is because the molecules are in the same position when 20 volts is applied across the layer as when 10 volts is applied. This is seen from the graph in Figure 6.20, showing the intensities of the vertically and horizontally polarised components. The ratio of the components does not change between 10 and 20 volts, showing the molecular structure is also changing very little. The change in the rise time is quite dramatic with only 0.05 seconds required to achieve the maximum extinction ratio.

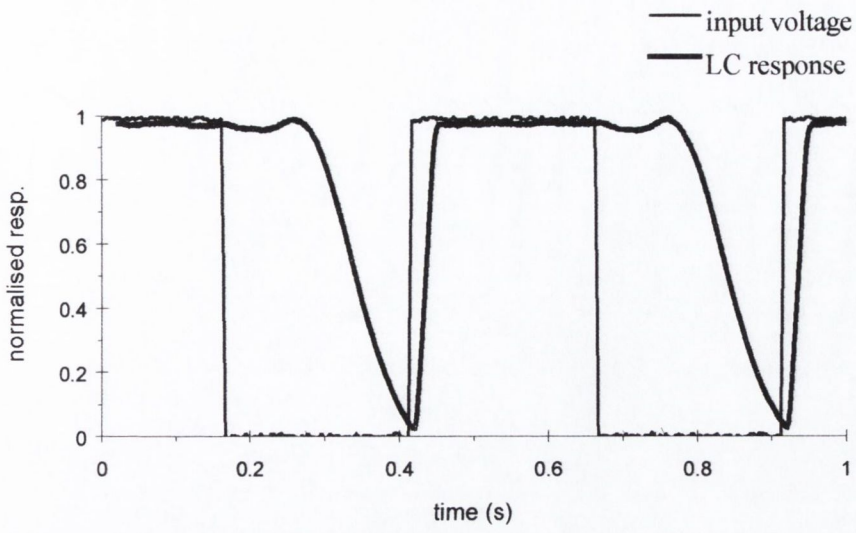

Fig. 6.22 LC-switch response to step input of 0 to 20V Pk-Pk.

In order to try to improve the fall or relaxation time the amplitude was changed from 2 to 10 volts instead of from 0 to 10 volts. In this way it was hoped that the low voltage would force the liquid crystal molecules back to their original position instead of letting the molecules relax. From the extinction ratio graph, a ratio of just under 100:1 is obtained at 2 volts. It can be seen from Figure 6.23 that the fall time does not improve, it actually increases to almost 0.6 seconds and again the rise time is comparatively fast. From these experiments the operating voltages were chosen at 0 and 10 volts. In the in-plane ESPI system the polarisation switch forms the basis of an optical switch that is used to change the illumination beams from one plane to another. This is done continuously and the object is illuminated in each plane for equal amounts of time. Ideally, the switch should be able to operate at the framing rate of the CCD camera (typically 25 – 50 Hz). As the object is illuminated in each plane for an equal amount of time, the rate at which the liquid crystal rotator can switch is limited by the longest of the rise and fall times. From the data below a switching rate of only 2 Hz is possible with these devices. However as the ESPI system will be fully automated and incorporate phase-shifting analysis, the phase-shifting algorithm analysis time will ultimately limit the system. It takes over 500 ms to produce the phase map of a 512 x 512 image so therefore a switching speed of 2 Hz is adequate. As with the phase-shifting devices, it was decided that a liquid crystal polarisation rotator would be used in

the system. However, research was also carried out into improving these devices by the use of different liquid crystal materials. This is discussed in the next section.

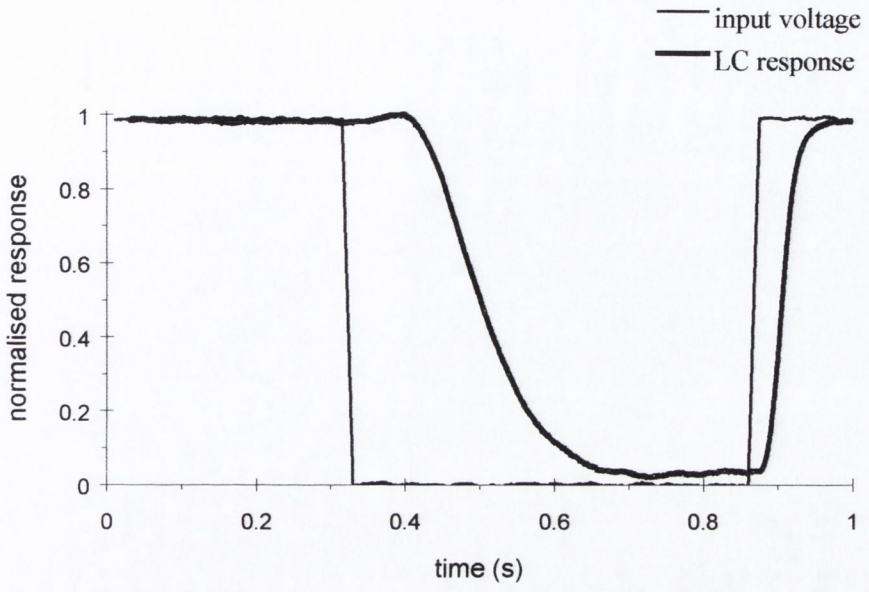

Fig. 6.23 LC-switch response to step input of 2 to 10V Pk-Pk.

6.5 Conclusion

The nematic liquid crystal phase shifting devices can provide a phase shift greater than 2π that is stable and repeatable. A 1kHz square wave is applied across the liquid crystal layer and the peak-to-peak amplitude, in the range 0 to 10 volts, controls the phase-shift. This amplitude modulated square wave can be produced from a D/A card on-board a computer, eliminating the need for amplifiers or external electronics. The devices are relatively cheap and can be easily incorporated into any optical system. They are mounted in circular Perspex holders with an outer diameter of just under 30 mm, making them ideal for use in Spindler and Hoyer Microbench equipment.

The disadvantages of the nematic devices described in this chapter are the relatively long response times and the non-linear phase-shift response to the applied voltage. The non-linearity causes a problem because the efficiency of the phase-shifting algorithm depends on the accuracy of the phase shifts. The

algorithm used in the ESPI system described in Chapter 4 takes four images, $\pi/2$ apart in phase. Therefore, the voltages required to perform these phase shifts must also be accurately known. If the phase shifter had a linear response the software can calibrate the device whenever the user wishes to. It does this in the exact same way as the piezo-actuator was calibrated in the previous section of this chapter. A ramp wave is applied to the device and the intensity at one point in the image plane is measured. The intensity modulation has a sinusoidal profile to which a sine wave can be fitted. The software can then work out the voltage needed to produce the 2π phase shift. This voltage is then simply divided by four to determine the voltage required to produce a phase shift of $\pi/2$. This procedure obviously does not work with the liquid crystal phase shifters because a sine wave cannot be fitted and, even when the voltage required for a 2π phase shift is known, it cannot simply be divided because of the non-linearity. Therefore, to overcome this, the devices have to be accurately calibrated before they are placed into the system. The user then inputs the voltages required to produce phase shifts of $\pi/2$, π and $3\pi/2$.

The slow responses of the devices are not always a problem. The four phase-shifted images are grabbed at the very start of the data acquisition before the ESPI subtraction starts. After the four images are acquired, the wrapped phase maps of all subsequent frames can be calculated using these four images, thus reducing the need for fast devices as the loading of the sample does not have to begin until the four images are grabbed. This reduces the need for the four phase images to be taken quickly. In this case the slow response of the liquid crystal devices is not important and two of these devices are used in the ESPI system for performing phase shifting in each plane. However, there are times when the conditions are not mechanically stable and there is a need for fast phase image acquisition. Therefore research was carried out to investigate improving the speed of the devices. The results of this research are given after a short discussion of the liquid crystal polarisation rotator, as it too needs to be improved to reduce the response times.

The twisted nematic liquid crystal polarisation rotator can rotate the plane of polarisation of linearly polarised light by 90 degrees. The device, like the phase shifter is easily incorporated into any optical system. It is aligned so that at zero

volts, the light transmitted has a plane of polarisation at 90 degrees to the light incident on the device. At 10 volts the light is allowed through without any change in the plane of polarisation. It has relatively high extinction ratios of approximately 100:1. Even though the maximum switching rate is relatively low, at 2 Hz, this is adequate as the phase-shifting algorithm takes about half a second to calculate the phase map for just one image. However faster switching speeds are desirable as the initial displacement fringe patterns in the ESPI system can be acquired at 25 Hz. It would be advantageous if the device could switch at this speed so the displacement fringe patterns could be obtained in both planes at this rate.

To improve the response times different liquid materials had to be investigated. After collaboration with the Russian State Optical Research group it was concluded there are two ways to improve the response times of the devices. One way is the use of nematic liquid crystals with low frequency inversion of the dielectric anisotropy constant. This type of material has positive dielectric anisotropy at low frequencies and negative dielectric anisotropy at high frequencies. For example, one such material has a dielectric anisotropy of +2.2 at a frequency of 200 Hz and –2.2 at 40 kHz, where the frequency is the frequency of the applied square wave. The liquid crystals described previously have a constant dielectric anisotropy over all frequencies. To use these devices, not only would the amplitude have to be controlled, but also the frequency of the square wave. However, more control over the molecular alignment is possible as the electric field can now be in either direction. This means that switching is now not just a matter of relaxation or increasing the magnitude of the electric field but a change in the direction of the field itself. This material allows switching times of 0.5 to 1.0 ms, so switching speeds of 1 kHz are possible.

The other way is to use ferroelectric liquid crystals, allowing typical response times of 50 to 100 microseconds. However these devices are far more expensive and require higher voltages and so, the original reasons for using liquid crystal devices would no longer apply.

The result of the research described in this chapter was a thorough understanding of the relevant properties of the liquid crystal devices. The behaviour and performance of the devices under different conditions has been established. The devices have also been accurately calibrated so that they can be successfully used in the dual in-plane ESPI system. The limitations of the devices were also ascertained, as were possible ways of improving their performance in the future. Two phase shifting devices and one polarisation rotator were successfully incorporated into the ESPI system, because they have all been accurately calibrated.

Chapter 7 Conclusions

7.1 White Light Interferometric Surface Profiler

The white light interferometric system has proven to be a very efficient surface profiler. It utilizes the short coherence length of the white light source to produce surface profiles with a resolution of 0.06 μm when profiling smooth surfaces and approximately 1-2 μm when measuring height variations on rough surfaces. Its range is only limited by how far the reference mirror can move, which is about 5 cm in the system developed and described in this thesis. Two data processing algorithms were developed and software written, which deal with the vast amount of data in a fast and simple manner enabling images of 512 x 512 pixels to be analysed efficiently. The optical configuration has been designed for optimum performance with almost perfect collimation and filtering at the Fourier plane of the telescope objective lens. The profiler does not suffer from the problems associated with phase shifting and does not involve complex algorithms. It was shown that the optical configuration of the profiler and the acquisition can be very easy to set up and use. For optimum performance, the system is designed to be as small as possible with short distances between the optical components. This reduces the problems caused by air turbulence and vibrations.

This system's theoretically unlimited range and the fact that it does not measure phase, so that step heights greater than λ do not introduce errors, give this system a distinct advantage over other optical profilers. Furthermore, the fact that the profiler has a high resolution when profiling optically smooth surfaces makes it the ideal technique for profiling smooth stepped surfaces. However, the efficiency of the system does decrease as the surfaces get rougher and more convoluted in shape. Even so, the system has still proved effective at profiling rough surfaces and is ideal when a resolution better than l_c is not required where l_c is the coherence length of the light source.

The frame acquisition and analysis rate is approximately 2.5 Hz. This means in two seconds, five 512 x 512 frames can be acquired and analysed. Objects can be easily put into the system and profiled quickly. The result is a three dimensional map of the surface. The system was used to measure optical thickness of glass and plastic, and step heights on both optically smooth and rough surfaces. The results obtained agreed with manufacturer's quotes as well as measurements taken using stylus profilometry. This system can easily be adapted to a specific application, such as the measurement of gauge block lengths.

7.2 Dual In-Plane ESPI System

The dual in-plane ESPI system has been developed to the status of a robust and portable industrial prototype. It is an innovative system that has no moving parts and still allows the quantitative measurement of displacement in both the vertical and horizontal in-plane directions. The stability requirements for this system are the same as they are for all typical ESPI systems that measure displacements of a fraction of a wavelength. However, the sources of instability have been reduced in this system. It has no moving parts as it uses liquid crystal devices for both switching between illumination planes and for phase shifting. The strong structural support means that the system is mechanically stable and it has been used outside the laboratory environment with good results. The ESPI system is controlled by advanced software, called ESPITest. This user-friendly software controls and synchronises the beam illumination with the image acquisition, by acquiring data from the frame-grabber while controlling the voltage across the liquid crystal switch. It also calibrates and controls the phase shifting devices in order to produce wrapped phase maps. These images are then unwrapped by the software to produce absolute phase maps. The user has the option to view the live image, displacement fringes, wrapped phase maps or unwrapped phase maps. The software also allows the user to control loading machines and to produce displacement versus load graphs.

The ESPI system can measure surface displacements in both the vertical and horizontal directions of less that one micrometer and, using phase shifting procedures, the resolution is improved to less than 50 nm. Unlike conventional mechanical techniques, such as strain gauges, it can provide information over the whole surface and no contact with the surface is necessary. The system has been used qualitatively to detect cracks and defects in real time, as ESPI subtraction fringe patterns can be produced at a rate of 25 Hz. When phase shifting is performed the system takes approximately 500 ms to calculate the phase map of a 512 x 512 image. As the liquid crystal switch allows the illumination beams to be switched at 2 Hz, the system is capable of producing both the x and y phase maps on the screen at a rate of 2 Hz. It is also possible to unwrap these images during acquisition, but this slows down the process considerably and it is recommended to unwrap only after the test is completed.

The system has been used to measure displacements in various materials, including clay, aluminium, concrete, brick and steel. It has been used for crack detection as well as for quantitative displacement measurements using the phase-shifting and phase unwrapping procedures. The easy-to-use ESPITest software allows total control over the system and post processing and filtering of the captured images. As mentioned in Chapter 4, the system design is presently being investigated by Ettemeyer [112], one the largest European manufacturers of commercial ESPI systems, with the objective of developing it into a commercial ESPI system. The system is portable, compact and robust, and capable of producing quantitative displacement data. The interferometer makes very efficient use of the illumination available, without the use of shutters. Only low voltage devices are used without the need for bulky or expensive electronics. The ESPI system can be taken into an industrial environment and used in-situ, by anyone, to produce accurate and useful data.

During the course of this research, different design options for systems having no moving parts were investigated. The feasibility of using liquid crystals devices was also studied. This required research into the theory and operation of these devices, followed by extensive testing. Two nematic devices are used to phase shift and a

twisted nematic device is used as a polarisation rotator in an optical switch. These devices were characterised in a series of tests performed to calibrate the devices and obtain response times. The use of liquid crystal devices in an interferometric system is new but the results of the tests show the devices to be very efficient phase shifters and polarisation rotators. Although the response times of the devices are relatively slow, these times were characteristic of the nematic liquid crystals. In order to improve these times to allow for rapid phase shifting and switching, nematic liquid crystals with low frequency inversion of dielectric anisotropy constant can be used.

7.3 Dual White light and ESPI contouring system.

The white light interferometric technique proved to be ideally suited to discontinuous smooth surfaces while rough and curved surfaces tended to cause significant errors. The white light technique was used together with an ESPI contouring system, which is more suited to profiling rough surfaces. This dual system can efficiently profile both rough and smooth surfaces. The ESPI technique is capable, when using phase-shifting algorithms, of measuring rough surfaces with a high resolution. ESPI contouring by wavelength modulation offers two great advantages over typical contouring systems, in that there are no moving parts and using an appropriate source the sensitivity can be continuously changed over a large range. With the developments in laser technology over the last few years and the emergence of tunable laser diodes, ESPI contouring by wavelength modulation is once again becoming an attractive way of measuring shape. Tunable laser diodes, with adequate output intensities, are still expensive and usually operate in the mid-infra-red region, beyond the sensitivity of the CCD camera, but it is only a matter of time before higher power tunable laser diodes with wavelengths compatible with CCD cameras become widely available.

It was with this in mind, that the ESPI contouring technique was combined with the white light system to produce an efficient surface profiler exploiting the similarities in the required optical setups. The resulting profiler is not limited to

use on any particular surface finish and has a relatively unlimited range. Using a Ti:Sapphire laser, the wavelength could be changed continuously from 700 nm to 850 nm with a resolution of 0.5 nm. The intensity of the light across this range varied very little and the direction of the emitted light remains unchanged.

The dual system is capable of profiling both optically rough and smooth surfaces. It has a resolution of 0.06 μm when profiling optically smooth surfaces and as low as 0.045 μm when measuring optically rough surfaces. To obtain this resolution the wavelength change must, of course, be made in steps and the calculated phase maps added together.

The versatility, range and resolution make this system ideal for profiling almost any surface. With the introduction of a tunable laser diode the system becomes very compact and simple. As the same optical components, camera and frame grabber are used for both techniques, the system is a relatively inexpensive tool for shape measurement.

7.4 Summary

The purpose of the research described in this thesis was to develop and optimise new advanced systems that could easily be used in an industrial environment. This objective has been realised with the development of the white light interferometric surface profiler and the dual in-plane ESPI system. It is clear that these systems overcome many of the reasons why optical techniques are not widely used in industry. The systems are stable, portable, robust and easy to use. The user-friendly software packages control the optical systems and peripheral equipment, such as a loading device, and facilitate rapid data analysis. The software is easy to use and produces colour coded graphical data. These developments will help the surface metrology industry move towards optical computer-controlled systems for measuring and analysing surface displacements and shape. It is hoped that in future systems like this will become commonly used in industry and research. Even in areas where there are already commercially available systems, for example optical

surface profilers, the systems described can be implemented at much lower cost than the price of a commercial instrument.

The in-plane ESPI system was shown to be very reliable and efficient and therefore it is most probable that most future ESPI metrology devices will in some way follow this design in that they will be compact, portable and will not have any moving parts. Instead they will use electro-optic devices to perform both the phase shifting and beam switching. From the tests on the liquid crystal devices, it has been shown that these devices could easily be incorporated into any interferometry system. Using the correct liquid crystal material, they are fast and efficient phase shifters and polarisation rotators. Also, as tunable laser diodes with enough output power become more widely available, the ESPI contouring technique will become a common tool for surface profiling. Such a system could use an electro-optic device for phase shifting thus allowing the system to have no moving parts. As the ESPI contouring system could only be used on rough surfaces, the dual system can easily be implemented by the addition of a white light source. This system could then efficiently profile surfaces with different finishes.

APPENDIX A

Equipment

A.1 White light profiler

CCD Camera

Technical Data	
Make & Model	Cohu 4912 CCIR monochrome
Pickup	Single CCD using frame transfer
Pickup area	6.4 x 4.8 mm
Number of active pixels	512 x 512
Pixel size	9.2 μm x 9.2 μm
Sensitivity	0.12 lux
Power consumption	4.2 Watts, 12 V DC/AC 50Hz
Spectral response	Visible / Ir – 400 to 1050 nm
Automatic gain control	On
Video output	1.0 V p-p
Sync Mode	Composite

DC Motor and Controller

Technical Data	
DC Motor	
Make & Model	Physik Instrumente (PI) M – 125.10
Travel range	25 mm
Resolution	0.06 μm
Backlash	5 μm
Max. Velocity	0.7 mm/s
Max. Load capacity	20 kg
Max. push/pull force	50 / 50 N
Weight	1.4 Kg
Motor Controller	
Make & Model	Physik Instrumente (PI) C - 832
Main Features	PC/AT bus mounted Two independently programmable channels Differential or single ended encoder interface 32-bit register for velocity, position and target C/ C++ Subroutines for programming

White Light Source

Technical Data	
Make & Model	Oriel Arc Lamp Model 6000
Bulb gas	Xenon
Maximum output power	75 watts
Mean wavelength	650 nm
Coherence length	1- 2 μm

Cooling	Convective
Voltage	12 volts

Frame Grabber

Technical Data	
Make & Model	Data Translation DT 2861
Main Features	PC/AT compatible Framing rate of 30 Hz 4 Mb of on-board memory for storing 16 512 x 512 x 8 bit images 8 bit arithmetic logic unit 8 bit Look-up tables (LUTs) Onboard external I/O ports which allow direct connection of auxiliary processing boards C/ C++ Subroutines for programming

A.2 In-Plane ESPI system

Off-Axis Paraboloids

Technical Data	
Make & Model	Ealing Diamond turned mirrors
Diameter	76.2 mm
Focal length	76.2 mm
Off-axis angle	60 degrees
Off-axis angle	88.0 mm

Lasers

Technical Data	
Make & Model	SDL – 5700 DBR laser diode
Wavelength	852 nm
Max. cw output power	150 mW
Spectral bandwidth	3 MHz
Cooling	TE Peltier Cooler
Mounting	TO-3 package
Make & Model	Ettemeyer laser diode
Wavelength	780 nm
Max. cw output power	50 mW
Spectral bandwidth	2 MHz
Cooling	None
Mounting	9-pin D-sub & cable

Laser Current Controllers

Technical Data	
Make & Model	Wavelength Electronics FPL–500-4
Output current range	0 – 500 mA
Compliance voltage	> 6 to 10 V

Stability	< 50 ppm
Input impedance	10 kΩ
Temperature coefficient	< 100 ppm / °C
Power requirements	± 12 to ± 15 VDC
Supply current	200 mA
Make & Model	Ettemeyer LDC 202
Output current range	0 – 200 mA
Compliance voltage	> 6 V
Temperature coefficient	< 50 ppm / °C
Power requirements	110/230V, 50/60 Hz
Operation temperature	0 - 40°C

Frame Grabber

Technical Data	
Make & Model	Data Translation DT 3152
Main Features	PCI Bus Can transfer directly to computer monitor 4 monochrome inputs Interlaced or non-interlaced Programmable gain 8-bit resolution Pixel acquisition rate of 20 MHz One 256 x 8-bit Look-up table Compatible Windows Software

D/A board

Technical Data	
Make & Model	National Instruments PC1200/AI
Main Features	PCI Bus Two channels 12-bit resolution 1 kS/s update rate 0 –10 V or ± 5 V output DC output coupling 0.2 Ω output impedance

A.3 Dual white light and ESPI contouring system

Argon Ion Spectra-Physics Stabilite 2016

Optical Characteristics		
Noise	-Power Mode	0.5% rms.
	-Current Mode	0.5% rms.
Stability	-Power Mode	±0.5%
	-Current Mode	±1.0%
Beam Diameter		1.4 mm
Beam Divergence, full angle		0.5 mrad
Cavity Length	-Without Prism	0.920 m
	-With Prism	0.960 m
Mode Spacing	-Without Prism	163 MHz
	-With Prism	156 MHz
Polarisation		100:1 vertical
Utilities		
Electrical	-Input Power	3 Phase with ground
	-Voltage	208 V ± 10 %
	-Current	42 A
	-Frequency	50/60 Hz
Cooling – Water		
	-Water Flow Rate (minimum)	8.4 l/min (2.2 gal/min)
Physical Dimensions		
Laser Head	-Size	110.6 x 17.8 x 14.6 cm
	-Weight	43 kg
Power Supply	-Size	51.1 x 42.5 x 15.5 cm
	-Weight	36. Kg
The optical characteristics were measured for 514.5 nm		

Acousto-Optic Tunable Filter - Gooch & Housego Limited

Model Number	TF 575 – 250 –2.5 – 3
Serial No	5551 – 1
Operational Wavelength	450 – 700 nm
RF Drive Frequency Range	65 – 115 MHz
Maximum RF Power	40 W
Interaction Material	Tellurium Dioxide
Size of Active Aperture	3 mm
Interaction Length	10.2 mm
Transmission @488 nm @RF 103.94 MHz	98%

CW Ti:Sapphire Laser Spectra-Physics Model 3900S

Optical Characteristics	
Average Power -5 W Pump	750 mW
Tuning Range	700 – 980 nm
Peak Wavelength	790 nm
Linewidth	<40 GHz
Noise	<1 %
Stability	<3 %
Spatial Mode	TEM00
Polarisation	>100 :1 Horizontal
Beam Diameter	0.95 mm
Beam Divergence, Full Angle	1.0 mrad
Utilities	
Water Pressure Range	1.1 kg/cm2 Min 5.3 kg/cm2 Max
Physical Dimensions	
Size	65.1 x 24.1 x 20.6 cm
Weight	14.1 kg

APPENDIX B

Computer Programs

```
/* The Coherence Radar Location of Position of Maximum Modulation

Date: 17-7-97

Brian Bowe

*/

#include <stdio.h>
#include <stdlib.h>
#include <isdefs.h>
#include <conio.h>
#include <dos.h>
#include <bios.h>
#include "drive628.h"
#include <needed.h>

int     pixel_array1[9600],pixel_array2[9600];
int     pixel_array3[9600];
int     n;

main()
{
void    max_intensity();
void    max_intensity_loop();

is_error_messages(1);
is_initialize();
is_init_luts();
is_set_sync_source(1);
is_frame_clear(1);
is_frame_clear(2);
is_frame_clear(3);
is_frame_clear(4);
is_frame_clear(5);

is_select_input_frame(0);
is_select_output_frame(0);
is_set_active_region(10,16,490,480);
is_passthru();
is_acquire(1,1);
is_select_input_frame(0);
is_set_active_region(10,16,490,480);
is_passthru();


init912(CHANNEL,1000,100,1000,1000,100,40);
drive628(CHANNEL,LTRJ,LOAD_POSITION,1);
drive628(CHANNEL,STT,0,0);
while(!(drive628(CHANNEL,RDSIGS,0,0)& ON_TARGET))
        printf("\rReal position:%8ld",drive628(CHANNEL,RDRP,0,0));
printf("\nReached the position of frame 2\n");
```

```
is_acquire(2,1);
max_intensity();

for(n=3;n<255;n++)
{
is_select_input_frame(0);
is_select_output_frame(0);
is_set_active_region(10,16,490,480);
is_passthru();

init912(CHANNEL,1000,100,1000,1000,100,40);
drive628(CHANNEL,LTRJ,LOAD_POSITION,1);
drive628(CHANNEL,STT,0,0);
while(!(drive628(CHANNEL,RDSIGS,0,0)& ON_TARGET))
        printf("\rReal position:%8ld",drive628(CHANNEL,RDRP,0,0));
printf("\nReached the position of frame %d\n",n);
is_acquire(3,1);
max_intensity_loop();
}

is_end();
}

void max_intensity()
{
int d,t;

for(d=10;d<500;d+=20)
        {
        t=0;
        is_select_output_frame(1);
        is_set_active_region(d,16,20,480);
              is_get_region(1,pixel_array1);
        is_select_output_frame(2);
        is_set_active_region(d,16,20,480);
              is_get_region(2,pixel_array2);

        for(t=0;t<9600;t++)
                {
                if(pixel_array1[t]>pixel_array2[t])
                        {
                                                pixel_array1[t]=2;
                                                pixel_array2[t]=1;
                        }
                else
                        {
                                                pixel_array2[t]=2;
                                                pixel_array1[t]=1;
                        }
                }
        is_put_region(4,pixel_array1);
        is_put_region(5,pixel_array2);
        }

for(d=10;d<500;d+=20)
        {
        t=0;
        is_select_output_frame(1);
        is_set_active_region(d,16,20,480);
              is_get_region(1,pixel_array1);
```

```
        is_select_output_frame(2);
        is_set_active_region(d,16,20,480);
              is_get_region(2,pixel_array2);


        for(t=0;t<9600;t++)
                {
                if(pixel_array1[t]>pixel_array2[t])
                        {
                        pixel_array3[t]=pixel_array1[t];
                        pixel_array1[t]=pixel_array2[t];
                        pixel_array2[t]=pixel_array3[t];
                        continue;
                        }
                if(pixel_array1[t]<=pixel_array2[t])
                        {
                        continue;
                        }
                }
        is_put_region(1,pixel_array1);
        is_put_region(2,pixel_array2);
        }
}

void max_intensity_loop()
{
int d,t;

for(d=10;d<500;d+=20)
        {
        t=0;
        is_select_output_frame(1);
        is_set_active_region(d,16,20,480);
              is_get_region(1,pixel_array1);
        is_select_output_frame(3);
        is_set_active_region(d,16,20,480);
              is_get_region(3,pixel_array2);
        is_select_output_frame(4);
        is_set_active_region(d,16,20,480);
              is_get_region(4,pixel_array3);


        for(t=0;t<9600;t++)
                {
                if(pixel_array1[t]>pixel_array2[t])
                        {
                        pixel_array1[t]=pixel_array2[t];
                                                pixel_array3[t]=n;
                        continue;
                        }
                if(pixel_array1[t]<=pixel_array2[t])
                        {
                        continue;
                        }
                }
        is_put_region(1,pixel_array1);
        is_put_region(4,pixel_array3);
        }

for(d=10;d<500;d+=20)
```

```
        {
        t=0;
        is_select_output_frame(2);
        is_set_active_region(d,16,20,480);
              is_get_region(2,pixel_array1);
        is_select_output_frame(3);
              is_set_active_region(d,16,20,480);
              is_get_region(3,pixel_array2);
        is_select_output_frame(5);
        is_set_active_region(d,16,20,480);
              is_get_region(5,pixel_array3);


        for(t=0;t<9600;t++)
                {
                if(pixel_array1[t]<pixel_array2[t])
                        {
                        pixel_array1[t]=pixel_array2[t];
                                                pixel_array3[t]=n;
                        }
                else
                        {
                        continue;
                        }
                }
        is_put_region(2,pixel_array1);
        is_put_region(5,pixel_array3);
        }
}

□


/* The Coherence Radar  Detection of Continuous modulation

Date: 2-7-97

Brian Bowe

*/

#include <stdio.h>
#include <stdlib.h>
#include <isdefs.h>
#include <conio.h>
#include <dos.h>
#include <bios.h>
#include "drive628.h"
#include <needed.h>


main()
{
int abs_lut[512];       /* Three arrays for loading the LUts */
int frame_ilut[256];
int zero_ilut[256];
int i,n,x,frame,threshold;

is_error_messages(1);
is_initialize();
```

```
is_init_luts();
is_set_sync_source(1);
is_frame_clear(4);
is_frame_clear(3);
is_frame_clear(5);
is_frame_clear(6);
is_select_input_frame(0);
is_select_output_frame(0);

printf("Enter the Threshold value:\n");
scanf("%d",&threshold);
delay(300000);

for(i=0;i<512;i++)                /* Loading the RLUT2 with values
such   */
      {                              /* that any value greater than
threshold*/
      n=256-i;                       /* level goes to 1, while any
value  */
      abs_lut[i]=(abs(n)>threshold)?1:255;   /* below goes to 255.
*/
      }
is_load_rlut(2,abs_lut);



      /* Initializes the array for ILUT2 with */

      /* values of zero */
for(x=0;x<256;x++)
      {
      frame_ilut[x]=0;
      }

for(x=0;x<256;x++)                /* Loading the ILUT1 with values
such */
      {                              /* that all input will be
unchanged */
      zero_ilut[x]=x;                /* except for the value 4
which is sent */
      }                              /* to zero */
zero_ilut[4]=0;
zero_ilut[255]=0;
is_load_ilut(1,zero_ilut);



is_select_ilut(0);
is_passthru();
is_acquire(1,1);
clrscr();
for(frame=1;frame<200;frame++)
{
is_select_input_frame(0);
is_select_output_frame(0);
is_passthru();
```

```
/* Moving the motor */

init912(CHANNEL,1000,100,1000,1000,100,40);
drive628(CHANNEL,LTRJ,LOAD_POSITION,1);
drive628(CHANNEL,STT,0,0);
while(!(drive628(CHANNEL,RDSIGS,0,0)& ON_TARGET))
      printf("\rReal position:%8ld",drive628(CHANNEL,RDRP,0,0));
printf("\nReached the position of frame %d\n",frame);

is_acquire(2,1);
is_do_alu(2,0,1,2,38,3);    /* Grab a frame and subtract it from 1,
then */
                                                        /* put the
result through RLUT2 into frame 3 */

is_frame_copy(2,1);          /* Copy grabbed frame into frame 1 */

is_add(3,4,4);               /* Add frame 3 and 4 and put result in
4 */

frame_ilut[4]=frame;         /* Load ILUT2 such that for any value
of 4 */
is_load_ilut(2,frame_ilut); /* input it is replaced by the "frame"
number */

is_perform_feedback(4,2,5); /* Inputs frame 4 into ILUT2 and
places the */
                                                        /* result
in frame 5 */

is_perform_feedback(4,1,4); /* Inputs frame 4 into ILUT1 and
places the */
                                                        /* result
in frame 4. */
is_add(5,6,6);


}
is_end();
return 0;
}□
```

LabView Programs

Hounsfield Loading Device

The dual in-plane ESPI system was used to observe the deformations in building materials. The bricks were placed in the Hounsfield Loading Device and compressed. The ESPI system was placed on a table in front of the loading device which was also set on the table. The front panel of the loading device was used to control the compression. However having to change settings, such as speed and direction, during a test using this panel sometimes caused mechanical vibrations on the table. As mechanical noise can cause poor fringe visibility the settings on the device could not be changed during a test.

To overcome this, a computer program was written using LabView which controlled the loading device. This meant that any of the settings could be changed at any time. The LabView program communicates with the loading device by using a serial connection. The front panel of the device was now displayed on the computer screen so the velocity and direction can then be chosen using the mouse. During the test the computer displays the actual real-time force and any errors that occurred during communication. After the scan the program displays a force versus time graph, total displacement and the time taken. The following figure shows the front panel as displayed on the computer screen:

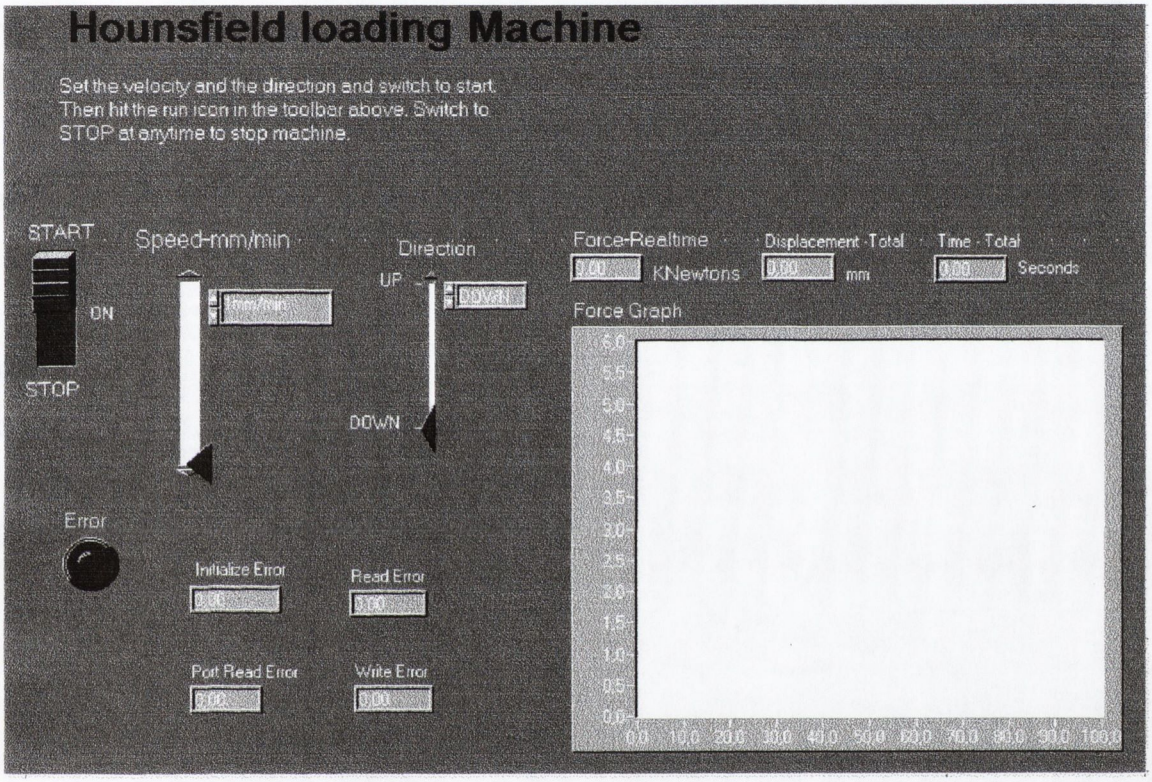

APPENDIX C

Polarisation and Retardation Theory

Polarisation

Light may be treated as a transverse electromagnetic wave composed of two orthogonal components. The so-called polarisation state of the light depends on the amplitudes of these components and the phase difference between them. We can represent the orthogonal components in the following way

$$E_x(z,t) = iE_{0x}\cos(kz-\omega t)$$

and

$$E_y(z,t) = jE_{0y}\cos(kz-\omega t+\varepsilon)$$

where ε is the relative phase difference between the waves. The resultant optical disturbance is the vector sum of these two perpendicular components.

$$E(z,t) = E_x(z,t) + E_y(z,t)$$

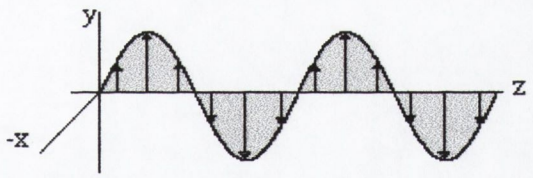

If $\varepsilon = 0$ or $\pm 2\pi$ (or an integral multiple) the waves are said to be in phase. The resultant wave has a fixed amplitude and it is linearly polarised meaning the electric field vector is confined to one plane whose orientation with respect to the x-axis depends on E_{0x}, E_{0y}. If ε= odd integer multiple of $\pm\pi$, the waves are 180° out of phase and the resultant wave is again linearly polarised, but the plane of vibration has been rotated to lie at angle to the x axis.

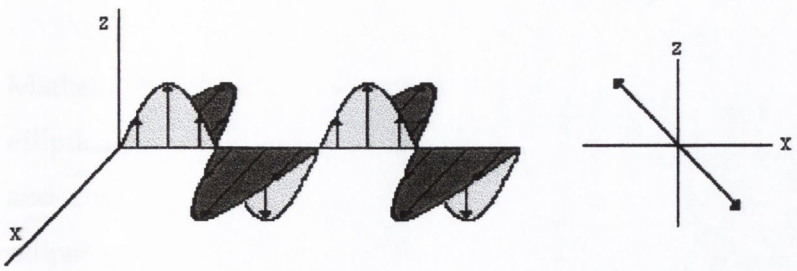

When both constituent waves have equal amplitudes and their relative phase difference $\varepsilon = -\pi/2 + 2m\pi$, where $m = 0, \pm1, \pm2, ...$, (In other words $\varepsilon = -\pi/2$ or any value increased or decreased from $-\pi/2$ by whole multiples of 2π) the scalar amplitude of E is a constant. But the direction of E is time-varying. The resultant electric field vector E is rotating clockwise at an angular frequency of ω, as seen by an observer toward whom the wave is moving. Such a wave is said to be right-circular polarised.

$$E = E_0 [i\cos(kz-\omega t) + j\sin(kz-\omega t)]$$

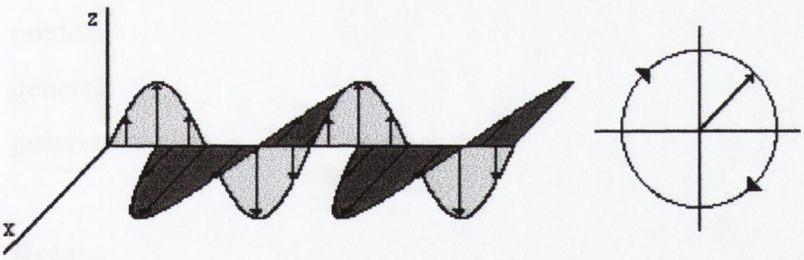

The E-vector makes one complete rotation as the wave advances through one wavelength. In comparison if $\varepsilon = \pi/2, 5\pi/2, 9\pi/2$ etc., i.e. $\varepsilon = \pi/2 + 2m\pi$ the amplitude is unaffected but now E rotates counter-clockwise and is referred to as left-circular

polarised. A linearly polarised wave can be synthesised from two circularly polarised waves of equal amplitude and opposite sense.

Mathematically, both linear and circular light may be considered to be special cases of elliptically polarised light. This means the resultant electric field vector E will rotate and change its magnitude as well. In this case the endpoint of E will trace out an ellipse given by the following expression

$$(E_y/E_{0y})^2 + (E_x/E_{0x})^2 - 2(E_x/E_{0x})(E_y/E_{0y})\cos\varepsilon = \sin^2\varepsilon$$

This is the equation of an ellipse making an angle α with the (E_x,E_y) co-ordinate system such that

$$\tan 2\alpha = (2E_{0x}E_{0y}\cos\varepsilon)/ (E_{0x}^2 - E_{0y}^2)$$

For an ordinary light source the polarisation changes in a completely unpredictable fashion. This is known as unpolarised light, but the light is actually composed of a rapid succession of wavetrains with different polarisation states. We can represent the light in terms of just two arbitrary, incoherent, orthogonal, linearly polarised waves of equal amplitude, i.e. waves for which the relative phase difference varies rapidly and randomly. A perfectly monochromatic plane wave is always polarised. Light is generally neither completely polarised nor completely unpolarised but is partially polarised.

Retarders

An optical device whose input is natural light and whose output is some form of polarised light is known as a polariser. An instrument that separates the two orthogonal polarisation states, discarding one and passing the other is known as a linear polariser. Retarders serve to change the polarisation of the incident beam. In principle the operation of a retarder is quite simple. One of the two component linear

polarisation states is somehow caused to lag in phase behind the other by a predetermined amount. Upon emerging from the retarder the relative phase difference between the two components has changed, thus the polarisation has changed as well. Most retarders are made from a birefringent material. Therefore to fully understand how a retarder works it is necessary to be familiar with the concept of birefringence.

Birefringence is the property whereby a material has more than one index of refraction. In the case of a liquid crystal, for example, light plane polarised parallel to the optic axis has a different index of refraction (that is to say it travels at a different velocity) than light plane polarised perpendicular to the optic axis. When light enters a birefringent material, it is broken up into the fast (called the ordinary ray) and slow (called the extraordinary ray) components. Because the two components travel at different velocities, the waves get out of phase. When they recombine as they exit the birefringent material, the polarisation state has changed because of the phase difference. The birefringence of a material is characterised by the difference in the indices of refraction for the ordinary and extraordinary rays. For a typical nematic liquid crystal, this difference may be between 0.1 and 0.2. The thickness of the sample is another important parameter because the phase shift accumulates as long as the light propagates in the birefringent material. Any polarisation state can be produced with the right combination of the birefringence and thickness parameters.

Many crystalline substances are also optically anisotropic. In other words their optical properties are not the same in all directions within any given sample. Glass and plastic are usually but not always isotropic. Light propagates through a transparent substance by exciting the electrons within the medium. The electrons are driven by the E-field and they re-radiate: these secondary waves combine with the incident wave and the resultant wave moves on. The speed of the wave and therefore the refractive index is determined by the difference between the frequency of the E-field and the natural or characteristic frequency of the bound electrons. An anisotropy in the binding force will therefore be manifest in an anisotropy in the speed of the wave. A material which displays two different indices of refraction is said to be birefringent.

Calcite or calcium carbonate ($CaCo_3$) is the most common material for making polarisers for use with high power lasers. Any number of planes can be drawn through the crystal so as to contain the optic axis, these are all called principal planes. Two waves emerge which are linearly polarised and orthogonal, the ordinary and extraordinary rays. The ordinary waves are formed by the incident light which is linearly polarised perpendicular to the optic axis. The extraordinary waves are formed by the incident light which is linearly polarised parallel to the optic axis. The extraordinary wave has a lower velocity than the ordinary wave velocity. The difference in refractive indices between the ordinary and extraordinary waves is a measure of the birefringence for a particular substance.

On account of its greater velocity, the e-wave will move through the specimen more rapidly than the o-wave. After traversing a plate of thickness d the resultant electromagnetic wave is the superposition of the e- and o- waves which now have a relative phase difference of $\Delta\phi$.

The relative OPD is given by

$$\Lambda = d(|n_o - n_e|)$$

since $\Delta\phi = k_0\Lambda$

$$\Delta\phi = (2\pi/\lambda)d(|n_o - n_e|).$$

The state of polarisation depends on the amplitudes of the waves and on $\Delta\phi$.

Full-Wave Plate : If $\Delta\phi$ is equal to 2π, the relative retardation is one wavelength: the e- and o- waves are back in phase and there is no observable effect on the polarisation of the incident monochromatic beam. When the retardance $\Delta\phi$ is 360° the device is

called a full wave plate. In calcite, the wave whose E-field vibrations are parallel to the optic axis travel fastest. The direction of the optic axis in a negative uniaxial material is therefore referred to as the fast axis. In a positive uniaxial crystal such as quartz its the slow axis.

Half-Wave Plate : This plate causes a relative phase difference of π radians or 180°. In a negative uniaxial material the e-wave will have a higher speed than the o-wave. When they emerge the relative phase shift is $\lambda_0/2$ ($2\pi/2$), with the effect that E will have rotated through 2θ, where θ is the angle between E and the optic axis. A half wave plate will flip elliptically polarised light. It will also invert the handedness of circular and elliptically polarised light. For a half-wave plate the thickness of the material is such that

$$d(|n_o - n_e|) = (2m+1)\lambda_0/2 \qquad \text{where } m = 0,1,2.....$$

A half wave plate is useful for rotating the plane of polarisation from a polarised laser to any desired plane.

Quarter-Wave Plate :This plate will cause a relative phase shift of $\Delta\phi = \pi/2$ between the o- and the e- components, which will convert linearly polarised to elliptically polarised and vice versa. It should be apparent that linearly polarised light incident parallel to either principal axis will be unaffected by any sort of retardation plate because one can not have a relative phase shift without having two components. When linear light at 45° to either principal axis is incident on a quarter-wave plate its o-and e- components have equal amplitudes. Under these special circumstances a 90° phase shift converts the wave into circularly polarised light. Similarly an incoming circularly polarised beam will emerge linearly polarised.

The thickness of the material should satisfy the equation

$$d(|n_o - n_e|) = (4m + 1)\lambda_0/4$$

The retardation of a wave plate can be increased by tilting it.

In dealing with problems involving polarised light, it is sometimes necessary to determine the effect a particular retarder has on the state of polarisation of a light beam. A method for calculating this effect is explained later in this appendix.

Polarisation Program

The methods of determining effects of polarisation sensitive devices on light are based on the fact that the polariser or retarder performs a linear transformation (represented by a matrix) on the vector representation of a polarised light beam. The Poincare sphere construction is a useful device for visualising the effects of polarisers and retarders on a beam of polarised light. The various states of polarisation are represented on the sphere as follows: The equator represents various forms of linear polarisation, the poles represents right and left circular polarisation and other points on the sphere represent elliptically polarised light. Every point on the sphere corresponds to a different polarisation state. The radius of the sphere is the intensity of the light beam which is usually assumed to be unity. The effects of polarisers and retarders are determined by appropriate displacements on the sphere.

The Poincare sphere is based on the Stokes parameters which are used to characterise the state of polarisation of a beam and the retarder, or polariser itself. Given in their simplest form the Stokes parameters of a plane monochromatic wave are the four quantities

$$S_0 = a_1^2 + a_2^2,$$
$$S_1 = a_1^2 - a_2^2,$$
$$S_2 = 2a_1a_2 \cos\delta,$$
$$S_3 = 2a_1a_2 \sin\delta,$$

where a_1 and a_2 are the amplitudes of the orthogonal components and δ is the phase difference between them.

The physical meanings of these parameters are as follows S_0 is the intensity of the light beam; S_1 is the difference in intensities between the horizontal and vertical components; S_2 is the intensity difference between the +45 and -45 degree components of the input; S_3 gives the preference for right or left circular polarised light. When the light is elliptical the three parameters are related in a simple way to the angle ψ, which specifies the orientation of the ellipse, and the angle χ, which characteristics the ellipticity of the ellipse, by the following equations (142):

$$S_1 = S_0 \cos 2\chi \cos 2\psi$$
$$S_2 = S_0 \cos 2\chi \sin 2$$
$$S_3 = S_0 \sin 2\chi$$

The intensity vector S_0 is related to the other three by the relation

$$S_0^2 = S_1^2 + S_2^2 + S_3^2$$

Once the polarisation of the input light has been mathematically described it must then be multiplied by the Mueller matrix M, which describes a waveplate with a retardance δ (in degrees) and an arbitrary fast axis orientation ϕ (measured from the horizontal), as follows:

M =

$$\begin{vmatrix} 1 & 0 & 0 & 0 \\ 0 & X^2 + Y^2 \cos\delta & XY(1-\cos\delta) & -Y\sin\delta \\ 0 & XY(1-\cos\delta) & Y^2 + X^2 \cos\delta & X\sin\delta \\ 0 & Y\sin\delta & -X\sin\delta & \cos\delta \end{vmatrix}$$

where:

$X = \cos(2\phi)$, and

$Y = \sin(2\phi)$

The input is defined by the vector S, where

S =

$$\begin{vmatrix} S_0 \\ S_1 \\ S_2 \\ S_3 \end{vmatrix}$$

The light output is calculated by **S' = MS**.

A computer program was written in Windows which performs all of the above calculations. The user inputs the polarisation state of the input light, i.e. whether it is:

A. Linear,

B. Circular,

C. Elliptical.

Depending on this choice the user must also input other parameters, e.g. if the input is linear the user must input the angle the linear light makes with the horizontal. If the input is elliptical the user has a choice whether to define its parameters using its elliptical shape (ratio of its minor to major axes and the angle the major axis makes with the horizontal) or the component values that produced the elliptical form (ratio of the component amplitudes, phase difference between the components). Once these are entered, the computer program then calculates the vector S.

The user then inputs the characteristics of the waveplate or retarder using the following quantities:

A. The retardance, e.g. 0.5 for a half-wave plate.

B. The angle the fast-axis of the plate makes with the horizontal axis.

The program then calculates the M matrix. It then multiplies the vector S by the matrix M to produce the vector S'. This vector is then analysed to output the polarisation state in one of the following ways:

A. Linear, defining the angle its plane of polarisation makes with the horizontal.

B. Circular, stating whether it is left or right circular.

C. Elliptical, defining the minor-major axis ratio and the angle the major makes with the horizontal.

The program is opened in Windows and displayed as follows:

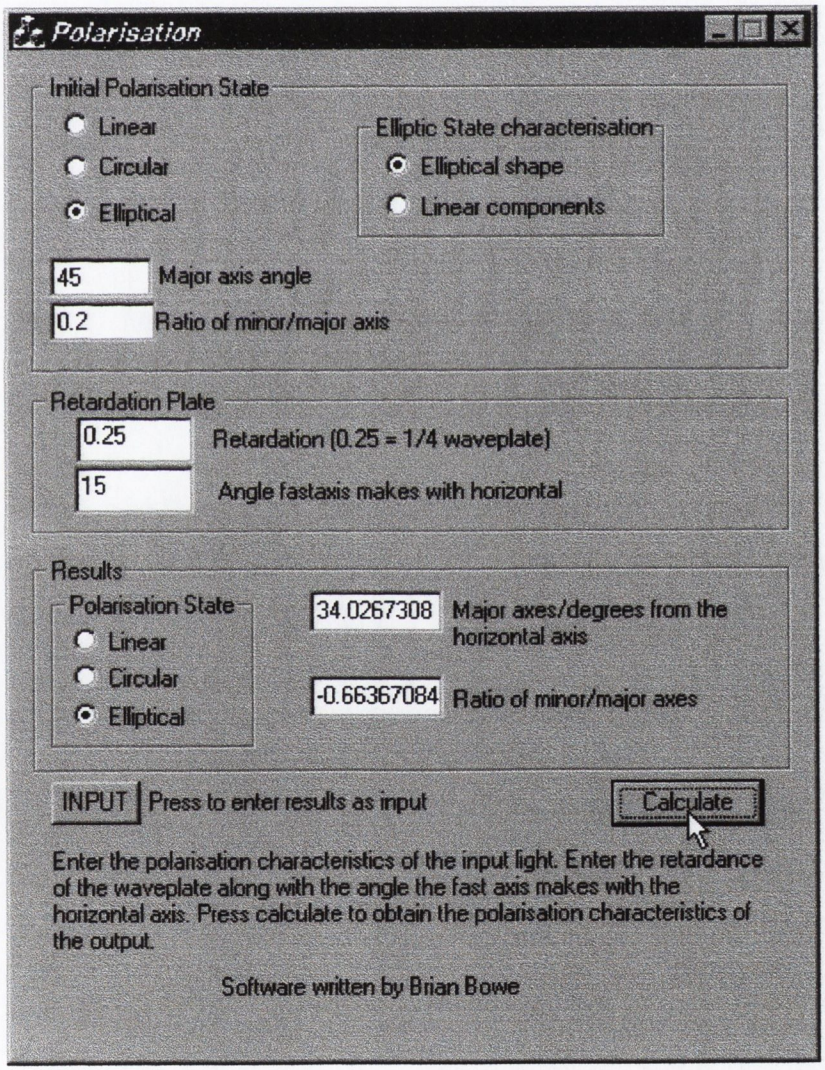

The following is the main C++ code for the polarisation program:

```
// PolarisationDlg.cpp : implementation file

#include "stdafx.h"
#include "Polarisation.h"
#include "PolarisationDlg.h"
#include <math.h>

#ifdef _DEBUG
#define new DEBUG_NEW
#undef THIS_FILE
static char THIS_FILE[] = __FILE__;
#endif


char *ELLIPT1="Major axis angle";
char *ELLIPT2="Ratio of y/x components";

char *RIGHTCIRC="Right circular";
char *LEFTCIRC="Left circular";

double q,u,v,r,a,an,a1,t,angle,eangle;
double r1,t1,t2,t3,t4,qr,ur,vr;
double x1,x2,x3,y01,y2,y3,z1,z2,z3;
double Pi = 3.14159265359;
int ch,trip,cv;

/////////////////////////////////////////////////////////////////////////////

BOOL CPolarisationDlg::OnInitDialog()
{
	CDialog::OnInitDialog();
	ASSERT((IDM_ABOUTBOX & 0xFFF0) == IDM_ABOUTBOX);
	ASSERT(IDM_ABOUTBOX < 0xF000);

	CMenu* pSysMenu = GetSystemMenu(FALSE);
	CString strAboutMenu;
	strAboutMenu.LoadString(IDS_ABOUTBOX);
	if (!strAboutMenu.IsEmpty())
	{
		pSysMenu->AppendMenu(MF_SEPARATOR);
		pSysMenu->AppendMenu(MF_STRING, IDM_ABOUTBOX, strAboutMenu);
	}

	SetIcon(m_hIcon, TRUE);			// Set big icon
	SetIcon(m_hIcon, FALSE);		// Set small icon

	// TODO: Add extra initialization here

	CheckRadioButton(IDC_LINEAR,IDC_ELLIPTICAL,IDC_LINEAR);
	CheckRadioButton(IDC_ELLIPTICALSHAPE,IDC_LINEARCOMPONENTS,IDC_ELLIPTICALSHAPE);
	PostMessage(WM_COMMAND,MAKELONG(IDC_LINEAR,BN_CLICKED));
	GetDlgItem(IDC_RESULT2)->ShowWindow(SW_HIDE);
	GetDlgItem(IDC_RESULT2TEXT)->ShowWindow(SW_HIDE);
	GetDlgItem(IDC_INPUTRESULT)->ShowWindow(SW_HIDE);
	GetDlgItem(IDC_PRESSINPUT)->ShowWindow(SW_HIDE);
	return TRUE;  // return TRUE  unless you set the focus to a control
}

void CPolarisationDlg::OnSysCommand(UINT nID, LPARAM lParam)
{
	if ((nID & 0xFFF0) == IDM_ABOUTBOX)
	{
		CAboutDlg dlgAbout;
		dlgAbout.DoModal();
	}
```

```
	else
	{
		CDialog::OnSysCommand(nID, lParam);
	}
}

HCURSOR CPolarisationDlg::OnQueryDragIcon()
{
	return (HCURSOR) m_hIcon;
}

BOOL CPolarisationDlg::OnCommand(WPARAM wParam, LPARAM lParam)
{
	// TODO: Add your specialized code here and/or call the base class
	if(HIWORD(wParam)==BN_CLICKED) {
		WORD curr_ID= LOWORD(wParam);

		switch(curr_ID) {

		case IDC_LINEAR:
			GetDlgItem(IDC_INPUT2)->ShowWindow(SW_HIDE);
			GetDlgItem(IDC_INPUTVALUE2TEXT)->ShowWindow(SW_HIDE);
			GetDlgItem(IDC_INPUTVALUE1TEXT)->SetWindowText("Angle of the linear light wrt
horizontal axis");
			OnPaint();
			break;

		case IDC_CIRCULAR:
			GetDlgItem(IDC_INPUT2)->ShowWindow(SW_HIDE);
			GetDlgItem(IDC_INPUTVALUE2TEXT)->ShowWindow(SW_HIDE);
			GetDlgItem(IDC_INPUTVALUE1TEXT)->SetWindowText("Rotational direction [-1=left
circular, 1=right circular]");
			break;
		case IDC_ELLIPTICAL:
			GetDlgItem(IDC_INPUT2)->ShowWindow(SW_SHOW);
			GetDlgItem(IDC_INPUTVALUE2TEXT)->ShowWindow(SW_SHOW);
			if (!((CButton *)GetDlgItem(IDC_ELLIPTICALSHAPE))->GetCheck()){
				GetDlgItem(IDC_INPUTVALUE1TEXT)->SetWindowText(ELLIPT2);
			}
			else {
				GetDlgItem(IDC_INPUTVALUE1TEXT)->SetWindowText(ELLIPT1);

			}
			break;

		case IDC_ELLIPTICALSHAPE:
			if (((CButton *)GetDlgItem(IDC_ELLIPTICAL))->GetCheck()){

				GetDlgItem(IDC_INPUTVALUE1TEXT)->SetWindowText(ELLIPT1);
				GetDlgItem(IDC_INPUTVALUE2TEXT)->SetWindowText("Ratio of minor-major
axis");

			}
			break;

		case IDC_LINEARCOMPONENTS:
			if (((CButton *)GetDlgItem(IDC_ELLIPTICAL))->GetCheck()){

				GetDlgItem(IDC_INPUTVALUE1TEXT)->SetWindowText(ELLIPT2);
				GetDlgItem(IDC_INPUTVALUE2TEXT)->SetWindowText("Phase difference
between linear components");

			}
			break;
		case IDOK:
			DoCalculation();
			break;
		case IDC_INPUTRESULT:
			if(((CButton *)GetDlgItem(IDC_RESULTLINEAR))->GetCheck()){
```

```
                        ((CButton *)GetDlgItem(IDC_LINEARCOMPONENTS))->SetCheck(0);
                        ((CButton *)GetDlgItem(IDC_CIRCULAR))->SetCheck(0);
                        ((CButton *)GetDlgItem(IDC_ELLIPTICAL))->SetCheck(0);
                        ((CButton *)GetDlgItem(IDC_LINEAR))->SetCheck(1);
                        m_input1=angle;
                        GetDlgItem(IDC_INPUT2)->ShowWindow(SW_HIDE);
                        GetDlgItem(IDC_INPUTVALUE2TEXT)->ShowWindow(SW_HIDE);
                        GetDlgItem(IDC_INPUTVALUE1TEXT)->SetWindowText("Angle of the linear light wrt
horizontal axis");
                        UpdateData(FALSE);

                        }

                        if(((CButton *)GetDlgItem(IDC_RESULTCIRCULAR))->GetCheck()){
                        ((CButton *)GetDlgItem(IDC_LINEARCOMPONENTS))->SetCheck(0);
                        ((CButton *)GetDlgItem(IDC_ELLIPTICAL))->SetCheck(0);
                        ((CButton *)GetDlgItem(IDC_LINEAR))->SetCheck(0);
                        ((CButton *)GetDlgItem(IDC_CIRCULAR))->SetCheck(1);
                        m_input1=vr;
                        GetDlgItem(IDC_INPUT2)->ShowWindow(SW_HIDE);
                        GetDlgItem(IDC_INPUTVALUE2TEXT)->ShowWindow(SW_HIDE);
                        GetDlgItem(IDC_INPUTVALUE1TEXT)->SetWindowText("Rotational direction [-1=left
circular, 1=right circular]");
                        UpdateData(FALSE);

                        }

                        if(((CButton *)GetDlgItem(IDC_RESULTELLIPTICAL))->GetCheck()){
                        ((CButton *)GetDlgItem(IDC_LINEARCOMPONENTS))->SetCheck(0);
                        ((CButton *)GetDlgItem(IDC_CIRCULAR))->SetCheck(0);
                        ((CButton *)GetDlgItem(IDC_ELLIPTICAL))->SetCheck(1);
                        ((CButton *)GetDlgItem(IDC_LINEAR))->SetCheck(0);
                        m_input1=a;
                        m_input2=eangle;
                        ((CButton *)GetDlgItem(IDC_ELLIPTICALSHAPE))->SetCheck(1);
                        GetDlgItem(IDC_INPUT2)->ShowWindow(SW_SHOW);
                        GetDlgItem(IDC_INPUTVALUE2TEXT)->ShowWindow(SW_SHOW);
                        GetDlgItem(IDC_INPUTVALUE1TEXT)->SetWindowText(ELLIPT1);
                        GetDlgItem(IDC_INPUTVALUE2TEXT)->SetWindowText("Ratio of minor-major axis");
                        UpdateData(FALSE);
                        }
                break;
                }
        }

        return CDialog::OnCommand(wParam, lParam);
}

void CPolarisationDlg::DoCalculation(){

UpdateData();

GetDlgItem(IDC_RESULT2TEXT)->ShowWindow(SW_HIDE);
GetDlgItem(IDC_RESULT2)->ShowWindow(SW_HIDE);
((CButton *)GetDlgItem(IDC_RESULTLINEAR))->SetCheck(0);
((CButton *)GetDlgItem(IDC_RESULTCIRCULAR))->SetCheck(0);
((CButton *)GetDlgItem(IDC_RESULTELLIPTICAL))->SetCheck(0);

if (((CButton *)GetDlgItem(IDC_ELLIPTICAL))->GetCheck()) ellip();
if (((CButton *)GetDlgItem(IDC_LINEAR))->GetCheck()) linear();
if (((CButton *)GetDlgItem(IDC_CIRCULAR))->GetCheck()) circular();
GetDlgItem(IDC_INPUTRESULT)->ShowWindow(SW_SHOW);
GetDlgItem(IDC_PRESSINPUT)->ShowWindow(SW_SHOW);
UpdateData(FALSE);

 return;
}

void CPolarisationDlg::linear()
```

```
{
double anr;
double qa,qb;
if(trip==10)
        goto Skip;
anr=0;
anr=(m_input1/180)*Pi;
qa=cos(anr)*cos(anr);
qb=sin(anr)*sin(anr);
q=qa-qb;
u=2*cos(anr)*sin(anr);
v=0;
r1=m_retardation*2*Pi;
a1=(m_retatdationfastaxis/180)*Pi;
Skip:;
trip=0;
t1=cos(r1);
if(t1<.01 && t1>=0)
        t1=0;
if(t1<0 && t1>-.009)
        t1=0;
t2=sin(r1);
if(t2<.01 && t2>=0)
        t2=0;
if(t2<0 && t2>-.009)
        t2=0;
t3=cos(2*a1);
if(t3<.01 && t3>=0)
        t3=0;
if(t3<0 && t3>-.009)
        t3=0;
t4=sin(2*a1);
if(t4<.01 && t4>=0)
        t4=0;
if(t4<0 && t4>-.009)
        t4=0;
x1=(t3*t3)+(t4*t4)*t1;
x2=(t3*t4)*(1-t1);
x3=(-1)*t4*t2;
y01=x2;
y2=(t4*t4)+(t3*t3)*t1;
y3=t3*t2;
z1=(-1)*x3;
z2=(-1)*y3;
z3=t1;
qr=(x1*q)+(x2*u)+(x3*v);
ur=(y01*q)+(y2*u)+(y3*v);
vr=(z1*q)+(z2*u)+(z3*v);
if(vr==0)
        {
        ((CButton *)GetDlgItem(IDC_RESULTLINEAR))->SetCheck(1);
        linear1();
        }
if(vr==1)
        {
        ((CButton *)GetDlgItem(IDC_RESULTCIRCULAR))->SetCheck(1);
        GetDlgItem(IDC_RESULT1TEXT)->SetWindowText(RIGHTCIRC);
        m_result1=1;
        }
if(vr==-1)
        {
        ((CButton *)GetDlgItem(IDC_RESULTCIRCULAR))->SetCheck(1);
        GetDlgItem(IDC_RESULT1TEXT)->SetWindowText(LEFTCIRC);
        m_result1=-1;
        }
if(!(vr==0 || vr==1 || vr==-1))
        {
        ((CButton *)GetDlgItem(IDC_RESULTELLIPTICAL))->SetCheck(1);
        ellip2();
```

```
        }
}
void CPolarisationDlg::linear1()
{
char *text;
double i1,i2;
double pw,ang;
int mul;
pw=-1*((qr-1)/2);
i1=sqrt(pw);
i2=asin(i1);
ang=(i2/Pi)*180;
mul=(ang+.001)*100;
t=mul/100.0;
if(ur>=0)
        angle=t;
else
        angle=-t;
        m_result1=angle;
if(angle==90)
        {
        text ="degrees from the horizontal axis(vertical linear)";
        }
if(angle==-90)
        {
        text="degrees from the horizontal axis (vertical linear)";
        }
if(angle==0)
        {
        text="degrees from the horizontal axis (horizontal linear)";
        }
else
        {
        text="degrees from the horizontal axis";
        }
GetDlgItem(IDC_RESULT1TEXT)->SetWindowText(text);
}

void CPolarisationDlg::circular()
{
q=0;
u=0;
if(cv==10)
        goto Jump;
v=m_input1;
Jump:;
r1=m_retardation*2*Pi;
a1=(m_retatdationfastaxis/180)*Pi;
t1=cos(r1);
if(t1<.01 && t1>=0)
        t1=0;
if(t1<0 && t1>-.009)
        t1=0;
t2=sin(r1);
if(t2<.01 && t2>=0)
        t2=0;
if(t2<0 && t2>-.009)
        t2=0;
t3=cos(2*a1);
if(t3<.01 && t3>=0)
        t3=0;
if(t3<0 && t3>-.009)
        t3=0;
t4=sin(2*a1);
if(t4<.01 && t4>=0)
        t4=0;
if(t4<0 && t4>-.009)
        t4=0;
x1=(t3*t3)+(t4*t4)*t1;
```

```
x2=(t3*t4)*(1-t1);
x3=(-1)*t4*t2;
y01=x2;
y2=(t4*t4)+(t3*t3)*t1;
y3=t3*t2;
z1=(-1)*x3;
z2=(-1)*y3;
z3=t1;
qr=(x1*q)+(x2*u)+(x3*v);
ur=(y01*q)+(y2*u)+(y3*v);
vr=(z1*q)+(z2*u)+(z3*v);
if(vr==0)
        {
        ((CButton *)GetDlgItem(IDC_RESULTLINEAR))->SetCheck(1);
        linear1();
        }
if(vr==1)
        {
        ((CButton *)GetDlgItem(IDC_RESULTCIRCULAR))->SetCheck(1);
        GetDlgItem(IDC_RESULT1TEXT)->SetWindowText(RIGHTCIRC);
        m_result1=-1;
        }

if(vr==-1)
        {
        ((CButton *)GetDlgItem(IDC_RESULTCIRCULAR))->SetCheck(1);
        GetDlgItem(IDC_RESULT1TEXT)->SetWindowText(LEFTCIRC);
        m_result1=-1;
        }
if(!(vr==0 || vr==1 || vr==-1))
        {
        ((CButton *)GetDlgItem(IDC_RESULTELLIPTICAL))->SetCheck(1);
        ellip2();
        }
}

void CPolarisationDlg::ellip()
{
double ea,ian,rt,cma,cmb;
if (((CButton *)GetDlgItem(IDC_ELLIPTICALSHAPE))->GetCheck())
        {
        ian=m_input1;
        rt=atan(m_input2);
        vr=sin(rt*2);
        ur=sin(2*ian)*cos(rt*2);
        qr=cos(rt*2)*cos(2*ian);
        }
else
        {
        ea=atan(m_input1);
        cma=cos(ea)*cos(ea);
        cmb=sin(ea)*sin(ea);
        q=cma-cmb;
        r=m_input2;
        u=2*cos(ea)*sin(ea);
        v=0;
        a=0;
        r1=(r/180)*Pi;
        a1=(a/180)*Pi;
        t1=cos(r1);
                if(t1<.01 && t1>=0)
                        t1=0;
                        if(t1<0 && t1>-.009)
                        t1=0;
                t2=sin(r1);
                if(t2<.01 && t2>=0)
                        t2=0;
                if(t2<0 && t2>-.009)
                        t2=0;
```

```
                t3=cos(2*a1);
                if(t3<.01 && t3>=0)
                        t3=0;
                if(t3<0 && t3>-.009)
                        t3=0;
                t4=sin(2*a1);
                if(t4<.01 && t4>=0)
                        t4=0;
                if(t4<0 && t4>-.009)
                        t4=0;
        x1=(t3*t3)+(t4*t4)*t1;
        x2=(t3*t4)*(1-t1);
        x3=(-1)*t4*t2;
        y01=x2;
        y2=(t4*t4)+(t3*t3)*t1;
        y3=t3*t2;
        z1=(-1)*x3;
        z2=(-1)*y3;
        z3=t1;
        qr=(x1*q)+(x2*u)+(x3*v);
        ur=(y01*q)+(y2*u)+(y3*v);
        vr=(z1*q)+(z2*u)+(z3*v);
        }
if(vr==0)
        {
        ((CButton *)GetDlgItem(IDC_LINEAR))->SetCheck(1);
        ((CButton *)GetDlgItem(IDC_ELLIPTICAL))->SetCheck(0);
        trip=10;
        q=qr;
        u=ur;
        v=vr;
        linear();
        }
if(vr==1)
        {
        ((CButton *)GetDlgItem(IDC_CIRCULAR))->SetCheck(1);
        ((CButton *)GetDlgItem(IDC_ELLIPTICAL))->SetCheck(0);
        cv=10;
        v=1;
        circular();
        }
if(vr==-1)
        {
        ((CButton *)GetDlgItem(IDC_CIRCULAR))->SetCheck(1);
        ((CButton *)GetDlgItem(IDC_ELLIPTICAL))->SetCheck(0);
        cv=10;
        v=-1;
        circular();
        }
if(!(vr==0 || vr==1 || vr==-1))
        {
        q=qr;
        u=ur;
        v=vr;
        ellip1();
        }
}
void CPolarisationDlg::ellip1()
{
r1=m_retardation*2*Pi;
a1=(m_retatdationfastaxis/180)*Pi;

t1=cos(r1);
if(t1<.01 && t1>=0)
        t1=0;
if(t1<0 && t1>-.009)
        t1=0;
t2=sin(r1);
if(t2<.01 && t2>=0)
```

```
            t2=0;
if(t2<0 && t2>-.009)
            t2=0;
t3=cos(2*a1);
if(t3<.01 && t3>=0)
            t3=0;
if(t3<0 && t3>-.009)
            t3=0;
t4=sin(2*a1);
if(t4<.01 && t4>=0)
            t4=0;
if(t4<0 && t4>-.009)
            t4=0;
x1=(t3*t3)+(t4*t4)*t1;
x2=(t3*t4)*(1-t1);
x3=(-1)*t4*t2;
y01=x2;
y2=(t4*t4)+(t3*t3)*t1;
y3=t3*t2;
z1=(-1)*x3;
z2=(-1)*y3;
z3=t1;
qr=(x1*q)+(x2*u)+(x3*v);
ur=(y01*q)+(y2*u)+(y3*v);
vr=(z1*q)+(z2*u)+(z3*v);
if(vr==0)
            {
            ((CButton *)GetDlgItem(IDC_RESULTLINEAR))->SetCheck(1);

            linear1();
            }
if(vr==1)
            {
            ((CButton *)GetDlgItem(IDC_RESULTCIRCULAR))->SetCheck(1);
            GetDlgItem(IDC_RESULT1TEXT)->SetWindowText(RIGHTCIRC);
            m_result1=1;
            }
if(vr==-1)
            {
            ((CButton *)GetDlgItem(IDC_RESULTCIRCULAR))->SetCheck(1);
            GetDlgItem(IDC_RESULT1TEXT)->SetWindowText(LEFTCIRC);
            m_result1=-1;
            }
if(!(vr==0 || vr==1 || vr==-1))
            {
            ((CButton *)GetDlgItem(IDC_RESULTELLIPTICAL))->SetCheck(1);
            ellip2();
            }
}

void CPolarisationDlg::ellip2()
{
double  ek,el,eq,ew,er,et;
GetDlgItem(IDC_RESULT2)->ShowWindow(SW_SHOW);
GetDlgItem(IDC_RESULT2TEXT)->ShowWindow(SW_SHOW);
eq=asin(vr);
ew=eq/2;
eangle=tan(ew);
er=cos(eq);
et=ur/er;
ek=asin(et);
el=ek/2;
a=(el/Pi)*180;
m_result1=a;
GetDlgItem(IDC_RESULT1TEXT)->SetWindowText("Major axes/degrees from the horizontal axis");
m_result2=eangle;
GetDlgItem(IDC_RESULT2TEXT)->SetWindowText("Ratio of minor/major axes");
}
```

APPENDIX D

Strain Calculation

The strain due to the applied load can also be predicted from theory [16,24]. The sag δ of a beam loaded at its midpoint and supported at its ends, is given by

$$\delta = \frac{8L^3P}{384EI}$$

where P is the applied load, L the length, E Young's modulus of elasticity and I the moment of inertia around the neutral axis.

δ is also given by

$$\delta(2R - \delta) = \frac{L^2}{4} \text{ and, since } R \text{ is very large, } \quad R \cong \frac{L^2}{8\delta}$$

$$\text{strain at upper surface} = \frac{w}{2R} = \frac{wLP}{12EI}$$

APPENDIX E

Calibration graphs for the Acousto-Optic Filter

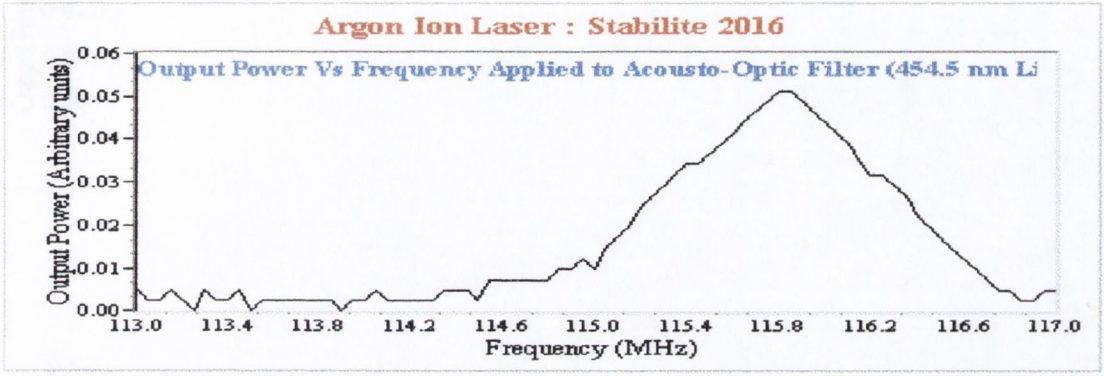

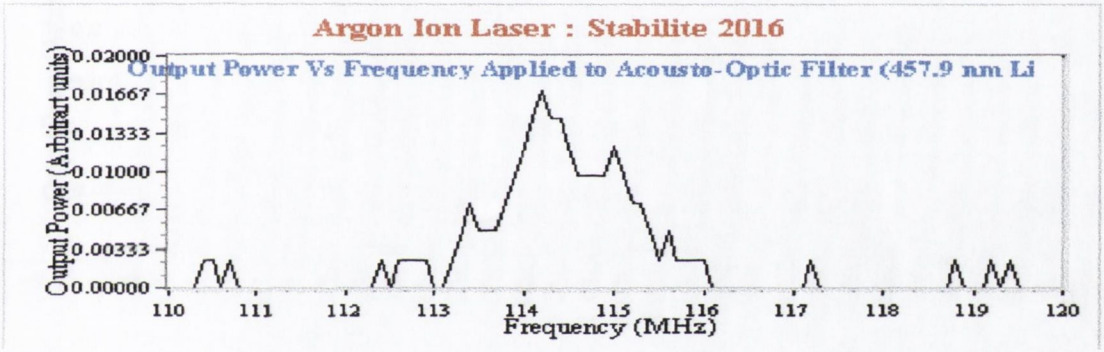

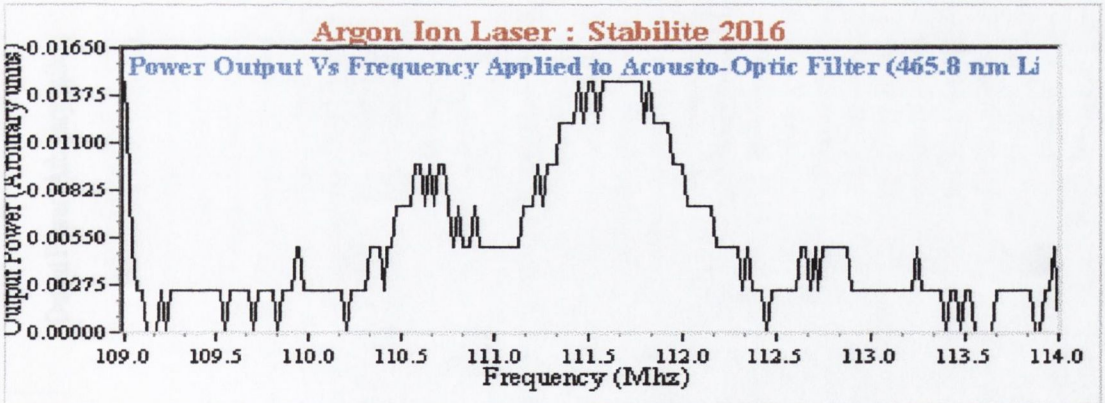

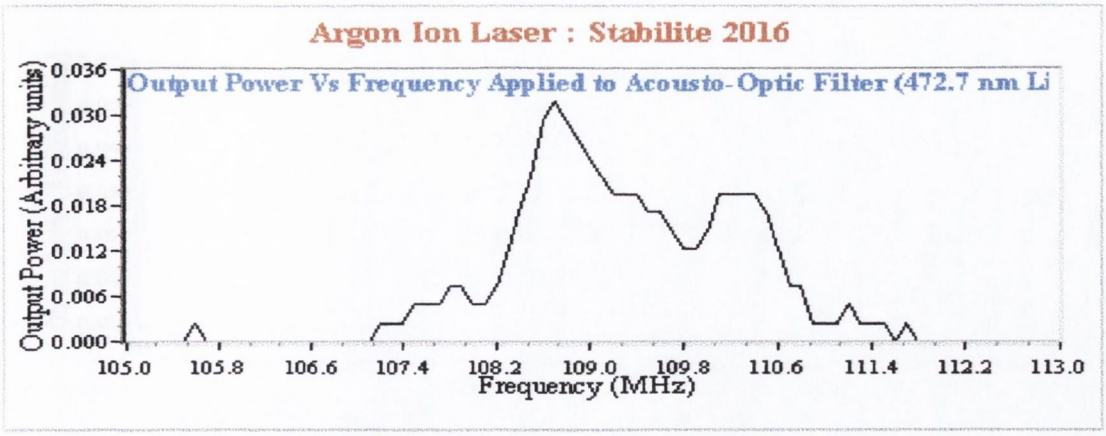
Argon Ion Laser : Stabilite 2016
Output Power Vs Frequency Applied to Acousto-Optic Filter (472.7 nm Li
Output Power (Arbitrary units)
0.036
0.030
0.024
0.018
0.012
0.006
0.000
105.0
105.8
106.6
107.4
108.2
109.0
109.8
110.6
111.4
112.2
113.0
Frequency (MHz)

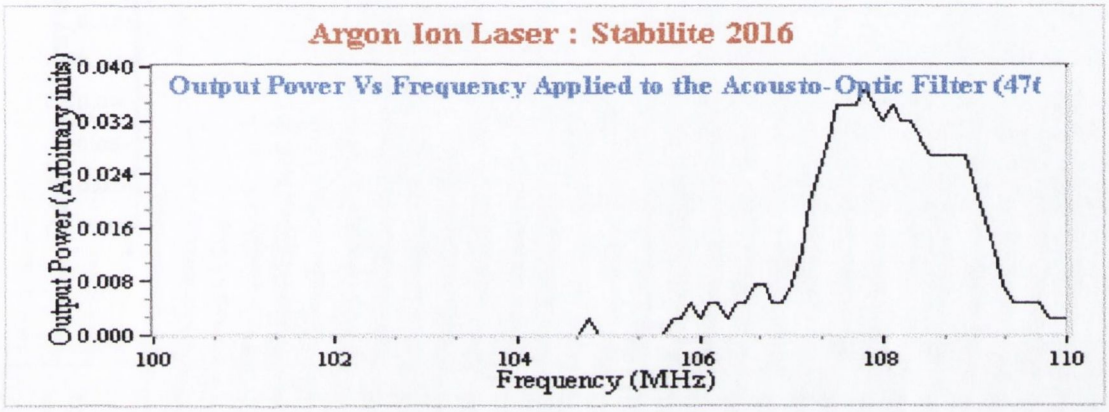
Argon Ion Laser : Stabilite 2016
Output Power Vs Frequency Applied to the Acousto-Optic Filter (47(
Output Power (Arbitrary units)
0.040
0.032
0.024
0.016
0.008
0.000
100
102
104
106
108
110
Frequency (MHz)

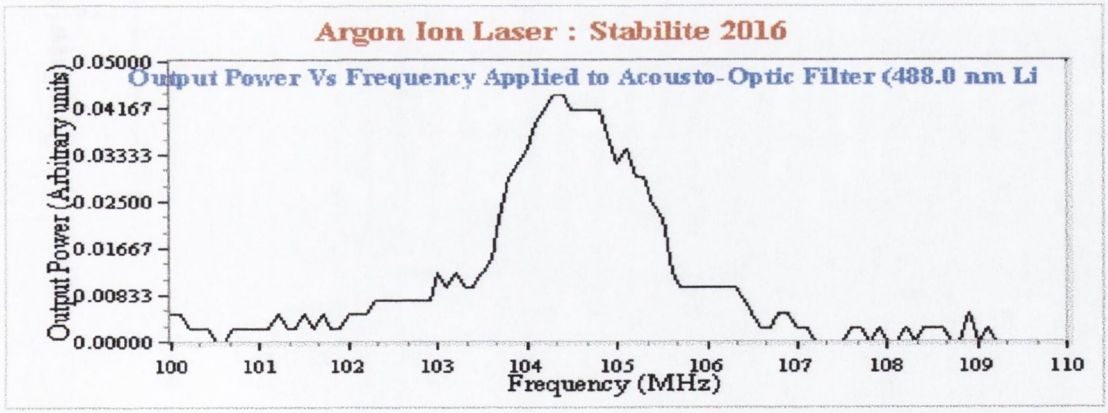
Argon Ion Laser : Stabilite 2016
Output Power Vs Frequency Applied to Acousto-Optic Filter (488.0 nm Li
Output Power (Arbitrary units)
0.05000
0.04167
0.03333
0.02500
0.01667
0.00833
0.00000
100
101
102
103
104
105
106
107
108
109
110
Frequency (MHz)

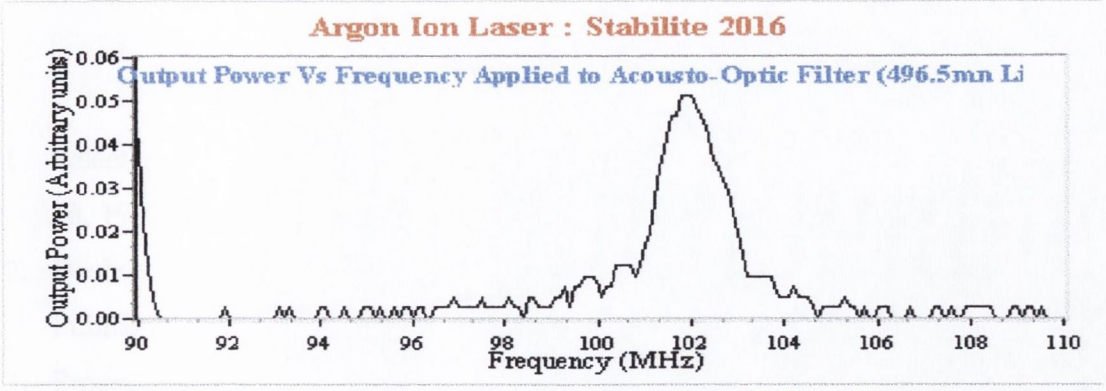
Argon Ion Laser : Stabilite 2016
Output Power Vs Frequency Applied to Acousto-Optic Filter (496.5nm Li
Output Power (Arbitrary units)
0.06
0.05
0.04
0.03
0.02
0.01
0.00
90
92
94
96
98
100
102
104
106
108
110
Frequency (MHz)

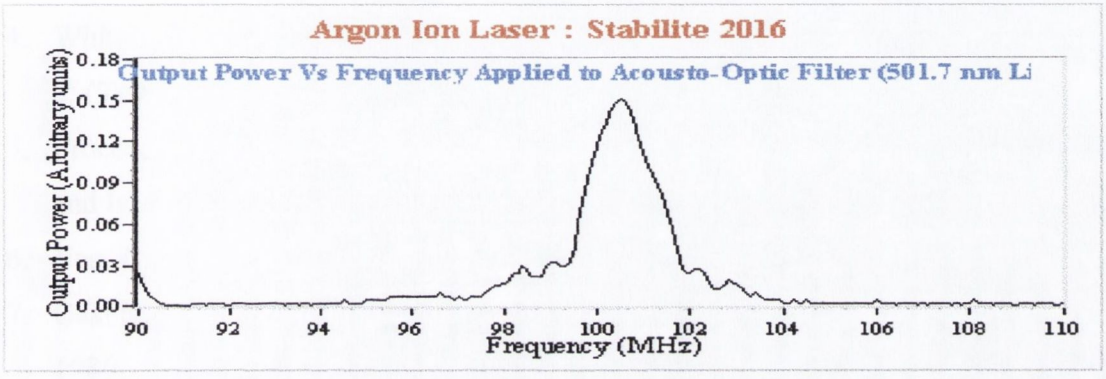
Argon Ion Laser : Stabilite 2016
Output Power Vs Frequency Applied to Acousto-Optic Filter (501.7 nm Li
Output Power (Arbitrary units)
0.18
0.15
0.12
0.09
0.06
0.03
0.00
90
92
94
96
98
100
102
104
106
108
110
Frequency (MHz)

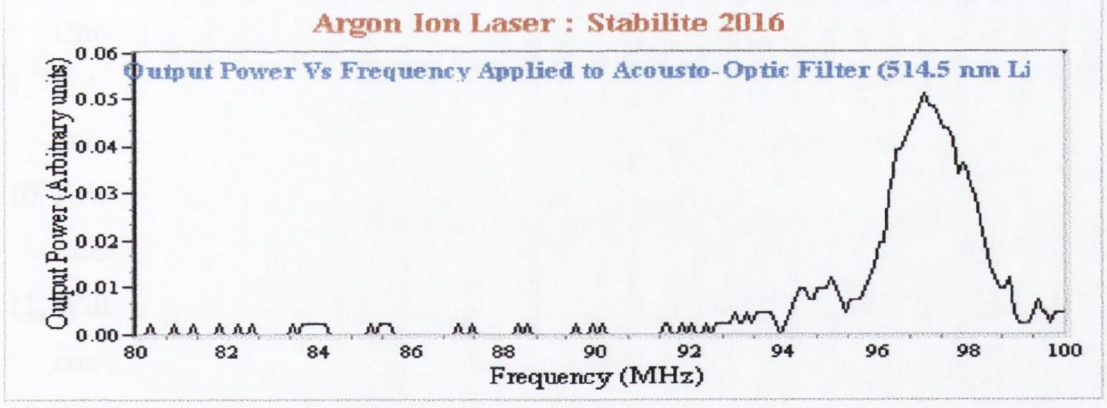
Argon Ion Laser : Stabilite 2016
Output Power Vs Frequency Applied to Acousto-Optic Filter (514.5 nm Li
Output Power (Arbitrary units)
0.06
0.05
0.04
0.03
0.02
0.01
0.00
80
82
84
86
88
90
92
94
96
98
100
Frequency (MHz)

REFERENCES

1. Selected Papers on Optical Shop Metrology, SPIE Milestone Series, Vol. MS 18, 1992.
2. Benham P.P., "Mechanics of Engineering Materials", Longman Singapore Publishers, 1988.
3. Proceedings of the "International Symposium on Non-destructive Testing in Civil Engineering", Berlin, September 1995.
4. Whitehouse, D.J. "Surface Metrology", Measurement Science & Technology 8: (9) 955-972 September 1997.
5. Proceedings of the "Industrial Optical Sensing and Metrology: Applications and Integration", Boston, September 1993.
6. Vest C.M., "Holographic Interferometry", John Wiley & Sons, 1979.
7. Gasvik, K. J, "Optical Metrology" John Wiley & Sons, Chichester, 117 – 140, 1986.
8. Jones R., Wykes C., "Holographic and Speckle Interferometry", Cambridge University Press, 1993.
9. P.A. Flourney, R. W. McClude amd G. Wyntjes, "White-light interferometric thickness gauge", Appl. Opt. 11, 1907-1915, 1972.
10. Fowler, T. J. "Acoustic Emission testing of glass fibre reinforced composites", International Corrosion Forum, Nace, Houston. Paper 251. March 1992.
11. Williams, J. H., "Ultrasonic evaluation of impact damaged graphite fibre composite", Materials Evaluation 38, 68 – 72, 1980.
12. Aman, J. K. et al., "Fundaments of radiography, Back to basics", Materials Evaluation, 36(4), 24 – 32. 1978.
13. "Handbook on Experimental Mechanics", Ed. Kobayashi A.S., Prentice-Hall, New Jersey, 1987.
14. Song, J. F., Vorburger, T. V., "Stylus Profiling at High Resolution and Low Force", Applied Optics 30, 42, 1991.
15. The WYKO NT 2000™ Surface Profiler, 1998, Veeco Instruments Inc.
16. Benham P.P., "Mechanics of Engineering Materials", Longman Singapore Publishers, 1988.

17. Cornwell, I., Mc Nab A., "Towards automated interpretation of ultrasonic NDT data", NDT & Evaluation International, 32 (2), 101 – 107, March, 1999.
18. Passi, G. S., Shoef, Y., Kritsky, M. V. "Reducting the influence of human-factors on the reliability of manual ultrasonic weld inspection", 37(10), 788-791, October, 1995.
19. Mc Donald, F. A. "On the precursor in laser-generated ultrasound waveforms in metals", Applied Physics Letters, 56: (3) 230-232 Jan 15 1990.
20. Sanderson, T., Ume, C., Jarzynski, J. "Laser generated ultrasound: A thermolelastic analysis of the source", Ultrasonics.
21. Prosser W. H., Jackson K.E., Kellas S., Smith B.T., McKeon J., Friedman A., "Advanced wave-form-based acoustic-emission detection of matrix cracking in composites", Materials Evaluation, 53: (9) 1052-1058 Sep 1995.
22. Kohn, D.H., Ducheyne, P., Awerbuch, J. "Acoustic emission during fatigue of TI-6AL-4V - incipient fatigue crack detection limits and generalized data - analysis methodology", Journal of Materials Science, 27: (12) 3133-3142 Jun 15 1992.
23. Poranski, C.F., Greenwald, E.C., Ham, Y.S. "X-ray backscatter tomography: NDT potential and limitations", Materials Science Forum, Part 1 & 2, 211-218, 1996.
24. Booresi, A.P., Schmidt, R..J., Sidebottom, O.M., "Advanced Mechanics of Materials", Wiley and Sons, New York, 1993.
25. Ajovalasit, A., Barone, S., Petrucci, G. "A review of automated methods for the collection and analysis of photoelastic data", Journal of strain analysis for engineering design, 33: (2) 75-91 Mar 1998
26. Briers, J.D., "Holographic, Speckle and moiré techniques in optical metrology", Progress in Quantum Electronics 17: (3) 167-233 1993.
27. Barone, S., Patterson, F.A., "Full-field separation of principal stresses by combined thermo- and photoelasticity", Experimental Mechanics 36: (4) 318-324 Dec 1996.
28. Takasaki, H. "Moire Topography", Applied Optics, 9(6) pages 1467 –1472. 1970
29. Hariharan, P., "Optical Holography Principles, Techniques and Applications", Cambridge Unvierstiy Press, 1984.

30. Johnson, P. "Strain field measurements in Industrial applications using dual-beam digital speckle photography", Optics and Lasers in Engineering, 30, 315 – 324, September, 1998.
31. Briers, J.D., Webster, S. "Quasi real-time digital version of single-exposure speckle photography for full-field monitoring of velocity or flow-fields", Optics Communications, 166 (1-3), 36-42, April 15, 1995.
32. Lökberg, O., "Electronic Speckle Pattern Interferometry", Physics in Technology, 11, 1980.
33. Butters, J.N., Jones, R.C., Wykes C., "Electronic Speckle Pattern Interferometry," in Speckle Metrology, R. K. Erf, Ed., pp. 111-157, Springer - Verlag, 1975.
34. Butters,J.N., Leendertz, J.A., "Holographic and Video Techniques applied to Engineering Measurement"' Transaction of the Institute of Measurement and Control, 1971.
35. Butters, J.N., Leendertz, J.A. "A double exposure technique for speckle pattern interferometry", Journal of Physics E: Scientific Instruments, 4, 277-279, 1971.
36. Rustad, R., Lokberg, O., Pederson, H.M., et al. "TV holography measurements of underwater acoustic fields", Journal of Acoustic Society of America 102, (3) 1904-1906, 1997.
37. Slettemoen, G. A., "Electronic speckle pattern interferometric system based on a speckle reference beam", Applied Optics, 19, 616-623, 1980.
38. Gulker, G., et al. "Electronic speckle pattern interferometry systems for in situ deformation monitoring on buildings", Optical Engineering 7, July 1990.
39. Green, R.J., Walker, J.G. "Investigation of the Fourier-transform method of fringe pattern analysis", Optics and Lasers in Engineering 8, 29-44, 1988.
40. Creath, K., "Phase-shifting Speckle Interferometry", Applied Optics, Vol. 24, 3053, 1985.
41. Proceedings of the "International conference on applied optical metrology", ed. Rastogi, P.K., Balatonfured, Hungry, June, 1998.
42. Jin, F., Chiang, F.P. "ESPI and digital speckle correlation applied to inspection of crevice corrosion on ageing aircraft", Research in Non-Destructive Evaluation, 10 (2), 63-73, 1998.

43. Zhang, Z.Y., Richardson.M.O.W., Tyrer, J.P., Petzing, J. "Application of phase stepping electronic speckle pattern interferometry to non-destructive testing of GRP composite materials", Insight, 40 (3), 183-187, March 1998.
44. Buckberry, C. H, Towers, D. P., "The application of automatic fringe analysis techniques in the automotive industry", Test Techniques, Rover Group, 1993.
45. Bosco C., Cadoni E., Facchini M., "Deformation Measurements by ESPI Technique on Clay Components used in Beam-block Concrete Floors". Proc. of the 2nd international conference on non destructive testing of concrete in the infrastructure", 17-25, SEM Pub., Nashville, USA, June 12-14, 1996.
46. Binda L., Facchini, M., Roberti, G.M., Tiraboschi, C. "Electronic speckle Interferometer for the deformation measurement in masonry testing", Construction and building materials 12: (5) 269-281, July, 1998.
47. Wang Z. G., Etteymeyer A., "Deformation and strain field analysis on spot welded joints with 3D-speckle measuring techniques", Technisches Messen, 65, 105-108, March, 1998.
48. Moore A. J., Hand, D. P., Barton, J. S., Jones, J. D. C., "Transient deformation measurement with electronic speckle pattern interferometry and a high-speed camera", Applied Optics, 38, 1159-1162, 1, 1999.
49. Lucia A. C., Zanetta, P. M., Facchini, M., "electronic speckle pattern interferometry applied to the study and conservation of paintings", Optics and Lasers in Engineering, 26, 221-223, 1997.
50. Malmo J.T., Lökberg O.J., Slettemoen G.A., "Interferometric Testing at very high Temperatures by TV Holography (ESPI)", Experimental Mechanics, p315, September 1988.
51. Lökberg O.J., Malmo J.T., Slettemoen G.A., "Interferometric Measurements of high Temperature Objects by Electronic Speckle Pattern Interferometry", Appl. Opt., Vol. 24, p3167, 1985.
52. Gonda S., et al., "Accurate topographic images using a measuring atomic force microscope", Applied Surface Science, 145: 505-509, April 1999.
53. Garratt J.D., Nettleton D.J., "A stylus instrument for roughness and profile measurement of ultra-fine surfaces", International Journal of Machining Tools and Manufacture, 32, 233-238, 1992.

54. "Surface Science : The first thirty years", Ed. Charles B. Duke, North-Holland, 1994.

55. Fruhauf J., "Problems of contour measuring on microstructures using a surface profiler", Measurement Science & Technology 9: (3) 293-296 March 1998.

56. Strand T.C., Katzir Y., "Extended unambiguous range interferometry", Applied Optics 26, 4274-4281, 1987.

57. Dresel T., Hausler G., Venzke H. "Three dimensional sensing of rough surfaces by coherence radar", Applied Optics 31, 919-925, 1992.

58. Lee B. S., Strand T. C. "Profilometry with a coherence scanning microscope", Applied Optics 29, 3784-3788, 1990.

59. Chim S.S.C., Kino G.S. "Correlation Microscope", Optics Letters, 15, 579-581, 1990.

60. Davidson M., Kaufman K., Mazor I., Cohen F. "An application of interference microscopy to integrated circuit inspection and metrology", Proceedings Photo-Optical Instrument Engineering, 661, 296-301, 1986.

61. Shang J.H., Cai L.L., "Profilometry using an optical stylus with interferometric readout", Measurement Science & Technology, 8 (5), 546-549, May 1997.

62. Laguarta F., Al-Khatib I., Artigas R., "Laser profiler based on the depth from focus principle", Journal of Optics-Nouvelle Revue D Optique, 29 (3), 236-240, June 1998.

63. Lehmann P., Patzelt S., Schone A., "Surface roughness measurement by means of polychromatic speckle elongation", Applied Optics, 36, 10, 2188-2197, April 1997.

64. Lehmann P., "Surface roughness measurement based on the intensity correlation function of scattered light under speckle-pattern illumination", Applied Optics, 38, (7), 1144-1152, March, 1999.

65. Laser focus world, "Tunable laser diodes support DWDM application", 35, 4, April 1999.

66. Herriott H., "Digital wavefront measuring interferometer for testing optic surfaces and lenses", Applied Optics 13, 2693, 1974.

67. Creath K., "Step height measurement using two-wavelength phase-shifting interferometry", Applied Optics, 26, 2810-2816, 1987.

68. Cheng Y.Y., Wyant J.C., "Multiple-wavelength phase shifting interferometry", Applied Optics, 24, 804-806, 1985.
69. Huang Y.C., Chou C., Chou L.Y., Shyu J.C., Chang M., "Polarized optical heterodyne profilometer," Japanese Journal of Applied Physics Part 1 – Regular Papers Short Notes & Review Papers, 37, (1), 351-354, January, 1998.
70. Caber P.J., "Interferometric profiler for rough surfaces," Applied Optics 32, (19), 3438-3441, July 1993.
71. Davidson M., Kaufman K., Mazor I., "First results of a product using coherence probe imaging for wafer inspection," Proceedings Photo-Optical Instrument Engineering, 921, 100-114, 1988.
72. Chim S.S.C., Kino G.S., "Phase measurements using the Mirau correlation microscope", Applied Optics, 30, 2197-2201, 1991.
73. Chim S.S.C., Kino G.S., "Three-dimensional image realization in interference microscopy", Applied Optics, 31, 2550-2553, 1992.
74. Vorburger T.V., Dixson R.G., Tsai V., Doi T., Song J.F., Renegar T.B., Fu J., "Problems in surface metrology", International Journal of Machine Tools & Manufacture, 38 (5-6), 417-418, 1998.
75. Browne, M. A., Akinyemi O., Boyde A., "Confocal surface profiling utilizing chromatic aberration", Scanning, 14, (3), 145-153, 1992.
76. Davidson M., Kaufman K., Mazor L., Cohen F., "An application of interference microscopy to integrated circuit inspection and metrology," Integrated circuit Metrology, Inspection and Process Control SPIE 775, 223-247, 1987.
77. Lin J.F., Su X.Y., "2-dimensional Fourier-transform profilometry for the automatic-measurement of 3-dimensional object shapes," Optical Engineering 34, (11), 3297-3302, November, 1996.
78. Hart M., Vaas D.G., Begbie M.L., "Fast surface profiling by spectral analysis of white-light interferograms with Fourier transform spectroscopy", Applied Optics 37, (10), 1764-1769, April 1998.
79. Sandoz P., "An algorithm for profilometry by white-light phase-shifting interferometry," Journal of Modern Optics, 43, (8), 1545-1554, August 1996.

80. Gasvik K. J., "Optical Metrology", 2nd ed., John Wiley & Sons Ltd., Chichester, England 1995.
81. Hecht E., Zajac A., "Optics", 2nd ed., Addison-Wesley Publishing Company, 1987.
82. Guenther R. D., "Modern optics", John Wiley & Sons Inc., U.S.A., 1990.
83. Deck L., De Groot P., "High –speed non-contact profiler based on scanning white-light interferometry", Applied Optics, 33. No.31, 1st November 1994.
84. WYKO Product brochure, "Range of white light surface profilers", WYKO Corporation, Tucson, Arizona, 1998.
85. Lee B. S., Strand T. C., "Profilometry with a coherence scanning microscope", Applied Optics, 29. No. 26, 10th September 1990.
86. Zygo Product brochure, "New view 100:3D imaging surface analyzer", Zygo Corporation, Middlefield, Conneticut, 1993.
87. Larkin K. G., "Efficient nonlinear algorithm for envelope detection in white light interferometry", Journal Of Optical Society Of America, A 13, 832-843, 1996.
88. Zankowsky D., "How to chose a digital imaging camera", Laser Focus World, 137-150, September 1997.
89. Oppenheim A. V., Shafer R. W., "Digital signal processing", Prentice Hall, 1975.
90. Bracewell R. N., "The Fourier transform and its applications", McGraw-Hill, New York, 1978.
91. Kino G. S., Chim S. S. C., "Mirau correlation microscope", Applied Optics, 29, 3775-3783, 1990.
92. Sirohi R. S., "Speckle Metrology", Marcel Decker, Inc., New York, 1993.
93. Goodman J. W., "Laser speckle and related phenomena", Chapter 2, ed. J.C.Dainty, Springer-Verlag: Berlin, 1975.
94. Dainty J.C., "Laser speckle and related phenomena", Topics in Applied Physics Vol 9, Springer-Verlag: Berlin 1975.
95. Francon M., "Laser speckle and applications in optics", Academic Press: New York, 1979.
96. Khetan R. P., Chiang F. P., "Strain analysis by one-beam laser speckle interferometry", Applied Optics 15, (9), September 1976.

97. Potorski, Olszak, "Digital in-plane electronic speckle patter shearing interferometry", Optical Engineering 36, (7), 2010-2015, July 1997.

98. Jones R., Butters J., "Some observations of the direct comparison of the geometry of two objects using speckle pattern interferometric contouring", Journal of Physics E:Scientific Instruments 1975, Vol. 8.

99. Malmo J. T., Lokberg O.J., Slettemoen G. A., "Interferometric testing at very high temperatures by TV holography (ESPI)", Experimental Mechanics, November, 1987.

100. Wykes C., Butters J. N., Jones R., "Fringe contrast in electronic speckle pattern interferometry", Applied Optics 20, (5), March 1st 1981.

101. Ganesan A. R., Joenathan C., Sirohi R. S., "Sharpening of fringes in digital speckle pattern interferometry", Applied Optics 27, (11), June 1998.

102. Hofling R., Osten W., "Speckle pattern correlation by digital image processing", at Symposium on Laser Application in Precision Measurement, Budapest, 19-21, November 1986.

103. Tyrer J. R., "Critical review of recent developments in electronic speckle pattern interferometry", Proceedings Photo-Optical Instrument Engineering, 604, 95, 1986.

104. Creath K., "Phase shifting interferometry," Applied Optics, 24, (18),, September 1985.

105. Roddier C., Roddier F., "Interferogram analysis using Fourier transform techniques", Applied Optics, 26, (9), May, 1668-1673, 1987.

106. Bone D. J., "Fourier fringe analysis: the two-dimensional phase unwrapping problem", Applied Optics, 30, (25), 3627-3632, September, 1991.

107. Fan H., Wang J., Tan Y. S., "Simultaneous measurement of whole in-plane displacement using phase-shifting ESPI", Optics and Lasers in Engineering 28, (4), 249-257, November 1997.

108. Pactrov V., Lau B., "Electronic speckle pattern interferometry with a holographically generated reference wave", Optical Engineering 35, (8), 2363-2370, August 1996.

109. The ESPI SD-30, Newport Catalog, Newport Instruments AG, Switzerland, 1998.

110. Clarke G. M., Cooke D., "A basic course in statistics", Edward Arnold Ltd., London, 1983.

111. Joenathan C., Khorana B. M., "Phase-measuring fiber optic electronic speckle pattern interferometer: phase step calibration and phase drift minimization", Optical Engineering 31, (2), February 1992.

112. Facchini M., Zanetta P., Paletti D., Schirripa Spagnolo G., "An endoscopic system for ESPI", Selected contributions to the Second International Conference on Optics Within Life Sciences, Germany, October 1992.Elsvier, Amsterdam 1993.

113. Ettemeyer Product Catalogue, 1998, Dr Ettemeyer GmbH & Co., Neu-Ulm, Germany.

114. Facchini M., "Optical techniques applied to the study of building materials and to the inspection of civil structures", PhD thesis, Loughborough University of Technology, 1996.

115. Lokberg O., Ledang O., "Vibration of flutes studied by electronic speckle pattern interferometry", Applied Optics 23, (18), September 15th 1984.

116. Dyrseth A., Skatter S., "Vibration analysis of logs with electronic speckle pattern interferometry", Applied Optics 36, (16), June 1st 1997.

117. Dyrseth A., Spooren R., "Measuring mixing dynamics of transparent fluids with electronic speckle pattern interferometry", Applied Optics 36, (25), September 1st 1997.

118. Neiswander P., Slettemoen G., "Electronic speckle pattern interferometric measurements of the basilar membrane in the inner ear", Applied Optics 20, (24), December 15th 1981.

119. Moore A. J., Tyrer J. R., "An electronic speckle pattern interferometer for complete in-plane displacement measurement", Measurement Science Technology1, 1024-1030, England 1990.

120. Zou et al., "Geometry for contouring by electronic speckle pattern interferometry based on shifting illuminating beams", Applied Optics 31, (31), November 1st 1992.

121. Robinson D. W., Reid G. T., "Interferogram Analysis : Digital Fringe Pattern Measurement Techniques", IOP Publising Ltd., 1993.

122. Creath K., "Phase-measurement interferometry techniques", Chapter 5, Progress In Optics, editor Wolf E., Elseveir Science Publishers B.V., 1988.

123. The Carre phase determination method, from Creath K., "Phase-measurement interferometry techniques", Chapter 5, Progress In Optics, editor Wolf E., Elseveir Science Publishers B.V., 1988.

124. Kujawinska M., Spik A., Wojciak J., "Fringe pattern analysis using Fourier transform techniques", Interferometry, SPIE Volume 1121, 130-135, 1989.

125. Kreis, T., "Digital holographic interference-phase measurement using the Fourier-transform method", Journal Optical Society of America A, Vol 3, 847-855, June 1986.

126. Creath K., "Comparison of phase unwrapping algorithms by using gradient of first failure", Applied Optics 35, (25), September 1996.

127. Veuster, et al., "Disk growing algorithm for phase map unwrapping : application to speckle interferograms", Applied Optics 35, (2), January 10th 1996.

128. Ghigila D. C., Romero L. A., "Robust two-dimensional weighted and unweighted phase unwrapping that uses fast transform and iterative method", Journal Optical Society of America. A., Vol. 11, January 1994.

129. Bothe T., Burke J., Helmers H., "Spatial phase shifting in electronic speckle pattern interferometry: minimization of phase reconstruction errors", Applied Optics 36, (22), August 1st 1997.

130. Stetson K. A., Wahid J., Gauthier P., "Noise-immune phase unwrapping by use of calculated wrap regions", Applied Optics 36, (20), July 10th 1997.

131. Huntley J. M., "Suppression of phase errors from vibration in phase-shifting interferometry", Journal of Optical Society of America 15, (8), August 1998.

132. Oreb B., "A quest for the elusive phase-shifting algorithm", IOP Conference Proceedings, Applied Optics and Optoelectronics, Ed. KTV Grattan, Reading, 1996.

133. Zygo product brochure, "Maxim GP™ Surface Profiler", Zygo Corporation, Middlefield, Conneticut, 1993.

134. Bowe B., Toal V., "A white light interferometer for surface profiling", IOP Conference Proceedings, Applied Optics and Optoelectronics, Ed. KTV Grattan, Reading, 1996.

135. Bowe B., Toal V., "White light interferometric surface profiler", Optical Engineering, 37, 1796-1799, 1998.

136. Bosco C., Iori I., "Fracture mechanics of clay blocks : experimental investigation of specimens in bending and analysis of characteristic parameters", Studi e Ricerche, Scuola di Perfezionamento Pesenti, Politechnico di Milano, Milano, 279-300, 1992.

137. Bosco C., "Experimental determination of fracture energy of clay elements", Conference Proceedings ESIS, Mechanisms and Mechanics of Damage and Failure of Engineering Materials and Structures, France, September 1996.

138. Bosco C, Cadoni E., Facchini M., "Crack propagation in clay elements determined by ESPI method", Conference Proceedings Photomechanics, Russia, September 1995.

139. Hu X. Z.., Wittmann F. H., "Fracture energy and fracture process zone", Materials and Structures, 25, 319-326, 1992.

140. Cedolin L., Dei Poli S., Iori I., "Experimental determination of the fracture process zone in concrete", Cement and Concrete Research, Vol. 13, 1983.

141. Goslowsky H., Menzel I., "Holographic surfac contouring using wavelength modulation of laser diodes", Optics and Lasers Technology, 22, 5, 317-321, 1990.

142. Volume 1 & 2, "Handbook of Optics", Ed. Michael Bass, Optical Society of America, McGraw-Hill, 1995.

143. Nayer J., Nagata H., Shimotsu S., Oikawa S., "Modulation characteristics of high-speed optical modulators with properly split asymmetry into their Mach-Zehnder arms", Electronic Letters, 31 (5), 3887-388, March 1995.

144. Veselka J.J., Korotky S. K., "Pulse generation for soliton systems using lithium niobate modulators", IEEE Journal of selected topic in quantum Electronics, 2 (2), 300-310, June, 1996.

145. Bahadur B., "Liquid crystals applications and uses" World Scientific Publishing, London, 1990.

146. Blinov L. M., "Electro-optical and magneto-optical properties of liquid crystals", John Wiley & Sons, Belfast, 1993.

147. Chandrasekhar S., "Liquid Crystals", Cambridge University Press, 1992.

148. Demus D. and Richter L., "Texture of Liquid Crystlas", Leonard Hill, London (1984).

149. Meadowlark Optics Catalog, "Polarization Solutions 1999-2000", Meadowlark Optics, Frederick, Colorado, USA.

150. Albrecht D., "Estimation of the 2D measurement error introduced by in-plane ESPI instruments", European Commission Technical Note No. I.99.23, February 1999.